Pluripotency state affects the mechanical phenotype of the embryonic stem cell nucleus

Xi He

Submitted in part fulfilment of the requirements for the degree of

Doctor of Philosophy

School of Engineering and Materials Science

Queen Mary University of London

Mile End Road

London, E1 4NS

2017

Abstract

The thesis aims at investigating the connection between nucleus mechanical characteristics with pluripotency state and differentiation associated with altered cell gene expression levels. The project investigates the deformation characteristics of the cell nucleus during unconfined compression in a 3D cell-seeded agarose constructs. The studies report modification in the mechanical behaviour of the nucleus in different embryonic stem cell phenotypes based on various pluripotent states (naïve or primed states) or following triggering of early differentiation. A multi-scale model is also presented to simulate dynamic details of mechanical perturbation to cells during compression.

The first chapter presents a review of the relevant literature to introduce current progress in the related research field and the second chapter describes the general methods used in the thesis including cell culture, agarose construct preparation, construct compression and microscopy recording. The third chapter presents findings of studies involving the application of compression to embryonic stem cells in naïve and primed sate within agarose scaffolds. A range of parameters relating to the relative cell/nucleus morphological modifications are recorded with analysis and discussion. Chapter four presents studies that investigate the early differentiation of embryonic stem cells from either the naïve and primed pluripotency, achieved by altering cell culture condition, and further reveals the nuclear mechanical characteristic changes. The fifth chapter describes a multi-scale model developed to simulating the 3D cell-seeded agarose compression reported in previous chapters. This model is also used to estimate cell mechanical parameters and show accurate deformation detail in different locations within the construct. A final discussion of the thesis is provided in chapter 6 with a plan for future work.

ACKNOWLEDGEMENTS

I dedicate this thesis to my beloved parents

First of all, I wish to express my most sincere gratitude and appreciation to my supervisor, Prof. David A. Lee for his patience, guidance and encouragement throughout the development of this project. I was greatly impressed by his extraordinary working attitude and tireless supervision on my project. From the deep of my heart, I see him as the greatest supervisor and I will remain my gratitude to him forever.

Thanks to all my friends in the Stem Cell lab and Cell and Tissue Engineering Lab. I will send my sincere appreciate to Stephen Thorpe first for his guidance on cell lab work and abaqus model tutorial at every Monday morning which led to the fulfillment of this project. Also, I will present my gratitude to Rui Martins. Without his guidance on cell culture and lovely Thursday Tea-Time Cell Course, it would be the Twelve Labours of Heracles for a material/engineering undergraduate student to discover the mysteries of the nucleus. Thanks to Olly Brookes and Hannah Heywood, the group meeting is always fun and active.

I would like to thank the following members of staff; Chris Mole, Shafir Iqbal, Dongsheng Wu, Ben Milson and Jonathon Hills for their great work in labs and school to support me in finishing this project.

Also, I would send my thanks to the China Scholarship Council (CSC) for funding my project and Prof. Xudong Li who provided full support to my postgraduate application. Besides, I would like to thank all my friends in the office and daily life. Rui Mao for the wonderful room-mate time and hoping our friendship lasts forever. Shuqun Chen and Guangchang Wu for the room hunting and daily shopping. Qiangying YI and Xiaolin Chen for cooking teaching. Without your care, I would be drained by loneliness in this Big London.

Lastly, and most important, I would like to thank my parents for their reminders and immense support to keep me on track through the ups and downs of this project. It is my greatest dream to make you proud. I would like to say thank you to all of you again, with the absent of any of you, I will not be able to live through these years and finish this project.

L'humaine sagesse était tout entière dans ces deux mots: Attendre et espérer!

- Alexandre Dumas (père)

TABLE OF CONTENTS

List of Figures

Chapter 1

Chapter 2

Chapter 3

Chapter 4

Chapter 5

Chapter 6

ABBREVIATIONS

2D	Two dimensions
3D	Three dimensions
AFM	Atomic force microscopy
AP	Alkaline phosphate
BME	2-Mercaptoethanol
DMEM	Dulbecco's modified Eagle's medium
DNA	Deoxyribonucleic acid
ECM	Extracellular matrix
F-ACTIN	Filamentous actin
FBS	Fetal bovine serum
PCR	Polymerase chain reaction
LIF	Leukemia inhibitory factor
mES cell	Moouse embryonic stem cell
mEF	Mouse embryonic fibroblast
RNA	Ribonucleic acid
rtPCR	reverse-transcriptional polymerase chain reaction

Chapter 1 Introduction

1.1 Stem Cell

1.1.1 Stem Cell Types and Embryonic Stem Cells

Stem cells are cells which have the ability for prolonged or unlimited self-renewal and the ability to differentiate into cells with specific functions. These attributes make them attractive for the study of a range of biological questions, associated with normal physiology and also many pathological conditions. In additional stem cells have great potential for the development of cell-based therapies for disease and other debilitating conditions.

Stem cells are often divided into three main cell categories: embryonic stem cells, fetal stem cells and adult stem cells. Embryonic stem cells (ES cells) are pluripotent cells, defined by their ability to differentiate into cell types of all three germ layers, derived from the inner cell mass of 5-day-old blastocysts in humans. They can undergo self-renewal and be able to differentiate into cells of the ectoderm, mesoderm and endoderm embryonic germ layers. With proper conditions, embryonic stem cell can theoretically differentiate into to all types of specialized cells. Adult and fetal stem cells include hematopoietic stem cells in the bone marrow, mesenchymal stem cells (MSCs) isolated from placenta, adipose tissue, lung, bone marrow and blood, neural stem cells, olfactory stem cells, intestinal stem cells, endothelial stem cells and neural crest stem cells. A further category of stem cells are induced pluripotent stem cells (iPS cells), which are not naturally occurring, but are derived via the reprogramming of adult cells (Takahashi et al., 2007). They were first reported by Shinya Yamanaka’s lab in 2006, with reprogramming based on introducing four specific genes encoding transcription factors (Takahashi et al., 2007). iPS cells are embryonic-like stem cells and exhibit features similar to embryonic stem cells.

Derived from the balstocyst stage early mammalian embryos (Figure 1.1), embryonic stem cells have attracted considerable attention due to their ability to differentiate into any cell type. Furthermore, embryonic stem cells have other properties important for regenerative medicine, notably maintaining high telomerase activity during extended population doubling, resulting in long-term proliferative potential. Since embryonic stem cell derivation results in blastocyst destruction, ethical issues arise for the derivation of human embryonic stem cells (ESHRE Task Force on Ethics and Law 2001). Therefore, mouse embryonic stem cell (mESC) are often used in basic research rather than human embryonic stem cell (hESC).

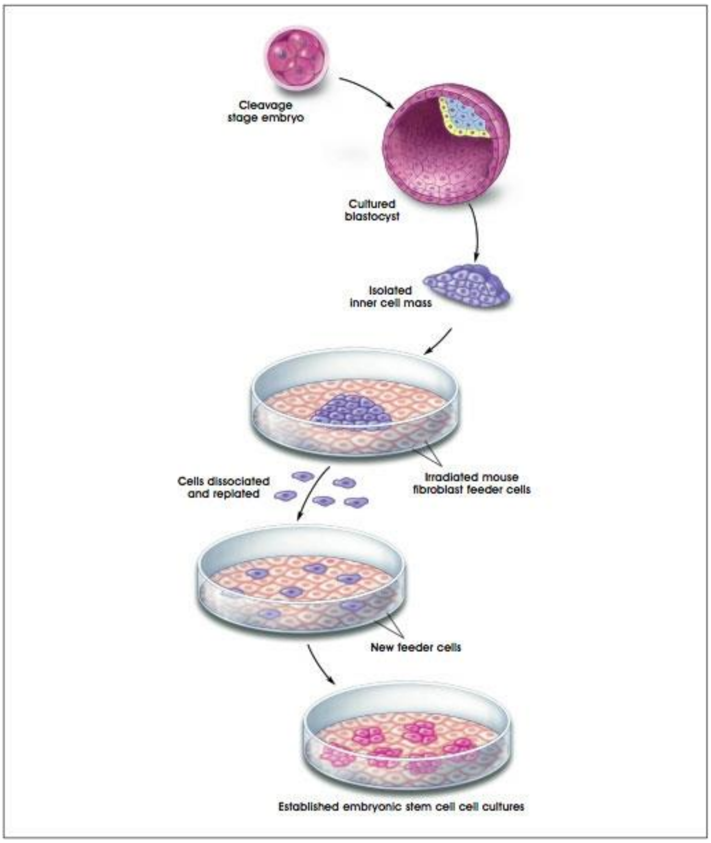

Figure 1.1 Techniques for Generating Embryonic Stem Cell Cultures (© 2001 Terese Winslow, Caitlin Duckwall)

Mouse embryonic stem cells (MES cells) were first derived using techniques based on embryonic carcinoma (EC) cell culture (Evans and Kaufman 1981, Martin 1981). The cells can propagate in culture, in an undifferentiated state, in the presence of leukaemia inhibitory factor (LIF) or a feeder layer of murine embryonic fibrobalsts (MEF) (Martin 1981). MES cells have proved valuable in many research fields, such as investigation of gene expression, the study of the initial stages of mammalian development and to further understanding of pluripotency and cell lineage specification (Evans and Kaufman 1981).

1.1.2 Pluripotency

Pluripotency represents the potential of a stem cell to differentiate into multiple cell lineages across germ layers (Kim et al., 2009), and possibly primordial germ cells (PGCs), but not extra-embryonic tissues (Weinberger et al., 2016). Embryonic stem cells with pluripotency potentially differentiate into lineages associated with all three germ layers: endoderm, mesoderm or ectoderm. Other stem cell types, for example mesenchymal stem cells have a more limited differentiation range, typically being restricted to lineages from one germ layer and are termed multipotential (Blin et al., 2010). However, recent studies suggesting that adult stem cells can differentiate to lineages associated with more than one germ layer challenges our understanding on adult stem cell differentiation (Abad et al., 2013).

Studies on mouse embryonic stem cells over recent years have determined that pluripotency is not a single state, but that various pluripotency states exist *in vivo*, that may be recapitulated within different *in vitro* culture conditions (Buehr et al., 2008). Epiblast cells are formed in the inner cell mass (ICM) in the final day of pre-implantation development in the mouse (Boroviak and Nichols, 2014, Cockburn and Rossant, 2010). This condition which supports the ability to give rise directly and clonally to embryonic stem cells is defined as naïve pluripotency state (Nichaols and Smith 2009). Upon implantation, embryonic stem cell forming capacity is abruptly lost, epithelialisation commences, global gene expression is reconfigured and DNA methylation increases, indicative of a profound cellular transition (Boroviak et al., 2014, Boroviak et al., 2015, Auclair et al., 2014). The late phase of pluripotency during gastrulation is termed primed, consistent with the expression of lineage specification factors. (Nichols and Smith, 2009, Hackett and Surani, 2014). The cellular and molecular phenotypes of naïve and primed pluripotent stem cells are distinct, leading to varying physical and biochemical characteristics (Guo et al., 2009). In regular culture conditions in vitro, mouse embryonic stem cells are grown in a state of naïve pluripotency. However, human cells are cultured in primed pluripotency conditions (Bates and Silva 2017). In this condition, similar to post-implantation epiblast, human embryonic stem cells present more primed-state attributes conducive to differentiate (Tesar et al., 2007). With the distinct pluripotency states exhibited by mouse and human embryonic stem cells, many embryonic stem cell pluripotency studies focus on mouse embryonic stem cells due to better characterization of pluripotency states and less disruption due to potential differentiation triggers. However, it has been reported that sub-populations of mouse embryonic stem cell cultures maintained in standard cell culture conditions exhibit characteristics similar to primed state mouse stem cells rather than the naïve state.

Consistent with a true differentiation event, one copy of the X chromosome in XX cells is epigenetically silenced as ESCs become EpiSCs, but reverse transition has not been observed without genetic or other manipulation (Guo et al., 2009). As a result, transferring naïve state embryonic stem cells into the primed state is easy to accomplish while reprogramming primed state embryonic stem cells into naïve cells is more challenging (Tesar et al., 2007). Several approaches to reprogramming primed state mouse embryonic stem cells have been considered. It is reported that a single factor, Klf4, can be the key to reprogramming primed state stem cells (Guo et al., 2009, Kanatsu-Shinohara et al., 2004). The induction of Klf4 results in cells that show reactivation of the X chromosome, exhibit the ESC-specific transcriptional profile, produce high contribution somatic chimeras and give germline transmission (Guo et al., 2009).

In addition, it is reported that Fgf4 and other extrinsic stimuli stimulate the ERK pathway, which is considered as critical to triggering naïve state ESC to transition to the prime state. Therefore, blocking this pathway has been successfully reported as a mechanism to retain in vitro embryonic stem cells in the naïve state. A variety of small molecular inhibitors of ERK pathway components are sufficient to block the pathway and further maintain embryonic stem cells with full naïve state pluripotency. Furthermore, it is reported that even without serum, naïve state pluripotency can be maintained in the presence of inhibitors and LIF (Guo et al., 2009, Sridharan et al., 2009). Therefore, blockage of Erk signalling plays an important role in maintenance of the naïve ground state of pluripotency (Buehr et al., 2008).

To prevent mouse embryonic stem cell transition from native state to primed state, cells are able to self-renew in the absence of external signals that may be considered to be pro-differentiation. Typically, specific signaling pathways are blocked, such as the MEK/ERK MAPK signaling axis and the GSk3d pathway, in part through its role in the degradation of b-catenin (Ying et al., 2008). In recent studies, pure naïve state mouse embryonic stem cell populations with few primed state cells can be maintained using specific defined media, an example is N2B27 medium supplemented with MEK inhibitor (1μM) and GSK3 inhibitor (3μM) plus Leukemia inhibitory factor (LIF). This medium, typically referred to as 2i medium (Betschinger et al., 2013). In mouse embryonic stem cells cultured in 2i medium, a genome wide reduction in DNA methylation is observed and this situation is similar to embryo *in vivo* (Smith et al., 2016, Leitch et al., 2013).

More clear standards with possible measurement in quantity were required to distinguish naïve state from primed state in mouse embryonic stem cell. Several transcriptional factors (Nanog, Oct4, Sox2 and Rex1) are believed to be involved in maintaining pluripotency in embryonic stem cell. (Loh et al., 2006) Their effects are believed to act via alterations in chromatin structure, involving modification to histones and DNA methylation, ultimately acting to regulate the transcription of key target genes. (Loh et al., 2006, Wang, J et al., 2006, Ben-Shushan et al., 1998)

In practical terms stem cell pluripotency can be identified by probing the expression of a panel of pluripotency markers, for example OCT4, Sox2, Nanog, Rex1 identified using RT-PCR methods, (Shi et al., 2006) immunochemistry for stage-specific embryonic pluripotency antigens (SSEA-3, SSEA-4, TRA-1-60, TRA-1-81), alkaline phosphatase activity and the methylation profiles of promoters of pluripotent-associated genes (, Ben-Shushan et al., 1998) These methods involve destruction or fixation of cells during analysis making live pluripotency monitoring impossible. Auto-fluorescent protein-based technologies such as those involving green fluorescent protein (GFP) may be used to probe pluripotency within live cells (Huangfu et al., 2008). GFP-based techniques can be used as reporters for gene expression modification in situ (Huangfu et al., 2008, Chen et al., 2008). A successful example involves OCT4-GFP, which has been used to monitor pluripotency modification in living embryonic stem cells in real time. (Boiani et al., 2002).

The transcriptional factors Oct4 and Nanog are involved in maintaining pluripotency in embryonic stem cells, with their effects achieved through alterations in chromatin structure, such as histone modification and DNA methylation (Loh et al., 2006, Shi et al., 2006, Wang et al., 2006). Oct4 is a POU domain–containing transcription factor encoded by Pou5f1 (Scholer et al., 1990). Pluripotent cells both in vivo (epiblast) and in vitro (ES cell) transition towards the trophoblast lineage in the absence of Oct4, indicating the importance of Oct4 in regulating molecule in the initial cell fate decisions during mammalian development (Nichols et al., 1998). Additionally, the increasing expression of Oct4 above the endogenous levels in ES cells leads to differentiation toward the extraembryonic endoderm lineage. These divergent effects of Oct4 suggest that Oct4 transcriptionally regulates genes involved in coordinating multiple cellular functions (Shimozaki et al., 2003). Nanog is a homeodomain-containing protein and studies indicate that Nanog is a key factor in maintaining pluripotency in embryonic stem cell. Embryos with insufficient Nanog give rise to pluripotent cells first but the cells will differentiate immediately. These findings suggest that Nanog might not be needed for early pluripotent cell production, but it is essential in maintaining the pluripotency state later (Loh et al., 2006). Furthermore, Nanog is required for chromatin remodelling in pluripotent cells (Novo and Gunn 2016).

These classic pluripotency markers are routinely used to understand pluripotency states in embryonic stem cells in response to altered environment conditions, which may involve the presence of defined chemical factors and/or biophysical perturbation (Shi et al., 2008, Ben-Shushan et al., 1998). The response of embryonic stem cells to mechanical stimuli provides a mechanism by which pluripotency states may be maintained or, alternatively, lineage-specific differentiation induced. While the actions of chemical stimuli have been extensively studies the role of mechanical perturbation remains relatively poorly understood.

1.2 Mechanical perturbation to cells – from outside to inside

It is widely reported that mechanical perturbation influences a wide range of biological processes, including development and differentiation processes and the maintenance and adaption of tissues. Furthermore mechanical forces are involved in pathological processes and tissue repair. Mechanical perturbation at the tissue level is transferred via the extracellular matrix to the resident cells. The interaction of the cell with its extracellular matrix and the relative mechanical properties of the cell and the surrounding matrix will determine the extent to which tissue-level deformation is transferred to the cellular level. Within the cell the nature of interactions between the adhesion sites, the cytoskeleton and the nucleus dictates the extent of nuclear deformation in response to a given cellular strain. Recent studies have indicated that mechanical perturbation applied to the cell may be transferred directly to the nucleus via connectivity between the extracellular matrix, cell and nucleus, with associated activation of mechanotransduction pathways (Thorpe and Charpentier 2017, Wang et al., 2009).

1.2.1 Cell deformation in response to mechanical perturbation

Mechanical forces and associated cell deformation impact on cells in various ways according to the nature of the perturbation involved and the active involvement of the cell. In particular a distinction may be drawn between situations where the external mechanical perturbation acts on the cell resulting in deformation, compared to situations where the active contractile processes within the cell are directly involved. Examples of the former are associated with the application of force at tissue-level, such as occurs during loading of musculoskeletal tissues or fluid shear with blood vessels. The latter may be induced during active cellular processes including those associated with cell adhesion and migration.

Cell migration through the extracellular matrix (ECM) is fundamental to many biological processes including tissue formation and the response to tissue injury and pathology (Sanz-Moreno et al., 2008). Cell migration has also been studied extensively in vitro in 2D and 3D model systems. Cell migration typically involved a variety of steps including actin pseudopod protrusion at leading edge of the cell, intergrin-mediated adhesion to the ECM, cell surface protease cleaving of ECM components, cell body tension originating from actomyosin-mediated contraction and cell body relocation (Friedl and Alexander, 2011). Each step is related to biochemical and mechanical signals involving adhesion regulation, cytoskeletal reorganization and cell body deformation in response to the dynamics of the ECM (Tong et al., 2012). Recent reports concluded that cell migration through the ECM depends on a physicochemical balance between cell deformability and physical tissue constraint (Wolf et al., 2012).

Cell deformability has been studies in vitro using micropipette aspiration, involving the application of a negative pressure to a cell inducing its aspiration into the confined space of the micropipette. The pressure required to induce partial of full aspiration provides a measure of cell and nucleus deformability and, by inference, stiffness. A common phenomenon observed during cell aspiration is nuclear deformation, with some studies reporting direct alteration to chromatin organization and potential DNA breaks (Irianto et al., 2017).

Tissue mechanical loading also results in cell deformation via transfer of strain through the ECM to the cell. The application of external mechanical perturbation, resulting in cell deformation, has been studies extensively using in vitro model systems either to understand basic cellular processes or in a tissue engineering context. Both stem cells and differentiated cell types have been studied. Model systems may be distinguished by those that apply stretch to cells in 2D, for example cultured on flexible membranes and more complex systems involving cells seeded within 3D constructs. Further, some systems are designed to apply loading to a population of cells while other systems are able to apply mechanical loading to a single cell. For the investigation of regulators of mesenchymal stem cell (MSC) differentiation, dynamic compression of cell-seeded scaffold has been adopted by a number of research groups, with the ability to vary key parameters of the applied mechanical perturbation, for example the magnitude, frequency, timing and duration of dynamic loading. These studies have explored the effect of mechanical perturbation on cell and nuclei deformation and associated alteration in gene expression (Steward et al, 2013). In distinct studies, optical probe microscopy and atomic force probe microscopy have used to induce mechanical deformation of cells for multiple purposes including triggering nuclear modification and measuring the mechanical parameters of cytoplasm and nucleoplasm (Krause et al., 2013, Wei et al., 2016)

1.2.2 Cytoskeletal and nuclear mechanotransduction

The application of external mechanical perturbation to cells has been demonstrated to result in nuclear deformation and alterations in chromatin organisation and condensation. The transfer of the mechanical stimulation from outer environment through the plasma membrane to the nucleus occurs via processes typically involving the cytoskeleton, LINC Complex and Lamins.

The physical interaction of cell with the extracellular environment emanates from the contact between the plasma membrane and the extracellular matrix, attached cells or fluid. Mechanical stimulate that reach the plasma membrane may induce a signaling cascade within the cell through a variety of mechanotransduction processes. Recent studies have revealed that multiple components on cell membrane are involved with mechano-sensing and mechanotransduction (Orr et al., 2006; Uzer et al., 2016). Any physical force may modify the original state of the membrane and lead to changes in connectivity with membrane-bound proteins and cytoskeletal components. The interaction between the cell and extracellular matrix are commonly via focal adhesion-based integrins (Cheresh et al., 1989; Geiger et al., 2009) while cadherin-based adhesion plays a major role in connection between cells (Lecuit et al., 2005). In addition, ion channels and G-protein coupled receptors are also active in transduction mechanical signals through the cell membrane (Eijkelkamp et al., 2013; Lansman et al., 1987; Chachisvilis et al., 2006).

The cytoskeleton (Shown as Figure 1.2) is a network of protein fibres that exists within the cell cytoplasm and may extend into the nucleus. Cytoskeletal components are found in all domains of life and are present in all eukaryotic cells. There are three major components the cytoskeleton: microfilaments (generated with protein actin), microtubules (generated with protein tubulin) and intermediate filament that may be formed from a range of proteins including vimentin, keratin and nuclear lamins. Rather than being fixed, cytoskeletal structures are highly dynamic, in which polymerisation and depolymerisation processes are constantly occurring (Leeb et al., 2011). The Cytoskeletal components are highly conserved across different organisms. Nevertheless, the structure, function and behaviour of the cytoskeleton can vary greatly between cell types (Leeb et al., 2011 Christophersen and Helin 2010). Even in the same cell type, cytoskeletal structure and function can be modified via complex interactions with cytoskeletal-associated proteins that may act as molecular motors, cross linkers, capping proteins and nucleation promotion factors (Christophersen and Helin 2010, Gomez de-Leon et al., 2014).

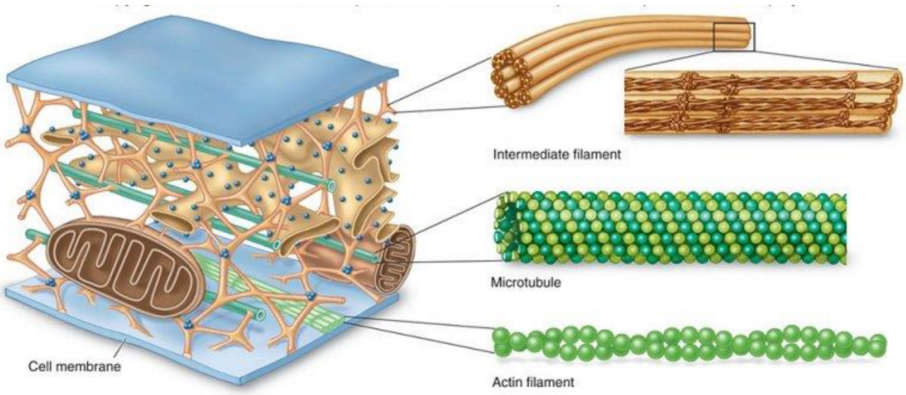

Figure 1.2 Structure of cytoskeleton

http://medicineconspectus.blogspot.co.uk/2014/01/cytoskeleton-cell-components-cell.html

The cytoskeleton exhibits multiple functions including: (1) supporting cell shape and offering resistance to mechanical deformation; (2) spontaneously contracting, which allows cell deformation for migration; (3) segregating chromosomes during cellular division; (4) guiding cell wall preparation as template; (5) forming specialized structures such as flagella and cilia; (6) involvement in cell signaling pathways, including those triggered by mechanical perturbation. It is well recognised that the cytoskeleton plays a major role in delivering the transfer of mechanical signals through cytoplasm to the nucleus in response to external stimuli.

Intermediate filament vimentin binds directly to nuclear lamina proteins providing interconnectivity to attachment sites on the plasma membrane (Georgatos and Blobel 1987). More recent research suggests that a physical link exists anchoring nuclear lamins to the cytoskeleton allowing mechanical transduction through the nuclear envelope. The molecular components involved are commonly defined as the Linker of nucleoskeleton and cytoskeleton (LINC) complex. The LINC complex is generally regarded as a major system involved in delivering physical signals from the extracellular matrix (ECM) into the nucleus.

LINC complexes largely comprise several KASH and SUN proteins (Figure 1.3), forming direct binding across the perinuclear space. KASH proteins are tail-anchored membrane proteins located on the outer nuclear membrane (ONM), which expose short peptide of residues into the perinuclear space at their termini (Sosa et al 2012). Vertebrates possess at least four different KASH proteins (Nesprin 1-4, also known as SYNE 1-4). Nesprin-1 and Nesprin-2 exist in several isoforms, and the giant ones interacts with actin via their N-terminal calponin-like actin-binding domain, a huge central spectrin-like domain and a carboxyl-terminal KASH domain (Worman and Gundersen 2006). Nesprin-3 and Nesprin-4 bind to plectin and kinesin-1, respectively bridging the nucleus to the intermediate filament and microtubule systems (Sosa et al., 2012). Recent studies indicate that cells with impaired nesprin-1, nesprin-2 and nesprin-3 exhibit decreased nucleus stiffness (Stewart-Hutchinson el al. 2008). The SUN proteins represent a further major component of the LINC complex. Tethered in the inner nuclear membrane (INM), SUN proteins expose their N-termini to the nucleoplasm (Crisp et al., 2006). Interaction between the Sun proteins (SUN-1 and SUN-2) and KASH proteins (Nesprin-1 and Nesprin-2) plays a significant role in chromatin organization and nuclear migration (Ding et al. 2007, Zhang et al., 2009). However it remains unclear exactly how SUN proteins and KASH proteins are located on INM (Puckelwartz et al. 2009).

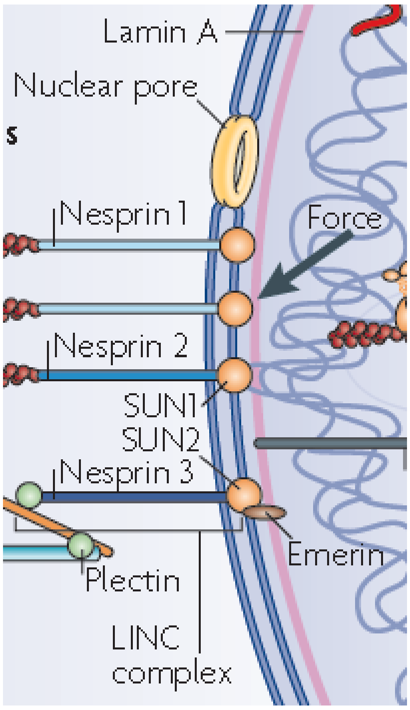

Figure 1.3 Structure of LINC complex *Ning et al Nature, 10, 75-82 (2009))*

Emerin is a nuclear membrane protein located on INM and it is anchored to Nesprin-3/SUN-2. An investigation in Emery-dreifuss muscular dystrophy patients found that loss or mutation of emerin is related to altered nuclear envelope elasticity, leading to increased nuclear fragility (Lammerding et al., 2006). In addition, as emerin interacts with splicing factors, forces transferred through the LINC complex may influence gene expression via modification of transcription or splicing factors (Wang et al., 2009). In addition the nuclear pores complex (NPC) can mediate mechanochemical conversation and gene expression via structural modifications and associated alterations in transport phenomena (Feldherr and Akin 1990). However, whether SUN-1 binds Nesprin-1, Nesprin-2 and NPC simultaneously needs further investigation.

The LINC complex is widely regarded as a critical system mediating the transfer of mechanical signal between cytoskeleton and nucleus. Disruption of the LINC complex, contributes to defects in nuclear positioning, impaired propagation of intracellular forces and disruption to the organization of the perinuclear actin and intermediate filament networks (Richards and Elgin 2002). As a result, disconnect between the nuclear lamina and the cytoskeleton decreases nuclear displacement and deformation in response to mechanical strain propagated from the extracellular matrix (Lombardi et al., 2011). In addition, there is evidence reporting that LINC complex disruption results in softening of the nucleus and altered nuclear structure (Richards and Elgin 2002). LINC complex knock-down studies reveal disrupted mechanical transmission through the nuclear envelope which influences nucleus deformation, cell migration and gene expression (Crisp et al., 2006, Pucklwartz et al., 2009, Lombardi et al., 2011).

Nuclear lamins, also known as Class V intermediate filaments, are fibrous proteins residing within cell nucleus (Cooper and Hausman 2000). The main function of nuclear lamins is to provide structural function and act as regulators of transcription. On the interior of nuclear envelope, nuclear lamins interact with membrane-associated proteins to form the nuclear lamina. Nuclear lamins are involved in reformation of nuclear envelope during mitosis and positioning of nuclear pores. In animal cells, there are three differentially regulated genes resulting in two major classes of lamins based on length and isoelectric point: A-type lamins and B-type lamins (Vijay et al., 2009). The most common A-type lamins are Lamin A and Lamin C, and they are splice variants of the LMNA gene found at 1q21. B-type lamins, Lamin B1 and Lamin B2, are expressed from the LMNB1 and LMNB2 genes respectively at 5q23 and 19q13. Compared with A-type lamins, B-type lamins are more commonly expressed and are present in almost every cell (Vijay et al., 2009).

Nuclear lamin are a key component in the systems that transduce mechanical signals through the nuclear envelope Lamins A/C, B1 and B2 contribute to nuclear-cytoskeletal coupling and mechanotransduction. Cells lacking lamins A and lamins C or expressing particular lamin A/C mutations exhibit disruption to perinuclear-cytoskeletal organization and reduced cytoskeletal stiffness, resulting in impaired cell migration (Vijay et al., 2009, Gruenbaum et al., 2000, Stuurman et al., 1998). Similarly, cells lacking functional lamin B1 display a nuclear anchoring defect with spontaneous and sustained nuclear rotation (Gruenbaum et al., 2000). Mice with deficient lamin B2 exhibit severe brain abnormalities, believed to be related to defective neuronal migration (Stuurman et al., 1998).

1.2.3 Nucleus modification

The mechanical properties of the nucleus are dictated by a combination of the nucleoplasm, chromatin and the nuclear lamina. It is generally considered that the internal nuclear organisation, comprising a mixture of chromatin and nucleoplasm is softer than lamina. The stiffness of nucleus varies according to the cell type and cell-ECM contact (Guilak et al., 2000). Reports show that differentiated cells typically possess stiffer nucleus than various stem cells types, including embryonic stem cells. In addition the embryonic stem cell nucleus in its naïve state is stiffer than in the primed state (Pagliara et al., 2014). Using mechanical perturbation achieved via atomic force probe microscopy or dynamic cell compression it is possible to deform the nucleus resulting in both geometry modification and chromatin relocation (Krause et al., 2013; Lee et al., 2000). These phenomena will potentially impact gene expression behaviour as discussed in section 1.3.

1.3 Epigenetic modification

Alteration to gene expression may be mediated by a wide variety of mechanisms. For example, the translocation of activated transcription factors that bind directly to DNA sequences and act to activate transcription. In addition the organisation of the DNA in higher order chromatin structures may act to silence genomic regions, or allow transcription. Chromatin and DNA organisation is regulated by modification to the DNA and histones, via epigenetic modifications commonly associated with methylation and acetylation. These transcriptional regulatory mechanisms occur as part of normal physiology and differentiation and are may be sensitive to mechanical perturbation. Further artificial methods exist to regulate genome function, for example manipulating genome content in an organism using genetic modification as an engineering tool. Alternatively knock-down of specific genes can be achieved by introducing siRNA.

1.3.1 Chromatin and its link with maintenance of pluripotency

Nuclear organisation and architecture plays a major role in the regulation of gene expression by modifying gene interactions. Chromatin, comprises DNA, proteins components including histones and RNA. The chromatin structure acts to package and protect genomic DNA and regulate genome function. Eukaryotic cells possess chromatin while prokaryotic cells have distinct organisation of DNA, known as genophore. Within the chromatin, histone proteins act to package and order DNA into structural units called nucleosomes, which protects the DNA and regulates function (Gruenbaum et al., 2000).

There are five major families of histone: H2A, H2B, H3 and H4 are known as the core histones, while H1/H5 are known as linker histones (Luger et al., 1997). The core histones form an octameric nucleosome core which is wrapped around by DNA. Histone H1 binds the nucleosome at the both ends of the DNA, which locates the DNA in place for higher order structure. During mitosis and meiosis, the condensed chromosomes are assembled through interactions between nucleosomes and other regulatory proteins (Gruenbaum et al., 2000). The four core histones are similar in individual structure and highly conserved featuring a 'helix un helix un helix' motif for easy dimerization (Luger et al., 1997). The nucleosome core is assembled with two H2A-H2B dimers and a H3-H4 tetramer and presented as an axially symmetric structure. There is a long tail on each of the histones which acts as the location for post translation modification. It is thought that histones are evolutionarily related to the helical part of the extended AAA+ ATPase domain, the C-domain, and to the N-terminal substrate recognition domain of Clp/Hsp 100 poteins (Calo et al., 2013). Despite the differences in their topology, they share a homologous helix-strand-helix (HSH) motif (Calo et al., 2013). Post-translation modification of H3 and H4 histones, involving methylation and acetylation at sites including H3K9ac, H3K4me3 and H3K27me3, have attracted great attention since they are involved the regulation of gene expression. Acetylation is mediated by dynamics of histone acetyltransferases (HATs) and histone deacetylases (HDACs). Early studies showed that acetylation is related to gene activation (Allfrey et al., 1964), and more recent studies have confirmed that total nuclear levels of H3K9ac are higher in stem cells than in differentiated cells, linked to different expression patterns (Krejci et al., 2014). Since HDACS and HATS have been reported to correlate with genes associated with pluripotency maintenance, such as Oct4, Sox and Nanog, the balanced between HAT and HDAC activity may be essential in determining the pluripotency state of embryonic stem cells (Abad et al 2013). Methylation also leads to specific epigenetic modification with mono-, di- or tri-methylation of histones known to activate or suppress specific gene expression. ChIP-seq has helped to define the epigenetic landscapes of pluripotent and differentiated cells by facilitating the description of specific epigenetic histone marks at all nucleosomal positions of the genome. Studies have demonstrated that euchromatin, measured by the amount of H4K36me2 and H3K4me3, is more prevalent in pluripotent cells than differentiated cells while heterochromatin, measured by H3K9me3, is reduced in pluripotent cells (Krejci et al., 2014). Chromosome territories are not randomly arranged in the nuclei and the positioning of chromosome territories relates to specific transcriptional states (Lieberman-Aiden et al 2009). Phenomena, such as chromatin decondensation and chromatin condensation, modifies transcriptional states, leading to gene activation and suppression. The chromatin condensation state is linked to histone landscape and epigenetic alterations and can define cell fate and/or maintenance of pluripotency (Lee et al., 1998).

1.3.2 Gene regulatory network

Since cells, regardless of cell type, share the same genome, cell fate is dictated by the gene expression profile. Guiding stem cell differentiation towards specific cell fate is not fully understood, but it is believed that the gene regulatory network has a great impact on cell fate, and one gene regulatory networks is shown as Figure 1.4. Working like internet network, the gene regulatory network receives input and creates output to respond external environment signals (Gilbert and Epel 2009). Current research reveals that gene regulatory network functions via a series of gene switches. The major types of molecular process for cell fate are through cell signalling pathways, triggered by a variety of stimuli, including soluble growth factors/cytokines, adhesion to the insoluble ECM and mechanical perturbation. The details of cellular signal transduction are complex are not completely clear, but many pathways share the following steps: (1) An extracellular event, such as ligand binding or mechanical perturbation, induces a conformational change in the receptor. (2) The activated receptor triggers reactions involving other protein within the cell, for example phosphorylation. (3) A cascade of phosphorylation reactions eventually activates a transcription factor which translocates to the nucleus to induce altered gene expression (Gilbert and Epel 2009).

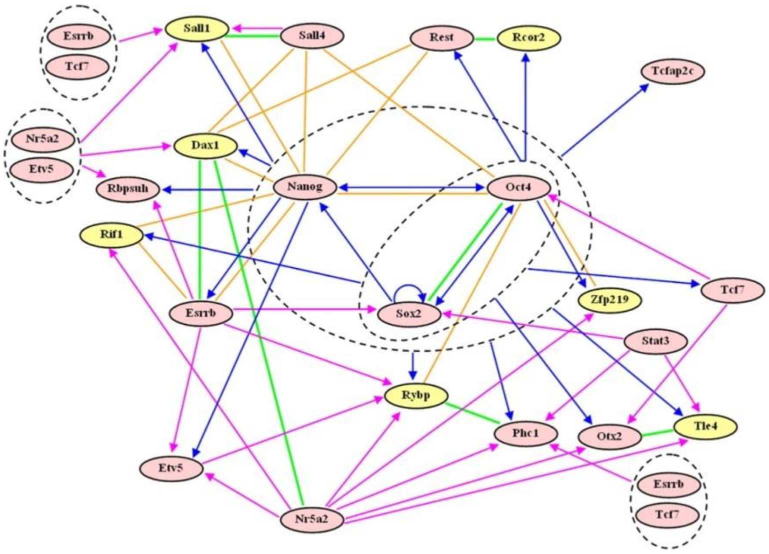

Figure 1.4 A gene regulatory networks in mouse embryonic stem cells *Qing Zhou et al PNAS vol. 104 no. 42 , 16438–16443*

Studying cellular signal pathway induction and transduction in response to a variety of triggers, including mechanical perturbation is key to the investigation of stem cell pluripotency maintenance and lineage-specific differentiation. Moreover the knowledge gained may be used within cell therapies and regenerative medicine approaches to control cell differentiation for therapeutic benefit.

1.3.3 Chromatin condensation from mechanical perturbation

Over the past 20 years an increasing number of studies have reported that nuclear structure, including chromatin organisation and location, can be modified by mechanical perturbation from the external environment or induced via the contractile mechanisms of the cell. Compressive or tensile strain applied to cells can trigger nuclear deformation and leads to chromatin condensation or decondensation events. As chromatin alteration relates to gene expression activation and suppression, mechanical perturbation may induce epigenetic-like modifications to alter cell fate. Accordingly, understanding the cell and nucleus as mechanical components is critical to elucidating how mechanically-induced nuclear deformation and alterations in nuclear architecture trigger epigenetic modifications.

Many techniques have been used to reveal and quantify cell and nuclear deformation and to estimate relative mechanical properties. Atomic force microscopy (AFM) is a well-established technique whereby the AFM acts both to apply mechanical perturbation and to detect the resultant nuclear deformation with the probe used to measure stiffness of cytoplasm and nuclei (Krause et al 2013). The advantage of AFM probe loading is that it directly contacts the cell membrane for for stiffness testing. However, AFM probe loading can only be meaningfully used for cells in suspension or during adherent 2D culture, which may not be representative of the in situ state for cells in 3D tissues (Akhremitchev et al 1999). Osmotic challenge, which is linked to compression in many tissues including cartilage, has been used to induce chromatin condensation and alterations in cell and nuclear properties (Irianto et al 2013). Physiological osmotic challenge leads to rapid and reversible alterations in the chromatin condensation states in chondrocytes (Irianto et al 2013). Micro-pipette aspiration and mechanical perturbation using optical tweezers have also been used to induce nuclear deformation and chromatin reorganisation. However, these methods have their disadvantages such as induction of damage to the nucleus and DNA complicated operation which can only gain data from a single cell at a time (Irianto et al 2016).

In the current study, we require a method to understand primary mechanical characteristics of cell and nuclei in embryonic stem cells during compression in differing pluripotency and differentiation states. Further the system should be suitable for visualisation of chromatin condensation states within the nuclei. A well-established system involves seeding cells within 3D agarose scaffolds, which has been used by many researchers to investigate the effects of compression on cells including chondrocytes, myoblasts and mesenchymal stem cells (Lee et al 1998). The cell-seeded agarose system allows cells to be embedded within the gel, with maintenance of cell and nuclear morphology for cells that do not typically adopt a adherent and spread morphology that is characteristic of cells culture in 2D monolayer systems. (Lee et al 2000). Furthermore compression applied to the agarose construct induces deformation of the embedded cells that provides a realistic model for 3D tissue loading with limited damage to cells.

Since the agarose compression is convenient to investigate with simple biological support, extended live recording is possible as well as biological characterization in bio-reactor systems.

1.3.4 Nuclear resistance to nuclear modification

Mechanical signals are generated by mechanical perturbation in the extracellular matrix, sensed by mechanosensing proteins on cell membrane and transmitted through mechanotransduction to nucleus. The nucleus receives the mechanical stimulation and may respond by deformating. Similar to the effects of the stiffness of the cytoplasm on cellular deformation, nuclear resistance to morphological modification is dictated by the mechanical properties of nucleus. Many factors impact the nuclear resistance to nuclear modification. The presence and organization of Lamins greatly influences nuclear resistance to deformation (Kirby et al., 2016). Results of Lammerding's research suggests that Lamin A/C plays a major role in regulating nuclear deformation rather than Lamin B (Lammerding et al., 2006). In addition chromatin packing also influences nuclear mechanical properties. Chalut's group found that an auxetic nucleus is observed when mouse embryonic stem cell transition to the primed state, and that pluripotency state alters nucleus stiffness (Kabla and Chalut, 2014, Pagliara et al., 2014, Chalut 2015). Moreover, recent studies reveal that differentiation brings significant modification of nuclear architecture and mechano-sensing (Heo et al., 2016).

1.4 Cell-Seeded Agarose compression and Multi-scale Finite Element Model

1.4.1 Agarose

Agarose (structure is shown as Figure 1.5) is a polysaccharide polymer extracted from sea weed. It is one of the two principal components of agar, and it is purified from agar by removing the other component of agar, agaropectin (Phillips 2000). Agarose can be dissolved in near-boiling water and form a gel when the mixture cools down. Agarose follows the thermal hysteresis phenomenon during liquid-and-gel transition and as a result its gelling temperature and melting temperature are different (Al-Assaf et al 2006). Gelling and melting temperature depends on both the type of agarose and the concentration of the gel. Typically, gelling temperature range between 34 °C and 38°C with melting temperature between 90°C to 95°C.

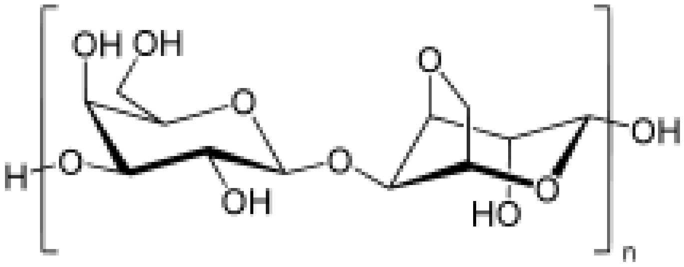

Figure 1.5 Structure of agarose polymer

Agarose is a linear polymer made up of the repeating disaccharide units comprising D-galactose and 3,6-anhydro-L-galactopyranose, linked by α-(1→3) and β-(1→4) glycosidic bonds (Gulrez et al 2011). Some D-galactose and L-galacose units can be methylated and pyruvate and sulfate are also foud in small quantities (Gulrez et al 2011). Each agarose chain contains ~800 molecules of galactose, and the agarose polymer chains form helical fibres that aggregate into a supercoiled structure with a radius of 20-30 nm (Shalaby et al 1993). The fibres are quasi-rigid and have a wide range of lengths depending on the agarose concentration (Mitchell 1998). When solidified, the fibres form a three-dimensional mesh of channels with diameters ranging from 50 nm to >200 nm depending on the concentration of agarose used, with higher concentrations yield lower average pore diameters. The 3D structure is held together with hydrogen bonds and can be disrupted by heating back to a liquid state.

The structure and physical behaviour of agarose gels have been extensively studied. Watase and Nishinari have reported a complete investigation of the effects of molecular weight upon the rheological characteristics of agarose gels. The behaviour of agarose was compared to previous investigations on alternative biopolymer gel systems, such as gelatine, alginates, and –carrageenan (Mitchell 1998). Regardless of the nature of the biopolymer, a fall in elastic modulus was demonstrated when the molecular weight is lowered at a constant weight concentration, following the relationship where the concentration c is expressed in gâL-1 (Phillips et al 2006). However, this relationship is rather empirical and was first proposed for application to gelatine gels. Agarose gel formation and aging mechanisms are different from those occurring in gelatin gels. Small differences in agarose gelation temperature have been observed for agarose solutions with different intrinsic viscosities. This is believed to be a linear function of the average molecular weight. In addition, differences have been noted for the agarose gel modulus, failure properties, and melting temperatures (Shalaby et al 1993).

1.4.2 Cell-Seeded Agarose Construct

In previous studies of mechnotransduction and the mechanical properties of cell, agarose was commonly use to provide a three dimensional scaffold to mimic the environment in tissue. Typically agarose constructs are seeding with cells and tested using static or dynamic compressive strain in order to observe the cell and nucleus deformation with associated alterations in biological phenomena (Huang et al 2004, Thorpe et al 2010). One of the most widely employed cells in agarose-cell system is chondrocytes as the agarose system closely replicates the cartilage and chondrocyte deformation in vivo (Huang et al 2004, Mauck et al 2006). Mechanical perturbation applied to chondrocyte-agarose constructs has involved: (1) compressive loading, including dynamic compression and stress-relaxation testing; (Mauck et al 2006, Kelly et al 2013) (2) osmotic challenge to chondrocytes (Inrianto 2013). A variety of bioreactor systems have been used to investigate biological modification and neo-tissue formation with long-term applied loading involving culture periods up to months (Gu et al 2003). The cell-agarose model is also used to investigation the role of mechanical perturbation in regulating chondrogenesis of chondrocyte progenitors and stem cells (Buckley et al., 2009). Experimental data obtained from the cell-agarose system are commonly combined with modelling and simulation approaches to estimate cellular mechanical properties that cannot be measured directly (Thorpe et al., 2008, Irianto et al 2013).

1.4.3 Multi-scale Finite Element Model

In mathematics, the finite element method (FEM) is a numerical technique for finding approximate solutions to boundary value problems for partial differential equations. This problem-solving idea is similar to linking a mass of tiny straight lines to approximate a large circle. A typical process of finite element analysis includes two steps: (1) dividing the whole problem into a collection of subdomains, with each subdomain containing a set of element equations representing the original problem; (2) resolving the equations in each subdomain and systematically recombining all sets of element equations into a global system of equations for final problem solution. In the finite element method the subdivision of a whole domain into simpler parts has several advantages: (1) Accurate representation of complex geometry; (2) Inclusion of dissimilar material properties; and (3) Easy representation of the total solution (Mercey et al 2010). The FEM encompasses methods for gathering simple element equations over many small subdomains, which are finite elements, to more complicated equation over a large domain. The global system of equations has known solution techniques and can be calculated from the initial values of the original problem to obtain a numerical answer (Rohlmann et al 2006).

The FEM is widely applied in cell/nucleus mechanical research. To test the role of particular mechanical behaviours on cell/nucleus deformation it is important to acquire accurate knowledge of local mechanical environment of the cell. In this respect, theoretical models of cells and tissues are particularly valuable for providing information on biophysical data which cannot be gained directly in situ at the cellular level. Examples include the stress-strain, fluid flow, physicochemical, and electrical sates in the immediate vicinity of cell (Guilak and Mow 2000).

Several in vitro model systems aiming at mimicking feature of physiological milieu and acquire biophysical measurements have been established. Comprehensive reviews of experimental technique for cell mechanics have been published by Huang and Loh respectively. In vitro model systems indicate that mechanical cues impact cell functions, including substrate stiffness, local surface topography and the three-dimensional structure of the matrix. As a case to prove the modelling conclusion, an investigation claims that substrate compliance governs the proliferation rate and lineage specification of stem cells towards neurons, myoblasts and osteoblasts.

1.4.4 Biphasic Model

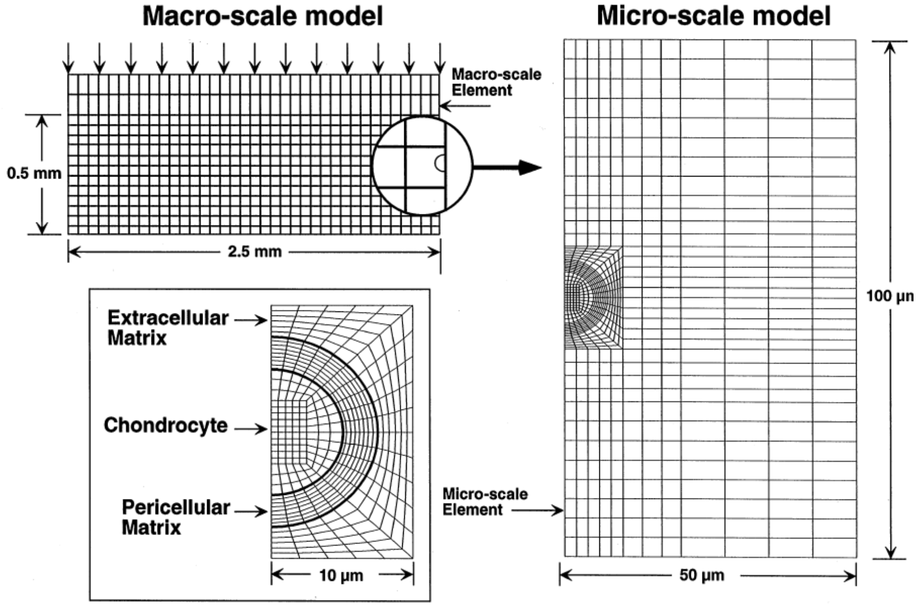

Figure 1.6. A biphasic multi-scale finite element method was used to model the mechanical environment of a single cell within the cartilage extracellular matrix. *Guilak 2000 Journal of Biomechanics 33 (2000) 1663}1673*

Many numerical and experimental studies have been conducted to understand the multiphase biomechanical properties of soft hydrated tissues, such as articular cartilage, intervertebral disk and cornea. In vitro unconfined and confined compression experiments are among the most widely used methods. Biphasic models are most commonly used with various mixture theories to numerically represent the compression process (Hatami-Marbini and Etebu 2013, Mow et al 1980). The biphasic model was first described in 1980 to studying the behaviour of articular cartilage by applying the mixture theory formulation of Green and Naghdi (Green and Naghdi 1970) and Bowen (Schonfeld et al 1976). The biphasic mixture theory assumes the tissue comprises a solid phase with linear elastic behaviour as skeleton and a viscous fluid phase within. This assumption leads to a system of coupled differential equations which can be solved analytically to reflect the mechanical behaviour of the tissue. The biphasic theory describes the compression and stress-relaxation behaviour of a hydrated tissue which is caused by the fluid flow within the porous solid skeleton (Mow et al 1984). The biphasic model simulates the behaviour of the tissue in unconfined compression with close agreement to the experimental data. Differences between experimental and modelled behaviour may be related to factors inclusing viscoelasticity, anisotropy, inhomogeneity and the nonlinear biomodular behaviour in the tissue (Hatami-Marbini et al 2013, Mow et al 1984). To improve the biphasic model, different theories have been developed to study the mechanical environment of the hydrated tissue.

Biphasic model consist of a porous solid skeleton matrix with fluid filled pores. This type of structure can be described based on theory of porous media (TPM), founded and supported by the work of Bowen (Guza and Bowen 1976, Stow and Bowen 1980), de Boer (de Boer and Ehlers 1986) and Ehlers (Polich et al 1986, Ehlers and Markert 2000, Ehlers and Markert 2001). It is applied to structures with contents that are interacted without fusing, and the internal interactions can be defined by the classical theory of mixtures and the concept of volume fractions. As a result, the components are distributed uniformly in the whole mixture and this homogenized model guarantees material points of each component element exist at each geometric location. The volume fractions are introduced as scalar structural variables that describe the local composition of the mixture. According to the theory of porous media, the material behaviour of the porous solid skeleton ranges from elastic (Pre ́vost, 1982, Ehlers 1997), viscoelastic (Wagner et al., 2013), elasto-plastic (Ehlers and Volk 1997) to elasto-viscoplastic (Ehlers and Volkl 1998).

To apply the biphasic model in this research, two basic assumptions are required. The first assumption is that the material of each component (skeleton material and pore-fluid) are incompressible. Further geometrically linear deformation is assumed, in which the skeleton structure is deformed by a linear viscoelasticity law based on a generalized rheological spring-dashpot model. Fluid viscosity is considered with drag force, where the permeability is deformation dependent, impacted by the actual porosity of the skeleton structure. Thermal effects and mass exchange between the components are not taken into account (Valhmu et al 1998). This pure mechanical, linear viscoelastic two-phase model is able to simulate the response of soft biological tissues under mechanical loading and the biphasic formulation helps understanding of the material behaviour inside the hydrated mixture (Hayes and Bodine 1978). A further development is the biphasic poroviscoelastic (BPVE) theory providing more focus on flow-independent viscoelastic effects (Spilker et al 1992). The TPM and BPVE are based on the same mixture approach found by Bowen and the same basic equations are applied, but the gap between the BPVE theory and the biphasic linear viscoelastic model lies on the constitutive material definition and the following operation on governing model equations (Mow et al 1980). The BPVE uses an integral-type viscoelasticity model with a continuous relaxation spectrum while TPM relies on a more descriptive differential representation of the linear viscoelasticity law deduced from a rheological spring-dashpot model (Mak et al 1982). In addition, based on the thermodynamics with internal state variables, TPM proves to be more convenient in upgrading definite deformation (Wu et al 1997).

The finite element formulation of the BPVE theory is based on the Galerkin weighted residual method with penalty treatment of the continuity equation. As a result, the pressure field is not taken into consideration and weak forms of the momentum equations for both components are defined in terms of the solid displacement and the fluid velocity (Mak et al., 1987). The corresponding numerical treatment applied by TPM within the finite element method proceeds from a displacement-pressure formulation of the governing field equations with respect to the whole mixture (Mak et al., 1987). Due to material incompressibility of components in mixture, the spatial discretization results in a combination of differential-algebraic equations in the time domain. The work of Brenan et al. proved that the numerical integration of this semi-discrete system can be efficiently functioned by a suitable time integration scheme.

In this work, the behaviour of cell-seeded agarose as a biphasic material including solid skeleton matrix (agarose and cell attached inside) and interstitial fluid (imaging media) is described. Like articular cartilage, this agarose contains viscoelastic behaviour thanks to flow-dependent fluid-solid interaction and the flow-independent viscoelastic skeleton properties. In addition, the role of deformation-dependent permeability is not ignored even in small deformations since it greatly contribute to transient compressive response of the whole system.

1.5 Aims and objectives

Current studies agree that alterations to nuclear organization, including epigenetic modifications, plays a key role in regulating gene expression. This bring a new perspective to the regulation of the differentiation of embryonic stem cells by mechanical perturbation to modify cell fate. Moreover, embryonic stem cells are dynamic, exhibiting differing pluripotency states, associated with alterations in the mechanical properties of the nucleus linked to chromatin packing and lamin expression. Characterizing the mechanical response of the mouse embryonic stem cell nucleus to external mechanical perturbation in various pluripotency states and during early differentiation is key to understanding mechanoregulation of stem cell biology.

This project builds on previous studies from the research group and further investigated the connection of nucleus and cell physical dynamics with pluripotency modification including early differentiation. We aimed to investigate the differences in nucleus stiffness in various phenotypic conditions, linked to pluripotency state. A range of techniques have been used, including gene expression assay, physical morphology alteration measurement during cell-seeded scaffold compression and biphasic mutli-scale modelling simulation. By comparing the difference of gene expression level in various embryonic stem cell phenotypes with distinct mechanical behaviours and differing structure alterations in response to similar compression, it is possible to determine the relationship between gene expression, linked to pluripotency state, cell and nucleus structure and variations in physical characteristics and response. With the application of multi-scale modelling simulation and measurement of physical characteristics of that scaffold materials, the mechanical properties of the cell and nucleus, which were hard to acquire experimentally, were estimated.

Accordingly this these test the following global hypotheses:

- Pluripotency state influences the organization of the mouse embryonic stem cell nucleus and its response to mechanical perturbation, involving compression in cell-seeded agarose constructs.

- Early differentiation influences the response of the mouse embryonic stem cell nucleus and its response to mechanical perturbation, involving compression in cell-seeded agarose constructs, in a manner determined by the initial pluripotency state.

The hypotheses are tested via the following objectives linked to experimental studies and theoretical model development:

- Culturing mouse embryonic stem cells under conditions that favour specific pluripotency states, with characterization of markers of pluripotency and early differentiation.

- Development and application of the cell-seeded agarose compression system to investigate the cellular and nuclear modification in mouse embryonic stem cells during application of compressive strain.

- Analysing the deformability of mouse embryonic stem cells and their nuclei in varying pluripotency states and during early differentiation.

- Development of a multi-scale model to estimate global agarose deformation in the construct under compressive strain and to predict cellular and nuclear mechanical properties.

Chapter 2 General Methods

2.1 Introduction

This chapter describes procedures frequently applied throughout the experimental work of this thesis including cell culture, microscopy analysis and molecular biology characterization. Procedures specific to a single chapter are described within the methods section of the appropriate chapter, and a fundamental introduction to multi-modelling is set-out in Chapter 5.

2.2 Mouse embryonic stem cell culture system

2.2.1 Mouse embryonic stem cell

The CCE mouse embryonic stem cell line is the only cell line used in this thesis. This cell line was already available in the research group at the outset of the work. The CCE cell line was derived from the 129/Sv mouse strain and the original vial of cells was acquired from The Jackson Laboratory, with permission, by Dr Rui Martins in our research group (https://www.jax.org/jax-mice-and-services). The cell line is one of the first to be adapted as a feeder-free LIF dependent strain (Keller et al., 1993). Many research groups have used this cell line with confirmation of its phenotypic properties as mouse embryonic stem cells, in part based on high expression levels of Oct4 and Nanog.

2.2.2 Regular mouse embryonic stem cell medium (LIF medium)

For regular mouse embryonic stem cell (mES cell) culture medium, basal medium was prepared by adding 37.5mL (15%) fetal bovine serum (FBS, stem cell qualified, Invitrogen 10439-024), 5mL MEM Non-Essential Amino Acids Solution (100X, Invitrogen 11140-035) and 5mL penicillin (100X, Invitrogen 15140-122) to 202.5 mL low glucose Dulbecco’s modified Eagle’s medium (DMEM, Invitrogen 31966-047). Aliquots were stored in -20 ^{o}C for up to 6 months. Prior to use aliquots were thawed in a 37 ^{o}C water bath.

For application in cell culture, mouse embryonic stem cell (mES cell) culture medium was prepared by adding 0.25mL 100X 2-Mercaptoethanol (also known as BME,100X, Sigma M7522) and 1000 U/ml of Leukemia inhibitory factor (LIF, Millipore ESG1107, 5 µL aliquot) to 25mL basal medium and stored at 4^{o}C for up to 7 days. This is defined as LIF medium and may also be described as primed state mouse embryonic stem cell medium.

Prior to usage, the medium was pre-warmed in a 37°C water bath. In the later section of this thesis, the mouse embryonic stem cells cultured in this medium are termed LIF mES cells.

2.2.3 Naïve state mouse embryonic stem cell medium (2i medium)

The basal medium for naïve state mouse embryonic stem cell (mES cell) culture was prepared by combining 205 mL low glucose Dulbecco's modified Eagle's medium (DMEM, 4.5 g/L Glucose + L-Glutamine + 25 mM HEPES, Invitrogen 21063-029), 5mL MEM Non-Essential Amino Acids Solution (100X, Invitrogen 11140-035) and 5mL penicillin (100X, Invitrogen 15140-122). Aliquots were stored at -20°C for up to 6 months. Prior to usage, the medium was pre-warmed in a 37°C water bath.

For application in naïve state cell culture, the final medium was prepared by the addition of 0.25mL N2 supplement (100X Invitrogen 17502048) and 0.25 ml B27 supplement (50X Invitrogen 0080085SA) with 4.8 µL MEK 1/2 inhibitor (10.4mM, Merck 444966-5MG), 38.2 µL GSK3b inhibitor (2.6 mM, Merck 191500-1MG), 0.5mL 2-Mercaptoethanol (100X, Sigma M7522) and 1000U/mL Leukemia inhibitory factor (LIF Millipore ESG1107, liquored in 10 µL). This is defined as 2i medium and may also be described as naïve state mouse embryonic stem cell medium. The medium was stored at 4°C for up to 7 days. Prior to use, the medium was pre-warmed in a 37°C water bath. Since the inhibitors (MEK 1/2 and GSK3b) are light-sensitive, the medium was protected from light by wrapping aluminium foil around vials containing aliquots of 2i medium. In later sections of this thesis, the mouse embryonic stem cell cultured in this culture medium are termed 2i mES cell.

2.2.4 Mouse Embryonic Stem Cell Monolayer Culture

Mouse embryonic stem cells were maintained in monolayer culture in Thermo Scientific™ cell culture flasks with culture areas ranging from 25cm^2 to 500cm^2 and no surface treatment. An initial seeding density of 10000 per cm^2 was used and a medium volume of 0.2mL for every cm^2 culture surface area was maintained. Prior to seeding cells, surface coating was achieved using a 0.1% gelatin gel. To achieve surface-coating 0.08mL of 0.1% gelatin gel (Sigma G1890) was added per cm^2 of culture surface and the flask was maintained at 37°C for 30 minutes. The gel was subsequently aspirated before adding medium containing cells. Cell attachment to the culture surface was typically achieved in 30min to 2 hours following seeding.

2.2.5 Trypsinising/Accutasing Adherent Cells

Passage of cells using trypsin was achieved as follows. For cells growing in culture flasks (Thermo Scientific™), the medium was aspirated and replaced with Phosphate Buffered Saline solution (PBS, Sigma-Aldrich) at a volume of 0.2mL for every cm^2 culture surface area. After 5 minutes the PBS solution was aspirated and replaced with 0.06mL trypsin-EDTA solution (Sigma-Aldrich T3924). The culture flask was placed into a 37°C incubator for between 2 to 5 minutes to allow detachment of cells. An equal volume of basal medium was added to the flask with light agitation to detach the cells from the culture surface. The resultant cell suspension was aspirated, collected into a 10 mL conical tube and centrifuged at 2000 rpm for 5 minutes. The supernatant was aspirated and the cells were resuspended in 0.04mL of fresh culture medium per cm^2 of original culture surface area.

For detaching cells using accutase, the medium was aspirated and replaced with an equal volume of PBS solution (Sigma-Aldrich). After 5 minutes the PBS solution was aspirated and replaced with 0.04mL per cm^2 of culture surface area of Accutase® solution (Sigma, A6964). The culture flask was maintained in a 37°C incubator for 5 to 7 minutes to allow for detachment of the cells. The enzyme solution was agitated by gently tapping the culture flask to facilitate cell detachment, the cell suspension was aspirated and collected in a 10mL tube and centrifuged at 2000 rpm for 5 minutes. The supernatant was aspirated and the cells resuspended in 0.04mL of fresh culture medium per cm^2 of original culture surface area for counting and trypan blue assay.

2i mES cells show weaker cell attachment to culture surface than LIF mES cells resulting in the presence of non-attached and floating 2i mES cells in medium that may remain viable during culture. Accordingly the initial aspired supernatant from 2i mES cell culture was retained for the trypan blue assay. The considerations for choosing either trypsin or accutase for detachment of adherent cells is based on reports that trypsin treatment may result in cell membrane damage during the detachment of adherent cells while accutase is claimed to avoid similar cell damage.

2.2.6 Trypan Blue Exclusion Assay

This assay involves the stain trypan blue (Sigma-Aldrich 72571) that can only penetrate into cells with compromised membranes, leaving viable cells unstained. The haemocytometer (Improved Neubauer, VWER, Lutterworth, UK) is a glass chamber with a defined height and incorporating nine distinct grids of known area. Each grid, therefore, has a known volume of 1×10^{-4} mL. An aliquot of cell suspension with a volume of 10 µL was mixed with 10 µL trypan blue solution to create the final solution for cell counting and viability assessment. The solution was carefully pipetted into the haemocytometer chamber and the cells were counted using a light microscope. Cells within five of the grids were counted and an average was calculated. For optimal assessment of cell concentration, the number of cells in every grid should ideally lie in the range from 100 to 300. Accordingly additional dilution of the cell suspension was sometimes required. The cell number (N) is calculated by:

$N=A\times D\times F\times V\times 10^4$

Where N is the number of cells within the cell suspension, A is the average number of cells counted in a grid, D is the dilution factor applied between the cell suspension and the trypan blue, and F is the magnitude of any additional dilution of cell suspension applied and V is the volume of cell suspension. The ratio of the unstained cell number and total cell number represents the cell viability and a ratio above 80% was regarded as high cell viability.

2.2.7 Alkaline Phosphatase Detection

Embryonic stem (ES) cells are pluripotent cells derived from the inner cell mass of pre-implantation mammalian embryos and are capable of unlimited, undifferentiated proliferation *in vitro*. Undifferentiated murine ES cells can be maintained *in vitro* for extended periods in media containing the cytokine, LIF. The undifferentiated state of ES cells is characterized by high level of expression of alkaline Phosphatase (AP), the expression of surface markers including SSEA and TRA antigens and the transcription factor Oct-4. In this thesis, an alkaline Phosphatase Detection Kit (MILLIPORE SCR004) was used as a specific and sensitive tool for the phenotypic assessment of ES cell differentiation by the determination of AP activity.

Embryonic stem cells were seeded at 2500 or 5000 cells/cm^2 in 6-well plates and cultured for at least 3 days prior to alkaline phosphatase detection, in which individual embryonic stem cell colonies were identified for good alkaline phosphatase stain visualization. After media aspiration, the cells were fixed with 4% paraformaldehyde for 1 minute. The fixative was removed and the plate wells were rinsed with 1X Rinse Buffer and maintained in the buffer prior to staining to avoid dehydration. The reagents for alkaline phosphatase staining were prepared as per the instructions of the MILLIPORE Alkaline Phosphatase Detection Kit and 2mL of the stain solution was added to cover each well surface, following aspiration of the rinse buffer. The plate was incubated in the dark at room temperature for 15 minutes. The wells were rinsed with 1X Rinse Buffer after aspiration of the staining solution. To prevent the wells from drying out the cell surface was covered with 1 X PBS. The number of colonies expressing AP (orange/red stem cell colonies, shown as Figure 2.1) was determined, versus the number of differentiated colonies (colourless). For undifferentiated stem cells greater than 90% of colonies are expected to express alkaline phosphatase.

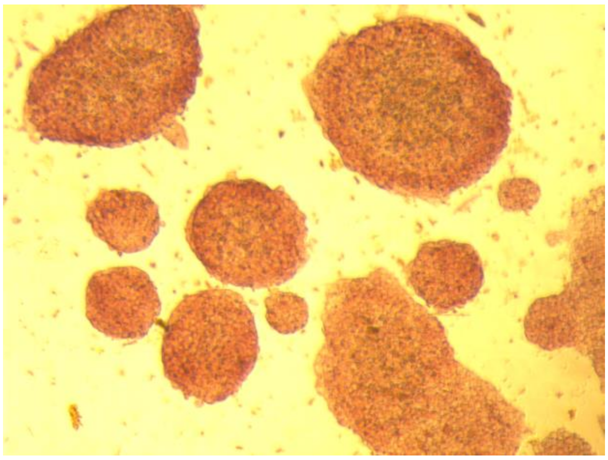

Figure 2.1 Microscopy image of embryonic stem cell colonies expressing alkaline phosphatase activity.

2.3 Cell-Seeded Agarose Compression

2.3.1 Cell-Seeded Agarose Preparation

In order to produce 5 mL of 6% (w/v) agarose solution, 0.3 g of agarose type VII-A (Sigma Aldrich 39346-81-1) was added to 5 mL of PBS without phenol red (Sigma-Aldrich). The agarose solution was sterilized and dissolved by autoclaving. The agarose solution was cooled first by placing it into a 60^{o}C oven for 10 minutes and subsequently by placement on a roller-mixer inside a 37^{o}C oven for 30 minutes. During the autoclaving and cooling down period, 5 mL of cell suspension with a density of 6×10^6 cells/mL was prepared, and the construct mould was sterilised in 85% ethanol under UV light overnight and assembled with sterile tape in cell working hood. The cell suspension was maintained at 37^{o}C and then added to an equal volume of agarose solution in a 20mL glass vial using a sterile 10mL syringe, creating 3% agarose-cell solution containing 3×10^6 cells/mL. The agarose/cell solution was mixed initially by placing the vial on a slow shaker (less than 200 rpm) for less than 15 seconds and subsequently by placing on a roller inside a 37^{o}C incubator for a maximum 5 minutes. Using a sterile 10mL syringe, the agarose/cell solution was injected into the mould, which was sealed and placed in a 4^{o}C fridge for 5 minutes or in room temperature cell working hood for 20 minutes to allow gelling of the agarose. The resultant agarose-cell constructs were carefully removed from the mould and placed into a Ø50 mm Petri dish filled with appropriate culture medium, ensuring the total immersion of the constructs. The constructs were cultured in a 37^{o}C incubator for further experiments.

2.3.2 Calcein AM and Ethidium Homodimer Viability Assay

In order to assess cell viability during culture in agarose constructs, the Calcein AM and Ethidium Homodimer live-or-dead assay was used. The acetomethoxy derivate of calcein (calcein AM, Sigma-Aldrich, 17783) is used as it can be transported through the cellular membrane of cells to be converted by esterase activity in viable cell to produce a fluorescent product. Ethidium homodimer (Sigma-Aldrich, 46043F) is a membrane-impermeable fluorescent dye which binds to DNA and will therefore only stain the nuclei of non-viable cells with compromised membranes. Accordingly, once a cell sample has been stained with 5μM calcein AM and 5μM ethidium homodimer, the living cells will display as green spots under 495/515 nm and dead cells are viewed as red spots under a UV-light microscope. Figure 2.2 illustrates live/dead staining for cell-seeded agarose constructs maintained in LIF cell medium in 2, 24 or 48 hours, with medium changes every 24 hours. The constructs were stained with calcein AM and ethidium homodimer for 30mins, and observed under confocal microscopy.

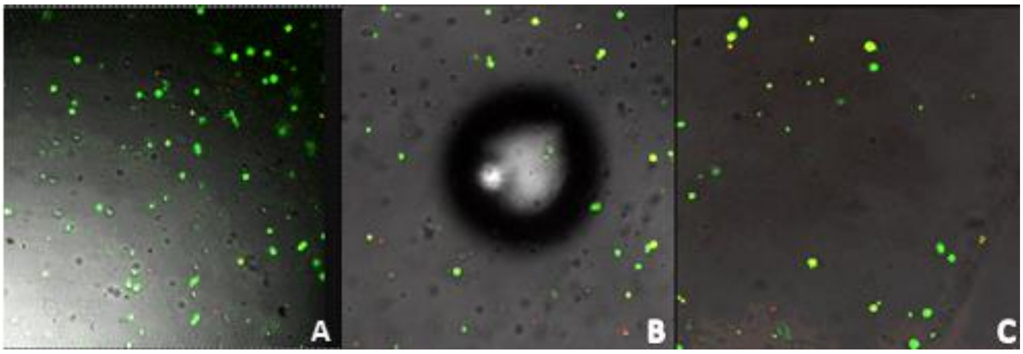

Figure 2.2 The Live/Dead assay involving staining with Calcein AM and Ethidium Homodimer in cell-seeded agarose constructs cultured for 2(A), 24(B) or 48(C) hours.

2.3.3 Cell-Seeded Agarose Compression

The system used to apply compression to cell-seeded agarose constructs is illustrated in Figure 2.3 (A) and comprises three main component systems: the mechanical loading components, power motor and a control system. The mechanical loading assembly comprises the mechanical rig which is used to hold the constructs and transfer mechanical compression under the regulation of the control system. The chamber is filled with media used during imaging to ensure that the cells within the agarose constructs are maintained in a hydrated and viable condition. The power motor supplies actuation to achieve compression with the control system linked to a laptop with self-programmed software (UI-processed design, Adobe). The compression loading components were set in three steps (Figure 2.3 (B)): 1. Assembly 2. Insert 3. Removing

Fixation part to allow compression

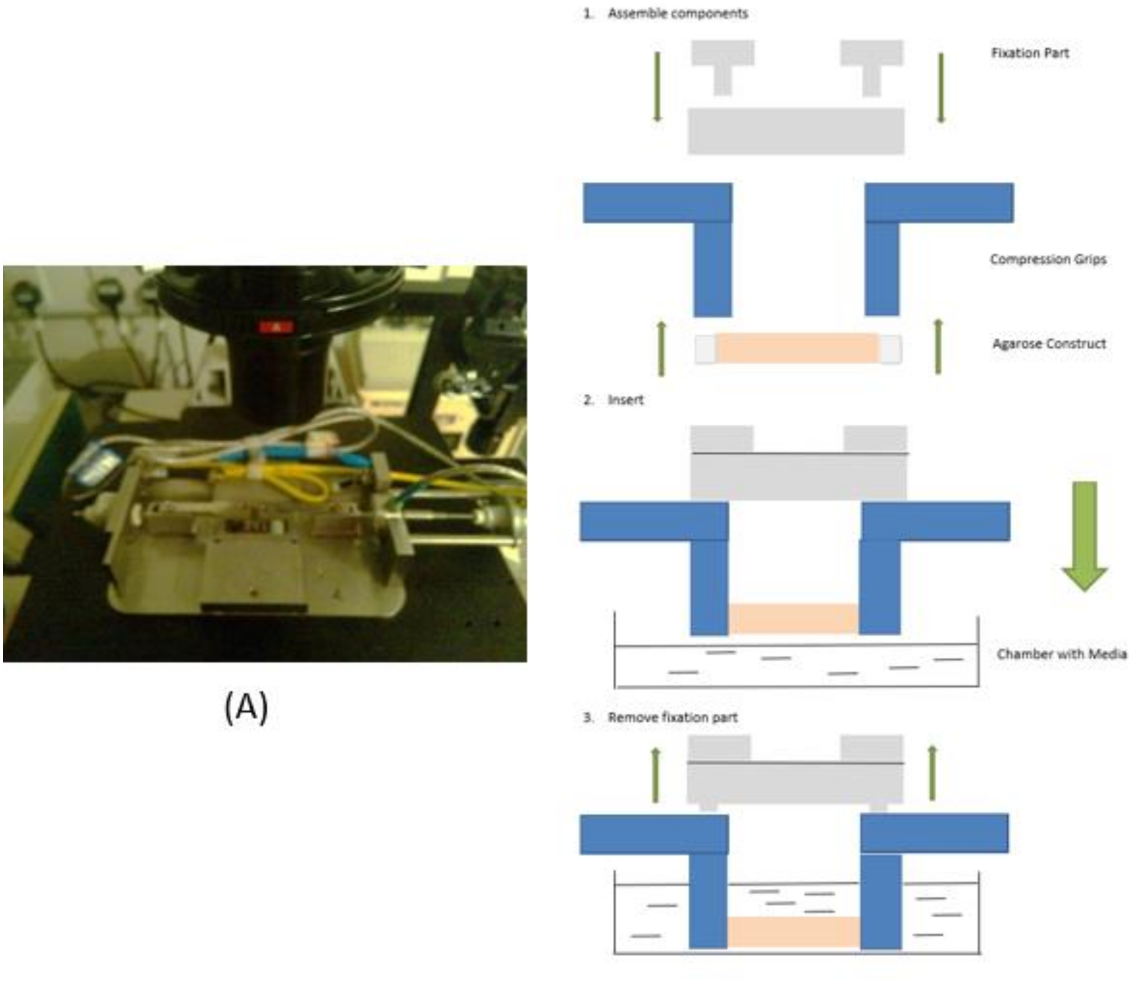

(A)

(B)

Figures 2.3 Introduction to cell-seeded agarose mechanical compression system (A) Image of the mechanical Loading components of the the cell-seeded agarose compression system. (B) Introduction to agarose construct loading components assembly.

The mechanical loading rig was assembled with a 50X20 coverslip mounted onto the bottom of the culture/loading chamber which was sealed with silicone glue. The system was tested for leaks. The culture/loading chamber was inserted into the main body slot of the mechanical loading rig and the whole system was transferred to the platform of the confocal microscope. A drop of oil was applied to the objective lens which was raised to allow imaging. The assembled compression grips were mounted in the main body of the mechanical loading rig and adjusted to allow insertion of an agarose construct. Individual cell seeded agarose constructs were transferred from culture and fixed between the grips. The chamber was filled with imaging medium, as shown in figure 2.4. The control system software controls the movement of the grips to apply a designated level of compressive strain over a defined time period. In this thesis, the main mechanical protocol involved application of 0-10% and 10-20% compression strain in 10 seconds with the strain held for 15-30 minutes to enable imaging.

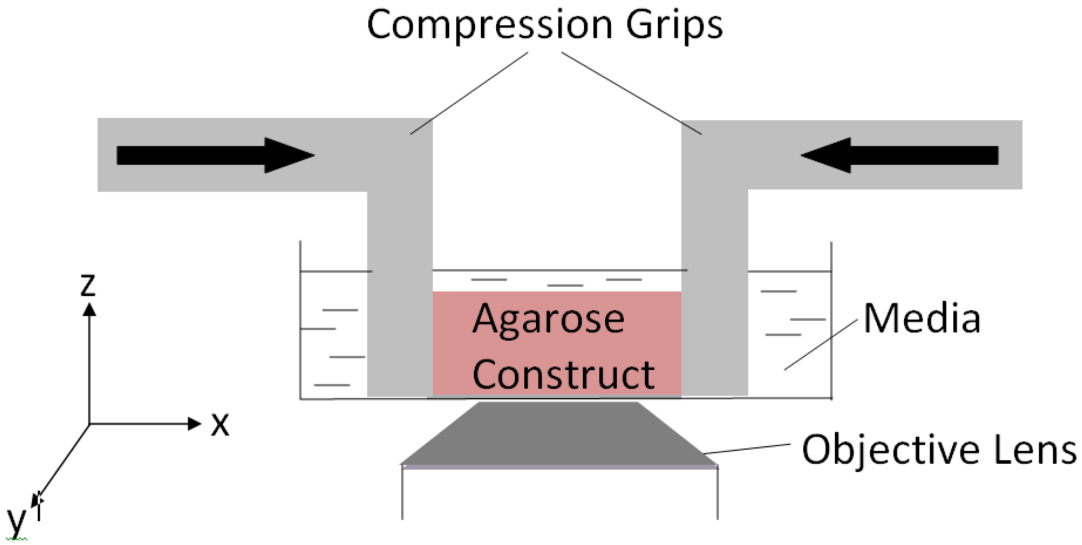

Figure 2.4. Schematic of the mechanical loading components and cell-seeded agarose construct used in compression studies.

2.4 Confocal Microscopy and Imaging Software

2.4.1 The confocal microscopy

In order to image live cells embedded within 3D constructs confocal microscopy was adopted in the work presented in this thesis. The basic principles of the technique are presented in the following section, which also focuses on limitations of the techniques, particularly relating to resolution in the three dimensions. This is important as it impacts on the ability to acquire analytical data relating to dimensions and dimensional alterations in cells and their nuclei during the application of mechanical compression.

In the confocal microscope, a pinhole (aperture) is placed a before the light source to limit the excitation filed of illumination and another aperture is set before the signal detector to filter background light emission (Figure 2.5). A laser beam is generated as the main light source which travels through the aperture and is focused by the objective lens on the focal plane exciting fluophores within the sample. When fluorescence light is emitted from fluophores in the sample in response to the laser excitation, it travels back with other background light along a similar path as the laser beam to reach a beam splitter. The beam splitter separates the fluorescence with a defined wavelength range and the fluorescence reaches the light detector. As the beam splitter removes background light, confocal microscopy can improve signal/noise interference from the background. However, emitted fluorescence may be of low levels of intensity and the exposure time is longer than normal light microscopy. This raises issues such as photobleaching and phototoxicity which will be described later.

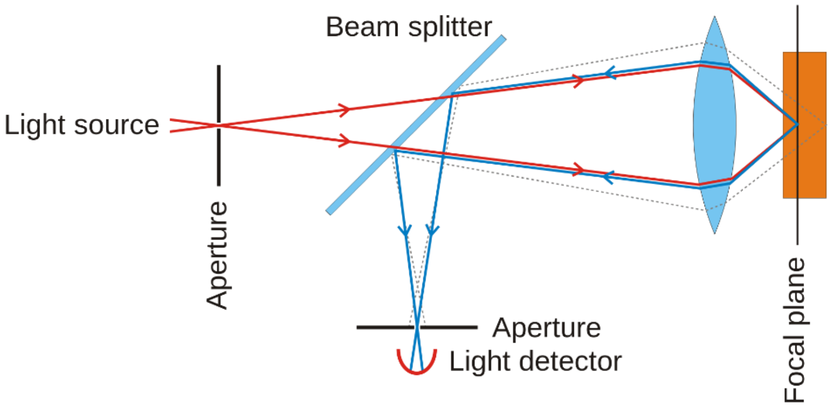

Figure 2.5 Schematic indicating the principle of confocal microscopy.

There are four types of confocal microscope: (1) Confocal laser scanning microscopy, (2) Spinning-disk confocal microscopy, (3) Dual spinning disk confocal microscopy and (4) Programmable array microscopy. In this thesis, we mainly used a confocal laser scanning microscope (Leica Laser Scanning Microscopy TCS SP2) and a spinning-disk confocal microscope (Perkin-Elmer Spinning-Disk Confocal Microscopy). Further sections introduce the key factors of the confocal microscopy systems to explain the selection of the two confocal microscopies for different studies.

2.4.2 Resolution

The resolving power is the ability of an imaging device to separate points of an object located at a small angular distance into individual positions. The term resolution defines the minimum distance between distinguishable objects in an image. In this study, most of the imaging was achieved using a 63× oil immersion objective, with a numerical aperture of 1.4 used in conjunction with the two confocal microscope systems. The Leica Laser Scanning Microscopy TCS SP2 can offer higher resolution due to a more powerful optical source and longer light exposure. The resolution of the Leica confocal images is 800 X 600 or 1280 X 1060.

2.4.3 Gain and Offset of PMT

Light intensity signals derived from the sample are recorded by a photomultiplier tube

(PMT), and the gain and offset setting in the PMT are analogous to contrast and brightness in image processing. Offset is applied in thresholding PMT data by resetting lower intensity signals to zero to remove them from the image. Increasing the whole signal level of the PMT image is achieved by adjustment of gain. An increase in gain will detect weak signals which may not be detected in lower gain situation. However, increasing gain attract problems such as noise and image saturation. The aim for gain and offset adjustment in both confocal microscope systems is to present images with rich and clear details, and this requires a moderate gain level (300-700V) and appropriate offset level to block background interruption.

2.4.4 Photobleaching and phototoxicity

Photobleaching is a term used to describe the photochemical alteration of a dye or a fluorophore molecule in which it becomes permanently unable to fluoresce. This is caused by cleaving of covalent bonds or non-specific reactions between the fluorophore and surrounding molecules. Long-time exposure with strong light intensities may cause photobleaching. The photobleaching may influence fluorescent molecule function and even permanently destroy the fluorophore. Loss of fluorescence activity caused by photobleaching can be controlled by reducing the intensity or time of light exposure, by increasing the concentration of the fluorophore and by reducing the frequency and thus the photon energy of the input light. Additionally, continuous laser exposure will also induce a degree of damage to living samples, often referred as phototoxicity, associated with the release of oxygen free radicals.

To avoid these effects on the sample and fluorophore during long time live monitoring, a confocal microscopy with low excitation energy is necessary. In spinning-disk confocal microscopy, a series of pinholes scans an area in parallel and each pinhole is allowed to remain over a specific area for a longer amount of time, thereby reducing the excitation energy needed to illuminate a sample when compared to laser scanning microscopes. Decreased excitation energies reduce phototoxicity and photobleaching making spinning-disc microscopy the preferred system for imaging live cells over extended periods. In this thesis, cell-seeded agarose compression was recorded using a Perkin-Elmer Spinning Disc Microscope.

2.4.5 Image J

ImageJ is a public domain, Java-based image processing program developed at the National Institutes of Health. ImageJ was designed with an open architecture that provides extensibility via Java plugins and recordable macros. User-written plugins make it possible to solve many image processing and analysis problems. In this thesis, we applied ImageJ to analyse images taken using both confocal and light microscopy. Image J was used to display, process and analyze 8-bit colour and grayscale JPG images from the Perkin-Elmer Scanning Confocal Microscopy and 32-bit colour and grayscale JPG images from Leica Confocal Microscopy.

For improved resolution and detail necessary for measurement and analysis, image processing was achieved using the toolkit in ImageJ. The first step in processing images is softening or sharpening images for specified purposes, as illustrated in figure 2.6 for an image of the cell. Sharpening images helps better identification of details, while softening of images is beneficial for the accurate identification of the periphery of the nucleus by blocking noise which shows as a serrated outline.

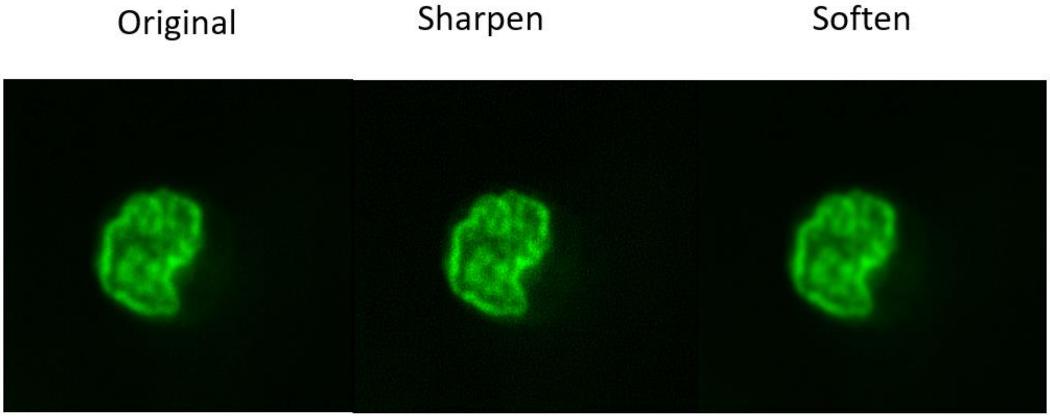

Figure 2.6. A representative image of the nucleus in its original form and following sharpening and softening via ImageJ.

Another step in image processing is to highlight target outline by blocking background. Two methods were applied to highlight the target area. For outlining the nuclei, thresholding was applied. Image J can automatically or interactively set lower and upper threshold values, segmenting the image into features of interest and background. In the dark ground thresholding option, the thresholded features are displayed in original colour and the background is displayed in red (Figure 2.7B). By reversing the step, the target area will turn red instead (Figure 2.7C). The wand tool in ImageJ is applied to outline a single feature (Figure 2.7D). Lower and upper threshold values can be adjusted. Sixteen different automatic thresholding methods is available with different value settings and the default one was selected in this thesis. The Auto button was used with the currently selected thresholding method to automatically set the threshold levels based on an analysis of the histogram of the current image or selection.

However, the thresholding method is not perfect in highlighting the cell periphery in greyscale images since the background is too complex to be blocked. Since mES cells commonly have a regular perphery and a near-elliptical shape, an alternative method for outlining the target area was applied by directly drawing an elliptical as the selected outline (Figure 2.8B).

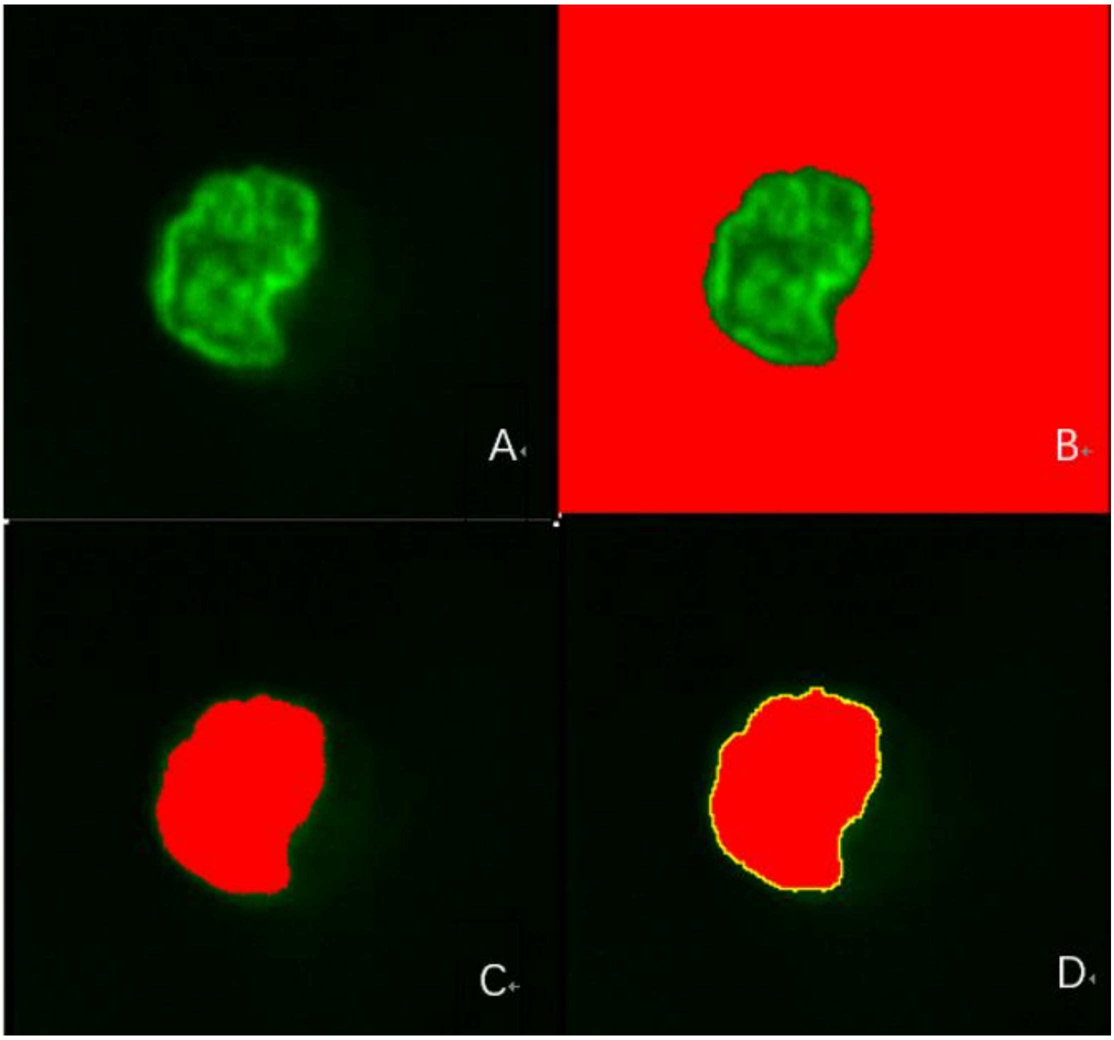

Figure 2.7. Steps in thresholding a nucleus image via Image J. A. The original nuclei image. B. Blocking background with red using the dark ground thresholding option. C. Reversing the thresholding effect in the highlighting target area. D Selecting the outline of the target area with the wand tool.

ImageJ can calculate area and pixel value statistics of user-defined selections and intensity-thresholded objects. It can measure distances and angles and can create density histograms and line profile plots. In this thesis, the following parameters were routinely measured:

1. Area - Area of selection in square pixels. Area is in calibrated units, such as square millimeters, if the Set Scale is used to spatially calibrate the image.

2. Bounding Rectangle - The smallest rectangle enclosing the selection including headings BX, BY, Width and Height, where BX and BY are the coordinates of the upper left corner of the rectangle.

3. Shape Descriptors (previously Circularity) - Calculate and display the following shape descriptors: AR (aspect ratio): major axis/minor axis. Enable "Fit Ellipse" in Analyze>Set

Measurements to have the major and minor axis displayed. Round (roundness): 4*area/(π*major_axis^2), or the inverse of the aspect ratio.

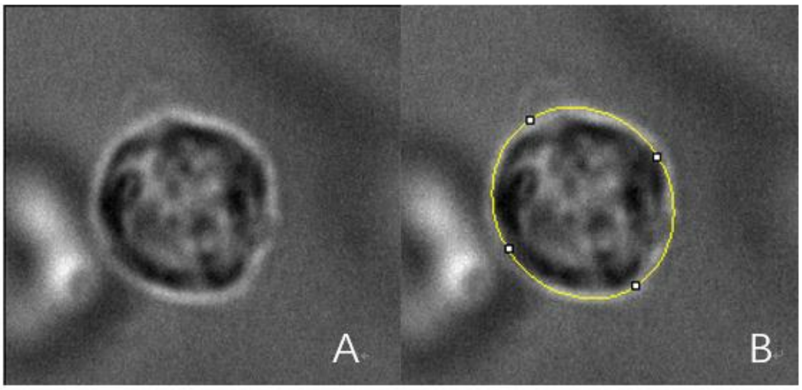

Figure 2.8. Outlining the cell periphery. A. The original image. B. The cell with an elliptical selection used to indicate periphery.

2.5 Gene Detection

In studying the biological and physical characteristics of embryonic stem cells it is necessary to monitor gene expression changes during various pluripotency states and during the earliest phases of differentiation. This section focused on methods used to determine expression profiles and introduces of key genes used as markers of pluripotency and differentiation.

2.5.1 Reverse-Transcriptional Polymerase Chain Reaction (rtPCR)

Reverse-Transcriptional Polymerase Chain Reaction (rtPCR) is widely recognized as a valid and effective method to detect alterations in gene expression by comparing the differences in mRNA levels in cells under different conditions. The polymerase chain reaction is a technique used in molecular biology to amplify a single copy or a few copies of a piece of DNA across several orders of magnitude, generating thousands to millions of copies of a particular DNA sequence. By synthesizing complementary DNA (cDNA) with corresponding mRNA fragment samples, rtPCR is able to detect the differences in cDNA samples for specific target gene from the samples.

2.5.2 RNA isolation and purification

RNA isolation and purification was achieved using RNeasy Plus Mini Kits (QIAGEN, Germany) for highly-purified RNA samples. To collect mRNA from approximately 1 million cells, the cells were seeded at a density of 10000 per cm^2 in 6-well plates. After 48 hours, the medium was aspirated and the cells were rinsed with PBS. After the PBS was aspirated, the cells were detached using a cell brush and 350 µl Rneasy RLT buffer (QIAGEN, Germany) with 1% BME was added. 700 µl 96% ethanol was added to 350 µl buffer to create a working solution which was centrifuged for 3 min at maximum speed. The supernatant was carefully removed and the homogenized lysate was transferred to a gDNA Eliminator spin column placed in a 2 ml collection tube. After being centrifuged for 30 s at ≥8000 x g (≥10,000 rpm), the flow-through was saved and the column was discarded.

The flow through was subsequently mixed with 350 µl 70% ethanol and transferred to an RNeasy spin column placed in a 2 ml collection tube with the lid closed. After centrifuging for 15 s at ≥8000 x g the flow-through was discarded and 700 µl Buffer RW1 was added in the RNeasy Mini spin column (in a 2 ml collection tube), followed by a further centrifuge step for 15 s at ≥8000 x g. The flow-through was discarded and the 500 µl Buffer RPE was added to the RNeasy spin column with centrifugation for 15 s at ≥8000 x g. The same volume of Buffer RPE was added to the RNeasy spin column with centrifugation for 2 min at ≥8000 x g (≥10,000 rpm). The RNeasy spin column was transferred to a new 2 ml collection tube and centrifuged at full speed for 1 min to dry the membrane. After placing the RNeasy spin column in a new 1.5 ml collection tube, 30µl RNase-free water was applied directly to the spin column membrane and the column was centrifuged for 1 min at ≥8000 x g to elute the RNA sample.

2.5.3 Reverse transcription

1000ng of RNA was mixed with 1µl 1mM dNTPS nonamers, 0.75 µl random oligomers and 0.75 µl oligo(dT)23 and nuclease-free water was added to make a working solution in 10 µl total volume. The solution was centrifuged to mix the components, incubated at 70^{o}C for 10 minutes and placed on ice for another 2 minutes. To prepare 10 µl of the reverse transcriptase solution, 1 µl M-MLV reverse transcriptase was mixed with 0.5 µl RNase Inhibitor (Rbotlock) and 6.5 µl nuclease-free water. The solution was added to a microcentrifuge tube and incubated at room temperature for 10 minutes. 2 µl 10X M-MLV Reverse Transcriptase Buffer was added to make the reverse transcriptase solution in 10 µl. The solution was mixed with the working solution and incubated in a reaction tube at 37^{o}C for 50 min. The reaction tube was heated to 90^{o}C for 10 min to denature the M-MLV reverse transcriptase. The synthesized cDNA was stored at -20^{o}C prior to further analysis.

2.5.4 PCR reaction preparation

An aliquot of the cDNA sample (20 µl) was diluted to 200 µl with nuclease-free water and primer mix (stock concentration 100 µM), comprising with 20 µl Fwd primer, 20 µl Rev primer and 160 µL nuclease-free water. The reaction solution was mixed with 5 µl SYBR green taq readymix, 1 µl primer mix, 1 µl diluted cDNA, 0.1 µl Rox reference dye and 2.9 µl nuclease-free water. The reaction solution was pipetted into a 96 well plate and sealed to avoid liquid leakage during the thermal cycling process. The plate was placing into the thermocycler (Mx3000P) which was set to run 50 cycles of the following regime, followed by a thermo-profile (melting curve):

1. [1 cycle] Hot Start (95^{o}C), 2 min

2. [50 cycles] Denature - 95^{o}C, 20 sec

   Anneal - 58^{o}C, 20 sec

   Extend - 72^{o}C, 30 sec

3. [1 cycle] Thermo-profile.

After the thermal cycling process, the 96 well plate was removed from the thermocycler and the recorded data saved for further analysis.

2.5.5 PCR primer selection

In this thesis, research focused on the maintenance of different pluripotency states and early differentiation linked to modification in cell culture. Accordingly the selection of PCR primers align with three groups as follows:

1. Pluripotency gene markers - to determine the pluripotency state in the stem cell cultures between differing culture conditions.

2. Differentiation gene markers – to determine whether early differentiation has been triggered within a stem cell group and to identify broad lineage induction.

3. Housekeeping gene markers – to monitor selected genes which are typically required for the maintenance of basic cellular function, and are expressed at relatively constant levels in most non-pathological situations.

In this study, we selected the genes indicated in Figure 2.9 which also indicates their respective primers with protocols optimisation accordingly. Throughout this thesis, two pluripotency gene markers (Oct4, Nanog), 2 differentiation gene markers (BMP4, Nestin) and a housekeeping gene marker (18 srRNA) were commonly used. Besides, we added two early differentiation markers (Otx2 and Fgf5) in later additional test in Chapter 4.

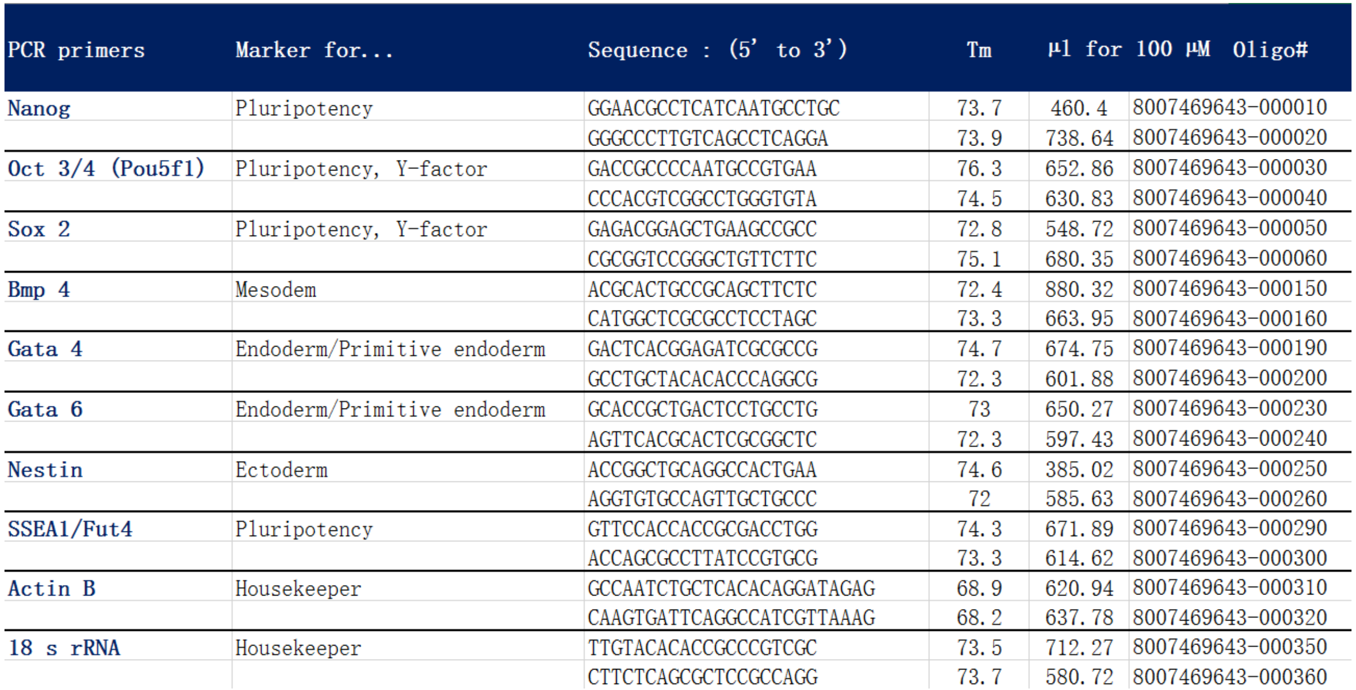

PCR primers	Marker for...	Sequence : (5' to 3')	Tm	µl for 100 µM	Oligo#
Nanog	Pluripotency	GGAACGCCTCATCAATGCCTGC	73.7	460.4	8007469643-000010
		GGGCCCTTGTCAGCCTCAGGA	73.9	738.64	8007469643-000020
Oct 3/4 (Pou5f1)	Pluripotency, Y-factor	GACCGCCCCAATGCCGTGAA	76.3	652.86	8007469643-000030
		CCCACGTCGGCCTGGGTGTA	74.5	630.83	8007469643-000040
Sox 2	Pluripotency, Y-factor	GAGACGGAGCTGAAGCCGCC	72.8	548.72	8007469643-000050
		CGCGGTCCGGGCTGTTCTTC	75.1	680.35	8007469643-000060
Bmp 4	Mesodem	ACGCACTGCCGCAGCTTCTC	72.4	880.32	8007469643-000150
		CATGGCTCGCGCCTCCTAGC	73.3	663.95	8007469643-000160
Gata 4	Endoderm/Primitive endoderm	GACTCACGGAGATCGCGCCG	74.7	674.75	8007469643-000190
		GCCTGCTACACACCCAGGCG	72.3	601.88	8007469643-000200
Gata 6	Endoderm/Primitive endoderm	GCACCGCTGACTCCTGCCTG	73	650.27	8007469643-000230
		AGTTCACGCACTCGCGGCTC	72.3	597.43	8007469643-000240
Nestin	Ectoderm	ACCGGCTGCAGGCCACTGAA	74.6	385.02	8007469643-000250
		AGGTGTGCCAGTTGCTGCCC	72	585.63	8007469643-000260
SSEA1/Fut4	Pluripotency	GTTCCACCACCGCGACCTGG	74.3	671.89	8007469643-000290
		ACCAGCGCCTTATCCGTGCG	73.3	614.62	8007469643-000300
Actin B	Housekeeper	GCCAATCTGCTCACACAGGATAGAG	68.9	620.94	8007469643-000310
		CAAGTGATTCAGGCCATCGTTAAAG	68.2	637.78	8007469643-000320
18 s rRNA	Housekeeper	TTGTACACACCGCCCGTCGC	73.5	712.27	8007469643-000350
		CTTCTCAGCGCTCCGCCAGG	73.7	580.72	8007469643-000360

Figure 2.9 Details of the PCR primers selected for this study.

2.6 Nuclei Acid Staining

The following section describes the selection of appropriate dyes and optimization of staining protocols to achieve the aims of the work, specifically imaging of cell and nuclei within living ES cells within agarose constructs.

2.6.1 Nuclei Staining Protocols on 2D coverslips

From previous work in the laboratory dye selection for mouse embryonic stem cell had been narrowed to two candidates: Hoechst 33258 and SYTO 16. Initially an appropriate 2D staining protocol was developed with imaging using the Leica scanning laser confocal microscope. Further optimization to allow imaging in 3D used the 2D protocol as a starting point.

To prepare samples, embryonic stem cells were seeded in T25 flasks at 5000 per cm^2 and maintained in culture for 2 days. The medium was aspirated and the flask was rinsed twice with PBS. The cells were detached from the culture surface with accutase at 37^{o}C for 5 minutes. Following centrifugation at 1200rpm for 5mins, the cells were collected in 5mL of warm medium. Aliquots, 1mL in volume, were transferred into a 2mL tube and 5µL of a solution containing 1 mg/mL Hoechst 33258 was added to give a final concentration of 5µM. The cells were incubated in the staining medium for 30 minutes. Following centrifugation, the staining medium was removed and 1 mL fresh warmed medium was added. 25 µL aliquots were aspirated and added to a coverslip, which was imaged using the Leica scanning laser confocal microscopy with UV laser. Representative images of nuclear staining in individual cells and for cells within colonies are shown as Figure 2.10. High quality staining and imaging was achieved with clear structural detail evident within the nuclei.

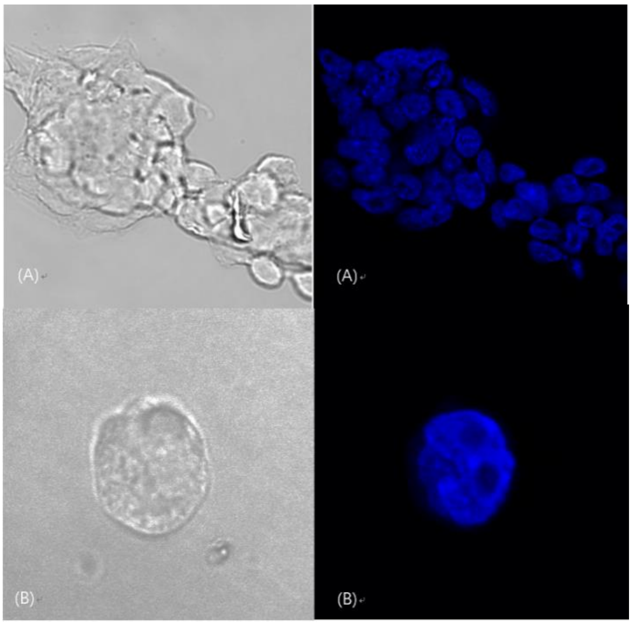

Figure 2.10. Representative confocal images of embryonic stem cells (grey) and their nuclei (blue) following staining with Hoechst 33258. (A) a colony of cells and (B) an individual cell.

A similar nucleus staining protocol was adopted using SYTO 16. Cells were resuspended in 1mL of medium and stained with 3µM SYTO 16 (1 mg/mL stock solution, 3µL added). The staining medium was removed by centrifugation after 30 minutes and 1 mL new warm medium was added. 25 µL aliquots were aspirated and applied to a coverslip with cells imaged using the Leica scanning laser confocal microscope with AR laser (488nm). Representative nuclear images obtained using a 20X lens and a 63X oil lens are shown as Figure 2.11. High quality staining and imaging was achieved with clear structural detail evident within the nuclei.

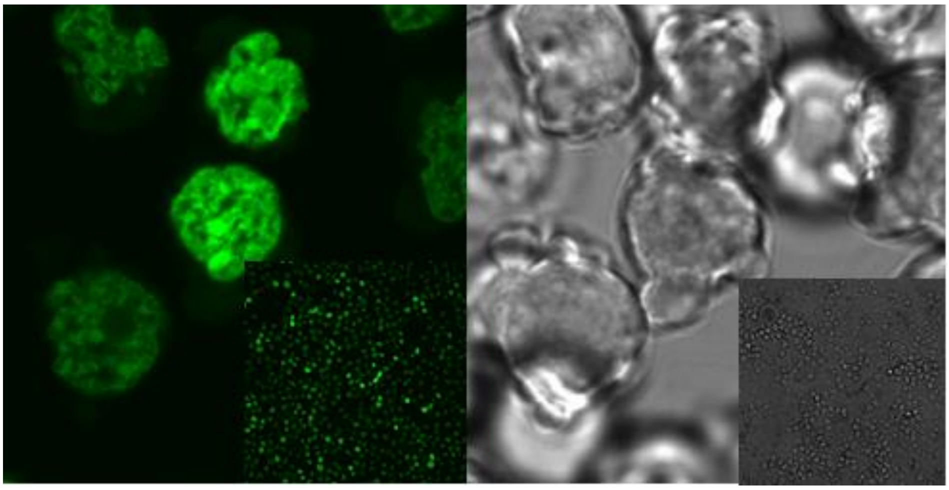

Figure 2.11 Representative confocal images of embryonic stem cells (grey) and their nuclei (green) following staining with SYTO 16. The main image is taken using a 63X oil lens and the insert via a 20X lens.

2.6.2 Nuclei Staining Protocol on 3D scaffold.

The nuclei staining protocol in 3D cell-seeded agarose used the 2D nuclei staining protocol as its starting point. However due to the additional complexity of dye availability and diffusion through the agarose constructs optimization studies were performed to select the appropriate combination of dye concentration and staining time for best staining performance and longest fluorescence maintenance. The cell-seeded agarose sample preparation is described in Section 2.3.1. An agarose construct was placed in a 2mL tube and submerged in 1mL imaging medium. The staining time selection of SYTO 16 was set as:

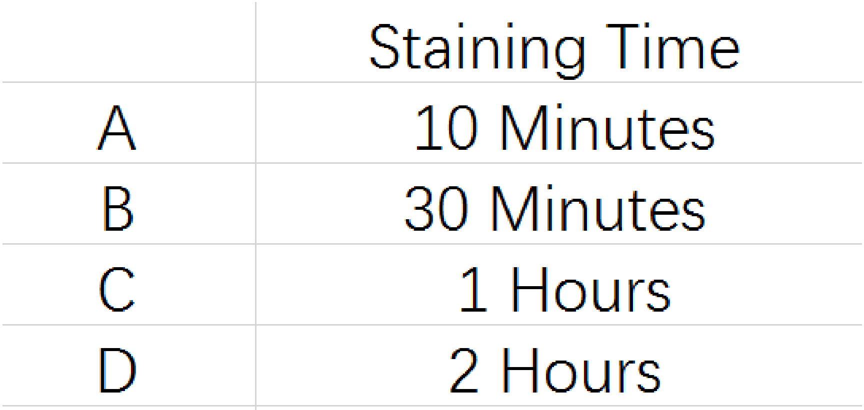

	Staining Time
A	10 Minutes
B	30 Minutes
C	1 Hours
D	2 Hours

Figure 2.12 presents the result of nuclei staining with varying staining times. Following staining for 10 minutes (Fig 2.11A) limited staining of nuclei was evident except for a small number of intensely stained focal regions. Extending the staining time to 30-60 minutes (Fig 2.11B and C) enhanced the quality of the images obtained, with clear chromatin structure evidence and a reduction in the prevalence of bright focal regions. However, when the staining time reached 2 hours (Fig 2.11D), a loss of delineation of internal nuclear structure was evident. Accordingly 30-60 minutes was regarded as the appropriate staining period for nuclei staining in 3D cell-seeded agarose.

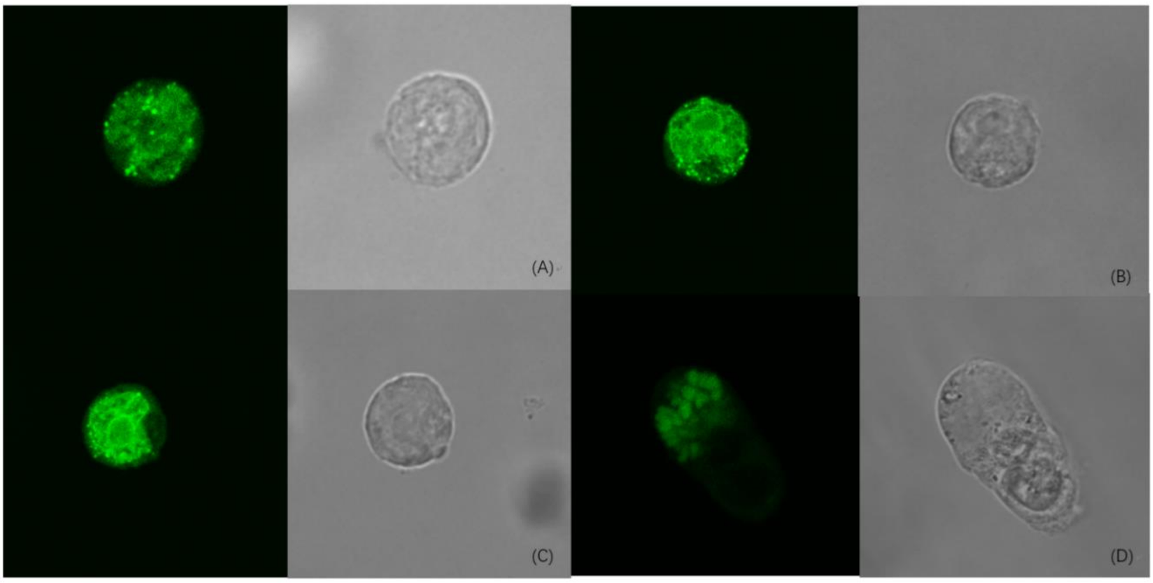

Figure 2.12 Confocal microscopy images of mouse embryonic stem cell (grey) and nuclei (green) stained with Syto 16 in various periods.

Besides staining time, the SYTO 16 concentration was also varied as follows:

	Staining Concentration （mg/mL)
A	1
B	3
C	10

Figure 2.13 presents the effect of varying Syto 16 concentration on nuclear staining. The Images were all obtained with the same gain (650 V) and offset (-4). The results shows that the low staining concentration (1 mg/mL, Fig 2.12A) failed to reveal acceptable levels of nuclear structure while the highest concentration (10 mg/mL) produced high fluorescence intensities resulting in a loss of nuclear detail in the image. High levels of nuclear detail were obtained using 3 mg/mL and this was adopted as the standard Syto 16 staining concentration in further experimentation in this study.

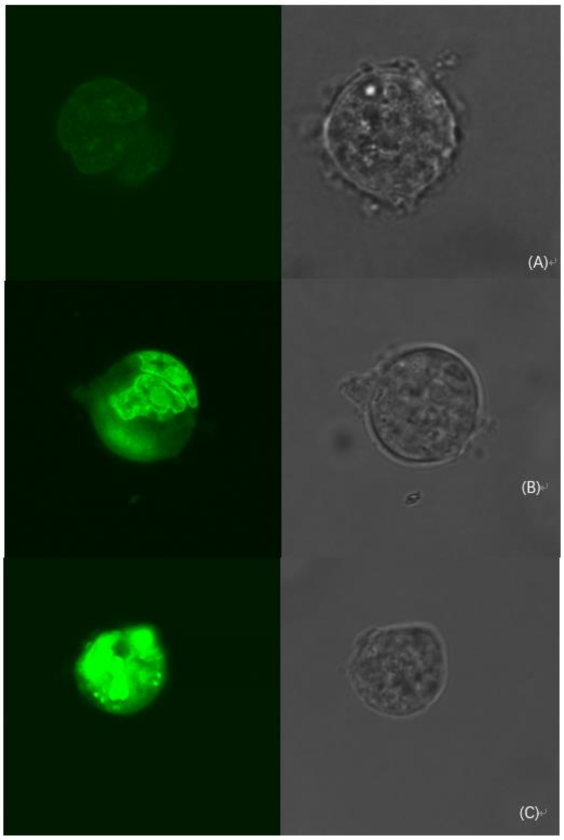

Figure 2.13. Confocal microscopy images of mouse embryonic stem cell (grey) and nuclei (green) stained with Syto 16 in various staining concentration A. 1 mg/mL, B. 3 mg/mL, C. 10 mg/mL.

Chapter 3 Nuclear Mechanical Characteristics in Different Pluripotency States

3.1 Introduction

Under mechanical perturbation, induced for example by compression, tension or shear stress, the cell is deformed often resulting in alterations in nuclear morphology as well as mechanical signal transduction. The deformation characteristics are dependent on the physical properties of cell and nucleus and their interaction via cytoskeletal and LINC complex components. Accordingly the application of mechanical perturbation may result in a variety of strain phenomena depending on the cell type, and its specific mechanical phenotype. Further, a variety of mechanical outcomes may occur in a population of cells nominally of the same type due to the presence of sub-populations with varying phenotype. Additionally the characteristics of individual cells associated with morphological variation and random orientational positions with regard to directional mechanical perturbation may play a role. In the current study specific culture conditions have been used to induce mouse embryonic stem cell populations to adopt different pluripotency states. The variation in pluripotency state has been used to test the hypothesis that nuclear deformation in mouse embryonic stem cells during compression within cell-seeded agarose constructs is distinct between naïve-like and primed-like state pluripotent cells.

3.2 Material and Methods

3.2.1 Cell culture for naïve-like and primed-like pluripotent states.

Mouse embryonic stem cells were cultured in 25cm^2 Hermo Scientific™ cell culture flasks as described in chapter 2.2.3. The cells were seeded as 10000 per cm^2, 5mL of regular mouse embryonic stem cell medium (LIF medium) was added and the flasks were incubated at 37°C for 48 hours without medium replacement. The cells were detached using accutase and collected following centrifugation. The cells were divided into two groups: (1) A LIF group which were maintained in the same culture conditions and (2) A 2i group that were cultured in 2i medium as described in chapter 2.

A schematic to indicate the experimental protocol is presented in Figure 3.1. For the LIF group, regular mouse embryonic stem cell medium (LIF medium) was used throughout as the culture medium. The cells were seeded at 10000 per cm^2 in a 25cm^2 cell culture flask and 5mL medium was added. The cells were incubated at 37°C for 48 hours without medium replenishment. The cells were harvested using accutase, collected by centrifugation and seeded at 10000 per cm^2 in a 75cm^2 cell culture flask with 15 mL medium and in the wells of a 6-well plate with 3mL medium in each plate. The flasks and plates were incubated at 37°C for 48 hours without medium replenishment. The cells within the flasks were harvested using accutase, collected by centrifugation and used in the preparation of cell-seeded agarose constructs for compression studies. The cells within the 6 well plates were used for gene expression analysis by PCR assay and for AP staining.

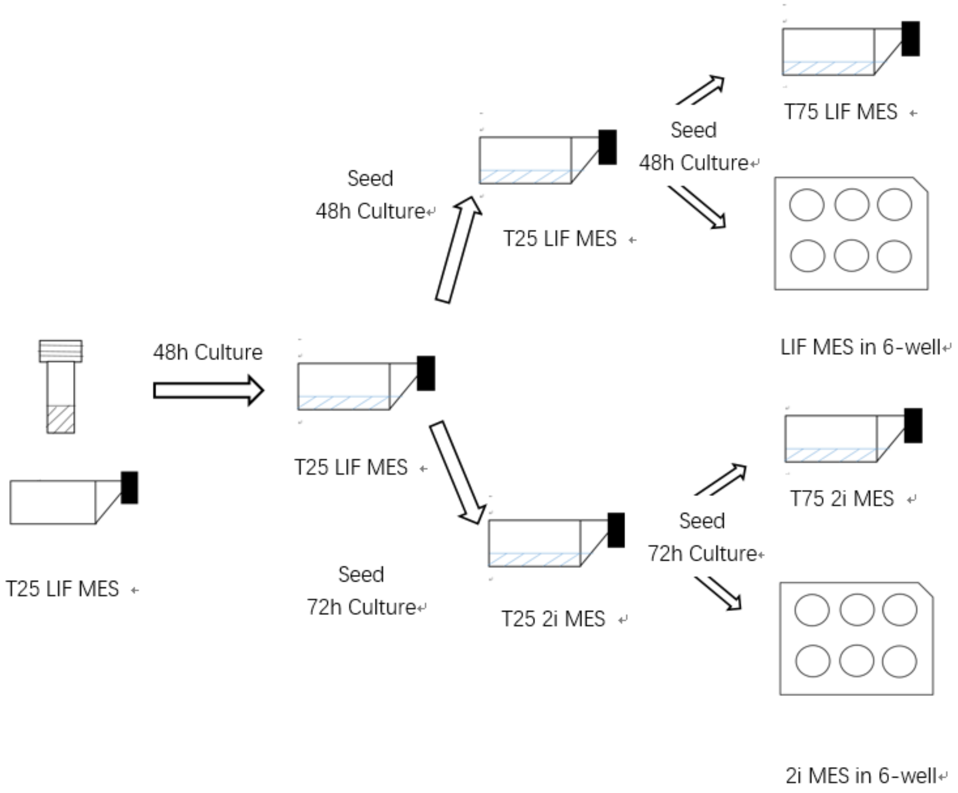

Figure 3.1 Schematic representing the cell culture protocol used for experiments in chapter 3.

For the 2i group, naïve-like state mouse embryonic stem cell medium (2i medium) was used as culture medium. The cells were seeded at 10000 per cm^2 in a 25cm^2 cell culture flask, 5mL medium was added and the cells were incubated at 37°C for 72 hours with the medium changed after 48 hours. The cells were harvested using accutase and seeded at 10000 per cm^2 in a 75cm^2 cell culture flasks with 15mL medium or the wells of 6-well plate with 3mL medium in each well. The flasks and plates were incubated for 37°C for 72 hours with the medium changed after 48 hours. The cells within the flasks were harvested using accutase, collected by centrifugation and used in the preparation of cell-seeded agarose construct from compression studies. The cells within the 6 well plates were used for gene expression analysis by PCR assay and for AP staining. The difference in culture time between passage for the two groups reflects differences in cell doubling time for cells maintained in the possible naïve and primed states.

3.2.2 Light microscopy and AP staining

Prior to passage, cells were visualised using phase contrast light microscopy and 5 representative images were recorded.

One well of the 6-well plate was used for the alkaline phosphatase staining assay using the method described in chapter 2. Five representative images were taken for each assay. Images were used to investigate the periphery of cell colonies in LIF mES cell and 2i mES cell. In comparison with alkaline phosphatase staining in cell colonies of LIF mES cell and 2i mES cell, it is possible to tell the difference of pluripotency maintained in LIF mES cell and 2i mES cell.

3.2.3 PCR assay

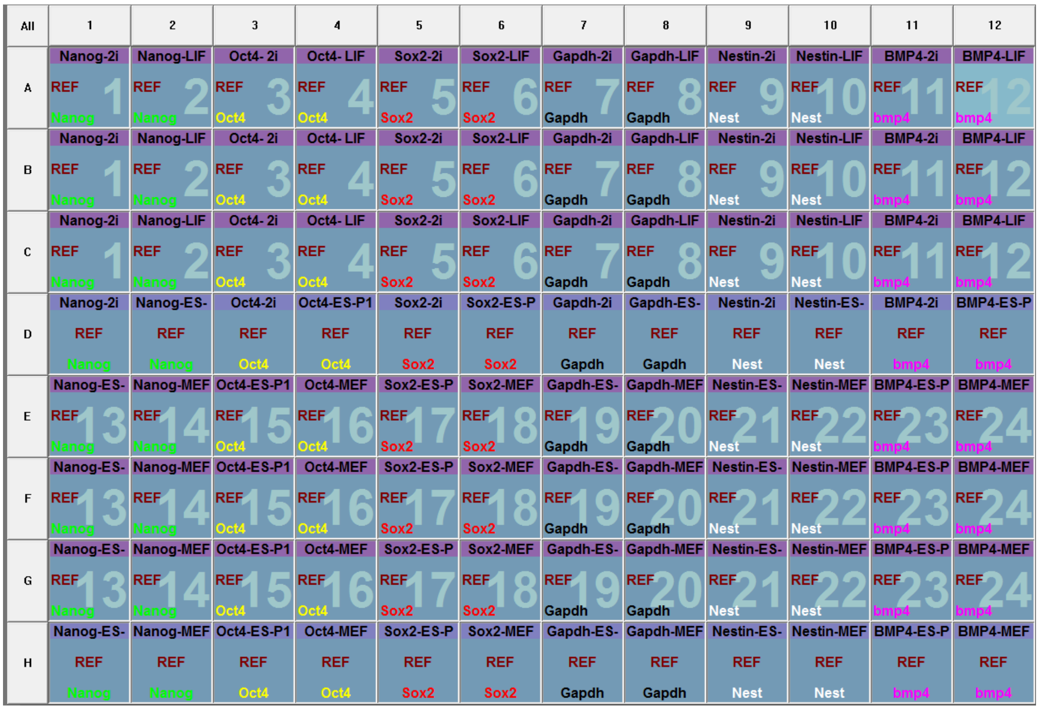

All	1	2	3	4	5	6	7	8	9	10	11	12
A	Nanog-2i REF 1 Nanog	Nanog-LIF REF 2 Nanog	Oct4- 2i REF 3 Oct4	Oct4- LIF REF 4 Oct4	Sox2-2i REF 5 Sox2	Sox2-LIF REF 6 Sox2	Gapdh-2i REF 7 Gapdh	Gapdh-LIF REF 8 Gapdh	Nestin-2i REF 9 Nest	Nestin-LIF REF 10 Nest	BMP4-2i REF 11 bmp4	BMP4-LIF REF 12 bmp4
B	Nanog-2i REF 1 Nanog	Nanog-LIF REF 2 Nanog	Oct4- 2i REF 3 Oct4	Oct4- LIF REF 4 Oct4	Sox2-2i REF 5 Sox2	Sox2-LIF REF 6 Sox2	Gapdh-2i REF 7 Gapdh	Gapdh-LIF REF 8 Gapdh	Nestin-2i REF 9 Nest	Nestin-LIF REF 10 Nest	BMP4-2i REF 11 bmp4	BMP4-LIF REF 12 bmp4
C	Nanog-2i REF 1 Nanog	Nanog-LIF REF 2 Nanog	Oct4- 2i REF 3 Oct4	Oct4- LIF REF 4 Oct4	Sox2-2i REF 5 Sox2	Sox2-LIF REF 6 Sox2	Gapdh-2i REF 7 Gapdh	Gapdh-LIF REF 8 Gapdh	Nestin-2i REF 9 Nest	Nestin-LIF REF 10 Nest	BMP4-2i REF 11 bmp4	BMP4-LIF REF 12 bmp4
D	Nanog-2i REF Nanog	Nanog-ES- REF Nanog	Oct4-2i REF Oct4	Oct4-ES-P1 REF Oct4	Sox2-2i REF Sox2	Sox2-ES-P REF Sox2	Gapdh-2i REF Gapdh	Gapdh-ES- REF Gapdh	Nestin-2i REF Nest	Nestin-ES- REF Nest	BMP4-2i REF bmp4	BMP4-ES-P REF bmp4
E	Nanog-ES- REF 13 Nanog	Nanog-MEF REF 14 Nanog	Oct4-ES-P1 REF 15 Oct4	Oct4-MEF REF 16 Oct4	Sox2-ES-P REF 17 Sox2	Sox2-MEF REF 18 Sox2	Gapdh-ES- REF 19 Gapdh	Gapdh-MEF REF 20 Gapdh	Nestin-ES- REF 21 Nest	Nestin-MEF REF 22 Nest	BMP4-ES-P REF 23 bmp4	BMP4-MEF REF 24 bmp4
F	Nanog-ES- REF 13 Nanog	Nanog-MEF REF 14 Nanog	Oct4-ES-P1 REF 15 Oct4	Oct4-MEF REF 16 Oct4	Sox2-ES-P REF 17 Sox2	Sox2-MEF REF 18 Sox2	Gapdh-ES- REF 19 Gapdh	Gapdh-MEF REF 20 Gapdh	Nestin-ES- REF 21 Nest	Nestin-MEF REF 22 Nest	BMP4-ES-P REF 23 bmp4	BMP4-MEF REF 24 bmp4
G	Nanog-ES- REF 13 Nanog	Nanog-MEF REF 14 Nanog	Oct4-ES-P1 REF 15 Oct4	Oct4-MEF REF 16 Oct4	Sox2-ES-P REF 17 Sox2	Sox2-MEF REF 18 Sox2	Gapdh-ES- REF 19 Gapdh	Gapdh-MEF REF 20 Gapdh	Nestin-ES- REF 21 Nest	Nestin-MEF REF 22 Nest	BMP4-ES-P REF 23 bmp4	BMP4-MEF REF 24 bmp4
H	Nanog-ES- REF Nanog	Nanog-MEF REF Nanog	Oct4-ES-P1 REF Oct4	Oct4-MEF REF Oct4	Sox2-ES-P REF Sox2	Sox2-MEF REF Sox2	Gapdh-ES- REF Gapdh	Gapdh-MEF REF Gapdh	Nestin-ES- REF Nest	Nestin-MEF REF Nest	BMP4-ES-P REF bmp4	BMP4-MEF REF bmp4

Figure 3.2 96-well plate design for the PCR assay.

The reverse transcript PCR (rt-PCR) assay was used to assess levels of expression of genes considered to be markers of pluripotency and early differentiation in the two cell groups used in the project, as described in chapter 2. Two pluripotency gene markers (Oct4 and Nanog) and three differentiating gene markers (Sox2, Nestin and BMP4) were analysed along with the housekeeping gene (GAPDH). The PCR plate design is shown as Figure 3.2. Acting as a differentiation reference, the cDNA from mouse embryonic fibroblast (mEF) was also analysed, to indicate gene expression levels in a cell type that does not express pluripotency markers at high levels but should express the differentiating gene markers.

3.2.4 Cell-seeded agarose construct preparation and compression

The protocol used to prepare cell-seeded agarose constructs incorporating two aluminium end pieces to act as grips is illustrated in Figure 3.3. A plastic mould comprising three pieces and incorporating 8 slots for construct preparation once assembled was used. The three mould pieces were sterilised in 70% ethanol under UV light overnight in a cell culture hood. The two bottom components of the mould were assembled and sealed with sterile tape on the back. The aluminium end pieces were inserted into each side of the slots. The agarose/cell suspension was prepared as described in chapter 2 and carefully injected into the mould to ensure the slots were entirely filled with the cell suspension with a slightly domed suspension surface to ensure that air bubbles are not created. The sliding top plate of the mould was carefully inserted to remove extra cell suspension to ensure complete filling of the slots. The whole mould was subsequently wrapped in sterile aluminium foil and maintained at 4^{o}C for 5 minutes or room temperate for 15 minutes to allow gelling of the agarose. The mould was carefully disassembled allowing the cell-seeded agarose constructs incorporating the two aluminum ends pieces to be removed. The resultant cell/agarose constructs were cultured at 37^{o}C in the relevant medium prior to compression.

The agarose constructs were stained using Syto16 as described in section 2.7.3 and subsequently mounted into the microscope-compatible compression rig, as described in chapter 2. The constructs were subjected to 10% and 20% compressive strain according to the protocol illustrated in figure 3.4. The compression rig was programmed to provide 0-10% and 10-20% strain in 10s, achieved by a series of five 2% strain processing steps. The construct were maintained for 15 minutes at the selected strain, to allow for agarose relaxation and images of the cells and their nucleus were acquired during a 5 minute imaging period, prior to any further application of compressive strain. The compression protocol was characterised through a modelling approach using Abaqus, which is described in Chapter 5, to allow spatial and temporal variations in strain profile to be revealed.

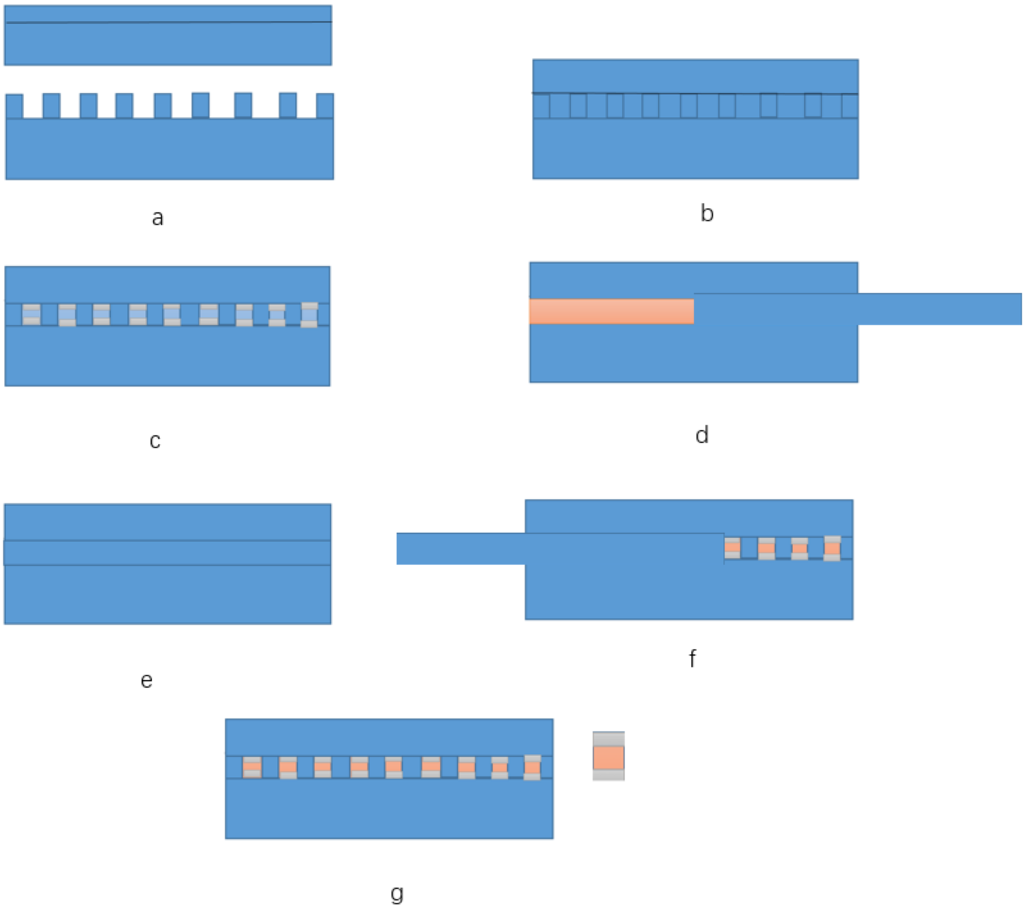

Figure 3.3. The preparation protocol for cell-seeded agarose contracts. (a) The bottom two mould pieces are assembled. (b) The bottom two mould pieces are fixed together using tape. (c) Aluminium end grips are inserted. (d) The cell/agarose suspension is added into the resultant wells in the mould (e) The top plate of the mould is assembled and maintained in place during the gelling process. (f) The top plate of the mould is removed after construct gelation. (g) The resultant constructs are removed from the mould.

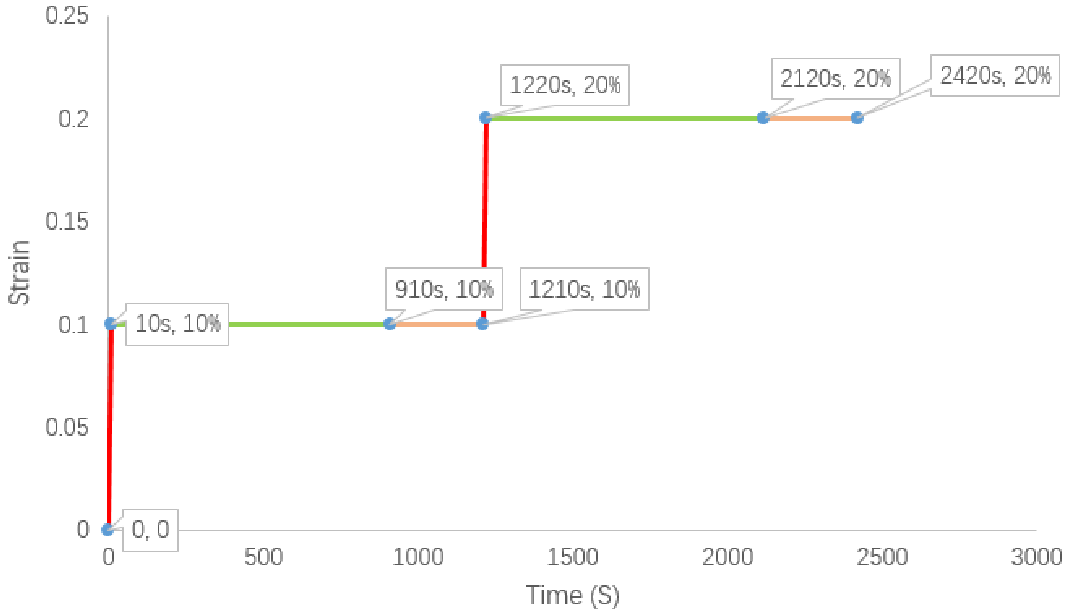

Figure 3.4. Schematic representing the agarose compression protocol used. Red: compression period. Green: agarose relaxation period. Pink: confocal image capture.

3.2.5 Confocal Microscopy Analysis

Representative cells and their nuclei were imaged at 0% strain and during the imaging period following the application of 0-10% and 10-20% strain as described above. Figure 3.5 presents representative images of the cell and nucleus during the compression process for cells culture under 2i and 1xLIF conditions and imaged using the Perkin Elmer confocal microscope. Figure 3.5 clearly reveals alterations in both cell and nuclear morphology with compressive strain and morphometric analysis was subsequently used to quantify modification of the morphology of the cell and nucleus.

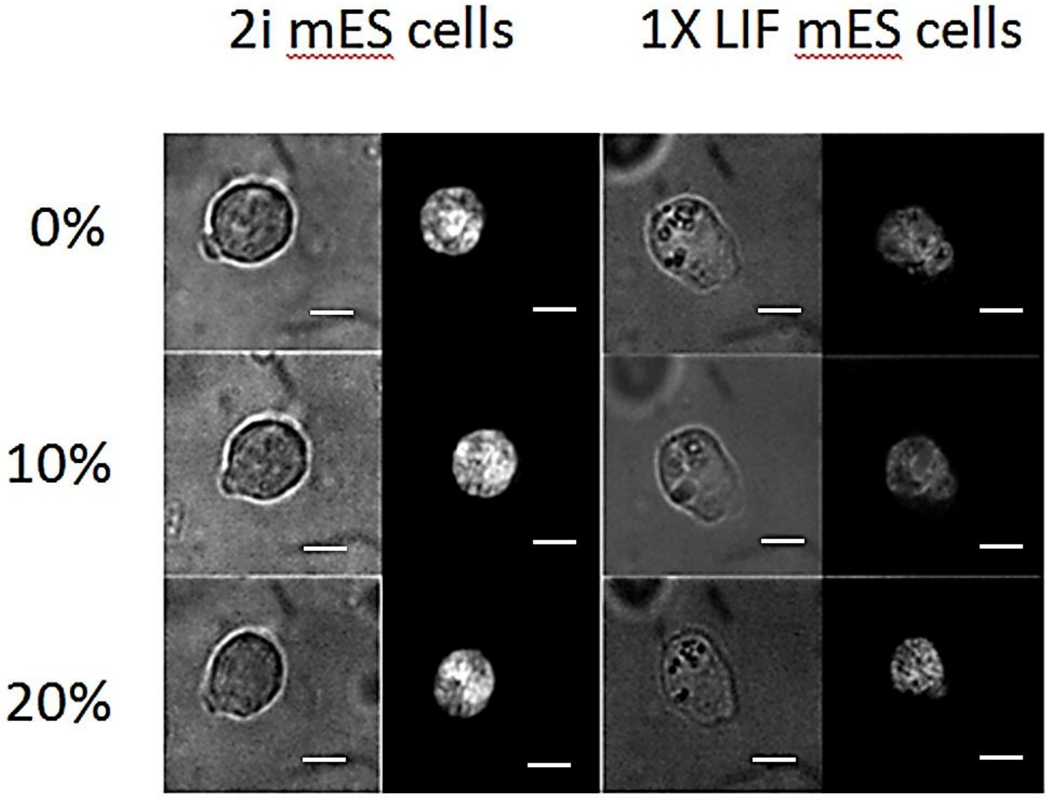

Figure 3.5. Representative confocal microscopy images of cell (grey) and nuclei (black and white) cells cultured under 2i (left) and 1X LIF (right) conditions at 0%, 10% and 20% compressive strain (Scale bar: 6.3 µm).

The measurements of the morphology of the cell and nucleus in confocal microscopy images prior to and following compressive strain focused on two distinct morphological phenomena: deformation and rotation. Figure 3.6 illustrates measurements acquired to assess deformation: (a) dimension modification of X-axis, which is parallel to the direction of compressive strain, and Y-axis, which is perpendicular to compression. (b) the cross-section area which is taken at the z-position with the maximum area. (c) aspect ratio (AR) = Major axis length (a) / Minor axis length (b). To record the rotation during compression, the angle of the nucleus relative to the axis of compression was determined, as defined in figure 3.7.

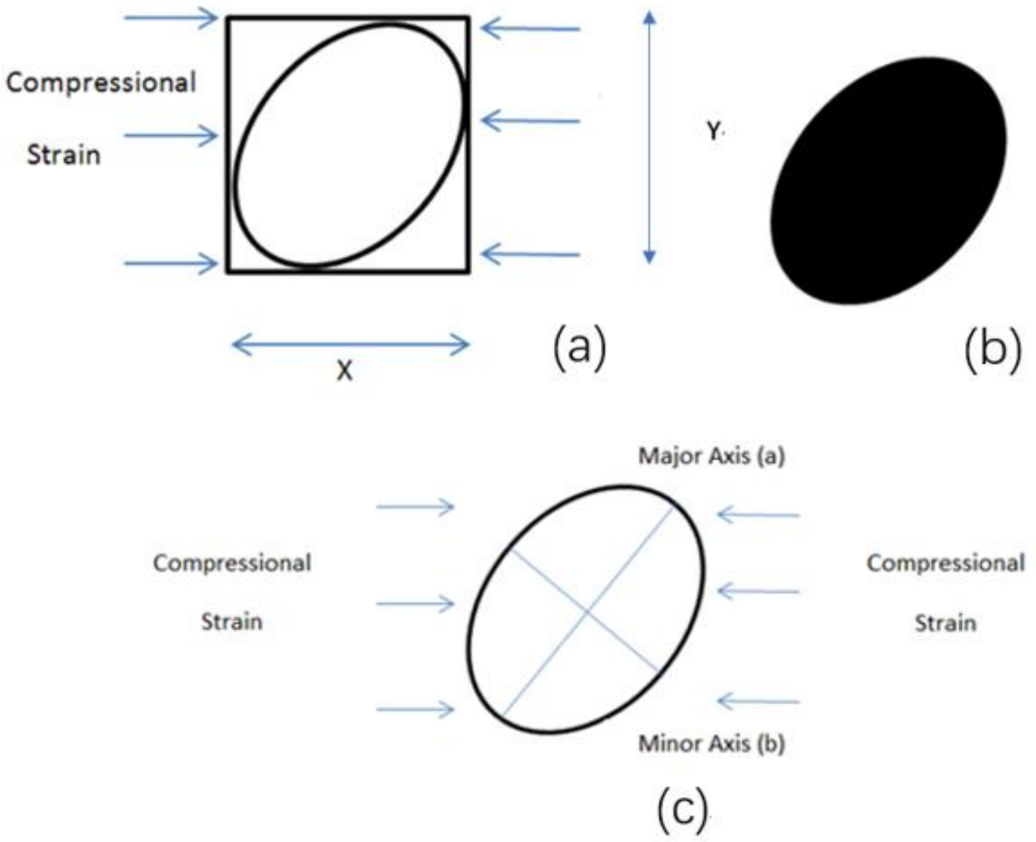

Figure 3.6. Measurements acquired from confocal images to assess deformation (a) X-axis and Y-axis dimension (b) Cross section area (black) and (c) Aspect ratio (AR).

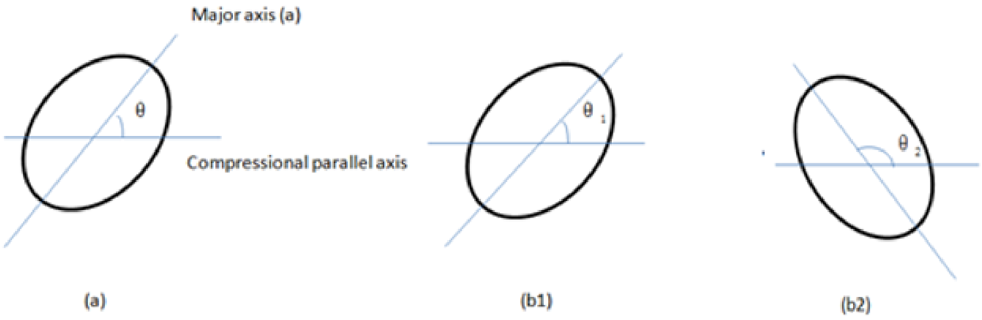

Figure 3.7. Definition of nuclear position angle θin (a) and true nuclear position angleθ_T in (b). When θ_1 <90 (b1), $\theta_T = \theta_1$. When θ_2 <90 (b2), $\theta_T = 180 - \theta_2$

3.3 Results

3.3.1 Cell culture modification leads to different pluripotent states in mouse embryonic stem cells.

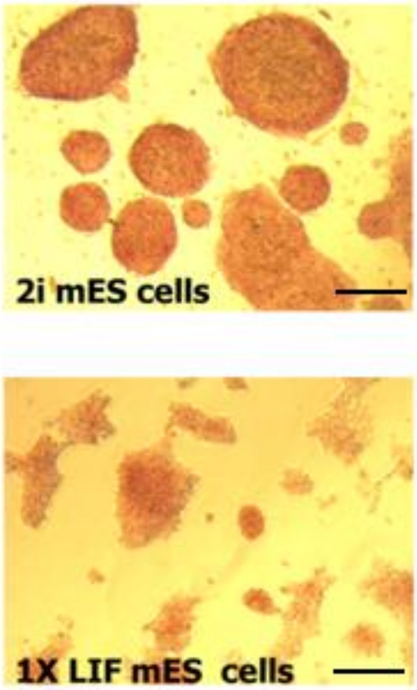

Figure 3.8. Representative images of 2i mES cells (top) and 1X LIF mES cells (bottom) stained for alkaline phosphatase (Scale bar: 100µm).

The alkaline phosphatase assay, as shown in Figure 3.8, revealed that 2i mES cell colonies were larger and had a more regular periphery than colonies formed from 1XLIF-cultured cells. Alkaline phosphatase staining was also more intense for the 2i colonies compared to those maintained in 1XLIF medium, suggesting higher pluripotency levels for the naïve 2i cells, compared to the primed 1XLIF cells. The results of PCR analysis for pluripotency marker genes, as shown in Figure 3.9 are consistent with this assertion. The 2i mES cells expressed significantly greater levels of the pluripotency markers Oct4 and Nanog when compared to 1xLIF mES cells. Negligible levels of either pluripotency marker gene were measured in the mouse embryonic fibroblast differentiating cell reference. Levels of the differentiating marker gene BMP4 and Nestin were significantly lower in the 2i mES cells compared to cells maintained in 1xLIF mES cells. While the levels of BMP4 and Nestin were approximately 20 times greater in 1xLIF cells when normalised to 2i cells the expression of these differentiation markers was still less than half of the levels measured the mouse embryonic fibroblast differentiating cell reference.

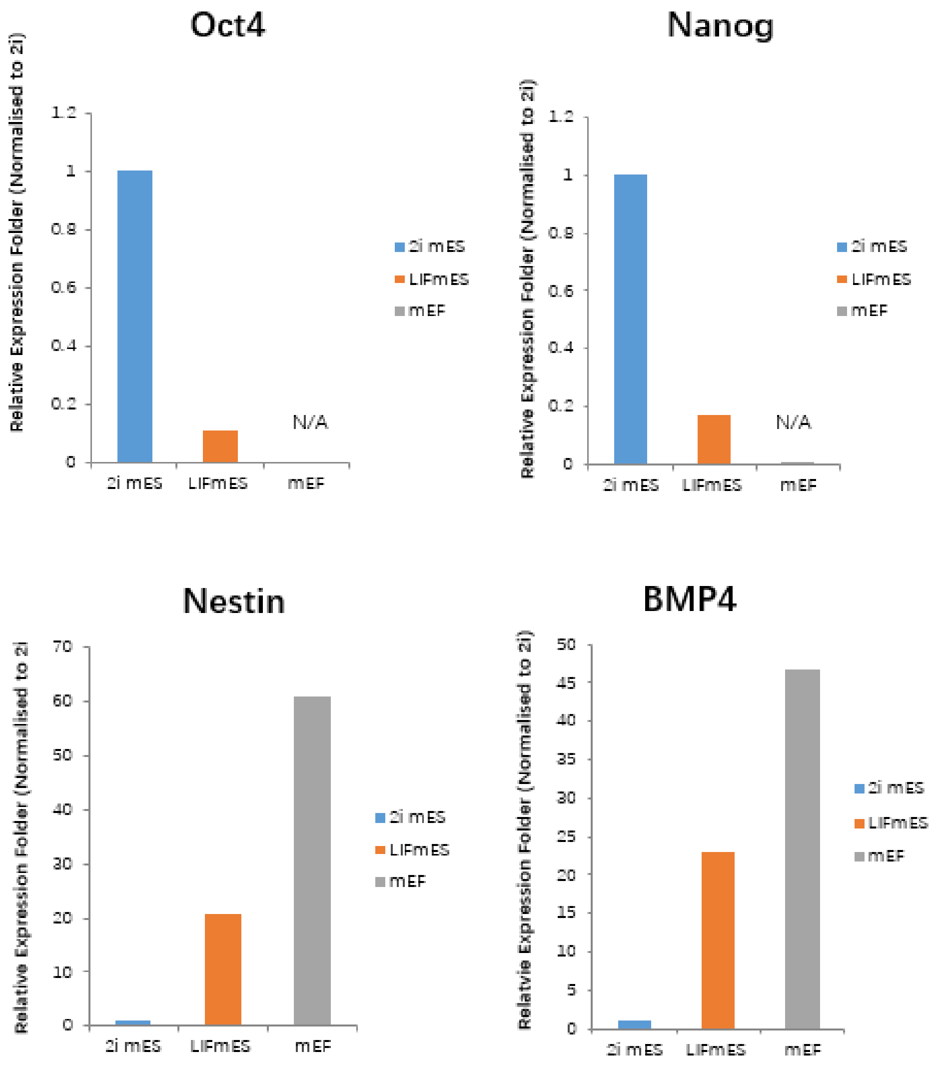

Figure 3.9. PCR assay of LIF MES Cell and 2i MES cell for pluripotency and differentiation gene markers.

3.3.2 Cell deformation in response to compressive strain

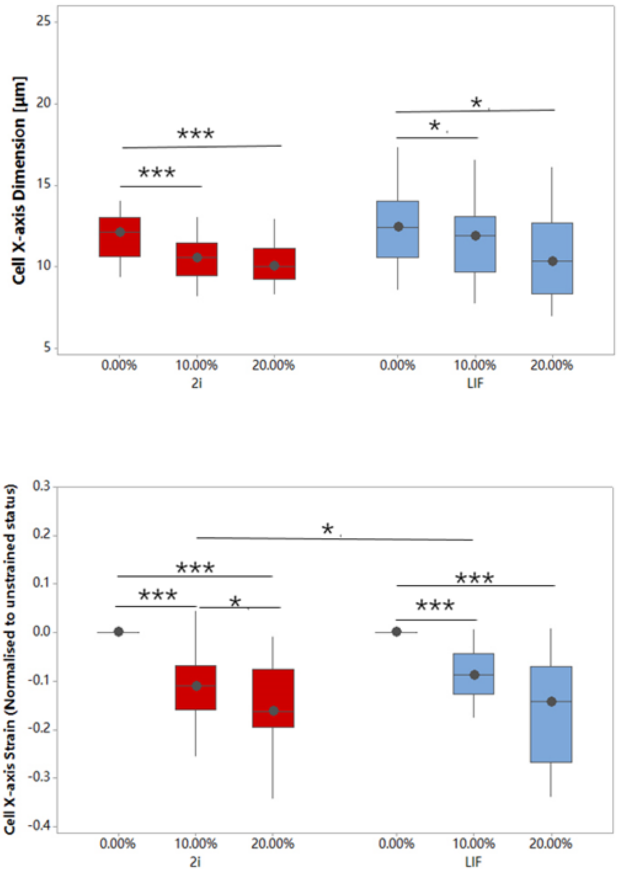

Figure 3.10. Cellular x-axis dimension (top) and x-axis strain normalised to the unstrained status (bottom) for LIF mES cells and 2i mES cells during unconfined compression in agarose. Values are represented as median and interquartile range of n(1X LIF) =41 and n(2i)=50. Mann-Whitney U test is applied where *: $P< 0.05$, **: $P<0.001$ and ***: $P<0.0001$. Mechanical compression modifies the cellular x-axis dimension with similar effects in 1X LIF mES cells and 2i mES cells.

In unstrained constructs the median x-axis dimension was similar for both 1xLIF and 2i mES cells, at approximately 12-12.5 µm (Figure 3.10). The 1xLIF cell population had a notably greater degree of variation in the x-axis cell dimension. On application of 10% compressive strain (Figure 3.10), LIF mES and 2i mES cells both deformed with the LIF mES exhibiting a significantly greater deformation at x-axis compared to the 2i mES cell. When agarose compression strain was increased to 20%, the differences in x-axis deformation between the two types of mES cell was no longer apparent, with cells in both pluripotency states exhibiting a median strain of 15% in the x-axis.

LIF mES cell exhibited significantly greater expansion in the y-axis compared to 2i mES cells (shown at Figure 3.11). This may be caused by the different cell compression-relaxation characteristics originating from the variation of cell Poisson's ratio rather than the cytoplasm stiffness. The mechanical difference in the cytoplasm in the two cell types is considered further in chapter 5.

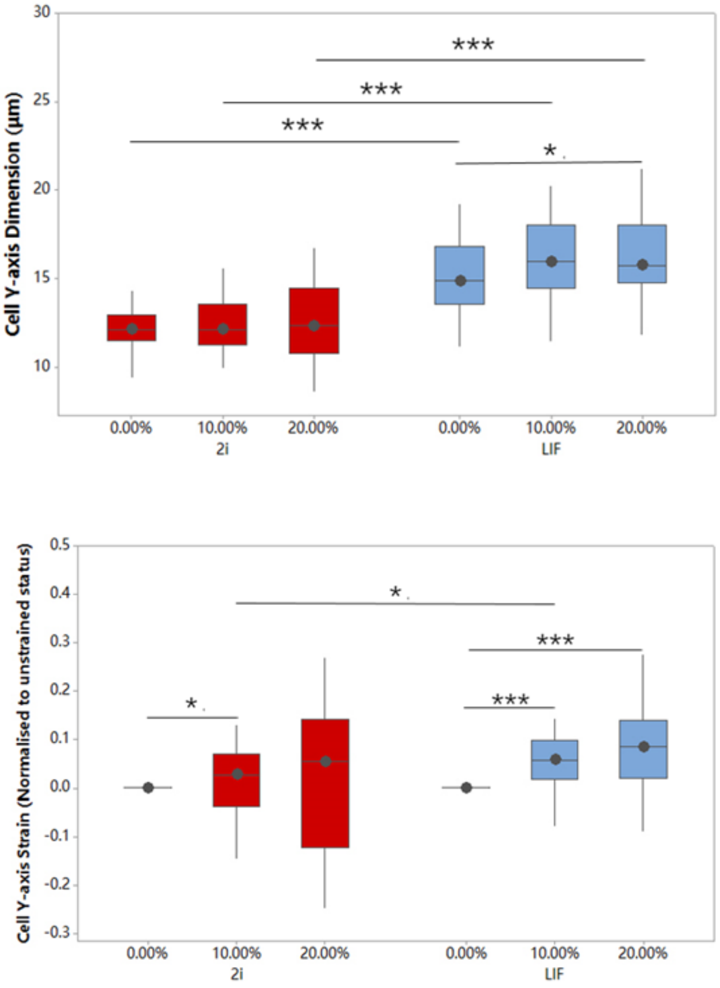

Figure 3.11 Cellular y-axis dimension (top) and y-axis strain normalised to the unstrained status (bottom) for LIF mES cells and 2i mES cells during unconfined compression in agarose. Values are represented as median and interquartile range of n(1X LIF) =41 and n(2i)=50. Mann-Whitney U test is applied where *: P< 0.05, **: P<0.001 and ***: P<0.0001. Mechanical compression modifies the cellular y-axis dimension and the same applied strain causes slightly greater effects in 1X LIF mES cells compared to 2i mES cells.

3.3.3 LIF mES cell has greater nucleus size and nuclear modification is different in LIF cell and 2i cells

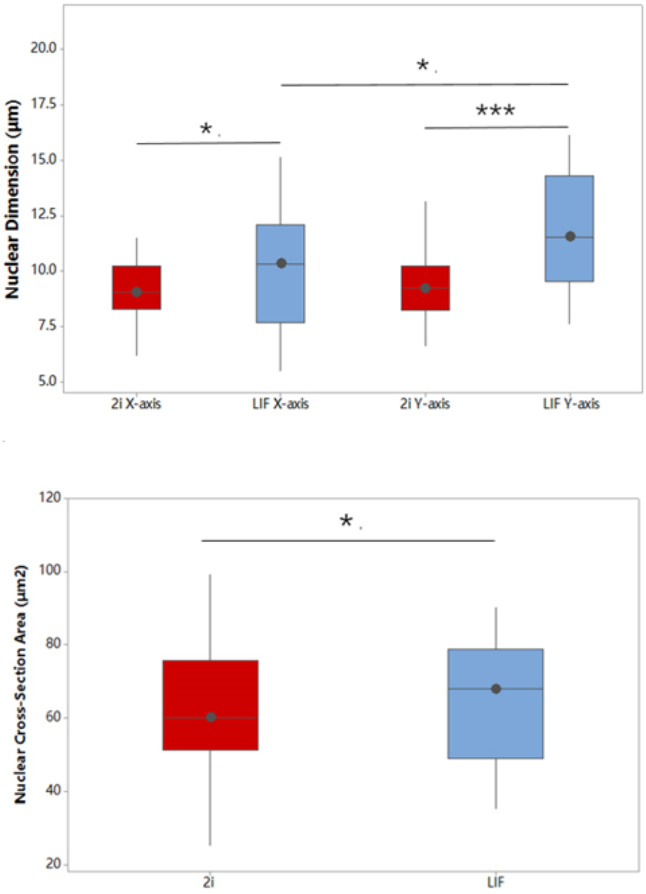

Figure 3.12. Nuclear x-axis and y-axis dimension (top) and nuclear cross section area (bottom) in the unstrained state for LIF and 2i mES cells in agarose. Values are represented as median and interquartile range of n (1X LIF) =41 and n(2i)=50. Mann-Whitney U test is applied where *: $P< 0.05$ and ***: $P<0.0001$. LIF mES cells have greater nuclear size than 2i mES cells, demonstrated by the two axis dimensions and the cross-section area.

As indicated in Figure 3.12, LIF mES cells exhibited significantly larger nuclei than 2i mES cells revealed as differences in x-axis dimension, y-axis dimension and the maximum cross-section area in unstrained status. During agarose compression, the nuclei of LIF mES cells exhibited greater deformation than 2i mES cell at x-axis dimension and y-axis dimension (Figure 3.13). Another interesting finding in Figure 3.14 indicated that with compressing loading to the two cell group, the gap of their x-axis dimension of nucleus was getting smaller and their size in x-axis dimension did not show significant difference in 20% strain.

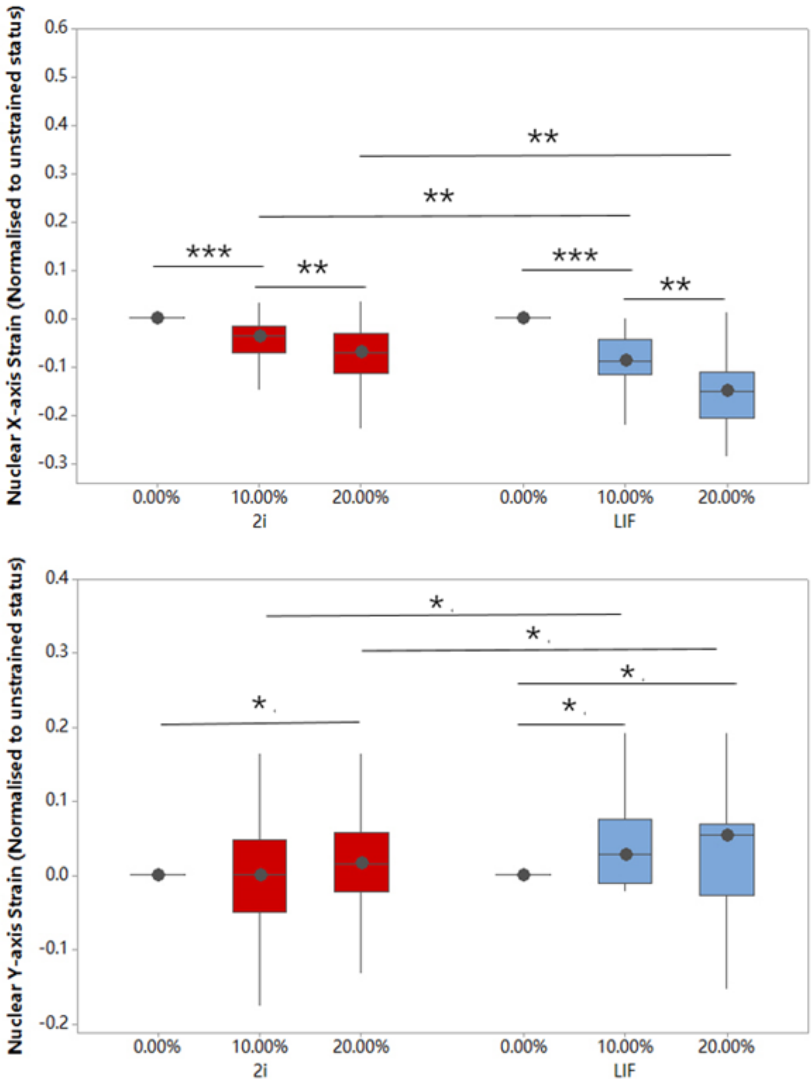

Figure 3.13 Nuclear x-axis strain (top) and nuclear y-axis strain (bottom) normalised to the unstrained state for LIF and 2i mES cells in agarose. Values are represented as median and interquartile range of n (1X LIF) =41 and n(2i) =50. Mann-Whitney U test is applied where *: P< 0.05, **: P<0.001 and ***: P<0.0001. LIF mES cell exhibit greater deformation than 2i mES cell in both x-axis and y-axis.

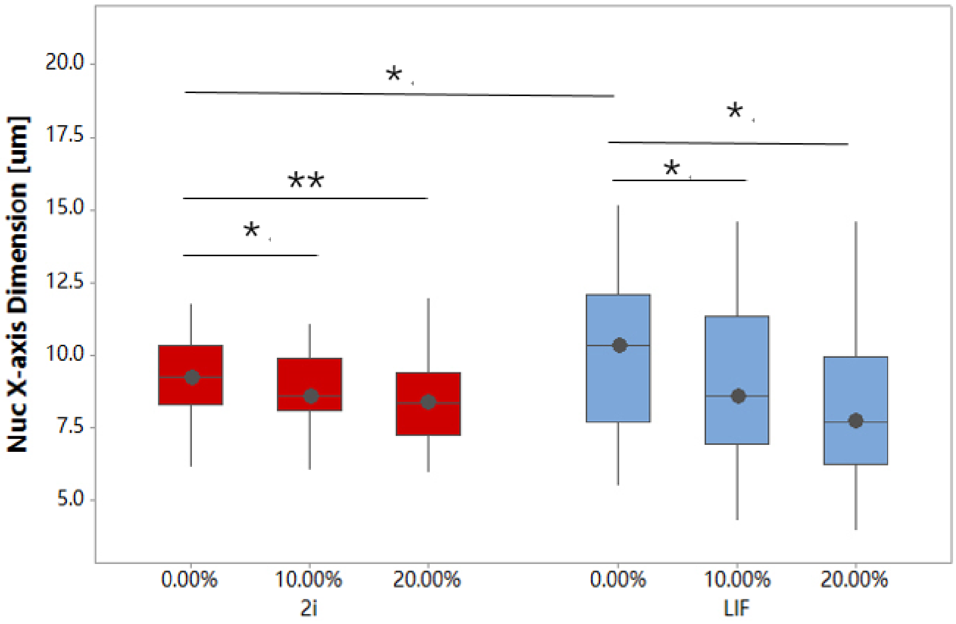

Figure 3.14. Nuclear x-axis dimension for LIF and 2i mES cells during the compression in agarose. Values are represented as median and interquartile range of n (1X LIF) =41 and n(2i) =50. Mann-Whitney U test is applied where *: P< 0.05 and **: P<0.001. Results indicate that the mechanical compression process modifies nucleus x-axis dimension and the average x-axis dimension of LIF mES cell becomes closer to the x=axis dimension of 2i mES cell during compression.

Figure 3.15 presents nuclear images taken from four representative cells in either LIF or 2i conditions. It is notable that the nuclei within 2i mES cells are similar in size and morphology. By contrast the nuclei in LIF mES cells differ considerably from each other in nuclear size and morphology. For further analysis, histograms of nuclear axis dimensions are presented (Figure 3.16 for x-axis and Figure 3.17 for y-axis). In both axes the nuclei for the population of 2i mES cells exhibits normalised distribution in the unstrained status with limited variation in size. By contrast the nuclei in the population of LIF mES cells are not normally distributed and may are divided into two sub-populations, with the group with smaller nuclear size having similar axis dimensions to the 2i mES cells. During the compression, the group with greater nuclear dimensions exhibits more obvious deformation than the group with smaller nuclei in the unstrained state.

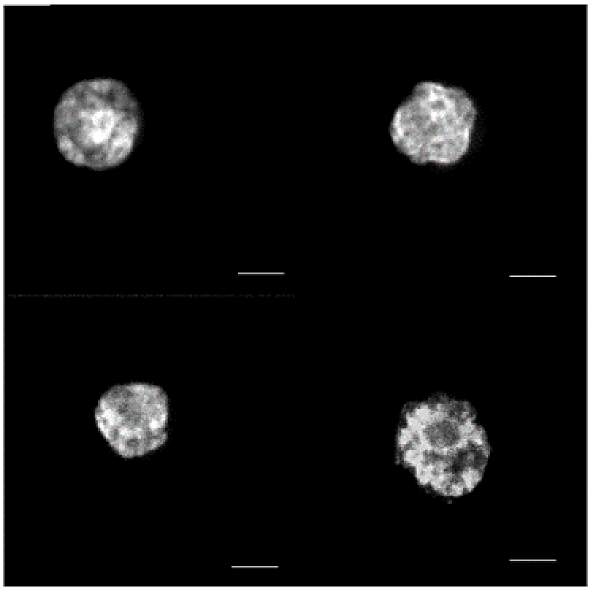
2I mES cell

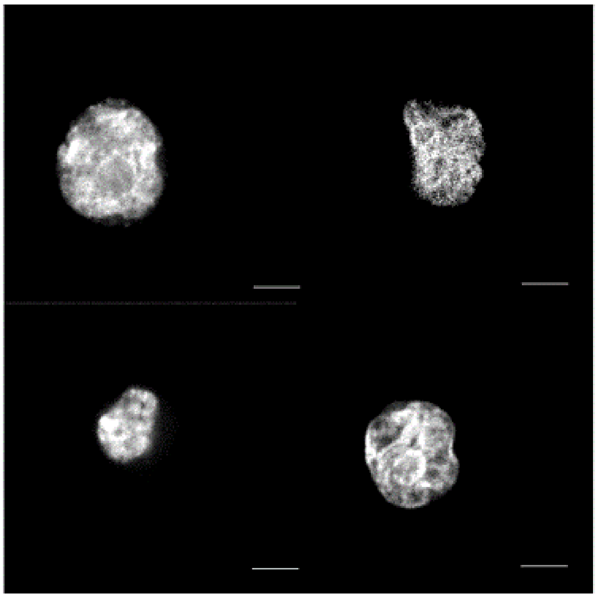
LIF mES cell

Figure 3.15. Confocal microscopy images of the nucleus in four 2i mES cells (top) and four LIF mES cells (bottom). The 2i cells have nucleus which are more consistent in size compared to the LIF mES cells (Scale bar; 6µm).

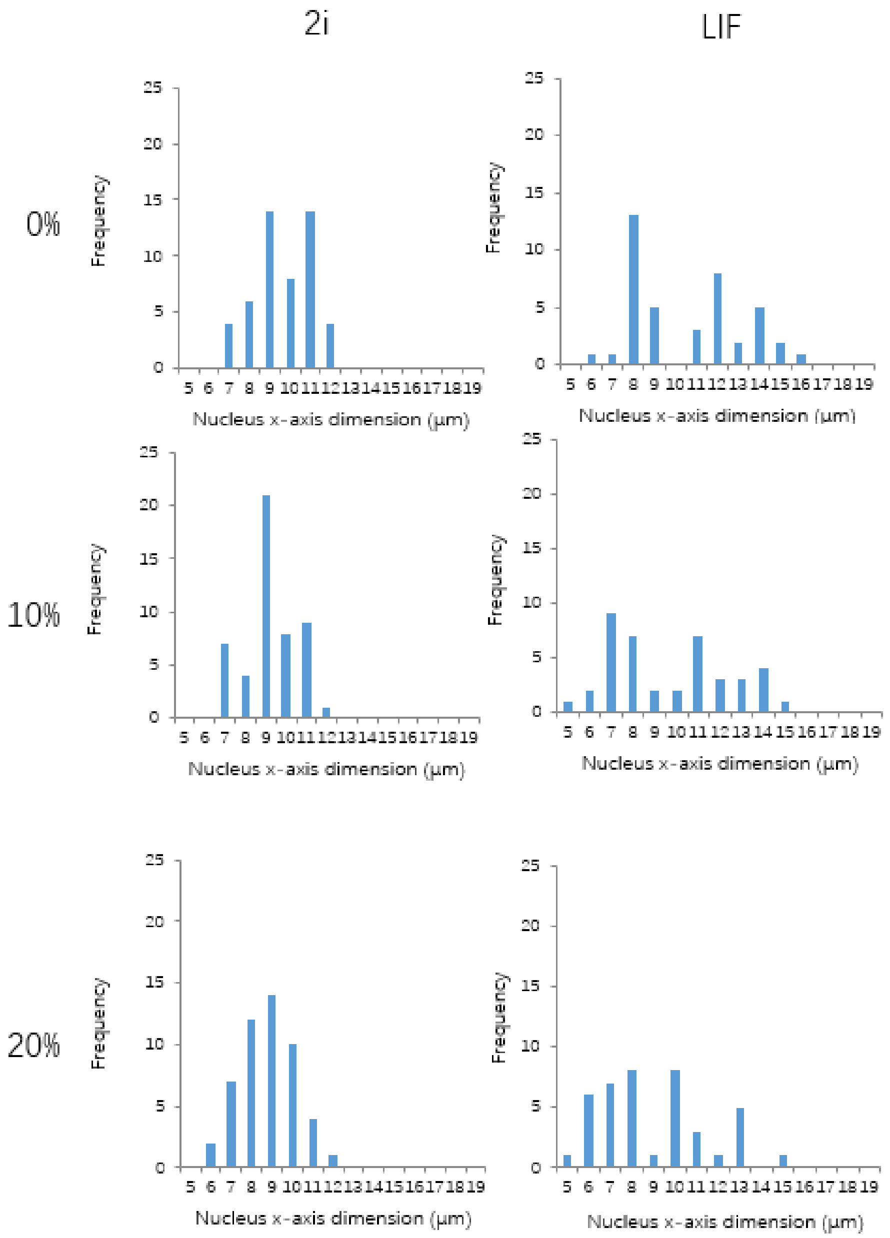

Figure 3.16. Histograms of nucleus x-axis dimension in 2i and LIF mES cells during compression in agarose (n(1X LIF) =41 and n(2i) =50).

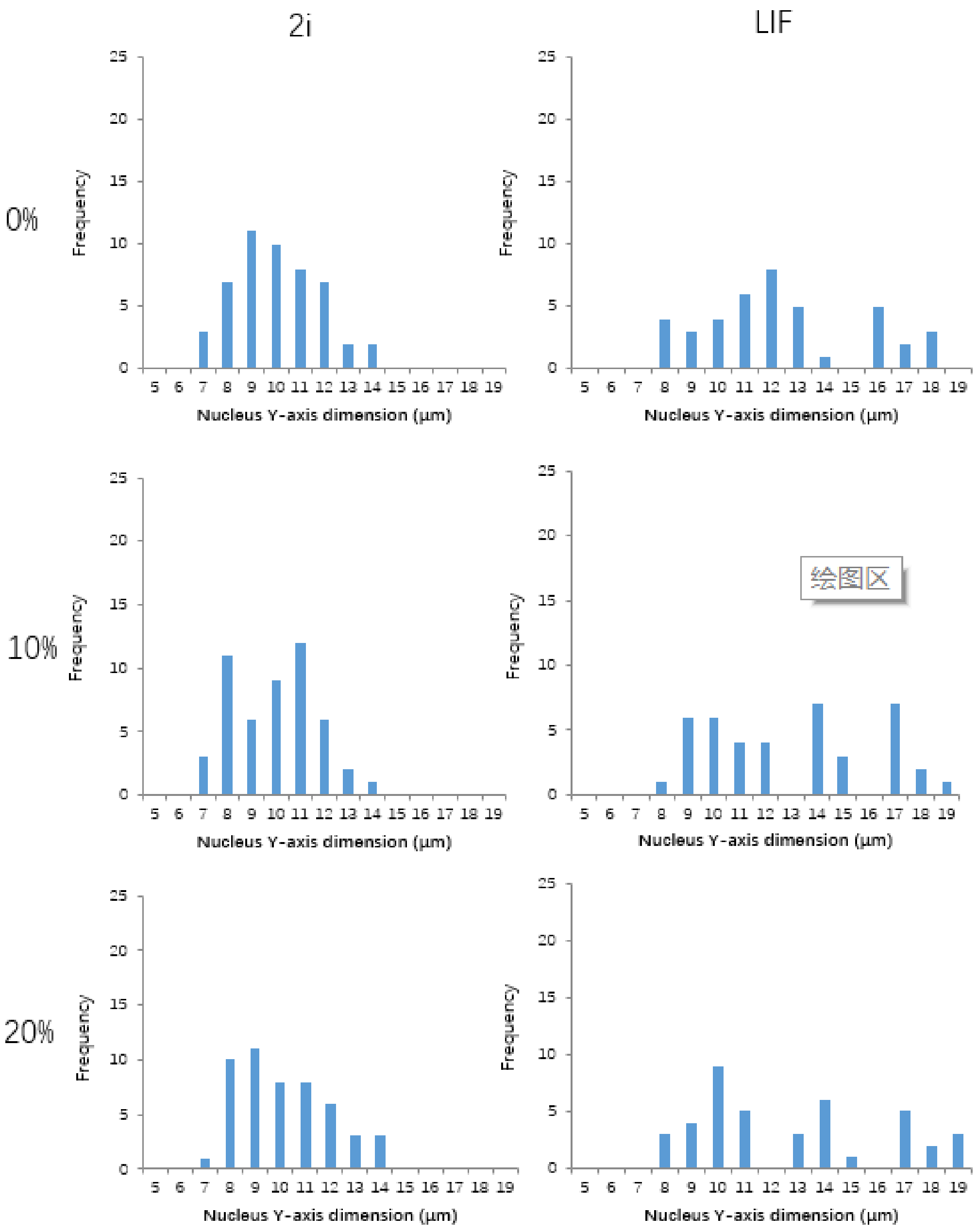

Figure 3.17. Histograms of nucleus y-axis dimension in 2i and LIF mES cells during compression in agarose. (n(1X LIF) =41 and n(2i) =50).

To further confirm our hypothesis, immunostatining of LIF (figure 3.18A) and 2i (figure 3.18B) cells was carried out to indicate both chromatin (blue) and Oct4 (red). Figure 18 revealed a greater variation in Oct4 staining in the LIF cells compared to 2i conditions. These data suggest a greater phenotypic heterogeneity in the LIF cell populations, consistent with the presence of sub-populations of cells with distinct pluripotency states, potentially both naïve-like and primed-like. By contrast the 2i culture conditions induces a greater homogeneity of pluripotency state. These data are consistent with the qPCR data presented in Figure 3.9.

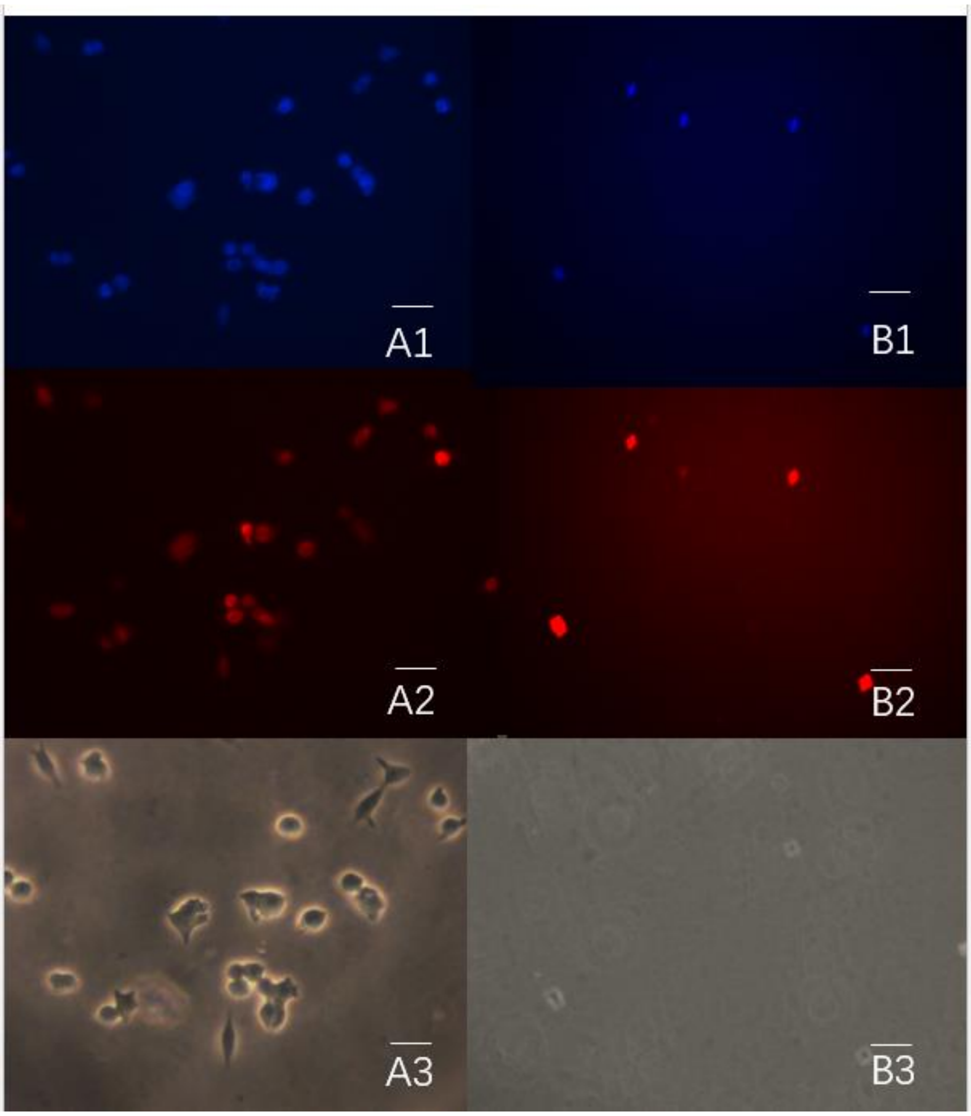

Figure 3.18. Epifluorescence microscopy images (20X) of immunostaining in LIF (A) and 2i (B) cell group (1.Blue: Nuclei with Hoechst 33258, 2.Red: Oct4 and 3. Grey Field). Scale bar: 47.2µm.

3.3.4 Nucleus is rotated during modification.

As revealed in figure 3.18 rotation of the nucleus was exhibited during agarose compression. Compared to nuclear rotation, the cell shows more obvious deformation rather than rotational re-orientation. This suggests that the behaviour of the nucleus and cell are distinct and therefore relatively independent in response to compression. Further analysis of the process of nuclear rotation is presented in figure 3.19 to indicate alterations in the angle of the major axis of the nucleus relative to the axis of compression. The images indicate that the nucleus is rotated towards y-axis depending on the orientation of the major axis in the unstrained state. When the angle between the major axis of the nucleus and the axis of compression is around 45^o the nucleus is more likely to rotate rather than being deformed. By contrast at major axis angles unstrained nearer to 0^o or 90^o deformation rather than rotation is favoured. This may explain why there is clear distinction of nuclei x-axis strain when cells received similar compression loading.

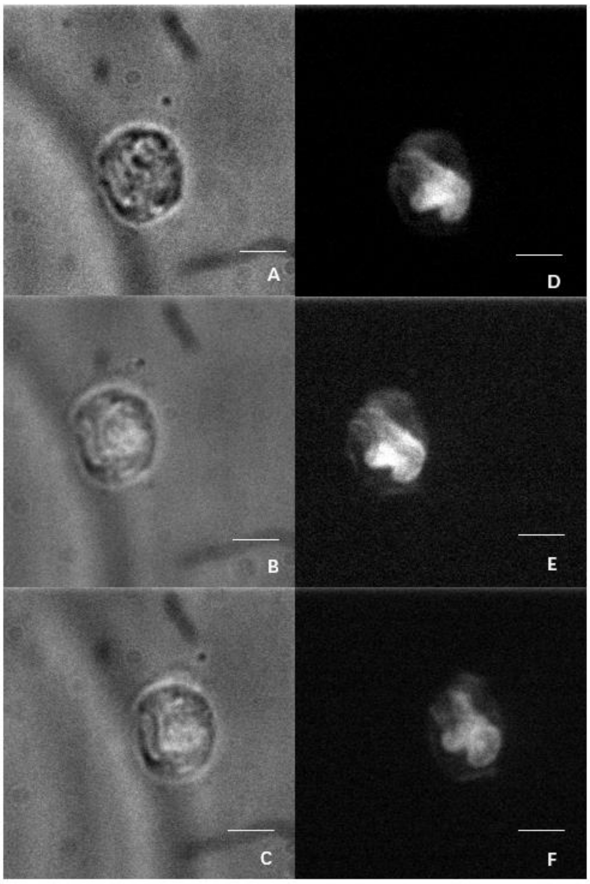

Figure 3.19 Confocal images of a LIF mES cell (grey) and its nuclei (black and white) at 0% strain (A and D), 10% strain (B and E) and 20% (C and F). The nuclei show clear rotation during compression while the cell is deformed. (Scale bar: 6μm).

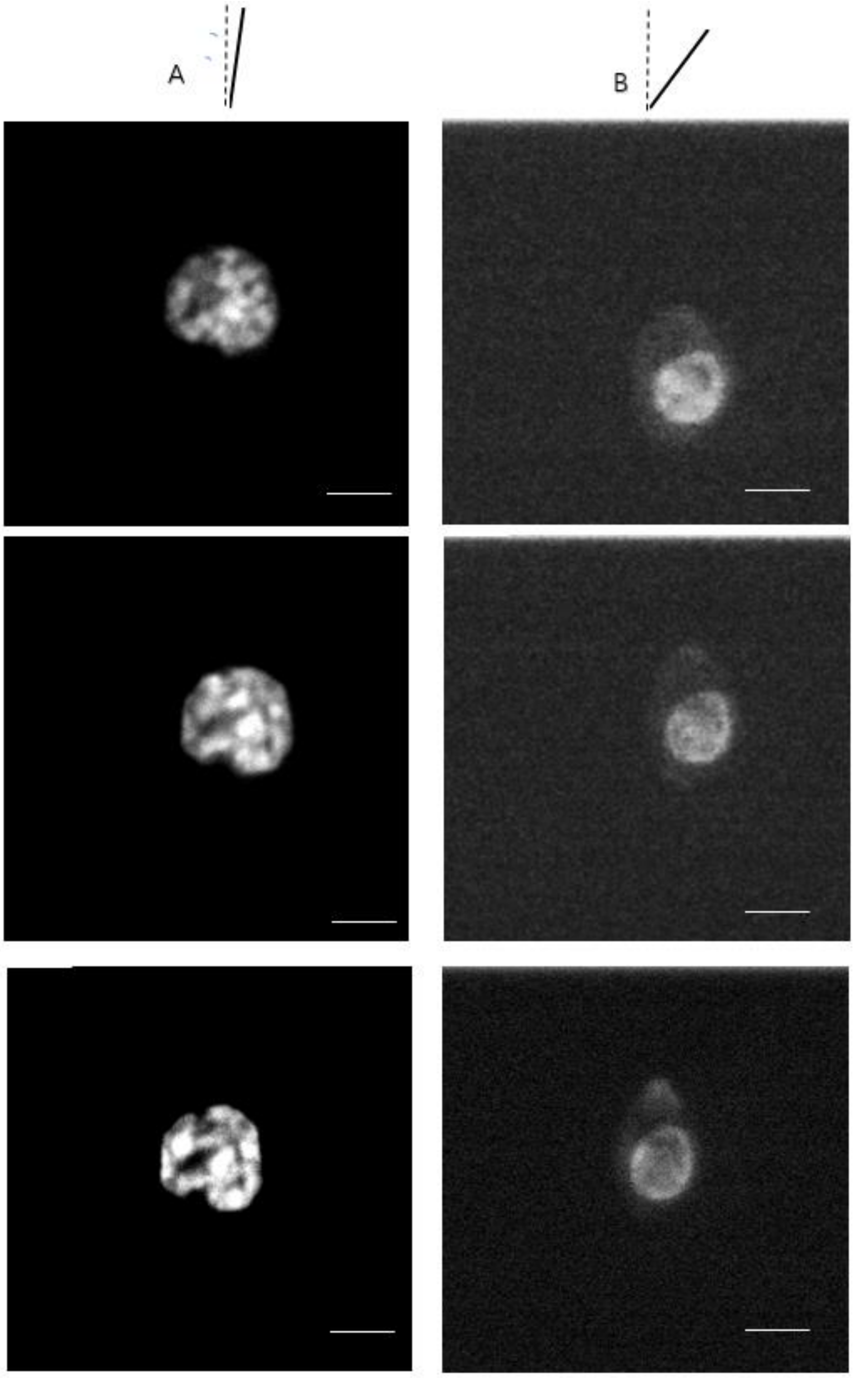

Figure 3.20. Confocal microscopy images of 2i nuclei at 0% strain (top), 10% strain (middle) and 20% (bottom). The images indicates that the nucleus oriented in the y-axis is deformed while the nuclei oriented at 45^{o} to the y axis shows obvious rotation (Scale bar: 6.2µm).

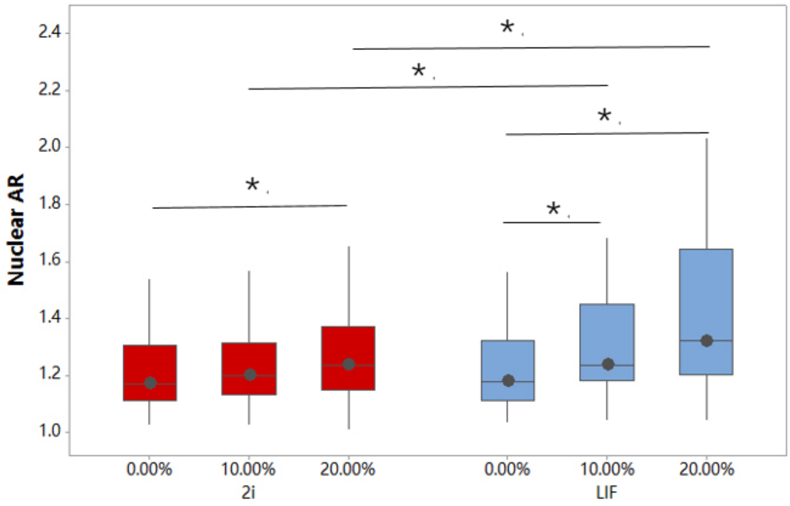

Figure 3.21 Nuclear aspect ratio for LIF and 2i mES cells in agarose and subjected to 10% or 20% compression. Values are represented as median and interquartile range of n (1X LIF) =41 and n(2i)=50. Mann-Whitney U test is applied where *: 0.05>p>0.001. Mechanical compression modifies the nuclear aspect ratio with LIF mES cell exhibiting greater alteration in nuclear aspect ratio than 2i mES cells.

Figure 3.20 indicates that LIF and 2i mES cell nuclei have similar aspect ratios in the unstrained state. The the LIF mES cell nuclei deformation is significantly greater than in 2i mES cell, revealed as alterations in aspect ratio at 10% and 20% strain compared to the unstrained state. Since the aspect ratio in the unstrained state in both pluripotency states is 1.17 rather than 1, the typical morphology of the nuclei is elliptical rather than round. The original angle of the major axis of nucleus relative to the axis of compression was recorded and the nuclei were categorized into two groups as follows: (a) Limited-rotation Area (LA), in which the nucleus has an angle in the unstrained state of between 75 degree and 105 degree and (b) Free-rotation Area (FA), in which the nucleus has an angle in the unstrained state greater than 105 degree or less than 75 degree. Figure 3.21 reveals that for both 2i and LIF mES cells nuclei categorized into the limited-rotation area has greater nuclear x-axis modification than nuclei categorized in the free-rotation area. Furthermore, figure 3.22 shows that cells in FA exhibited greater rotation than cells in LA. Notably, 2i mES cell nuclei exhibited significantly greater rotation during compression compared to the LIF cell nuclei.

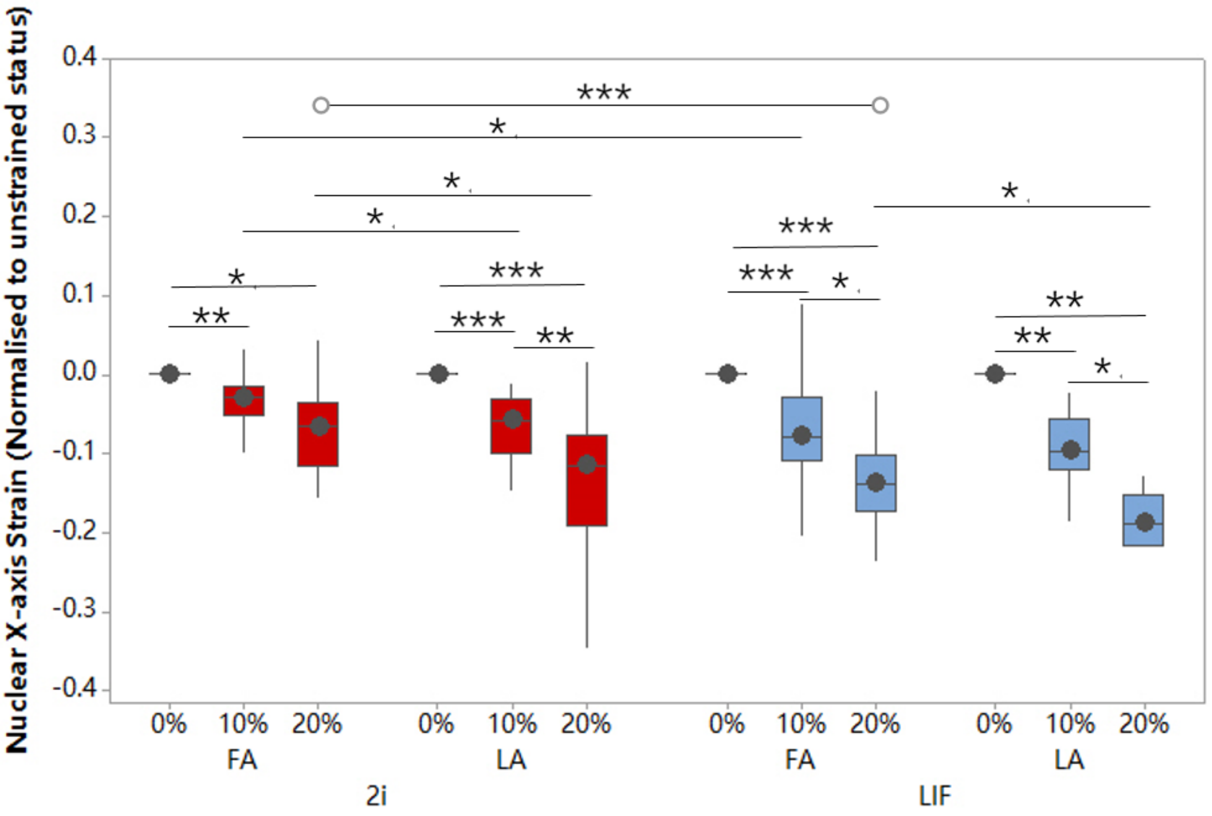

Figure 3.22. Nuclear x-axis dimension modification normalised to the unstrained state for 2i mES cells (red) and LIF mES cells (blue) during compression in agarose. The nuclei are categorized as Limited-Rotation Area (LA) and Free-Rotation Area (FA). Values are represented as median and interquartile range of n (1X LIF LA) =11 n (1X LIF FA) =29 and n (2i LA)=12 n (2i FA)=38. Mann-Whitney U test is applied where *: P< 0.05 and **: P<0.001. Mechanical compression induces greater alterations in x-axis dimension in the LA group.

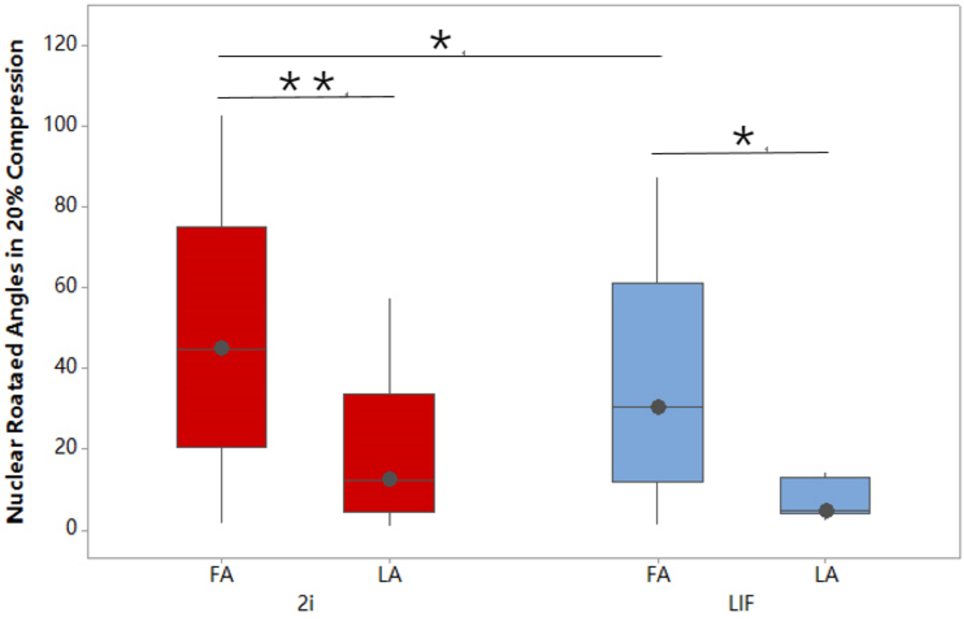

Figure 3.23. Nuclear rotated angle compared to the unstrained status for 2i mES cells (red) and LIF mES cells (blue) during compression in agarose. The nuclei are categorized as Limited-Rotation Area (LA) and Free-Rotation Area (FA). Values are represented as median and interquartile range of n (1X LIF LA) =11 n (1X LIF FA) =29 and n (2i LA) =12 n (2i FA)=38. Mann-Whitney U test is applied where *: P< 0.05 and **: P<0.001

3.4 Discussion

In this chapter, mouse embryonic stem cells were cultured in medium that maintains two distinct pluripotency states, with investigation of the mechanical properties of cell and nucleus during the application of compressive strain to cell-seeded agarose constructs. Studies over the past decade have indicated that embryonic stem cells can exist in more than one pluripotency state (Guo et al 2009). Pluripotency is considered to be highly dynamic and the various states with different phenotypic characteristics exist (Hackett 2014). Researchers have defined two major pluripotency states as the naïve and primed state based on origin of the cell line and expression of key markers. (Tesar et al 2007). Markers such as Rex1 and Fgf4, are present at high levels only in naïve state stem cells. (Tesar et al 2007). Although both types of stem cell share several pluripotent factors, such as Oct4, they have different gene expression levels (Hyun Woo Choi, 2016). Expression of Nanog is reported to correlate highly to pluripotency level. In our study, we found that the 2i mES cell population had significantly greater Oct4 and Nanog expression levels than the LIF cell population while expression of these two genes was negligible in the mEF differentiation reference. The LIF mES cells also has higher Nestin and BMP4 expression compared to the 2i cells, which is considered as a sign of induction of differentiation (Michalczyk et al 2005, Knöchel et al 2001), Gene expression levels in LIF mES stem cell group were significantly lower than in the mEF differentiation reference. Accordingly and consistent with previous studies, the 2i mES cells were maintained in a higher pluripotency state than the LIF mES stem cell group. Since we did not acquire reference samples of naïve and primed state stem cells, it was concluded that the 2i cell group were more naïve-like while stem cells cultured in LIF medium were more primed-like.

Naïve state stem cells can transition to the primed state in culture (Guo et al 2009). However, natural reversal of primed state stem cells to the naïve state is not considered to happen, so the role of 2i medium in maintaining the high pluripotency levels may not to induce primed-like to naïve-like state transition. It has been suggested that the 2 inhibitors (MEK inhibitor and GSK3 inhibitor) which are key components of 2i media induce loss of viability of non-naïve stem cells (Nichols and Smith 2009). This may explain why more rapid population doubling is reported in LIF mES cell conditions compared to 2i. Furthermore these finding suggest that the LIF medium supports a heterogeneous population of stem cells in both the naïve and primed state, recently reported as metastable pluripotent stem cells (Hyun Woo Choi 2016). The nucleus size distribution, presented in Figure 3.15, suggests the presence of distinct sub-populations of cells with different nuclear sizes exist in LIF mES cell culture conditions. The nuclei in the 2i mES cells were smaller on a population basis and less variable. Notable one sub-population of LIF cells had nuclei of similar size to those in the 2i conditions which may represent the naïve state stem cells in the LIF cell culture. The LIF sub-population containing larger nuclei may represent the primed state stem cells. The LIF mES cell culture conditions were able to maintain populations of pluripotent cells over extended culture periods without evidence of differentiation. This indicates that a metastable state is formed in LIF mES culture conditions, which contains two pluripotency states and preventing further differentiation.

It has been reported that when embryonic stem cell exit pluripotency their nuclei exhibit auxetic characteristics in response to mechanical perturbation (Stefano et al 2014). The results presented in this chapter are consistent with these earlier findings, with a proportion of the nuclei exhibiting reductions in both x and y-axis dimensions during compression, as indicated in Figure 3.11. This effect appeared to be most pronounced in the 2i cell population. It should be noted that the current study and the work of Stefano et al used markedly different systems for mechanical perturbation and therefore auxeticity may be a fundamental feature of the nuclei of embryonic stem cells in specific pluripotency states.

In the current study, we found similar cellular deformation was exhibited during the compression in agarose in both cell groups. These findings suggest that the response of cells to the specific mechanical perturbation adopted in the naïve-like state does not differ from that in the primed-like state. Accordingly, while pluripotency state and transition affects gene expression and cytoskeletal organization there appears to be limited shift in mechanical phenotype at the cellular level. These findings are broadly in agreement with a previous study (Pagliari et al. 2014). However, in this study a third category of cells, defined as transition stem cells, was also analysed and found to have mechanical properties distinct from either the primed-like or naïve-like state. We were unable to identify the transition cell population in the current study and cells with these features may appear in both the LIF and 2i conditions.

The similarity in cellular deformation in the primed-like and naïve-like states suggests that the nucleus in two groups may receive similar mechanical signaling through mechanical transduction. However in contrast of whole cell deformation the mechanical response of the nucleus was distinct between the two cell groups. In our study, we found that 2i mES cell nuclei were deformed less in x-axis than the nuclei in the LIF conditions. Moreover, LIF mES cell nuclei expanded more than 2i mES nuclei in Y-axis leading to significantly greater aspect ratio modification. These suggest that the nuclei in the naïve-like state are more resistant to deformation, potentially indicating that the nuclei are stiffer in the naïve-like state than in the primed-like state stem. During further analysis using a population approach (Figure 3.16) we observed that the bi-model distribution of nuclear x-axis dimension in LIF conditions became less pronounced following compression, resulting in LIF cell group becoming more similar in nucleus x-axis dimension to the 2i mES cell group. Figure 3.12 also shows that at 20% strain, the two groups has similar nuclear x-axis dimensions.

The work of Stefano and co-workers suggested that chromatin decondensation drives an auxetic phenotype in the nucleus (Stefano et al 2016). Related to our work, it can be hypothesized that the transition from the naïve state to primed state is linked to chromatin decondensation with associated gene expression modification. Further that mechanical perturbation may induce alterations in chromatin condensation state and chromatin stacking density allowing the primed state stem cell nucleus to return to a similar state as the naïve state stem cell. Since the reverse transition from primed state to naïve state is only achievable by reprogramming (Russell and Silpa, 2016), it may be exciting to investigate whether epigenetic medication with mechanical perturbation could induce the primed state cell nucleus to transition to a quasi-naïve state condition.

In our study, nucleus rotation during compression was observed and became the subject of further analysis. There is a clear interaction between the angle of compression loading with the orientation angle of the nucleus in its unstrained Depending on the initial nuclear orientation loading may resolve into pressure to deform nucleus and shear stress for nucleus rotation. Our study demonstrated that the nuclei in the 2i mES cell group were significantly more likely to rotate and less likely to deform compared to LIF cells. These findings are consistent with greater nucleus stiffness in the 2i mES cell group. Nucleus deformation and distortion may lead to chromatin condensation and reorganisation with impact on gene expression (Lee et al., 1995). Nucleus rotation, which limits distortion and volumetric changes can be considered to protect the nucleus from distortion and association chromatin reorganisation and preclude direct mechano-regulated gene expression modification. In the unstrained state the nuclei are randomly oriented at differing orientation angles. Depending on the initial orientation of the nucleus, the loading process induced distinct phenomena, specifically greater rotation in the FA group and nucleus deformation in the LA group. Accordingly, the same mechanical perturbation to induce distinct nuclear and epigenetic modification in individual cells depending on their initial nuclear orientation.

In summary, in this chapter has demonstrated a link between embryonic stem cell pluripotency state and the response of the cell and nucleus to mechanical perturbation induced by compression in agarose. The finding suggest that chromatin condensation state may influence not only gene expression but the resistance of the nucleus to mechanical perturbation. Further our analysis reveals nuclear rotation as a key process in the mechanical response and this refines our understanding of the variation in nucleus deformation. In chapter 4 our understanding is extended to the early differentiation phase induced from cells in the differing pluripotency states.

Chapter 4 Nuclear Mechanical Characteristics during Early Differentiation

4.1 Introduction

In the previous chapter the mechanical response of the cell and nucleus of embryonic stem cells to the application of compressive strain in agarose was investigated in two pluripotency states. The suppression of pluripotency gene expression will result in embryonic stem cells differentiating through a series of stages toward differentiated cell types dependent in lineage specific triggers. The early stages of differentiation are distinction depending on the initial pluripotency state, with naïve state cells likely to transition to a primed stage prior to differentiation. As the mechanical response of the nucleus to compression was distinct in the naïve and primed pluripotency states, it is interesting to consider whether differences remain as the cells undergo the earliest differentiation stages. During differentiation the nucleus is highly dynamic with structure modification potentially resulting in distinct mechanical characteristics. In this chapter, we triggering differentiation from the LIF and 2i mES cell pluripotency conditions by altering the culture conditions involving LIF withdrawal and investigated alterations in the mechanical characteristics of the cell and nucleus during early differentiation.

4.2 Material and Methods

4.2.1 Cell culture modification for triggering differentiation.

Mouse embryonic stem cells were initially cultured in 25cm^2 Hermo Scientific™ cell culture flasks as described in chapter 2.2.3. The cells were seeded as 10000 per cm^2, 5mL of regular mouse embryonic stem cell medium (LIF medium) was added and the flasks were incubated at 37°C for 48 hours without medium replacement. The cells were detached using accutase and collected following centrifugation. The cells were divided into two groups: (1) LIF group which were cultured under the same cell culture and (2) 2i group which were cultured as follows.

For the 2i group, naïve state mouse embryonic stem cell medium (2i medium) was used as culture medium. The cells were seeded at 10000 per cm^2 in a 25cm^2 cell culture flask, 5mL medium was added and the cells were incubated at 37°C for 72 hours with the medium changed after 48 hours. The cells were harvested using accutase, collected by centrifugation and seeded at 10000 per cm^2 in 75cm^2 cell culture flasks with 15mL medium and 4 wells of 6-well plate with 3mL medium in each well. The flasks and plates were incubated for 37°C for 72 hours with the medium changed after 48 hours. The cells within the flasks were harvested and used in the preparation of cell-seeded agarose construct from compression studies. The cells within the 6 well plates were used for gene expression analysis by PCR assay and for AP staining. To induce early differentiation LIF was removed from the medium and the cells were cultured for a further one or two passages. In addition for the 2i conditions the inhibitors were also removed. The protocols are illustrated in Figures 4.1 and 4.2

.

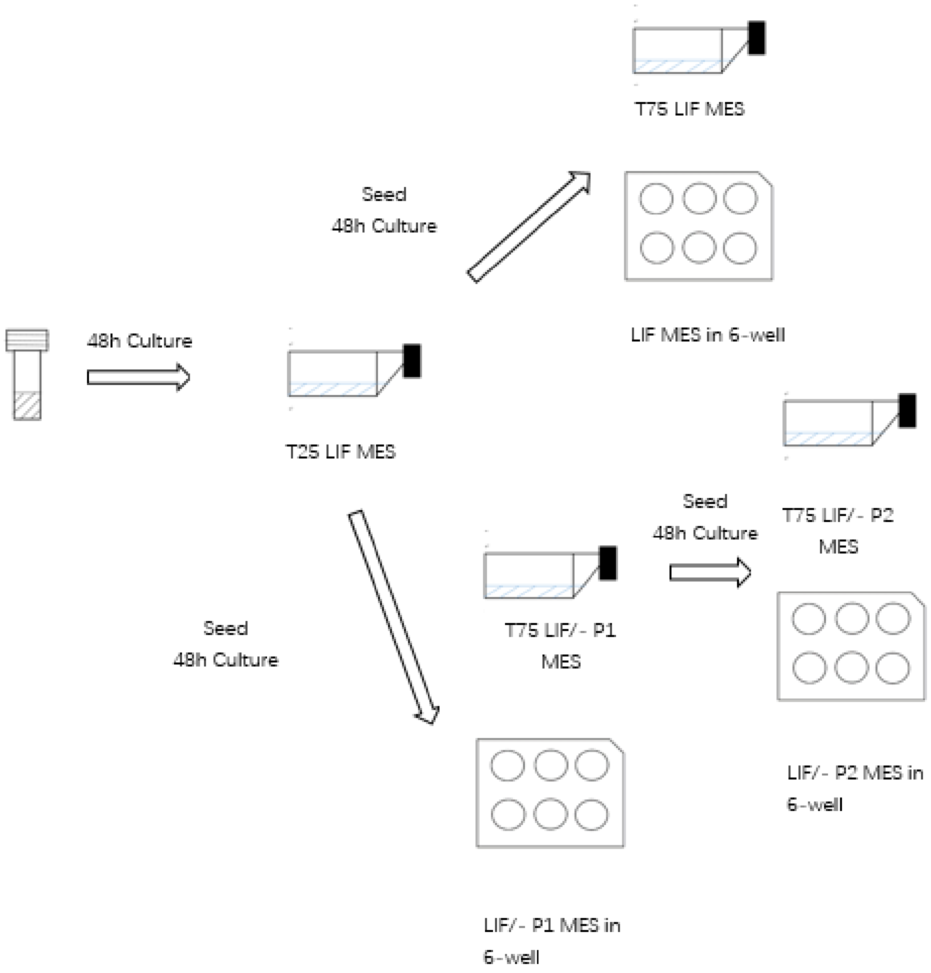

Figure 4.1. Schematic representing the LIF-removal cell culture protocol used for the LIF mES cell group.

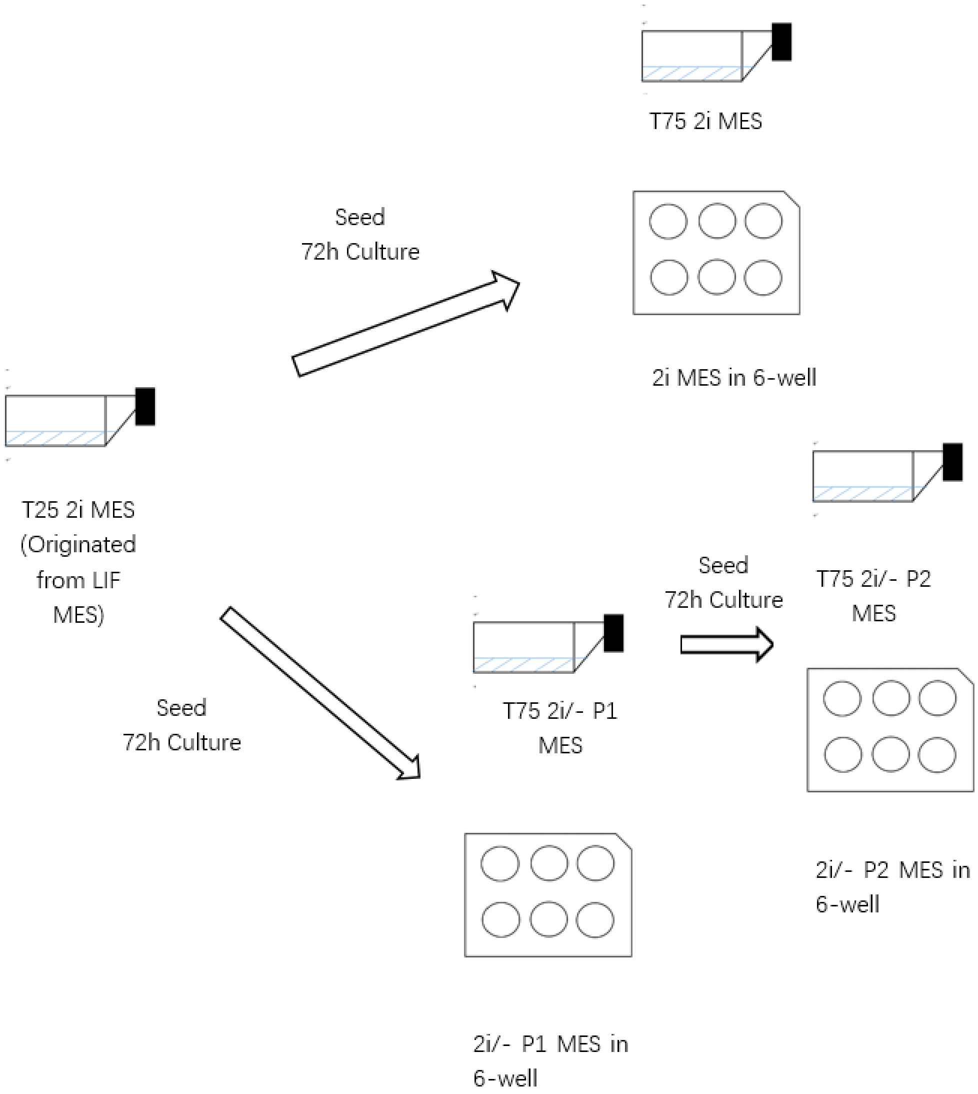

Figure 4.2. Schematic representing the LIF-and-inhibitors-removal cell culture protocol used for the 2i mES cell group.

4.2.2 Alkane Phosphate staining and PCR assay

One well of the 6-well plate was used for alkane phosphatase staining assay using the method described in chapter 2. Five representative images were taken for each assay.

The reverse transcript PCR (rt-PCR) assay was used to assess levels of expression of genes considered to be markers of pluripotency and early differentiation in the five cell groups (2i, 2i/- P1, LIF, LIF/-P1 and LIF/-P2) used in the project, as described in chapter 2. Two pluripotency gene markers (Oct4 and Nanog) and five differentiating gene markers (Sox2, Nestin, BMP4, Otx2 and FGF5) were analysed along with the housekeeping gene (GAPDH). The cDNA of mouse embryonic fibroblast (mEF) was also applied as a differentiation reference.

4.2.3 Cell-seeded agarose construct preparation and compression

Cell-seeded agarose constructs were prepared and compressed using the protocol described in Section 3.2.3. The cell-seeded agarose construct compression study included four conditions, namely; (1) LIF mES cells with or without LIF-removal and (2) 2i mES cells with or without LIF-and-inhibitors-removal.

Prior to passage, cells were visualised using phase contrast light microscopy and 5 representative images were recorded. One well of the 6-well plate was used for the alkaline phosphatase staining assay using the method described in chapter 2. Five representative images were taken for each assay.

4.2.4 Confocal Microscopy Analysis

Representative cells and their nucleus were imaged at 0% strain and during the imaging period following application of 0-10% and 10-20% strain as described in chapter 3. Images of cells and their nuclei were taken using the Perkin-Elmer confocal microscope system and the visual software Volocity. Measurement was achieved with ImageJ using the methods described in Section 3.2.4. As the upgrading software for Perkin-Elmer confocal microscopy, Volocity permits 32bit coloured images with higher resolution, which improves the images of cells and nuclei. Meanwhile, the aims and steps in processing velocity images are still same as what was described in chapter2.

4.3 Results

4.3.1 LIF-removing causes alteration of cell pluripotency state in embryonic stem cell

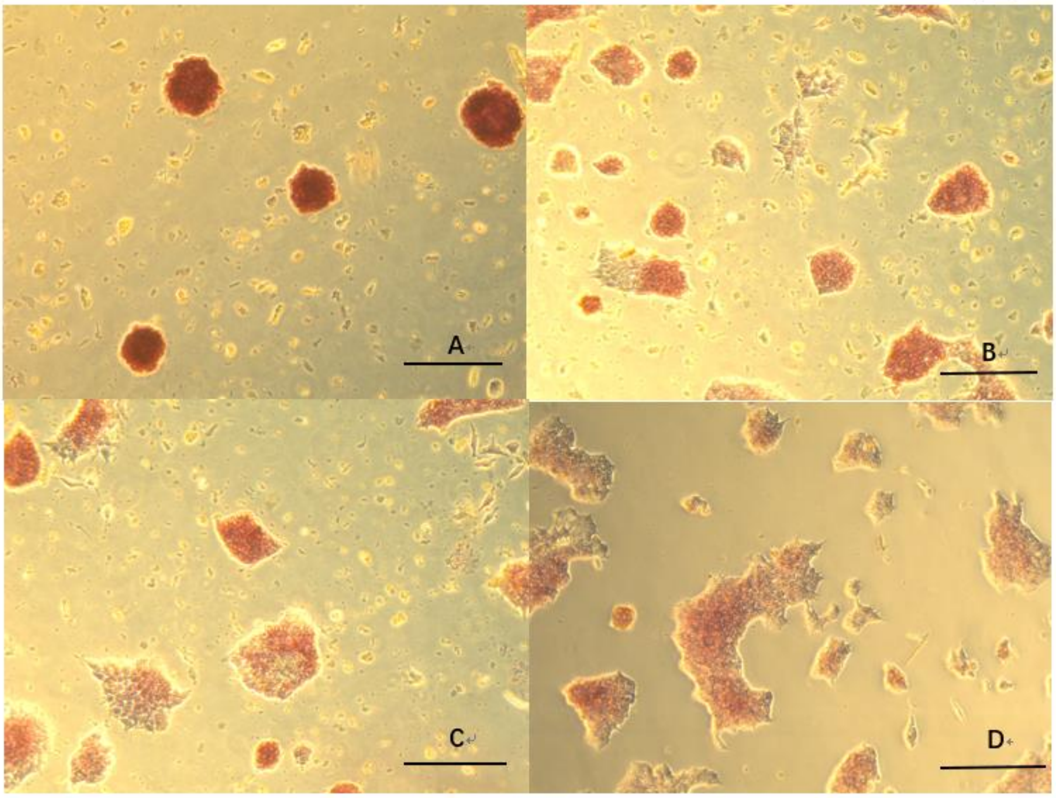

Figure 4.3 Representative images of 2i mES cells (A) and 2i/-P1 mES cells (B), LIF mES cells (C) and LIF/- P1 mES cells (D). Colonies were stained for alkaline phosphatase (Scale bar: 100μm)

The alkaline phosphatase assay results are presented in Figure 4.3. The removal of LIF and inhibitors for the 2i condition resulted in a less regular cell colony morphology, particularly evident at the periphery. Moreover AP staining was less intense than for the pluripotent 2i mES cells (Figure 4A and B). A similar effect was observed for LIF-removal from the pluripotent LIF mES cells (Figure 4C and D). Extending the LIF-removal protocol to the second passage (LIF/-P2) resulting in the alkaline phosphatase staining being hardly visible in the cell colonies. Accordingly the LIF-removal protocol appeared to decrease pluripotency levels for the embryonic stem cells whether originally maintained under LIF or 2i conditions.

Reverse transcript PCR analysis further revealed the loss of pluripotency markers following removal of LIF and inhibitors for the 2i mES cells. Figure 4.4 displays that 2i/-P1 mES cell has reduced expression of the pluripotency genes Nanog and Oct4 expression and enhanced expression of Nestin and BMP4 compared to the 2i mES cells. However, the 2i/-P1 mES cells retained greater pluripotency marker expression and reduced differentiation marker expression compared to mouse embryonic fibroblasts (mEF), which act as a differentiation reference.

The analysis of pluripotency and differentiation gene expression in LIF, LIF/-P1 and LIF/-P2 mES cell group is shown in Figure 4.5. LIF-removal reduced pluripotency markers and increased differentiation markers compared to the LIF mES cells. By passage 2 of LIF removal (LIF/- P2) differentiation gene expression had attained levels similar to the mouse embryonic fibroblasts (mEF), suggesting that a majority of cells by LIF/-P2 mES cell had exited pluripotency and were differentiating.

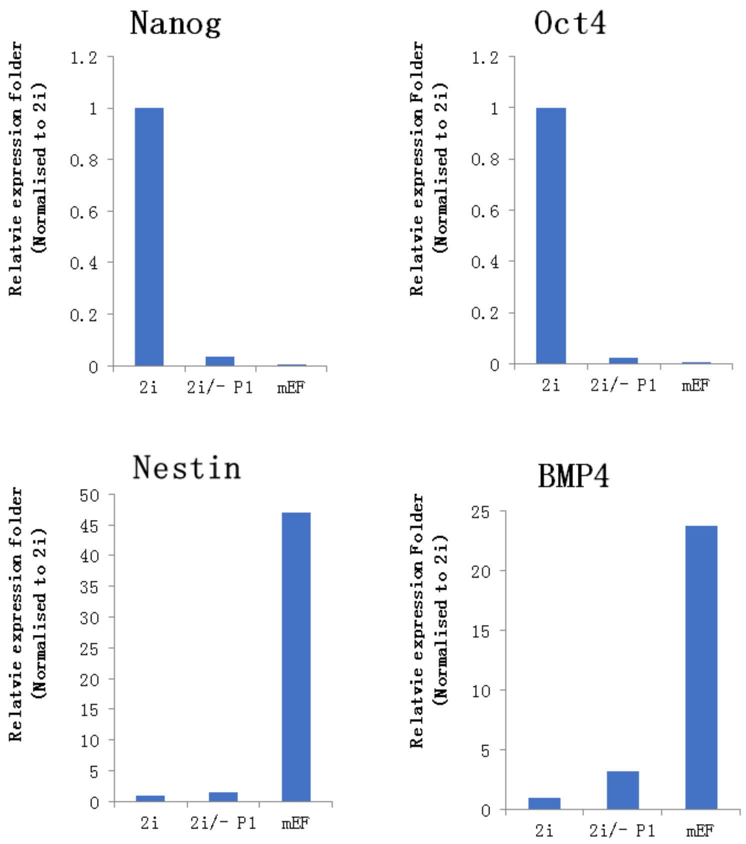

Figure 4.4. PCR assays of 2i mES cells, 2i/- P1 mES cell and mouse embryonic fibroblasts (mEF) for pluripotency and differentiation gene markers.

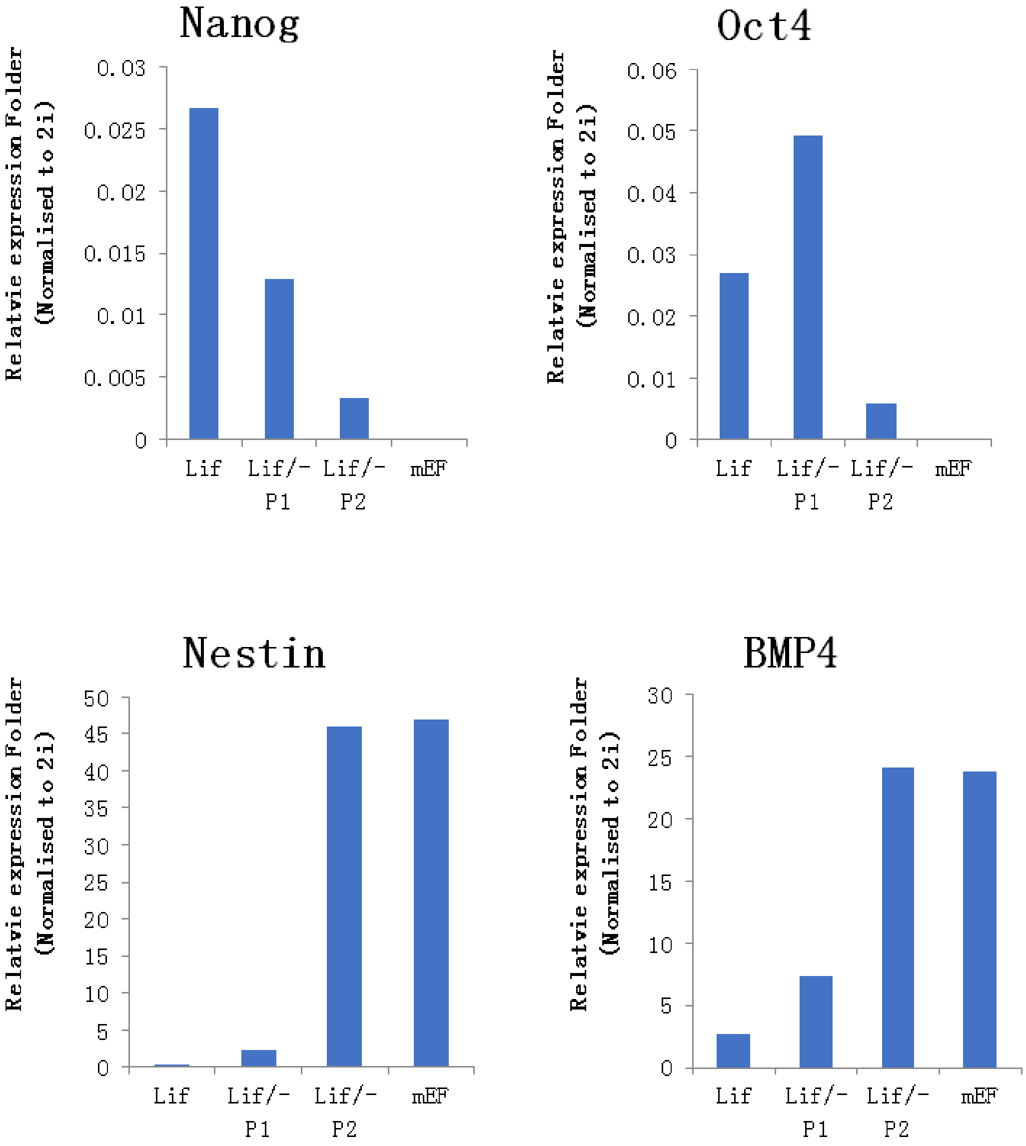

Figure 4.5. PCR assays of LIF mES cells, LIF/- P1, LIF/- P2 mES cells and mouse embryonic fibroblasts (mEF) for pluripotency and differentiation gene markers.

Since Nestin and BMP4 were regarded as differentiation marker to present the late differentiation. Adiitional differentiation markesrs were reuqired to prove early differentiaon of mES cell upon LIF removal. Two earlly differntiation markers (Otx2 and Fgf5) were applied for further PCR assay (Fi0gure 4.6). Figure 4.6 indicated the gaps of Otx2 and Fgf5 expression in LIF, LIF/- P1 and LIF/- P2 mES cell were clear and early differntiation was ahieved in two passages of LIF-removal cell culutre.

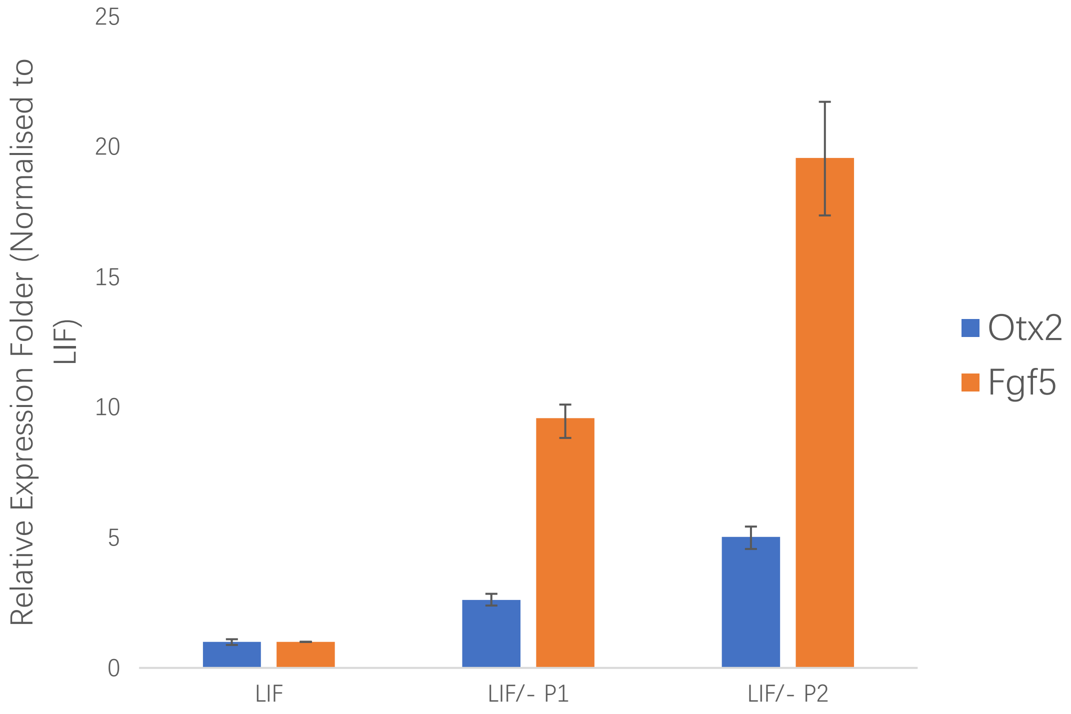

Figure 4.6. PCR assays of LIF mES cells, LIF/- P1 and LIF/- P2 mES cells for early differentiation gene markers Otx2 and Fgf5

4.3.2 LIF-removal causes alterations in cell and nuclear morphology and response to compressive strain

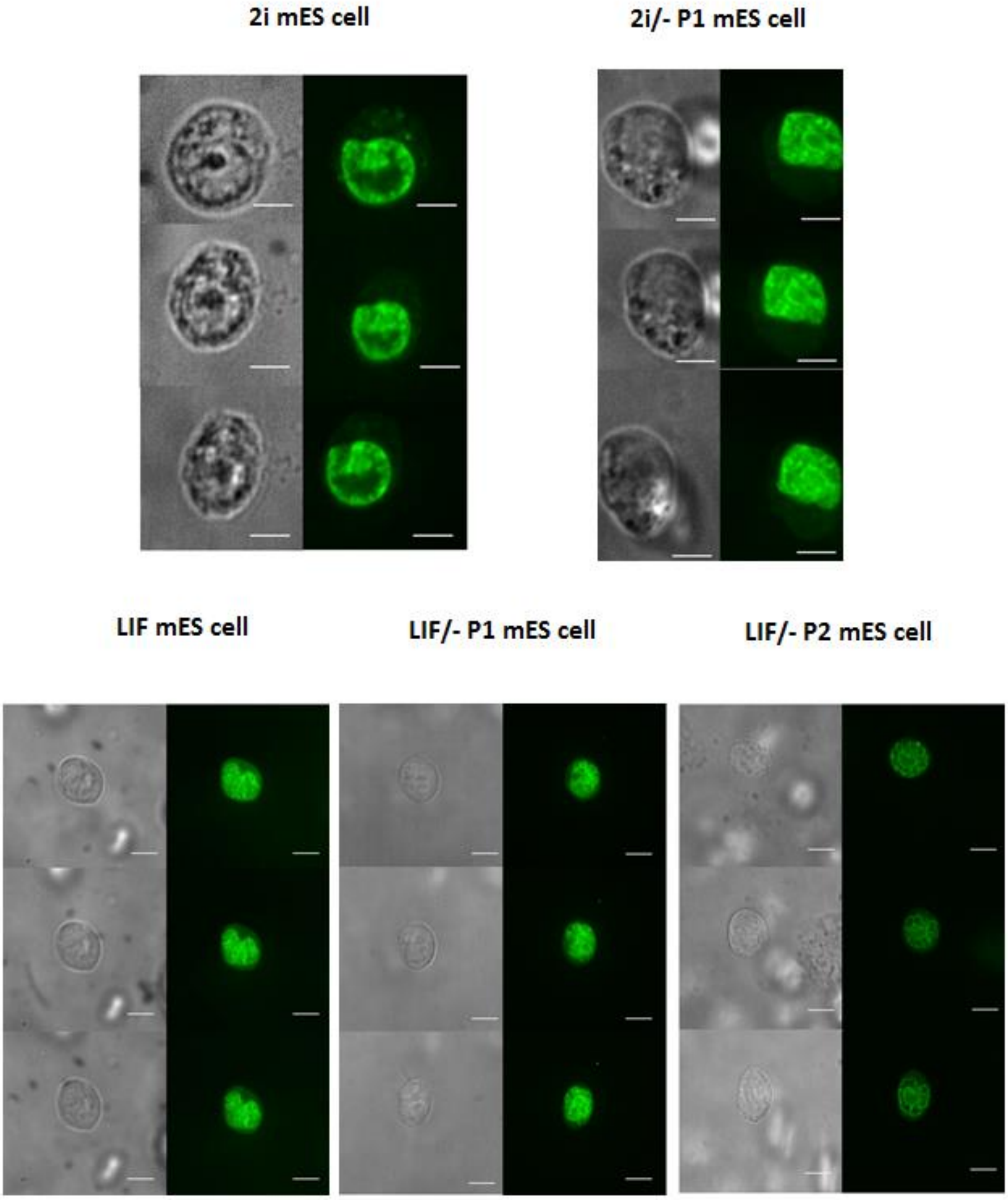

Figure 4.7. Confocal microscopy images of cell (grey) and nuclei (green) for cells cultured in five conditions. Each group provides images at 0%, 10% and 20% compressive strain from top to bottom. (Scale bar: 10 μm).

Representative confocal images of the five cell groups during compression loading are presented in Figure 4.7. Measurments of cell and nucleus parameters under compressive strain were taken for analysis of morphological modification and mechanical characteristics. The rtPCR assay results indicate that LIF-removal induced a loss of pluripotency and early differentiation. Analysis of nuclear dimensions during cell-seeded agarose compression provided further information on pluripotency state transition towards differentiation.

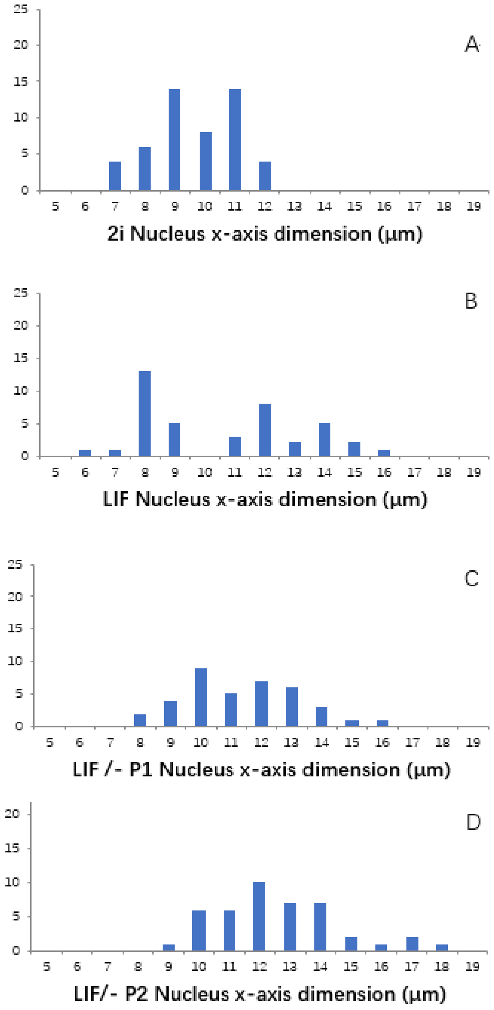

Figure 4.8. Histograms of nucleus x-axis dimension for 2i, LIF, LIF/-1 and LIF/-P2 mES cells in the unstrained state. (n (2i) =41, n(LIF)=39, n(LIF/P1)=40 and n=(LIf/-P2)=38.) The Y-axis of each histogram represents the frequency.

Figure 4.8 presents the the x-axis dimension distribution under various conditions in cell-seeded agarose. Figure 4.8A and B indicate that in the pluripotent state cells cultured in 2i and LIF medium exhibit distinct distributions of nuclei x-axis dimension with a clear bimodal distrubution of the LIF cells. When LIF was removed from the culture medium, the distinct bimodel distribution was lost, with an increasing trend over time toward a single distrubution with similar dimension distribution curve to the larger sub-population of the LIF cells, thought to represent the primed mES cells (Figure 4.8C and 4.8D). The smaller sub-population, that is similar in dimensions to the 2i cells was lost, suggesting that LIF-removal alters the balance of the primed and naïve states in LIF mES cell group driving naïve state cells toward the primed state.

Alterations in nuclei x-axis dimensions during compression are presented in Figure 4.9. The figure reveals that although LIF/-P1 and LIF/- P2 cells have similar x-axis dimensions in the unstrained state, LIF/- P2 appear more resistant to dimensional change compared to LIF/-P1 and the pluripotent state.

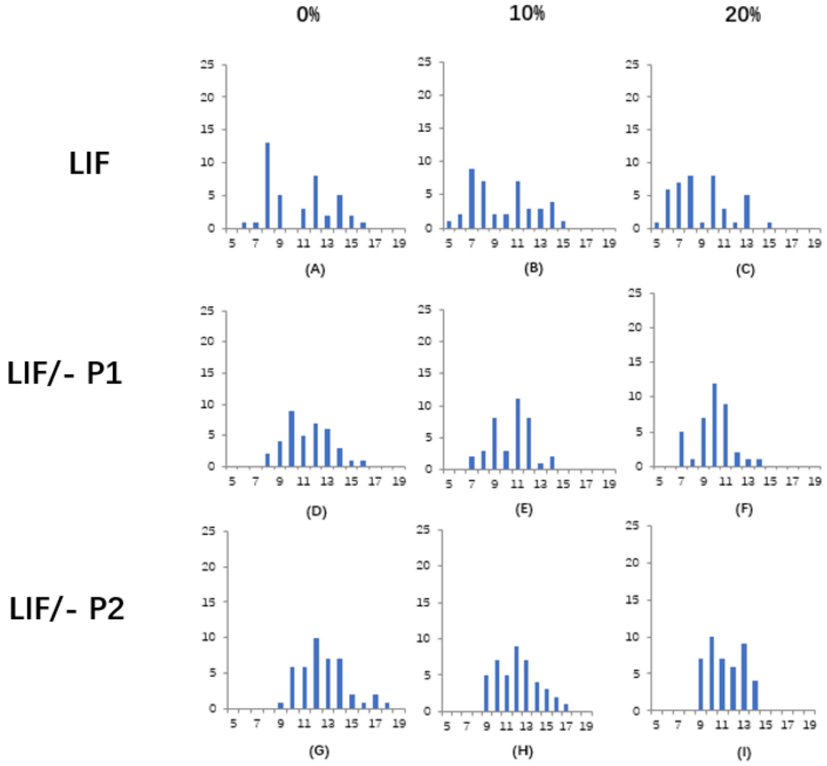

Figure 4.9. Histograms of nucleus x-axis dimension for LIF, LIF/-1 and LIF/-P2 mES cells at 0% 10% and 20% compressive strain. (n(LIF)=39, n(LIF/P1)=40 and n=(LIf/-P2)=38). The Y-axis of each histogram represents the frequency.

Figure 4.10 presents nuclei x-axis dimension modification during compression in 2i and 2i/- P1 mES cells. The x-axis distribution dimension of 2i/- P1 mES cell is similar to LIF mES cells both in unstrained and stained state. This suggests that 2i mES cells exprerience transfer from naïve-like state to primed-like state when LIF and inhibitors were removed from culture medium.

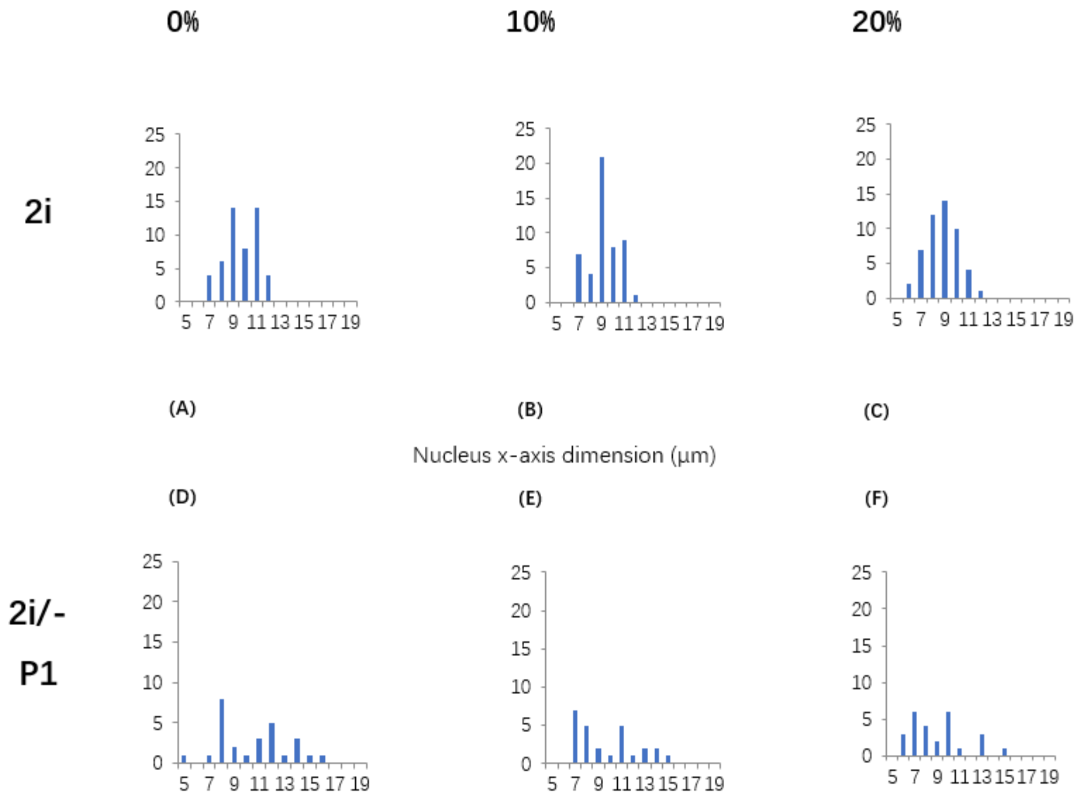

Figure 4.10. Histograms of nucleus x-axis dimension for 2i and 2i/-P1 mES cells at 0%, 10% and 20% compressive strain. (n (2i) =41, n(2i/- P1)=40). The Y-axis of each histogram represents the frequency.

4.3.3 2i mES cell transfer to meta-phase state during LIF-removal

Figure 4.11 indicates the celluar x-axis dimension and strain for 2i and 2i/- mES cells during compression. LIF-removal did not significantly alter the cell dimension in the unstrained state, not celluar mechanical charateristics. Figure 4.12 presents nuclear x-axis dimension and strain data during compression in 2i and 2i/- P1 mES cells. The nuclei in 2i/- P1 mES cells were larger in the unstrained state and also exhibited greater deformation during compession compared to the pluripotent 2i mES cells. In agreement with the rtPCR analysis and nuclear x-axis dimension data, 2i/-P1 mES cells shows similar mechanical and molecular characteristics to the LIF mES pluripotent cell population

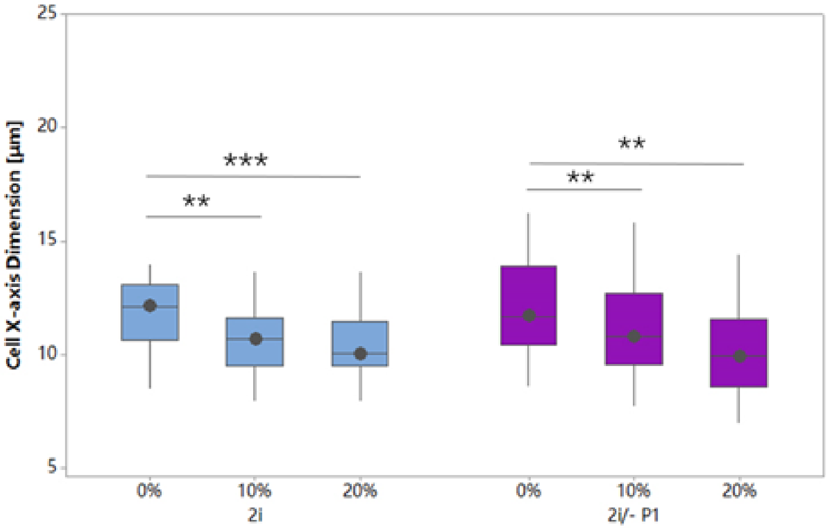

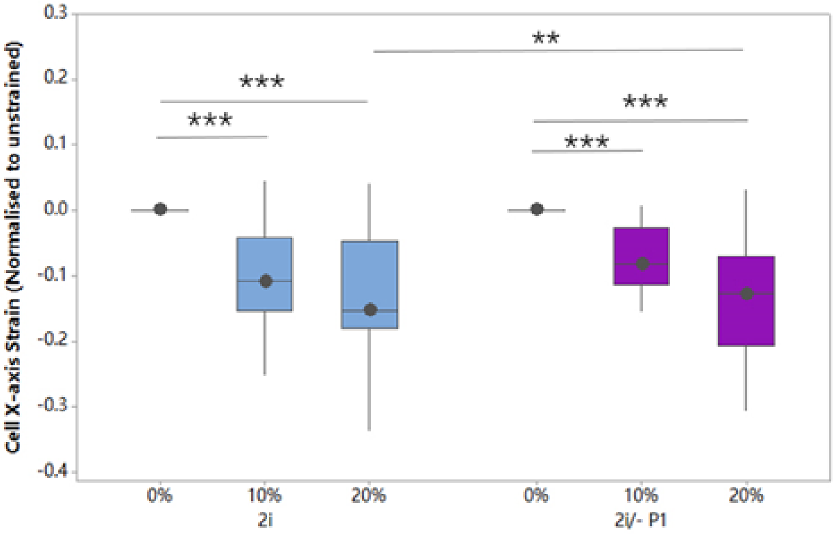

Figure 4.11. Cellular x-axis dimension (top) and x-axis strain normalised to unstrained status (bottom) for 2i and 2i/-P1 mES cells during unconfined compression in agarose. Values are presented as median and interquartile range of n(2i) =41 and n(2i/- P1)=40. Mann-Whitney U test is applied where *: P< 0.05, **: P<0.001 and ***: P<0.0001.

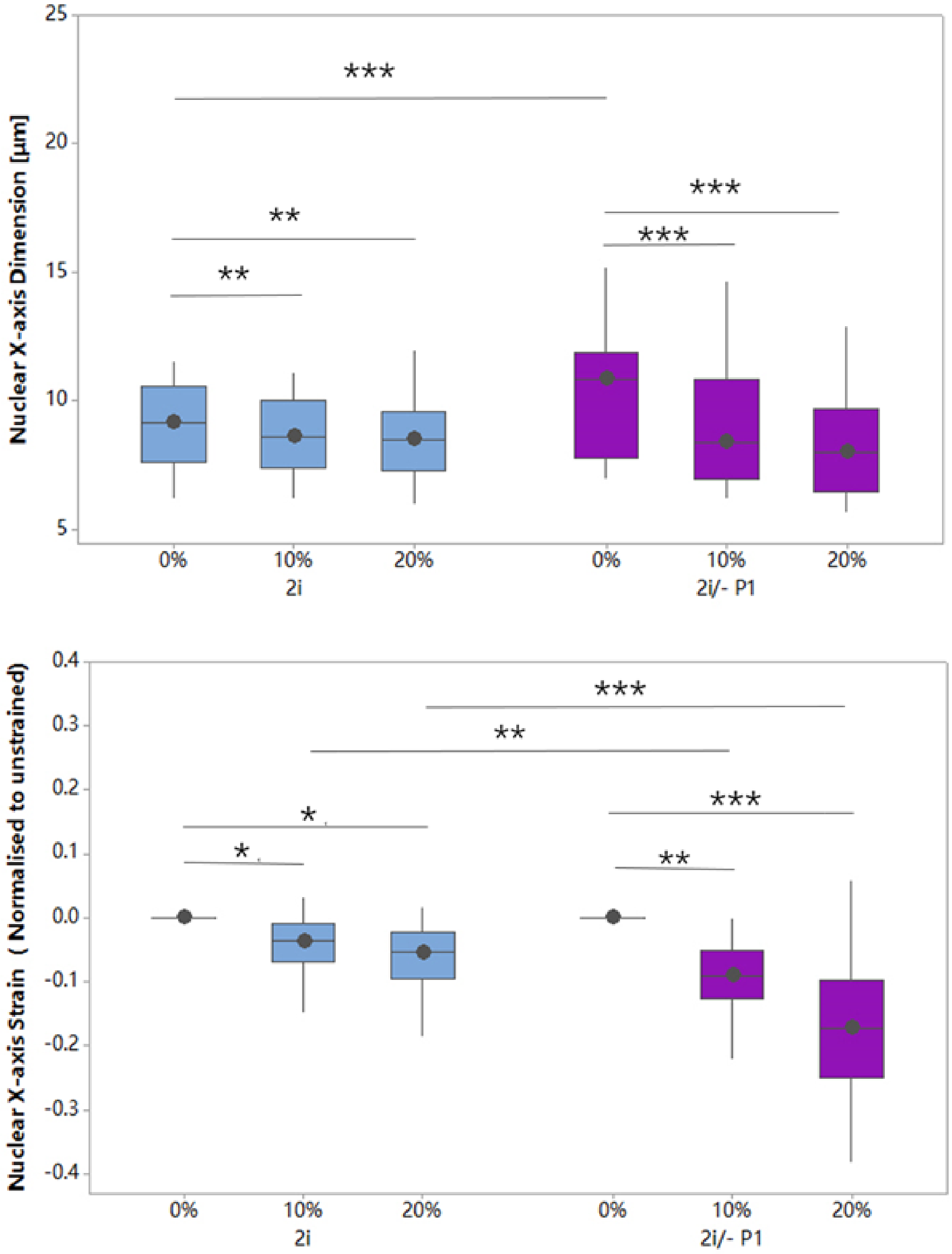

Figure 4.12. Nuclear x-axis dimension (top) and x-axis strain normalised to unstrained status (bottom) for 2i and 2i/- P1 mES cells during unconfined compression in agarose. Values represented the median and interquartile range of n(2i) =41 and n(2i/- P1)=40. Mann-Whitney U test is applied where *: P< 0.05, **: P<0.001 and ***: P<0.0001.

To further identify similarities between 2i/- P1 mES cells and LIF mES cells, Figure 4.13 presents nuclear Y-axis dimension and strain of 2i and 2i/-P1 mES cells during compression. Significant differences between the 2i and 2i/-P1 mES cells were revealed with the 2i/-P1 mES cells expressing characteristics which are similar to LIF mES cells. Furthermore, the nuclear aspect ratio of 2i and 2i/- P1 mES cell shown in Figure 4.14 further prove that 2i/- P1 mES cell exist in a meta-phase state which is similar to LIF mES cell, indicated by greater alterations in nuclear aspect ratio in repsonse to strain compared to the pluripotent 2i state.

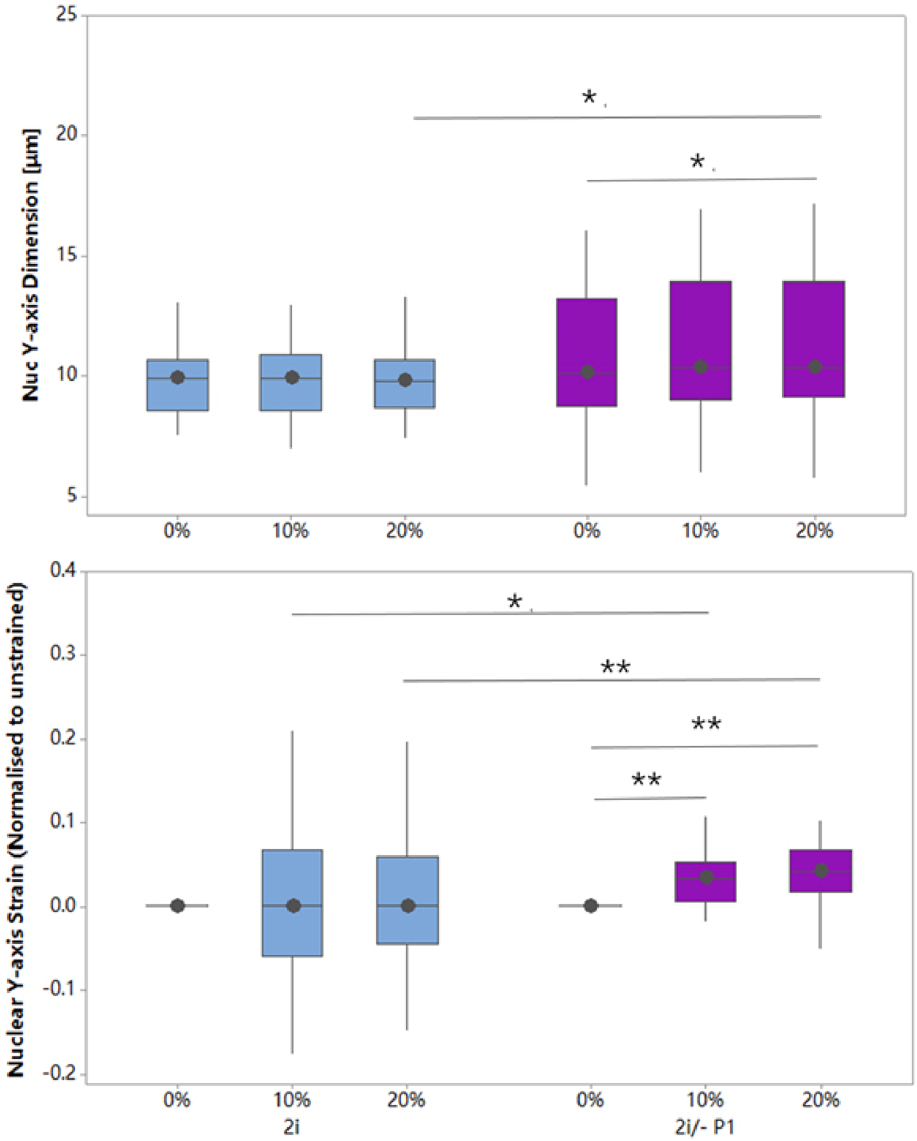

Figure 4.13. Nuclear Y-axis dimension (top) and Y-axis strain normalised to unstrained status (bottom) for 2i and 2i/-P1 mES cells during unconfined compression in agarose. Values are presented as median and interquartile range of n(2i) =41 and n(2i/- P1)=40. Mann-Whitney U test is applied where *: P< 0.05, **: P<0.001 and ***: P<0.0001.

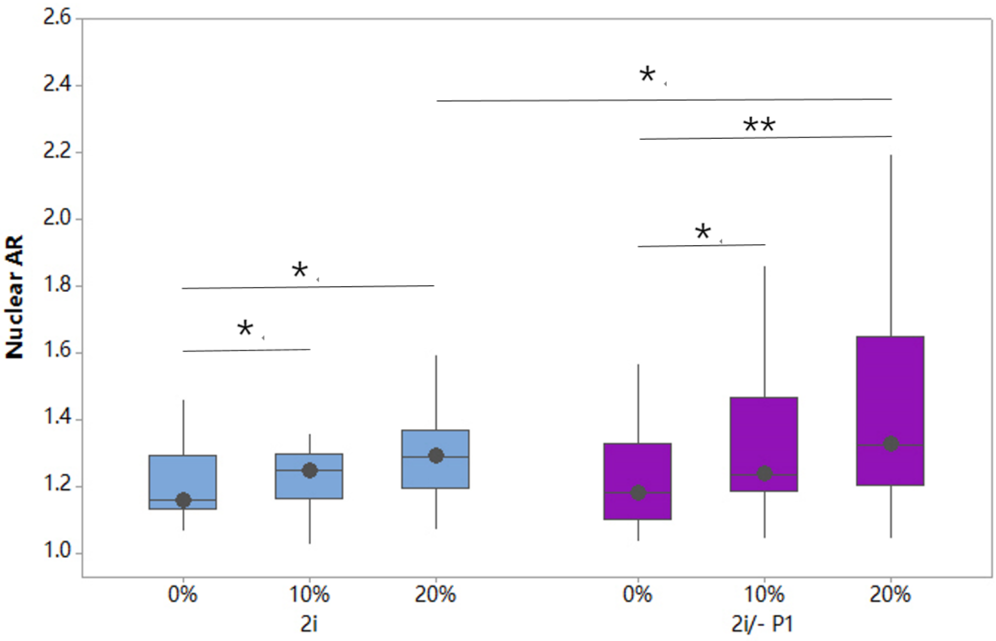

Figure 4.14. Nuclear aspect ratio (AR) for 2i and 2i/-P1 mES cells during unconfined compression in agarose. Values are presented as median and interquartile range of n(2i) =41 and n(2i/- P1)=40. Mann-Whitney U test is applied where *: P< 0.05, **: P<0.001 and ***: P<0.0001.

4.3.4 LIF removal induces progressive alterations in nuclear properties with passage.

In section 4.3.2 it was suggested that LIF removal for the LIF mES cells triggers both naïve state cell transitioning towards the primed state and also inducing differentiation from the primed state. Additional analysis of celluar and nuclear mehcanical properties of LIF/- cells offeres more evidence in support of this assertion.

Figure 4.15 presents celluar x-axis dimension and strain data for LIF mES cells and following LIF-removal during compression. By LIf/-P2 the cells were significantly larger in the x dimension in the unstrained state. The removal of LIf resulted in an alteration in cellular strain during agarose compression, but the differences at LIf/-P1 and LIf/-P2 were not consistent. Accordingly the link between LIF withdrawal, loss of pluripotency/differentiation and cellular mechanical charactersitcs may be complex, consistent with the suggestion of a multi-step action of LIF withdrawal on the primed and naïve cells in the LIF pluripotency condition.

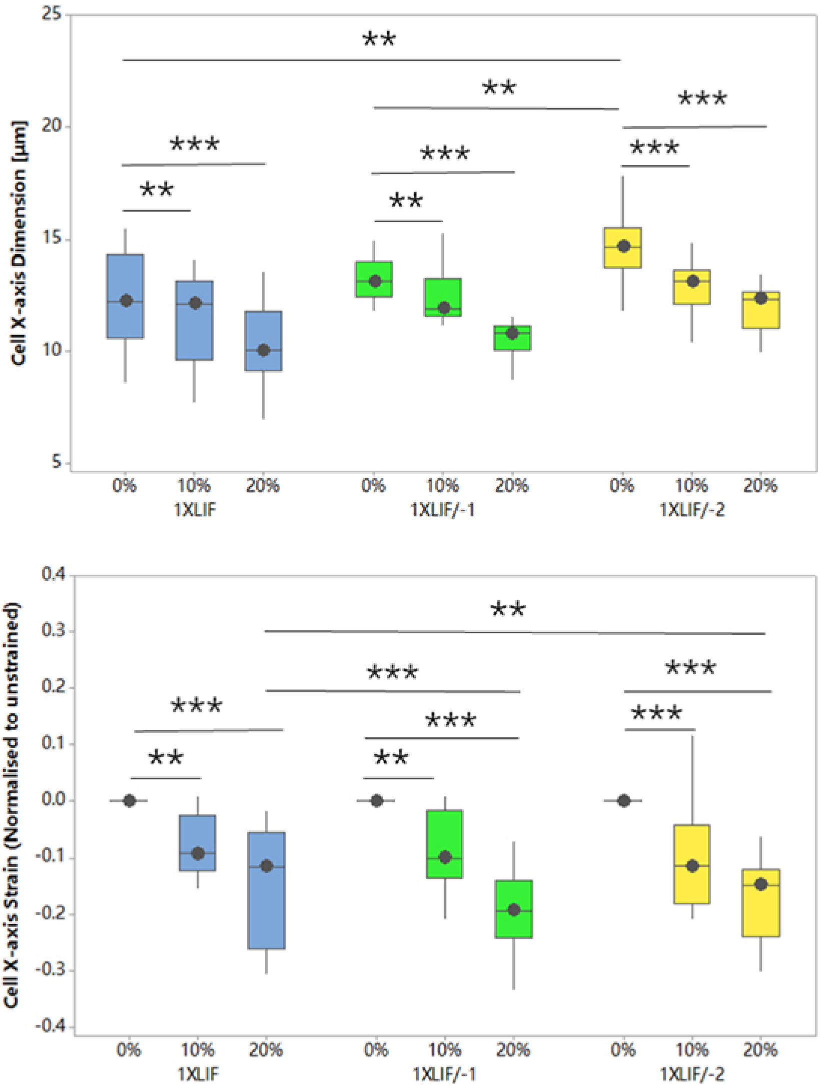

Figure 4.15. Cellular x-axis dimension (top) and x-axis strain normalised to unstrained status (bottom) for LIF (1XLIF), LIF/-P1 (1XLIF/-1) and LIF/-P2 (1XLIF/-2) mES cells during unconfined compression in agarose. Values are presented as median and interquartile range of n(LIF)=39, n(LIF/P1)=40 and n=(LIf/-P2)=38. Mann-Whitney U test is applied where *: P< 0.05, **: P<0.001 and ***: P<0.0001.

The nuclear x-axis dimension and strain of LIF and LIF/- mES cell during compression is shown in Figure 4.16 and reveals clear effects of LIF removal. With progressive LIF removal over two passages the nuclei increased significantly in their x dimension.

Moreover the nuclei in LIF/- P1 and LIF/- P2 cells exhibited significantly reduced nuclear strain in response to compression compared to LIF, with progressive effects with passage. These data suggest that differentiating cells following LIF removal had stiffer nuclei than the pluripotent stem cell. There is a notable increase in the variation in nuclear X-axis strain at LIF/- P1 mES cell consistent with two main effects of LIF removal. Specifically that the nuclei soften as the naïve state cell transitions into the primed state cell and nuclei stiffen with differentiation from the primed state.

Figure 4.17 presents nuclear y-axis dimension and strain data for LIF and LIF/- mES cells during compression. The Y-axis dimension of all three cell groups did not significantly increase during compression and there were slight differences between the y-axis dimension of LIF and LIF/- P2 at 0% and 20% compressive strain. The Y-axis strain of LIF/- P2 mES cell was slightly greater than LIF mES cell at 10% and 20% compressive strain. The data presented in both Figure 4.16 and Figure 4.17 are consistent with LIF-removal simultaneously triggered transition of naïve state cells to the primed state and differentiation of primed state cells with effects on the muclear mechanical characteristics. When LIF-removal culture proceeds to the second passage, transmission from primed state to naive state may be complete with the remaining primed state cell continuing to differentiate. This suggestion aligns with the PCR data indicating that the differentiation gene marker expression in the LIF/-P2 mES cell group is similar to mouse embryonic firoblasts.

Figure 4.18 introduces the nuclear aspect ratio modification in three groups of mES cells during compression process. The data indicate that the LIF/- P2 mES cells have a more regular round shape, with aspect ratio closer to 1, in the unstrained status compared to LIF and LIF/- P1. Compression resulted in nuclear deformation and alterations in the aspect ratio in three cell groups. While the data are not fully consistent there is a trend toward reduced modification of aspect ratio with compression for the the LIF/- P2 mES cells, with differences significant at 10% strain.

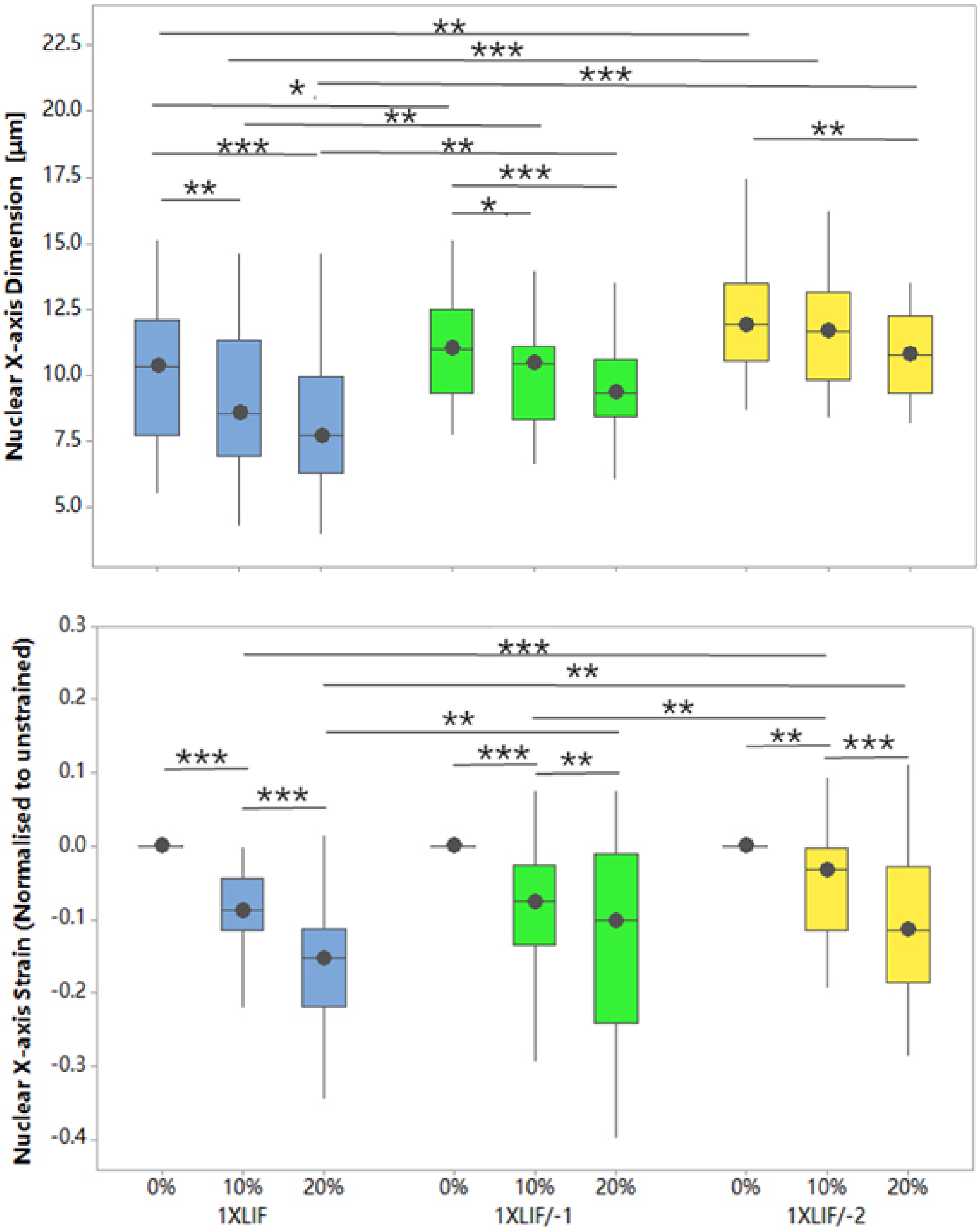

Figure 4.16. Nuclear x-axis dimension (top) and x-axis strain normalised to unstrained status (bottom) for LIF (1XLIF), LIF/-P1 (1XLIF/-1) and LIF/-P2 (1XLIF/-2) mES cells during unconfined compression in agarose. Values are presented as median and interquartile range of n(LIF)=39, n(LIF/P1)=40 and n=(LIf/-P2)=38. Mann-Whitney U test is applied where *: P< 0.05, **: P<0.001 and ***: P<0.0001.

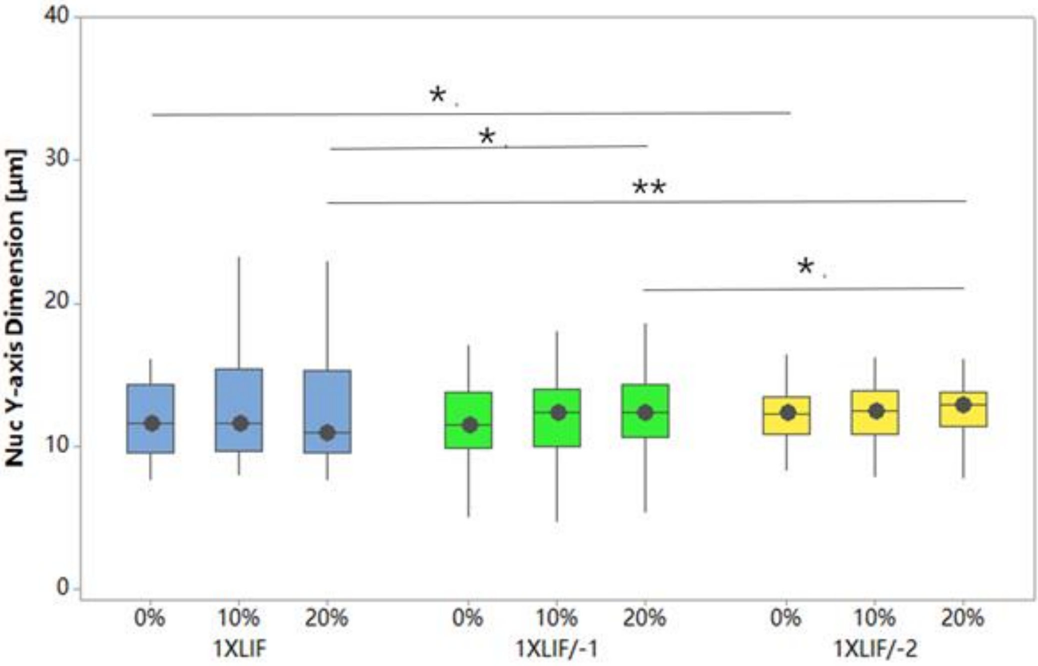

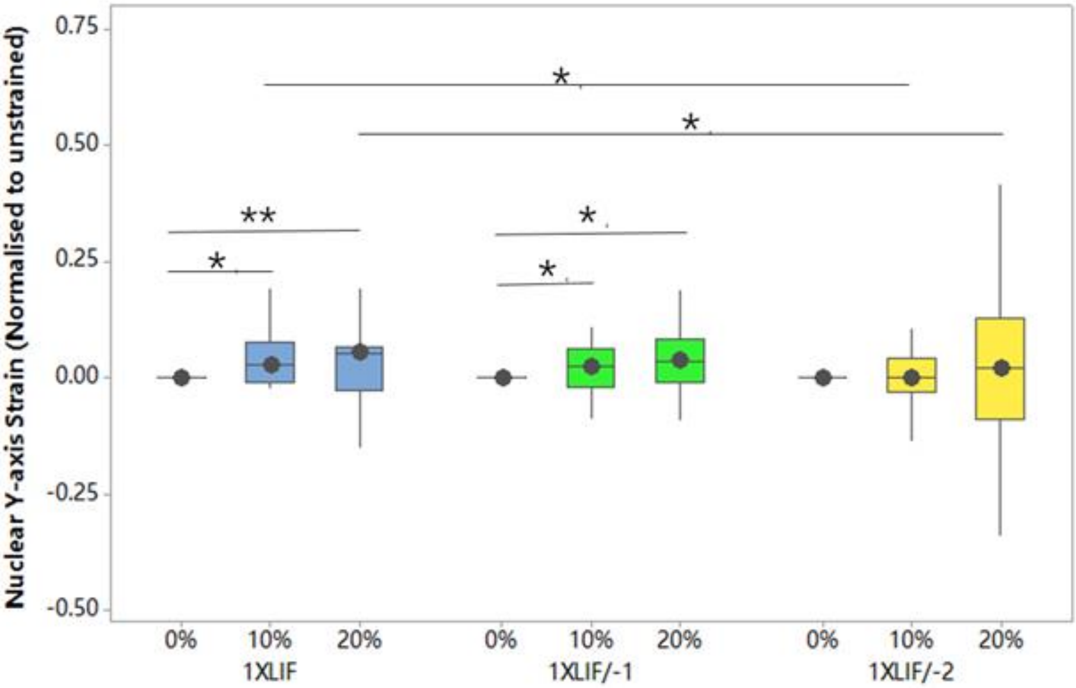

Figure 4.17. Nuclear Y-axis dimension (top) and Y-axis strain normalised to unstrained status (bottom) for LIF (1XLIF), LIF/-P1 (1XLIF/-1) and LIF/-P2 (1XLIF/-2) mES cells during unconfined compression in agarose. Values are presented as median and interquartile range of n(LIF)=39, n(LIF/P1)=40 and n=(LIf/-P2)=38. Mann-Whitney U test is applied where *: P< 0.05, **: P<0.001 and ***: P<0.0001.

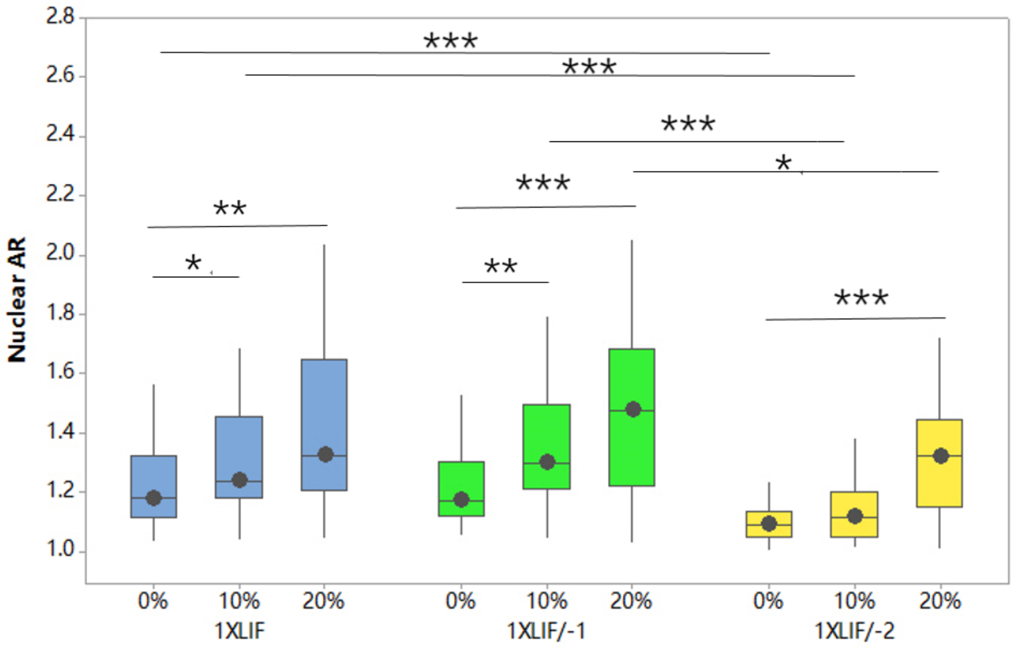

Figure 4.18 Nuclear aspect ratio (AR) or LIF (1XLIF), LIF/-P1 (1XLIF/-1) and LIF/-P2 (1XLIF/-2) mES cells during unconfined compression in agarose. Values are presented as median and interquartile range of n(LIF)=39, n(LIF/P1)=40 and n=(LIf/-P2)=38. Mann-Whitney U test is applied where *: P< 0.05, **: P<0.001 and ***: P<0.0001.

4.4 Discussion

In this chapter, we induced early differentiation of mouse embryonic stem cell by removing leukemia inhibitory factor (LIF) from culture medium during the cell culture process. Alkaline phosphatase staining assay demonstrated a reduction in pluripotent level both both 2i and LIF mES cell cultured with their respective LIF-free culture medium, which involved the additional removal of the 2 inhibitors for the 2i condition. Studies have reported that the role of the two inhibitors in 2i medium are to induce primed state cells to differentiate or lose viability to achieve a majority existence of naïve state cells in 2i mES cell condition with high pluripotency levels (Nichols and Smith 2013). Removal of the two inhibitors allows primed state cells to survive progressively resulting in increased proportions of primed cells in the heterogeneous culture. When combined with LIF removal to allow differentiation, a reduction in pluripotency markers initially to levels similar to LIF mES cells is expected and which was demonstrated (Figure 4.4 and 4.5). Futhermore, comparing cellular and nuclear mechanical parameters between 2i/-P1 mES cells and LIF mES cells, similarities were evident both in nucleus auxetic behaviour and the softening of the 2i cells with LIF removal such that they exhibited characterstics similar to LIF LIF mES cell. This implies that removing LIF and the inhibitors drives the 2i mES cell population originally with a majority of naïve state cells towards a balance where the primed and naïve cell states together exist. This meta-phase transimition in embryonic stem cell is also reported in other studies (Weinberger et al., 2016).

LIF-removal from the LIF mES cell cultures allowed the complex multi-stage process of trasition from naïve to primed state and subsequently toward differentiation to be examined over 2 passages (Rahman et al., 2017). However, only one passage was possible for 2i mES cells following LIF and inhibitor removal due to progressive loss of adherent cells. The loss of viability may be due to the serum-free nature of the 2i culture medium. Serum provides a range of factors necessary for adherence and growth and with LIF removal the 2i medium resulted in low cell attachement and slow cell growth (Nichols and Smith 2013).

The investigation of changes of LIF mES cells cultured with LIF-removal indicated that differentiation proceeded, but a complex process was revealed with several steps proceeding simultaneously. Comparing the nuclear x-axis dimension distribution between LIF and LIF/-P1 mES cell suggests that LIF-removal disrupted the original balance of naïve and primed states that existed in LIF mES pluripotent cells. The data are consistent with the remaining naïve state cells progressively transiting towards the primed state, resulting in a nuclear size increase. However, a further process involving the differentiation of the primed state cells that is occuing simulateously in the same cell population also affects nuclear morphology and response to mechanical perturbation. By LIF/-P2 it is likely that the naïve to primed state transition is largely complete with differentiation predominating. The results of both the alkaline phosphatase staining and PCR assay are consistent with this notion, particulary when comparing the with mouse embryonic fibroblasts. In conclusion, we can regard LIF/-P1 mES cell group as a mixture of primed state cell and differentatied state cell and LIF/-P2 mES cell group as a group with a majority of differentiated state cells.

The comparison between LIF, LIF/-P1/ and LIF/- P2 mES cells cellular x-axis dimension and strain data during compression indicates that the cells become bigger and softer when the cell exits the pluripotency state, and this further descrbies the study of auxetic nucleus when cell exit pluripotency (Pagliara et al., 2014). Notably the LIF/- P2 mES cells showed greater defomation at 20% strain than the pluripotent cells. Figure 4.16 and 4.17, indicate that nuclear x-axis and y-axis dimensions increased when LIF mES cells were cultured in LIF-removal culture medium for 2 passages. This might relate to the development of auxeticity in the nuclei as the cells transition from the naïve to primed the state, as reported previously (Kabla and Chalut 2014). Consistent with this suggestion are data indicating a significant shift in the response of the nuclei to compression following LIF removal. At passage 2, LIF/-P2 mES cells showed a reduction in nuclear strain in the x axis compared to LIF and LIF/-P1 with indicates that LIF/- P2 mES cell has overall stiffer nucleus as more stem cells exit pluripotency. Additionally at LIF/- P2 there was an enhanced variation in y-axis strain compared to LIF and LIF/-P1 including a significant proportion of cells that demonstrated a reduction in y-axis dimension during compression in conjunction with reduced x-axis dimension. These findings provided further evidence of nuclear auxeticity with is manifested in a sub-population of cells that exist during specific phases of the progressive process of naïve to primed state transition and subsequent differentiation, which fits the description of Pagliara's study (Pagliara et al., 2014) .

It is reported that various Lamins are differentially expressed or reorganised during ealry differentiation from embryonic stem cells. For example lamin A/C is not expressed in the pluripotent state but is upregulated during differentiation (Constantinescu et al., 2006). Furthermore the organisation of lamin B1 alters as pluripotency decreases in embryonic stem cells (Kim et al., 2011). The nuclear lamin play an important role in maintaining nuclear structure and are reported to markedly influence the mechanical properties of the nucleus (Kirby and Lammerding 2016). Based on the mechanical and biochemical analysis, we raised the hypothesis that alterations in lamin organisation and expression as the cells exit pluripotency acts to stiffen the nucleus. Moreover changes in chromatin organisation, including condensation state may further affect the mechanical characteristics of the nuclues (Stephens et al., 2016). Accordingly alterations in chromatin and the nucleoplasm may also contribute to altered mechanical properties. These suggestions provide avenues for further investigation of the mechanical resistance of the differentiated cell nucleus and it role in altering gene expression triggered by nucleus deformation.

In this chapter, we induced mouse embryonic stem cell to exit the pluripotent state and induced early differentiation with LIF-removal. Alteration in both molecular markers of pluripotency and differentiation, and nuclear mechanical properties were revealed. The LIF-removal process induced dynamic shifts in the heterogeneous cell populations consistent with naïve to primed state transition and subsequent differentiation.

Chapter 5 Multi-Scale Model of Cell-Seeded Agarose Compression

5.1 Introduction

In this chapter we applied a multi-scale finite element model for simulation of the transfer of strain through the agarose to the seeded cells. The Finite element model was involved building blocks or elements of homogenous materials (Figure 5.1A). During the modelling work, the whole model construct was divided into discrete elements by meshing and boundary conditions were applied to each element. When mechanical perturbation was applied to the model, the deformation of each element in locations subjected to force was calculated, and the force was delivered to nearby elements as an interaction force. With force passing through the whole structure, a description of the whole structure deformation was obtained as well alteration in each element in every location of model. (Figure 5.1B) In additional, elements in specific location were selected from the macro-scale structure as the micro-scale model structure which incorporated the cells (Figure 5.1C).

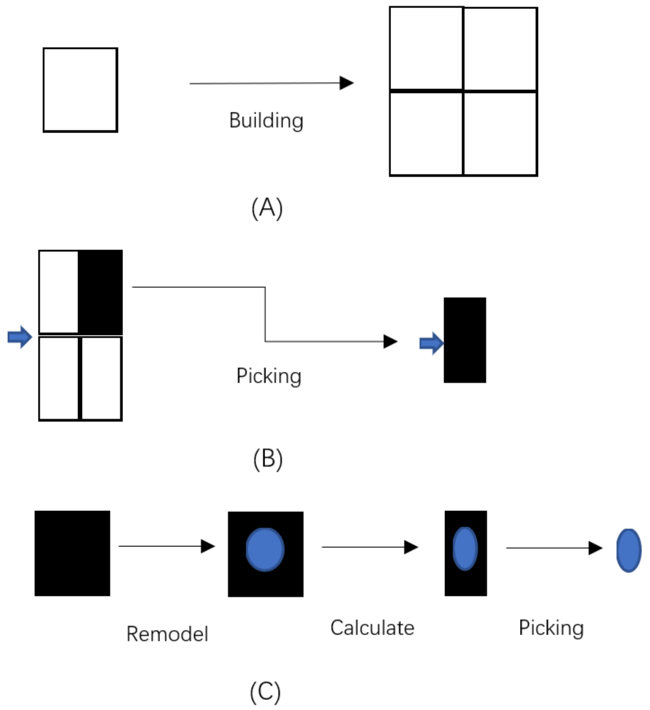

Figure 5.1 Description of multi-scale finite model. (A) presents the structure built with elements of homogenous materials. (B) presents the deformation of selected elements in specific locations. (C) presents the procedure of multi-scale model calculation.

In this chapter, a multi-scale model of cell-seeded agarose compression is described, which aligns with the experimental data provided in last two chapters. The initial sections describe the model design and parameter testing. The macro-scale model is used in 2D and 3D to simulate strain dynamics during the different compression loading steps adopted for the experimental work. Using the deformation characteristics of the agarose at specific locations within the construct, obtained in the macro-scale model, a micro-scale model of agarose/cell interactions was developed to estimate the mechanical parameters of cell through comparison between deformation predicted in the model and the experiment results. A simulation predication approach is adopted to determine the validity of the multi-scale model.

5.2 Methods and results

5.2.1 Mechanical characteristics of agarose

In developing a macro-scale modelling for cell-seeded agarose compression simulation, It is important to define the mechanical characteristics of the agarose with appropriate accuracy for input. In this project, we used 3% Type VII agarose as the porous material with linear elastic property.

Agarose compression testing was performed using an Instron 3342 Mechanical Testing System. The Instron 3342 dual column universal testing system is an electromechanical, universal testing machine, commonly used for static testing in a tensile or compression mode within a single frame. For the preparation of agarose constructs as test samples 0.3g type VII low-gelling agarose (Sigma) powder was added to 9.7ml phosphate buffer solution (PBS) solution (Sigma) and the solution was placed on a shaker for better mixing. The solution was autoclaved (121°C) for 15 minutes to create an agarose solution which was subsequently cooled to 37°C. The agarose solution was carefully added to the cylindrical wells in a custom designed mould, as described previously in Chapter 2. The mould was maintained at 4°C for 5 minutes to allow gelling of the agarose. The resulting cylindrical agarose constructs, 5mm in diameter and 5mm in height were carefully removed from the mould and maintained in PBS for 2 hours prior to testing. For testing, an individual agarose construct was located on the testing area and subjected to compression using the Instron 3342 Mechanical Testing System. The compression testing protocol applied 0% to 20% strain in a linear manner over a 60 s period. Hydration during testing was achieved by immersing the construct in culture medium throughout the agarose compression and monitoring period. The mechanical testing system recorded the displacement and load allowing strain/stress dynamic curves to be presented based on the known dimensions of the construct. Representative strain/stress curves for 4 agarose construct compression tests are shown in Figure 5.2 (A). The stress-strain curves of the 4 samples are near linear. The peak stresses at 20% strain was approximately 20kPa and the relaxation stress varied between 1.5 to 3.5 kPa.

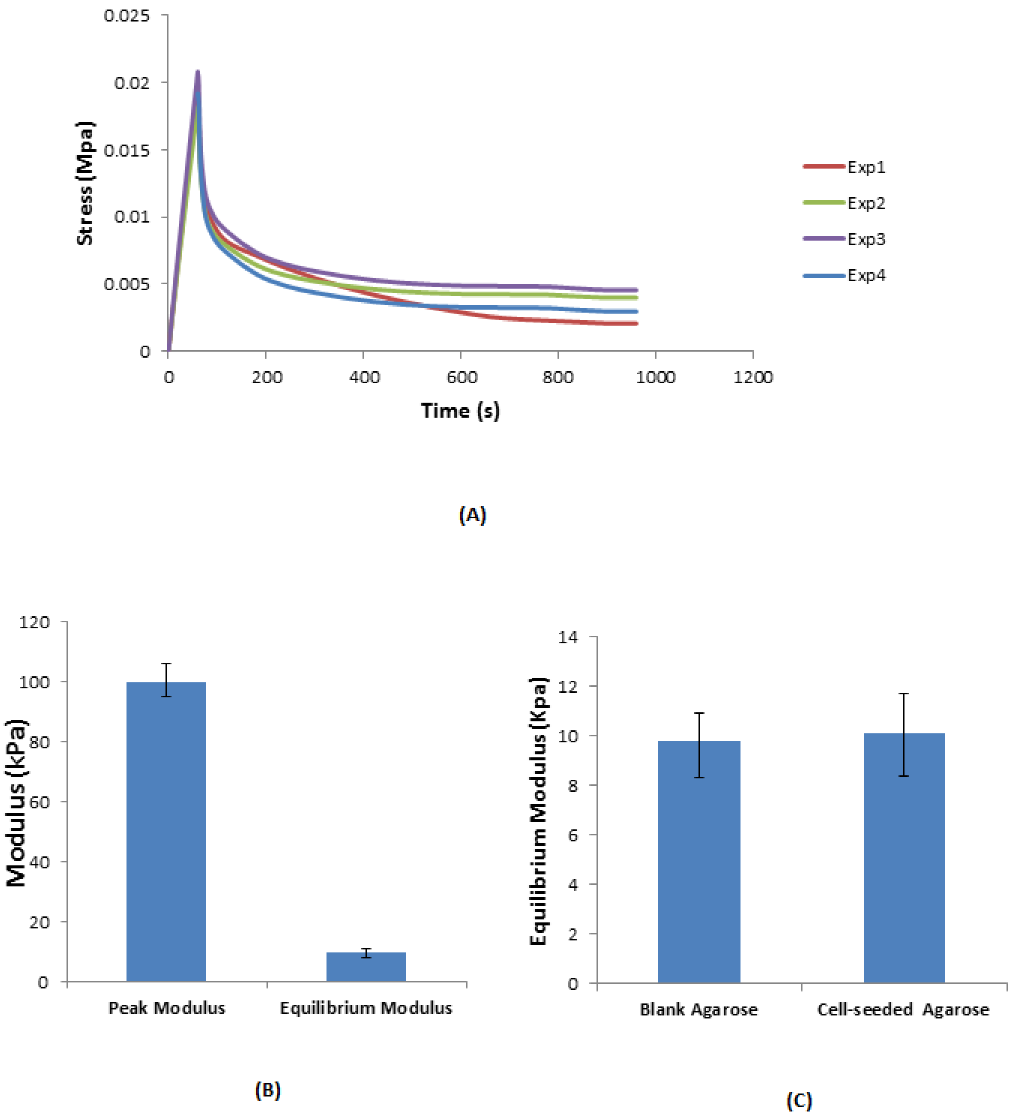

(A)

(B)

(C)

Figure 5.2 Measurement of Young's modulus of agarose (A) Stress-Strain curves of agarose samples in 20% compression test. (B) Static result of 3% type 7 agarose in peak modulus and equilibrium modulus (n=15). (C) Comparison of Young's modulus static results of blank agarose (n=15) and cell cell-seeded agarose (n=10).

Figure 5.2(B) illustrates the equilibrium modulus for 15 sample tests, with a median value of 9.8 kPa. To investigate whether the presence of cells within the agarose results in any modification of the stiffness of agarose further 3% agarose constructs seeded with 3 × 10^6 cells/mL were created as described in section 2.3.1. The resulting constructs were tested in the same manner as for cell free constructs. The testing results (shown at Figure 5.2 (C)) indicate that there was no significant difference in the equilibrium modulus between cell-seeded and cell-free agarose constructs.

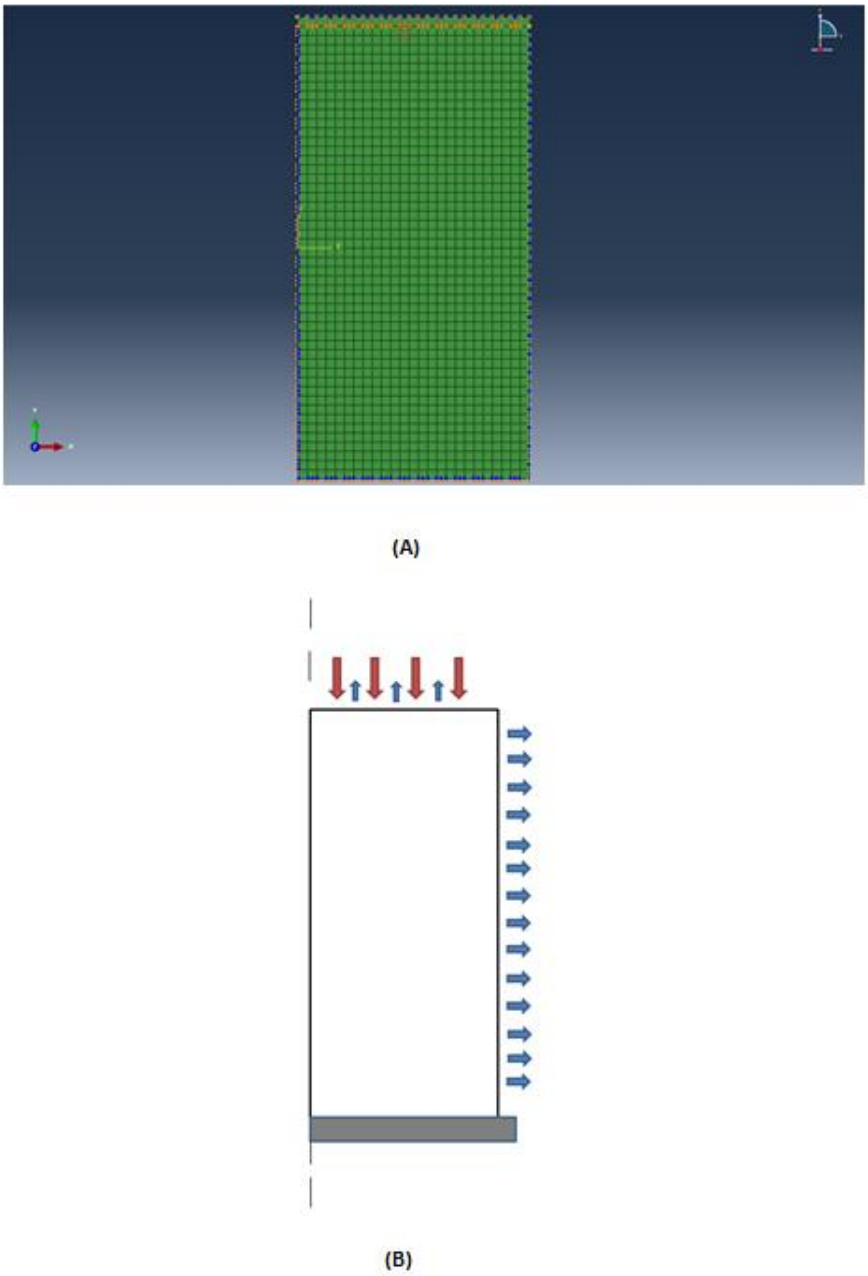

Figure 5.3 2D Modelling of unconfined agarose compression in agarose compression test. (A) Agarose cylindrical symmetry modelling with mesh (seed: 20μm). (B) Loading set in compression process. Red arrows show compression and blue arrows show pore pressure.

Since the agarose is a gel material with porous structure, pore pressure may contribute to mechanical properties in the agarose. To simulate this poroelastic behaviour, a cylindrical symmetry model (shown as Figure 5.3 (A)) was established to simulate unconfined agarose compression. The cylinder dimensions were set at a height of 5 mm and a radius of 5 mm. The mesh size adopted was 20μmx20μm and the element type applied with C3D8RP, which is an 8-node brick style with trilinear displacement, trilinear pore pressure, reduced integration and hourglass control. The mechanical loading distribution is displayed at Figure 5.3(B). The fluid flow runs through the whole agarose cylinder except the bottom at the compression direction since an impenetrable metal platform is set at the bottom area. As we did not acquire poroelastic inputs of 3% type VII agarose from our current testing, we applied the type VII agarose parameters setting from the literature (Thorpe et al 2013) and adjusted the inputs to match stress-time curves in compression test results.

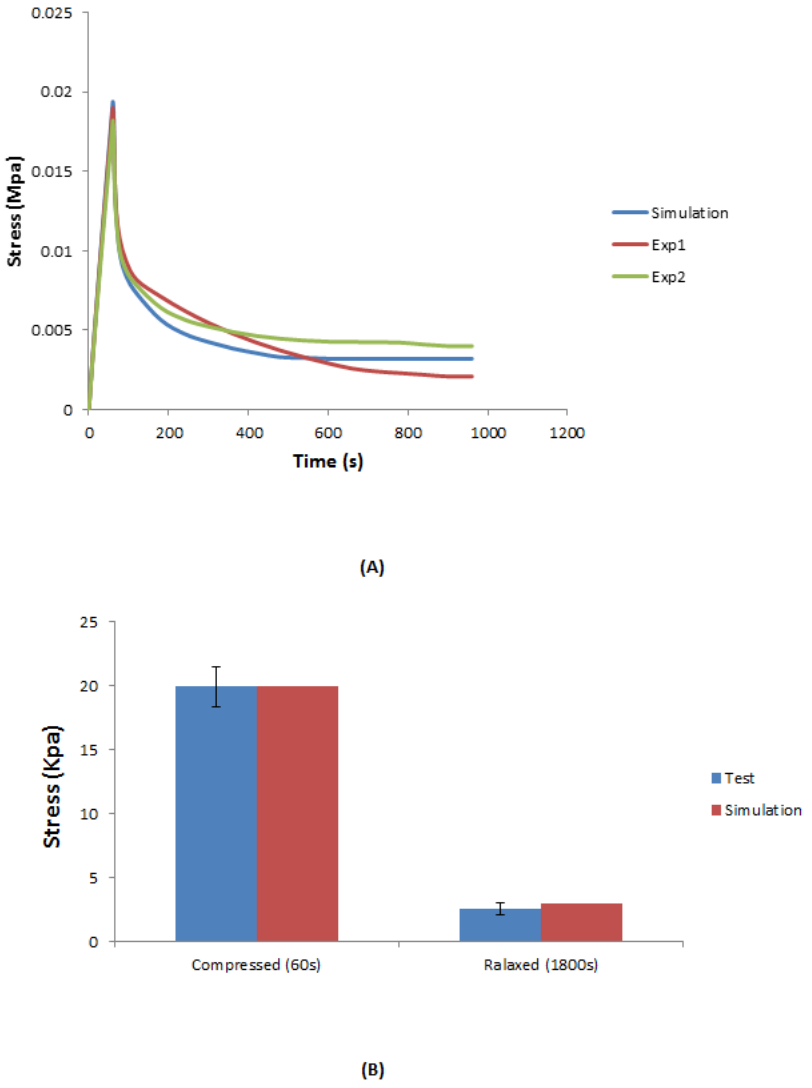

Figure 5.4 Test of poroelastic parameters setting. (A) Stress-Time curves of agarose compression-relaxation test and simulation curves. (B) Static results of reaction stress, recorded at two time points during the agarose testing (blue) and simulation (red).

To investigate the stress characteristics at a fixed strain, to determine relaxation and assess the validity of the poroelastic setting, a compression test was performed in which the 20% strain was achieved in 60s and the agarose was maintained at 20% strain for 15 minutes with stress recorded throughout. The model was adjusted to simulate the experimental loading step with adjustment of the poroelastic parameters to simulate the stress dynamics. An element at the top of the cylinder was chosen as the stress recording point in the model. The results are shown in Figure 5.4 (A). All the test curves show similar characteristics as the simulation predicts in which the reaction stress decreases during maintenance of the agarose under 20% strain. Figure 5.4(B) exhibits the reaction stress at the end of the compression phase and following relaxation for 15 minutes in the experimental analysis and compared to the simulation result. The similar results obtained from the experimental data and simulation suggests that our pore-fluid/stress axisymmetric model is valid and the inputs of agarose mechanical characteristics including poroelastic properties are suitable. Accordingly these parameters were adopted as the basis of our further macro-scale modelling for cell-seeded agarose compression.

5.2.2 2D Macro-scale model

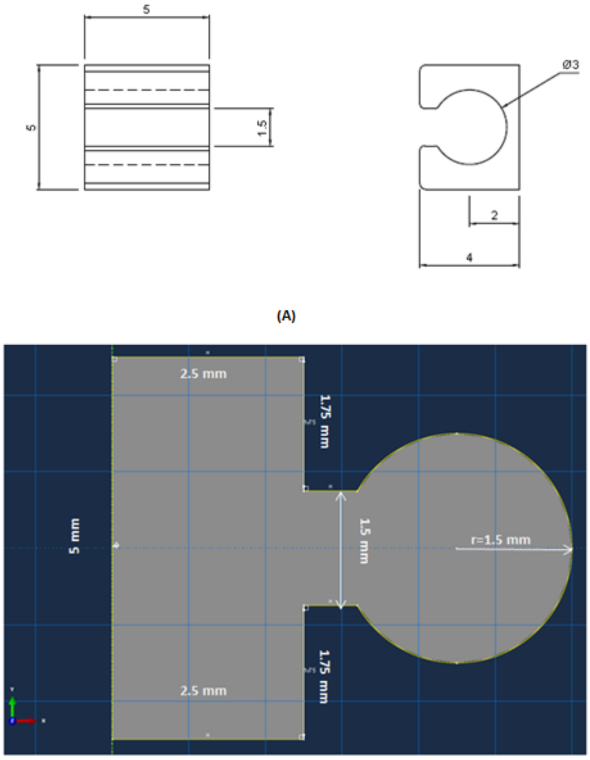

(A)

(B)

Figure 5.5 Design of 2D axial symmetry macro-scale of agarose construct. (A) Sketch of aluminium end-plates holding the agarose construct. (B) Abaqus sketch of axial symmetry of the agarose construct.

The cell-seeded agarose construct is formed with axial symmetry by the geometry of the specific plastic mould which incorporates two aluminium end pieces (Figure 5.5(A)). In experimental studies the construct is compressed from both ends perpendicular to axial symmetry of the construct. Therefore, the 2D macro-scale model of agarose is sketched with axial symmetry as illustrated in Figure 5.5(B).

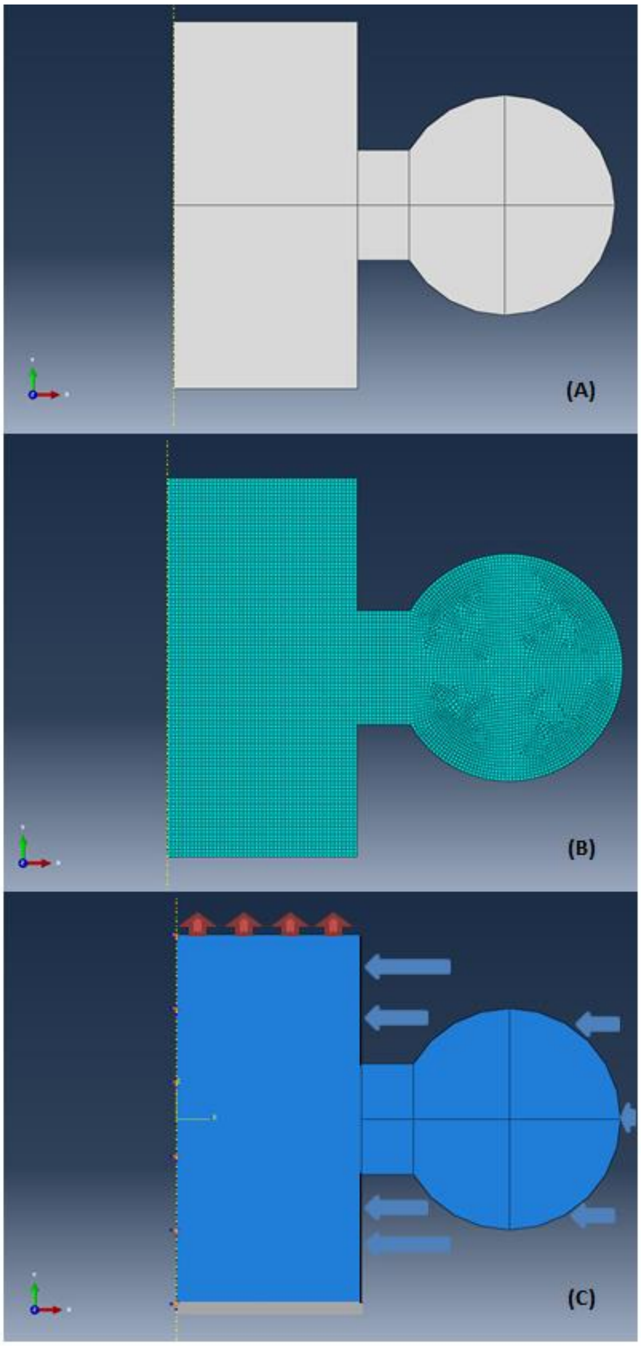

Figure 5.6 Description of 2D axial symmetry macro-scale model. (A) Additional cutting lines for better meshing quality. (B) Mesh of model. (C) Loading to construct in compression process. Blue arrows present mechanical compression effort and red arrows present pore pressure.

The agarose construct used within the experimental studies is not a regular shape due to the presence of agarose protruding into the recessed part of the aluminium end pieces. Accordingly modelling required the assembly of several geometry elements into the macro-scale model compared with the simple cylindrical agarose construct used in the unconfined compression test model. Extra plane cutting lines are included (shown in Figure 5.6(A)) for a better mesh strategy for the whole model. The mesh size was set at 50µm x 50µm and the element type was C3D8RP (Figure 5.6 (B)). The compression loading approach is demonstrated in Figure 5.6 (C) and the pore fluid plane does not include the bottom (due to its proximity to the glass slide in the experimental system), the compression reaction surface (due to the presence of the impermeable aluminium end plates) and the symmetry axis.

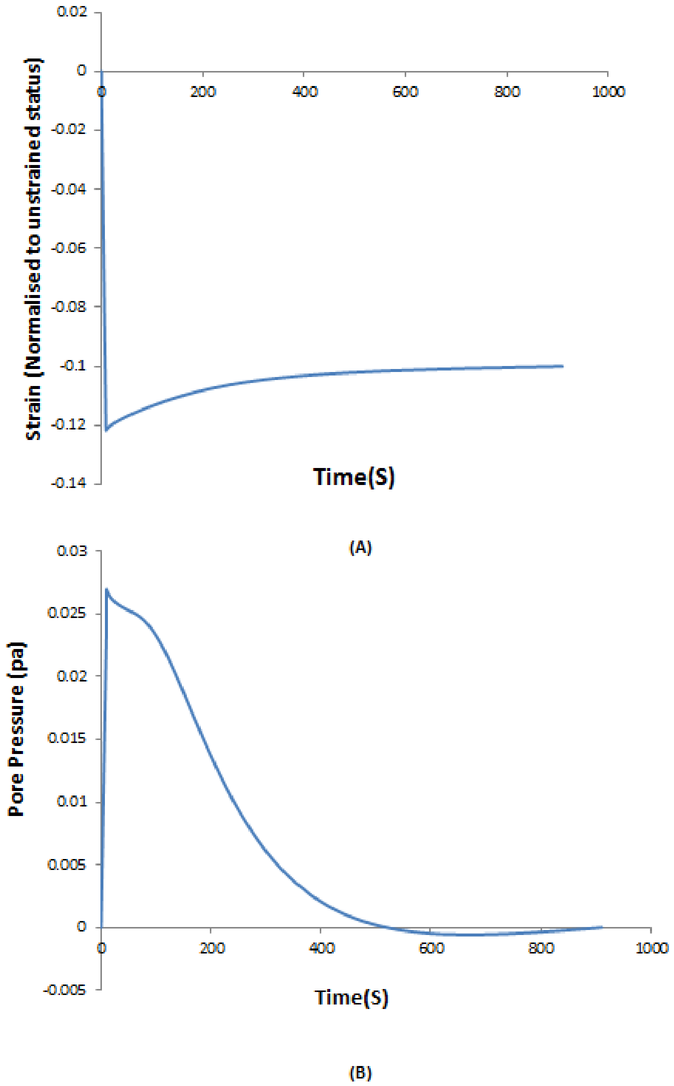

Figure 5.7 Calculation of relaxation step time. (A) Simulated compression strain-time curve during the compression process. (B) Simulated pore pressure-time curve during the compression step.

Since the cell-seeded agarose compression is performed within the imaging media, the pore pressure cannot be ignored in gel relaxation behaviour. The results of the strain dynamics in the model simulation (Figure 5.7(A)) shows that the strain at the centre of the agarose construct drops during the stress relaxation period and the strain stabilized after about 15 minutes. The pore pressure dynamics in the simulation (Figure 5.7(B)) predicts that the pore pressure drops rapidly over the 15 minute relaxation period, consistent with the stabilisation of the strain.

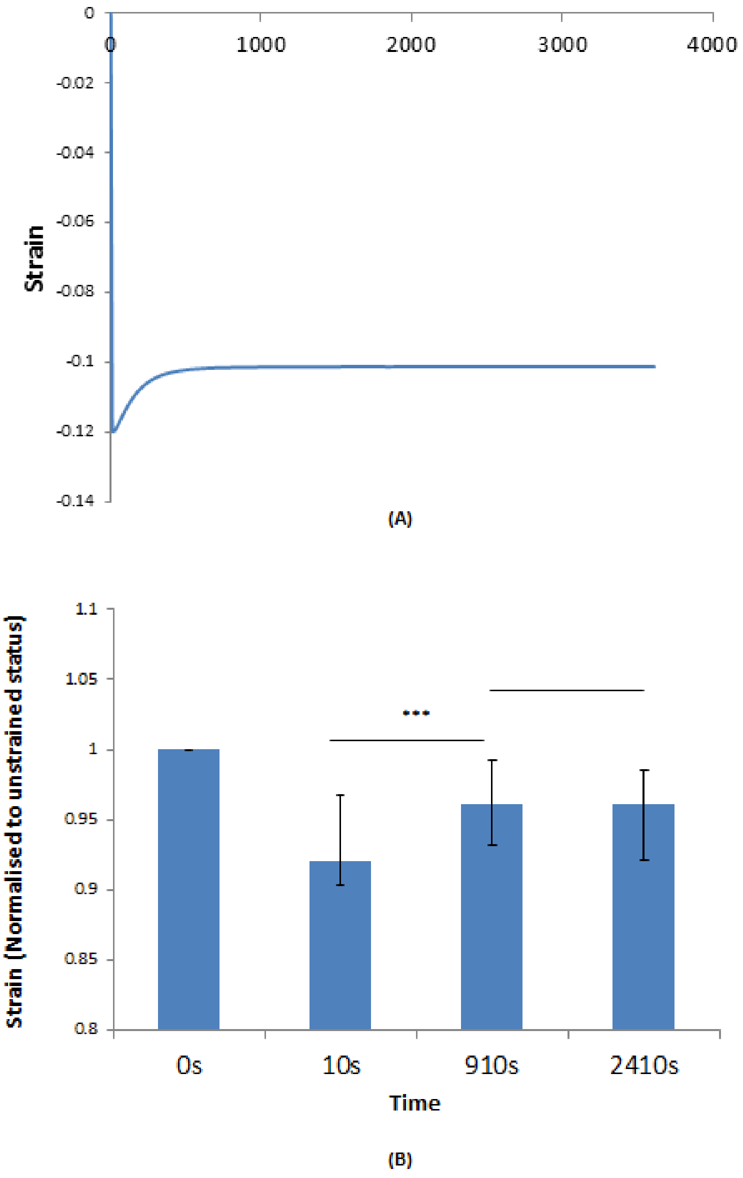

Figure 5.8 Testing the relaxation step simulation with experiment result. (A) Simulated compression strain-time curve during the compression process. (B) LIF nucleus strain at 10% compression with relaxation step. Data are presented as median and quartiles for LIF cell (n=20). ***: P<0.0001 blank: P>0.05.

To further test relaxation theory, we conducted a regular LIF cell-seeded agarose compression experiment but with an increase in the relaxation time from 15 minutes to 40 minutes. The result in Figure 5.8(B) shows that the nucleus x-axis strain alters significantly between 10s and 910s while a longer relaxation time did not bring significant change in nucleus x-axis strain when compared to 910s. These data match the simulation prediction (Figure 5.8A)). These findings indicate that consideration of the relaxation process in the agarose compression experiments is essential and that a 15-minute-relaxation period is sufficient to ensure consistent results.

5.2.3 3D Micro-scale Model

For better simulation of the agarose compression process with more accurate outputs, further model updating is required. Since fluid flow is blocked by the coverslip at the bottom surface of the agarose, the pore pressure distribution is not equal through the height of the agarose construct. Therefore an adapted model is required to account for non-homogeneity in third dimension thereby capturing further information such as pore pressure dynamics with height, element deformation in the third dimension and the effect of more sophisticated modelling of fluid flow on the previous 2D simulation results.

The 3D model is similar to 2D model with the incorporation of a side-stack. However, we had to adjust our mesh strategy to meet the new requirements for the 3D model. Since the imaging depth limited in the confocal microscopy experimental set-up we can only investigate cells up to 300 µm from the bottom of the agarose construct. The cell may be considered to a spherical object with a radius of 10 µm, with a single element of not more than 50µm X 50µm. So the 2D model was redesigned as indicated in Figure 5.9(A) with detail of the region close to the coverslip provided in Figure 5.9(B). Above 250µm from the bottom of the construct, the height of element was set as 1mm, while the height closest to the coverslip was 25µm. With the new 2D model meshing, we further introduced the 3D meshing.

Two issues arose from this meshing method. The first is that too many elements were created. There are 22500 elements and 71452 variables in the 2D model, and millions of elements when the model is transferred to 3D. This greatly increases the working time in simulating the agarose compression process. Moreover, we only need to simulate element deformation at the bottom of agarose, and any results from agarose elements beyond the imaging depth of the microscope not relevant to our research. With these considerations, a simpler meshing was adopted. Secondly only the central area needs to be considered, as this aligns with the imaging protocol introduced in section 2-5, in which imaging was restricted to the centre point between the loading platens. With these two points in mind, a further meshing update was adopted.

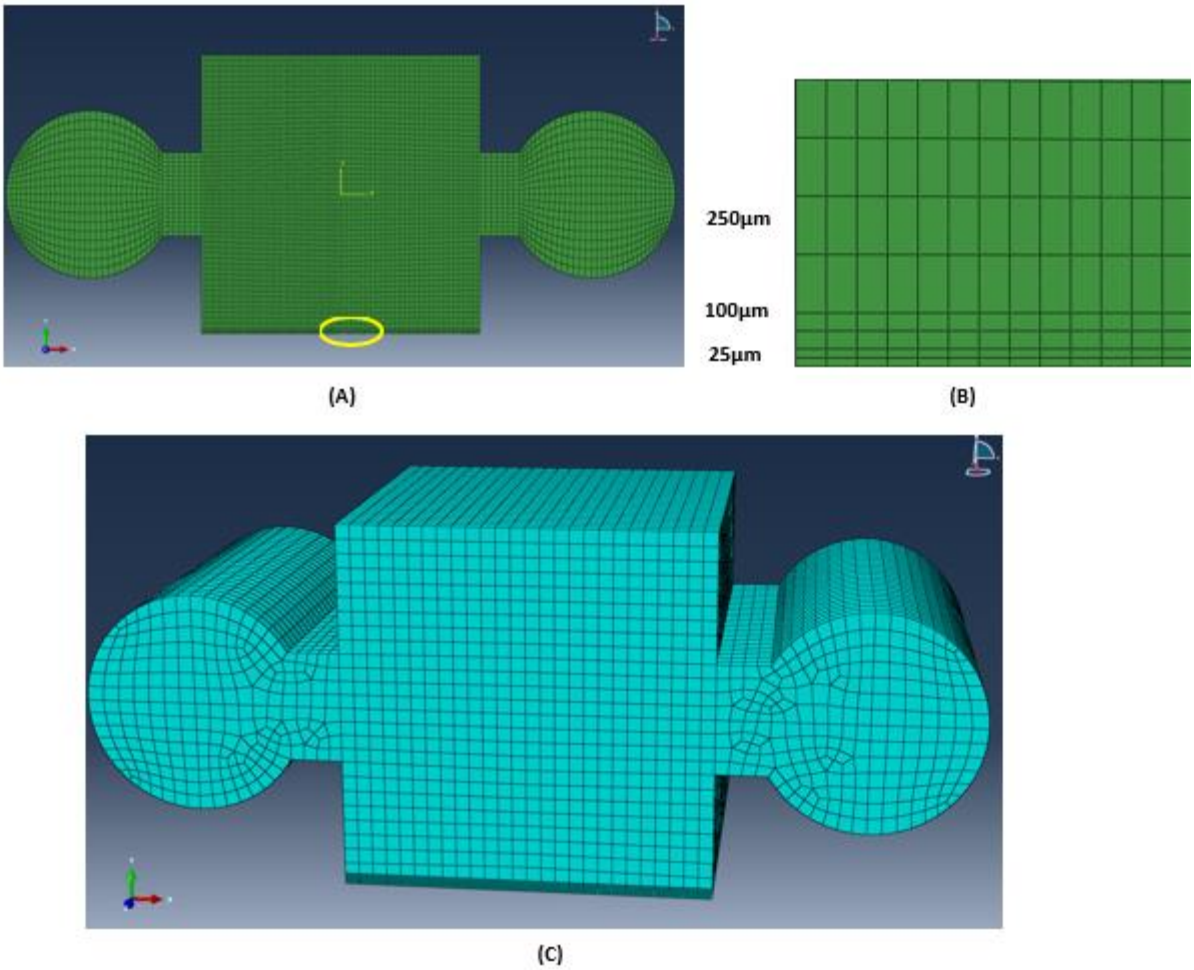

Figure 5.9 Upgrading of 2D macro-scale model and 3D macro-scale model. (A) Updated meshing of the 2D model. (B) Refined mesh seeding strategy at the bottom of the construct (yellow area in (A)) (C) Primary mesh of 3D model

Two changes are made in the meshing update. The first step is to increase the meshing element size. Above 500 µm, the seed size is set to 250 µm and below 500 µm is set as for the 2D model. Figure 5.10(C)) shows the meshing result. However, the element number (125000) is still larger than abaqus recommendation, which is less than 100000. The second step is to further increase the seed size above 500 µm to 500 µm (Figure 5.10(A)) and cut the middle 1mm plane in x-axis and z-axis for an area of 1mm X 1mm in the centre (Figure 5.10 (A)(B)), The centre is therefore isolated for deep meshing (Figure 5.10(C)), and the size decreased from 500 µm to 50 µm. With these two steps included, the element in the observation region is formed of a 50µm cube (Figure 5.10(D)).

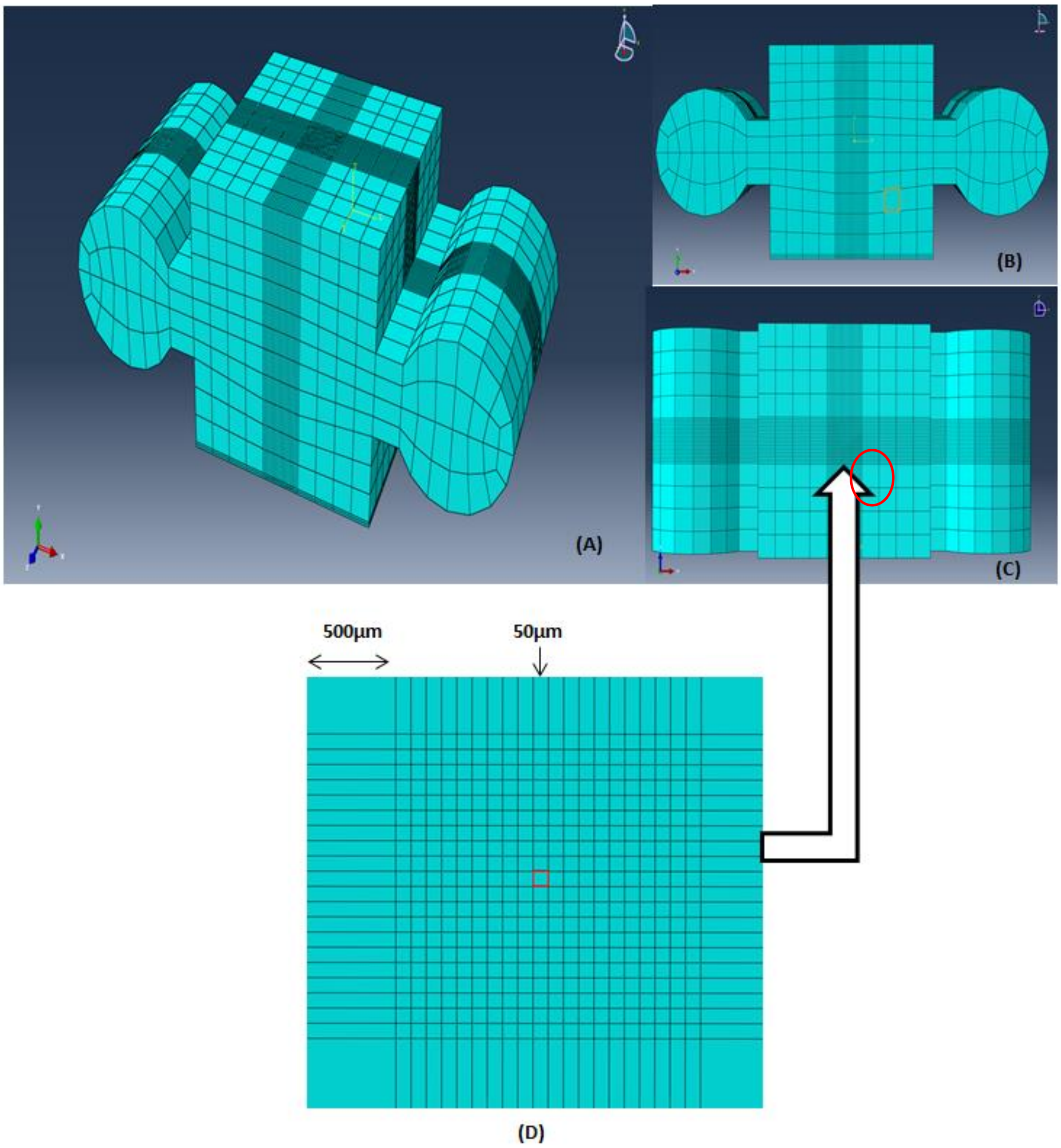

Figure 5.10 Further upgrade of 3D model meshing. (A) Overall new meshing of 3D agarose construct. (B) Defining the centre area for various seeding density. (C) Centre area at agarose bottom for deep meshing (D) Description of deep meshing area.

With the cutting plane re-divided, the model is shown as in Figure 5.11 (A). The orange arrows show the compression load and the face with yellow cubes. In abaqus software and confocal microscopy images, the y-axis and z-axis are opposite (Figure 5.11(B)) and we used the microscopy axis as standard. The 10% compression contains three steps. The first step is the preparing step, in which the pore flow predefine plane is set and the axial fixed setting is made. The second step starts agarose compression, and the process is shown as Figure 5.11(C). The third step is the relaxation step in which the 10% strain is maintained on the compressed agarose construct for 15 minutes (shown in Figure 5.11(D).

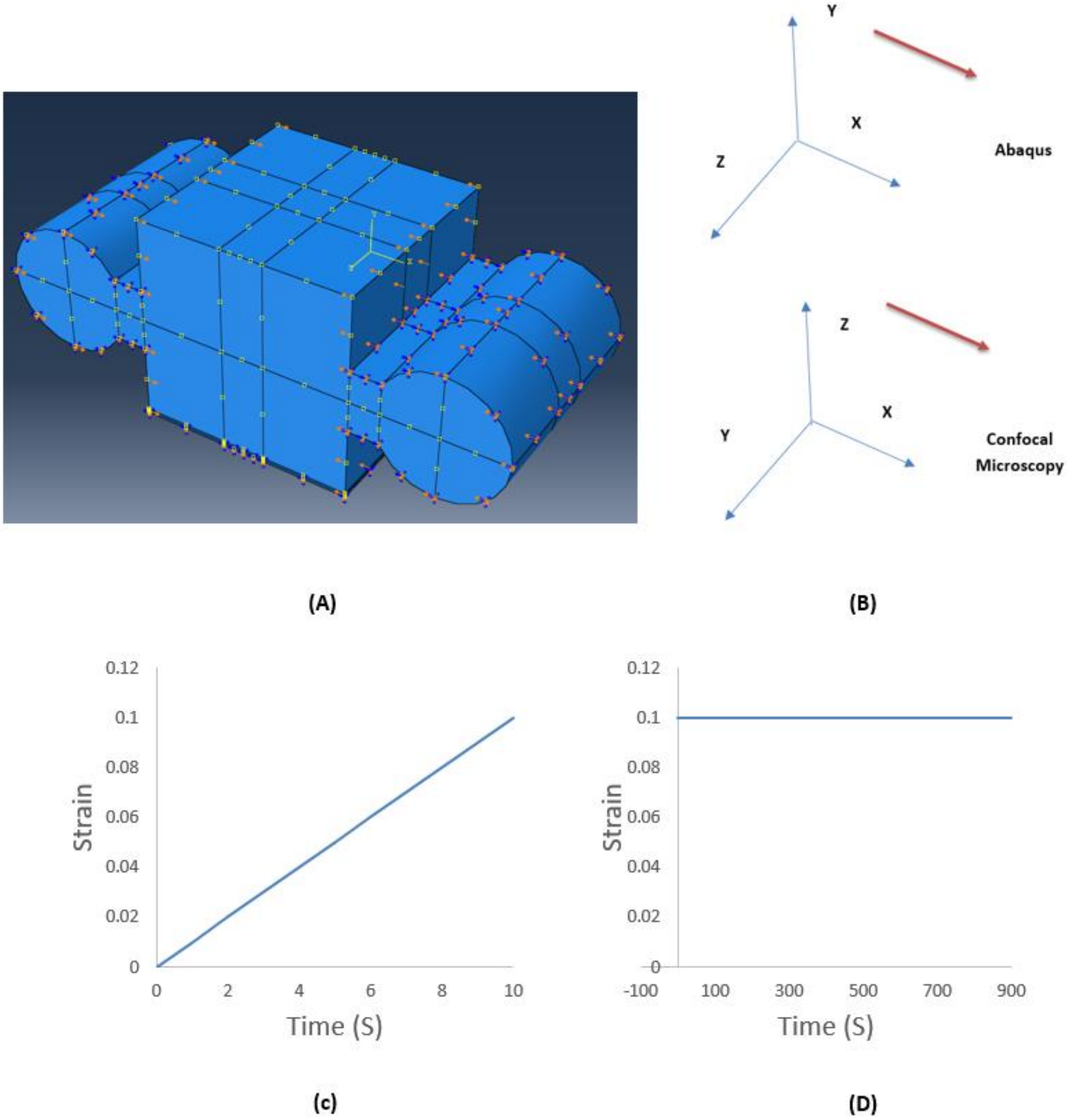

Figure 5.11 Description of the 3D model loading and loading step. (A) Loading Set in 3D agarose compression. Orange arrows show compression loading, blue mark show plane fixation and surfaces with yellow cubes show the fluid flow planes. (B) Axis definition in Abaqus and Confocal microscopy. Red arrow shows the compression direction. (C) Time-strain curve in the compression step. (D) Time-strain curve in the relaxation step.

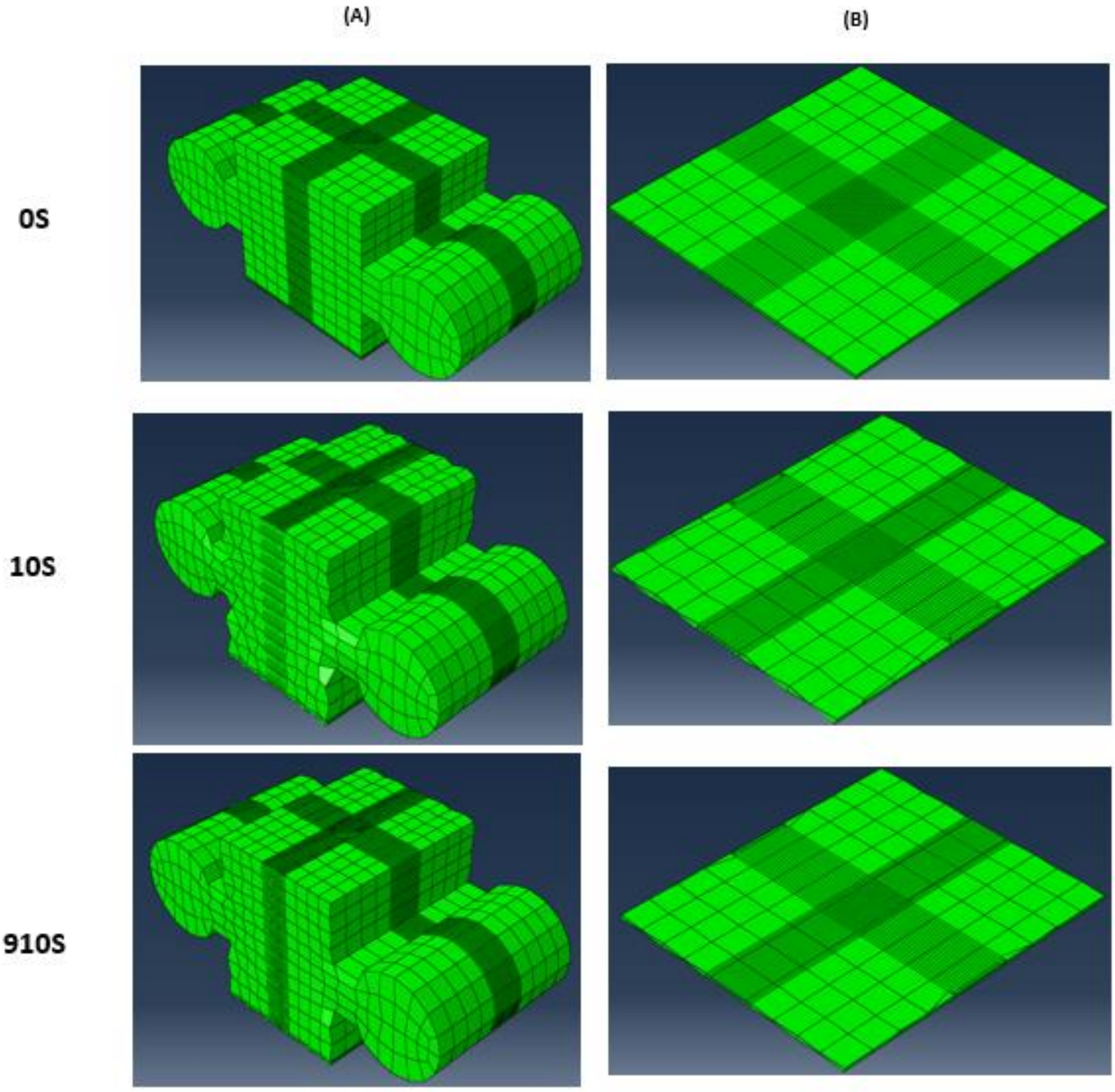

Figure 5.12. 3D agarose construct deformation in the whole structure (A) and bottom plane (B).

Figure 5.13 shows the construct deformation during the whole process. By comparing the construct deformation at 0S (preparing step) and 10s (compression step), it is obvious that construct is compressed in compression direction while expansion occurs laterally. At the end of the relaxation period, the lateral expansion is reduced compared to the end of the compression period and the bottom plane is flat.

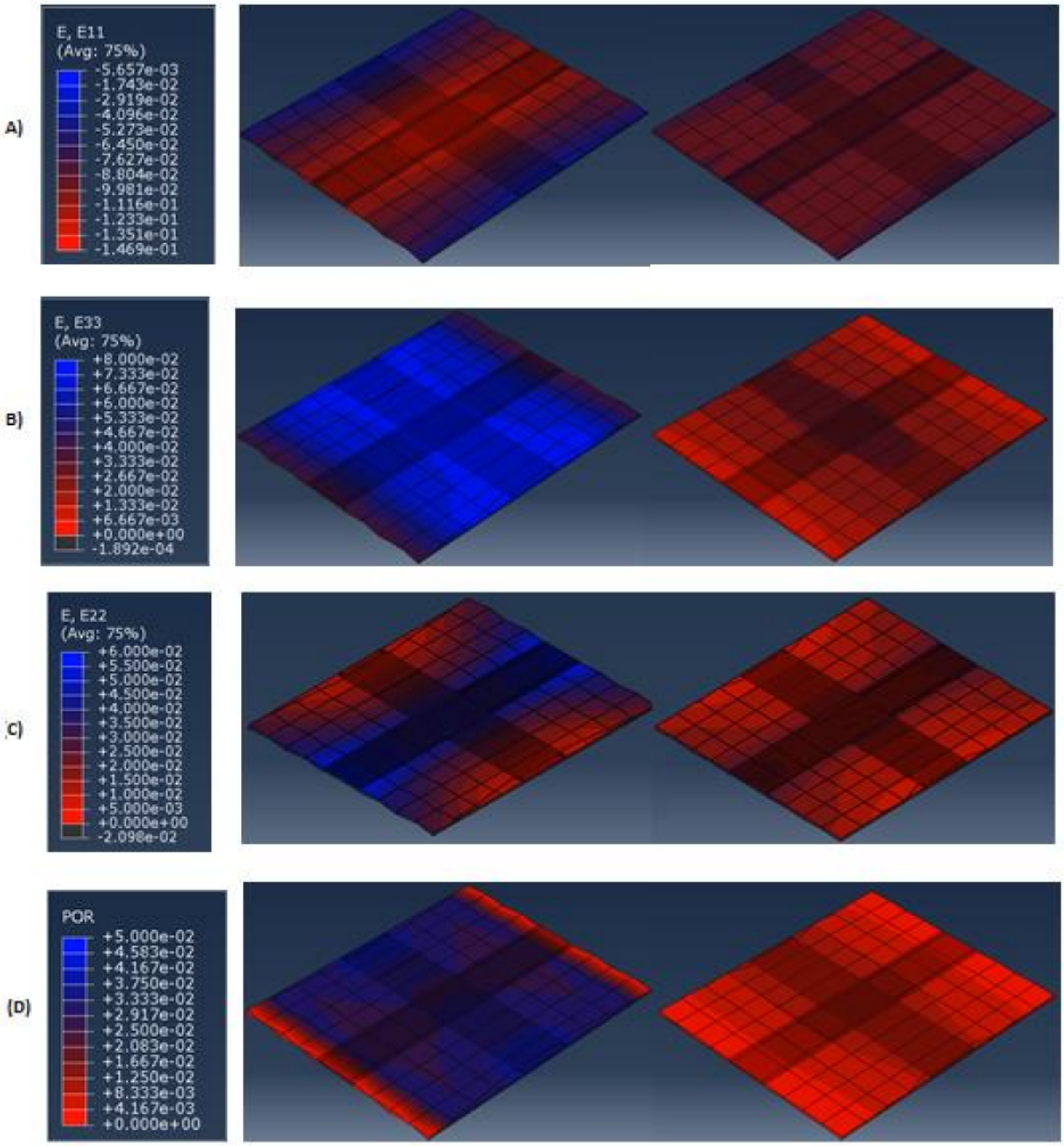

Figure 5.13 Blue-Red pseudo-colour recording of various parameters, at the bottom plane, at the end of the compression step (10s, left) and after the relaxation period (900s, right). The recorded parameters are (A) E11: x-axis strain (B) E33: y-axis strain (C) E22: z-axis strain (D) POR: pore pressure.

Figures 5.13 indicate various parameters (strain in x-axis, y-axis, z-axis and pore pressure) after the compression step and relaxation period. After compression, the distribution of x-axis strain is concentrated at the centre and equilibrates during the relaxation period. The y-axis and z-axis strain reduce toward the end of the relaxation period due to fluid flow, with an associated reduction in pore pressure.

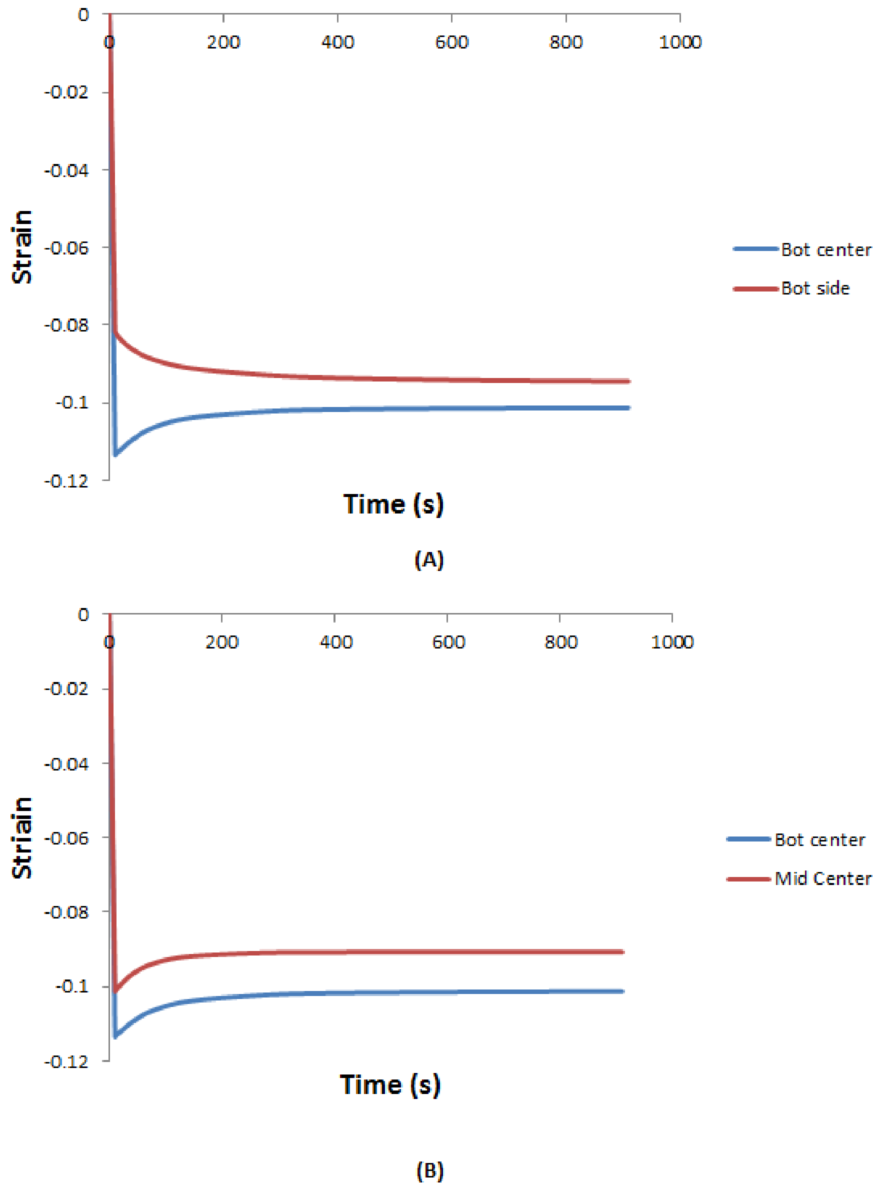

Figure 5.14 Strain curves at different location with time. (A) Strain at the bottom centre area and bottom side area. (B) Strain at the bottom centre area and middle centre area.

Figure 5.14 displays curves of x-axis strain during the relaxation process in different locations of the agarose construct. In Figure 5.14(A), the strain at the bottom side location is less than at the bottom centre, but differences were reduced after the relaxation process. The distinction between strain for elements at the bottom centre and middle centre (figure 5.14B) existed during compression, and were maintained during the relaxation period.

5.2.4 2D Micro-scale Model

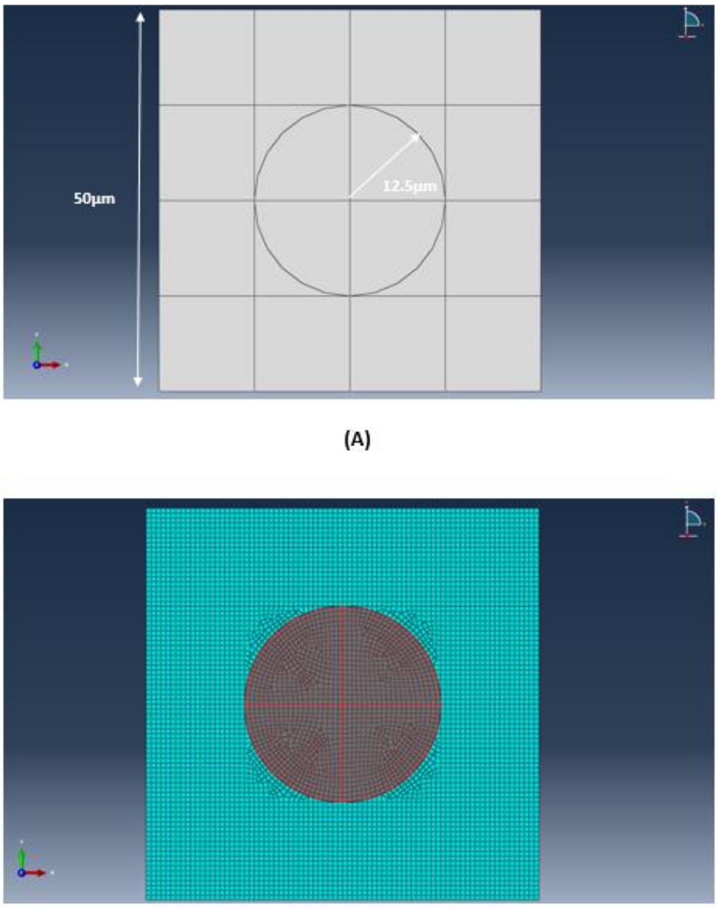

(A)

(B)

Figure 5.15. Design of the 2D micro-scale model. (A) Sketch of the 2D model. (B) Individual meshing of agarose (Blue) and cell (Red).

With the strain dynamics of agarose element at the bottom centre obtained from the 3D macro-scale model, it was possible to establish a micro-scale model of agarose-cell compression. The micro-scale model is set as a 2D solid square model of 50 μm (Figure 5.15 (A)). A circle area in the centre is isolated and defined as the cell (the red area in Figure 5.15(B)) and the remaining area is set as agarose (green area in Figure 5.15(B)). The meshing seed is 0.5μm and the element style is CPS4R, which is a 4-node bilinear plane stress quadrilateral meshing with reduced integration and hourglass control.

5.2.5 Experiment match and simulation prediction

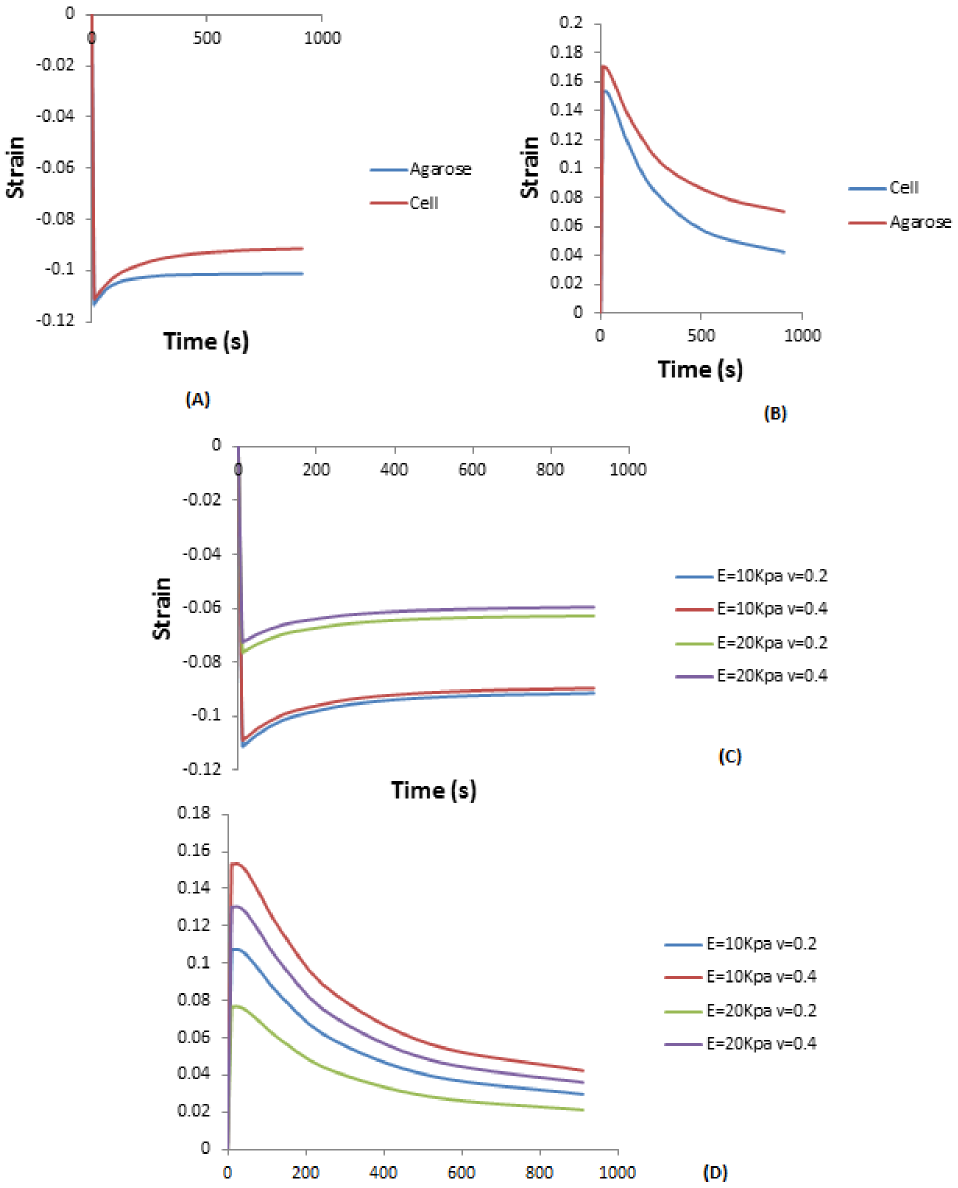

Figure 5.16. Strain simulation test of agarose and cell. (A) X-strain dynamic simulation curve of agarose and cell at 10% compression (B) Y-strain dynamic simulation curve of agarose and cell at 10% compression. (C) X-strain dynamic simulation curve of cell with different parameters set at 10% compression. (D) Y-axis dynamic simulation curve of cell with different parameters set at 10% compression.

In the micro-scale model, the mechanical properties of agarose are selected from the results in section 5.2. Since the micro-scale model is simplified as a solid interaction model the x-axis and y-axis strain of the agarose element are inputted to simulate the previous agarose compression with the pore pressure effect. The cell is set with two parameters (Young modulus E=10Kpa and Poisson's ratio v= 0.4) at first to test the model operation. Figure 5.16 (A) and (B) shows the x-axis and y-axis strain of the agarose and cell during 10% compression respectively. The result indicates that the cell is deformed less in the x-axis than the agarose due to its greater stiffness setting. Meanwhile, the greater expansion of the cell in y-axis is originated from higher Poisson's ratio input.

We investigated the role of Young modulus and Poisson's ratio in regulating cell deformation in two axial settings. Figure 5.16(C) suggested that a higher Young modulus leads to less x-axis strain while Poission's ratio barely effects the strain modification. In the y-axis strain, figure 5.16(D), greater Young modulus and reduced Poisson's ratio result in greater element expansion. With these rules obtained, it is possible to test the micro-scale model by choosing different set of mechanical inputs.

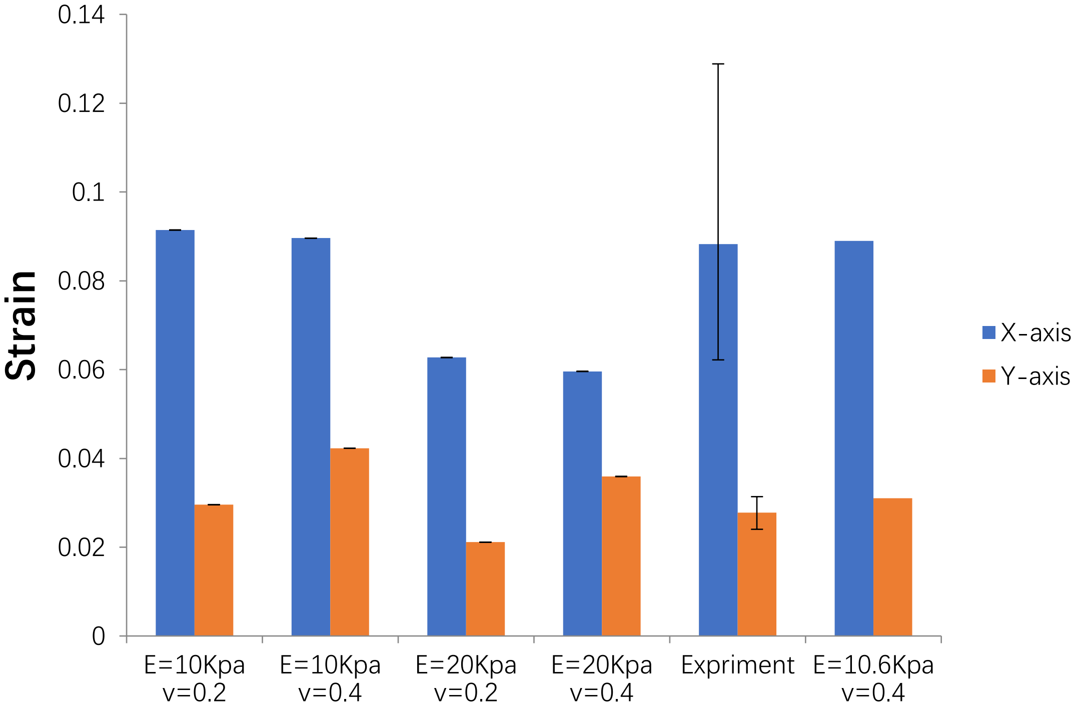

Figure 5.17. Results of x-axis and y-axis strain in 10% compression of simulation with different cell parameters and real experiment of LIF mES cell compression. The result is analysed with median and quartile method of LIF cell (n=41).

Figure 5.17 displays the cell strain in both x and y axes in several simulations and experimental results from LIF cell compression. By comparing four trial tests with the experiment data, the best match was obtained by setting the cell Young modulus to 10kPa and the Poisson's ratio to 0.4. Further simulations refined the model with more inputs resulting in the following pair of parameters (E=10.6KPa and v=0.4) which best replicated result from the LIF cell compression experiment.

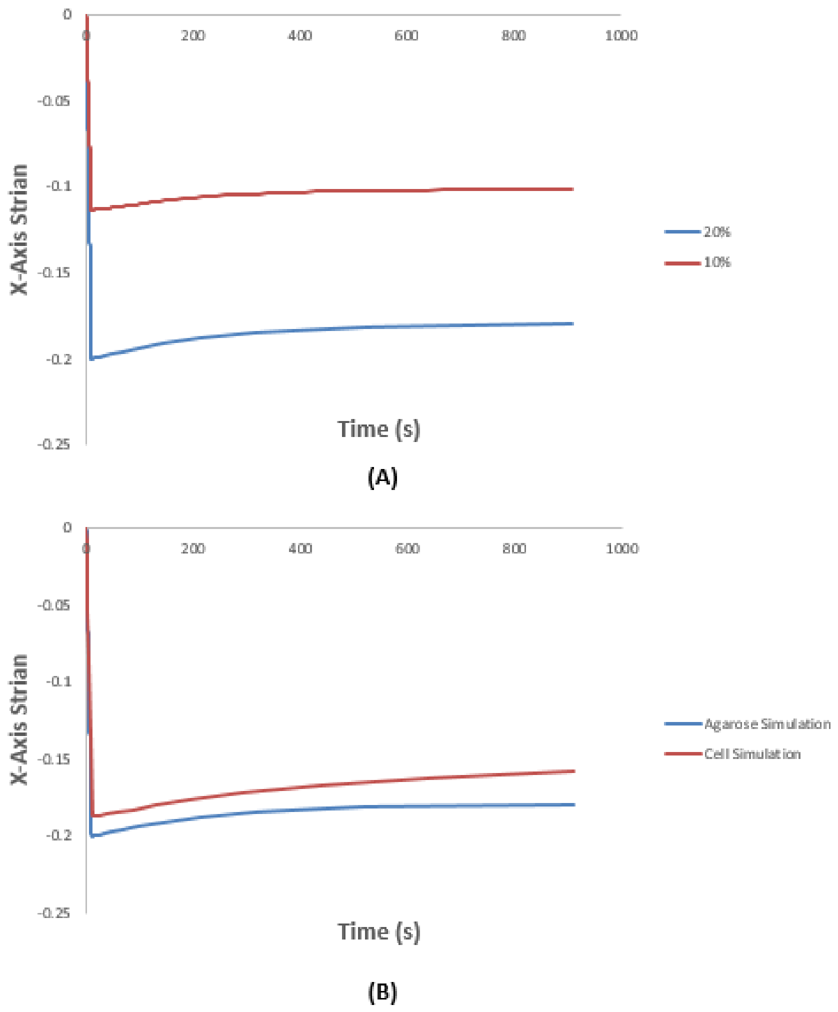

Figure 5.18. Strain dynamic simulation of 20% agarose compression (A) Strain dynamic simulation of agarose in 10% compression and 20% compression. (B) Strain dynamic simulation of agarose and cell in 20% compression.

To further test the parameters in the 10% micro-scale model simulation, we ran a 20% agarose compression simulation from the 3D macro-scale model to the 2D micro-scale model. Figure 5.18(A) exhibits the x-axis strain of agarose element at the bottom centre. Figure 5.18 (B) shows that the cell deformed less in the x-axis than the agarose which is similar to the 10% agarose compression simulation.

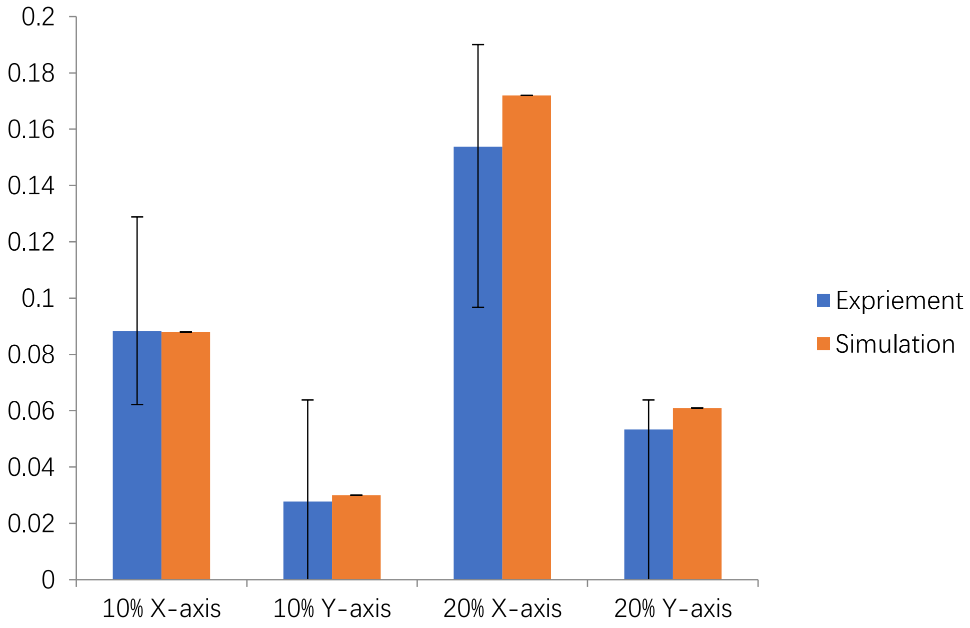

Figure 5.19 Results of cell x-axis and y-axis simulation with real experiment results from LIF cell compression. The result is analysed with median and quartile method of LIF cell (n=41).

The Figure 5.19 shows the x-axis strain of the cell in the simulation and in LIF cell experimental compression. The result the simulation more accurately reflected experimental data at 10% than 20% with cell deformation observed in the experimental results less than the simulation at 20% strain.

5.3 Discussion

In this chapter, we established a multi-scale model to simulate the cell-seeded agarose compression used previously in our study. The model offers details of agarose deformation at specific locations and allows estimation of the mechanical parameters of the cell and nucleus in combination. Since our project utilised 3% type VII agarose as the scaffold to contain cells for compression, it is important to understand the mechanical properties of the agarose, including its elastic and poroelasitc properties. Poroelastic behaviour plays crucial role in the viscoelastic and relaxation properties of the agarose and manifests as a distribution of stress, strain and pore pressure (Buckley. 2009).

In the 2D model, a complexity of different mesh scale seeding towards the target location was applied. In general, there exists a difference of approximately two orders of magnitude in the characteristic length scales of meshing (Guilak & Mow 2000). In Guilak's work, the micro-scale model was directly inserted into the macro-scale model

(Guilak & Mow 2000). In the current study, we tried a similar model design and failed since fluid flow could not efficiently function due to fluid impermeable boundaries as reported in other works (Mauck et al 2007). To overcome this problem, we independently set the micro-scale model as a solid model with less than 5 cell radius scale (Guilak & Mow 2000). As the replacement for the fluid flow effect in the micro-scale model, the element strain in x-axis and y-axis obtained from macro-scale model was applied to simulate the pore pressure. In agarose compression testing, confined compression differs greatly from unconfined compression due to the different pore pressure distribution (Thorpe 2013). Accordingly the 2D model could not accurately simulate compression because of the presence of aluminum end plates which partly confine agarose construct in compression.

One major goal in establishing a multi-scale model is to estimate deformation characteristics in locations which cannot be detected by current experimental technology including confocal microscopy. Figure 5.20(A) shows the x-axis strain of agarose element at the surface after relaxation step and figure 5.20(B) displays the x-axis strain of agarose element at the centre. The data suggest that agarose elements in the different locations share a similar x-axis strain in compression.

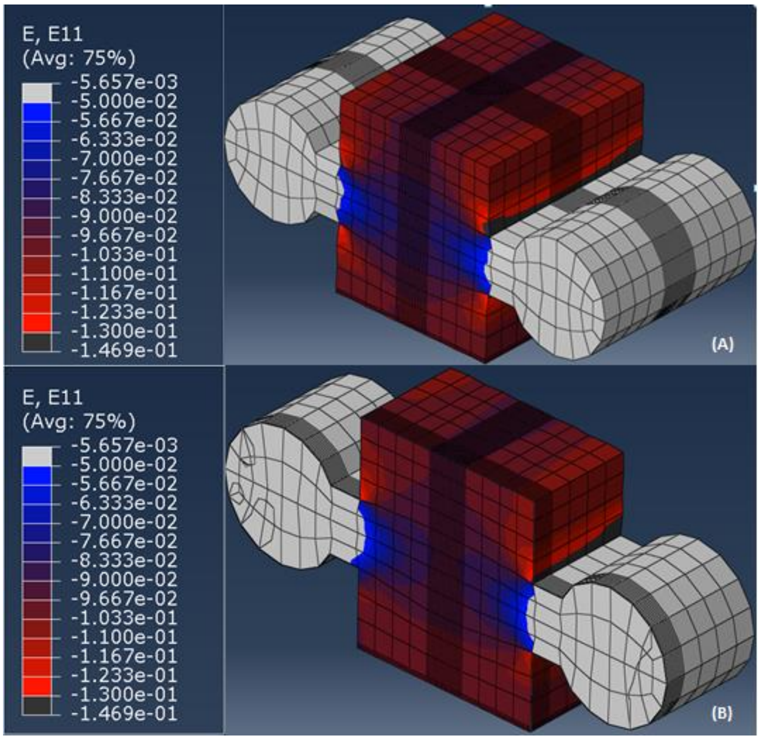

Figure 5.20 Blue-Red recording of x-axis strain at side surface (A) and middle surface (B).

The model was also used to simulate porous pressure dynamics during the agarose compression process. In figure 5.21(A), we found that the pore pressure in the agarose elements was similar following compression in the internal region of the construct, but was reduced at the edge next to the fluid. In contrast to the uniform distribution of pore pressure in the middle, the surface close to aluminum end plates presented the highest pore pressure (figure 5.21(C), and this may be caused by the confining effect of aluminum end plates which block flow fluid through the y-axis (Thorpe 2013). Figure 5.21 (B) and (D) shows that after relaxation for 15 minutes, the pore pressure is mostly reduced but with significant variation in both y and z axes.

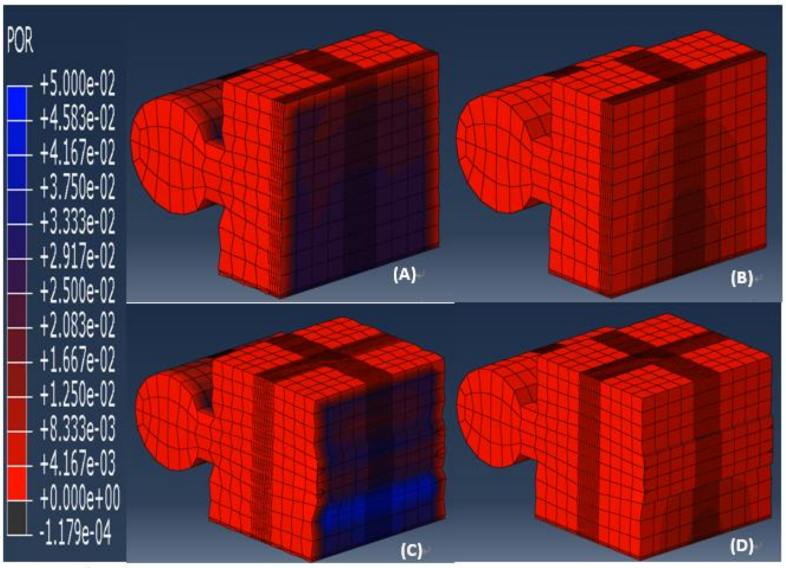

Figure 5.21 Blue-Red recording of pore pressure at middle surface (A and B) and side surface (C and D) after compression step (A and C) and relaxation step (B and D).

With the proper model set up, it is possible to estimate cell deformation in each location of agarose construct using the multi-scale model theory shown in section 5.2.3 and 5.2.4. As an example, we can calculate the deformation of cell in the central area of the construct used during imaging. Figure 5.22 presents simulation strain results in the x-axis and y=axis at 10% and 20% compression after relaxation. However, the prediction based on simulation does not perfectly match up with the experiment results. Several factors cause this mismatch. The simulation is based on our setting of agarose construct with a uniform distribution of pores. In reality the pores in agarose are randomly located with normally distributed size. This might lead to spatial variation in loading and an error in measurement exists. Secondly, we set the micro-scale model of the cell as a solid and homogenous construct, thereby averaging the properties of the cytoplasm, cytoskeletal fibres and nucleus. It is recently report that pre-stress in the cytoskeleton should be considered when determining cell properties (Lim et al 2015). Moreover it has been suggested that the cytoplasm should be treated as a pyroclastic material instead of a solid material. (Moeendarbary et al 2013).

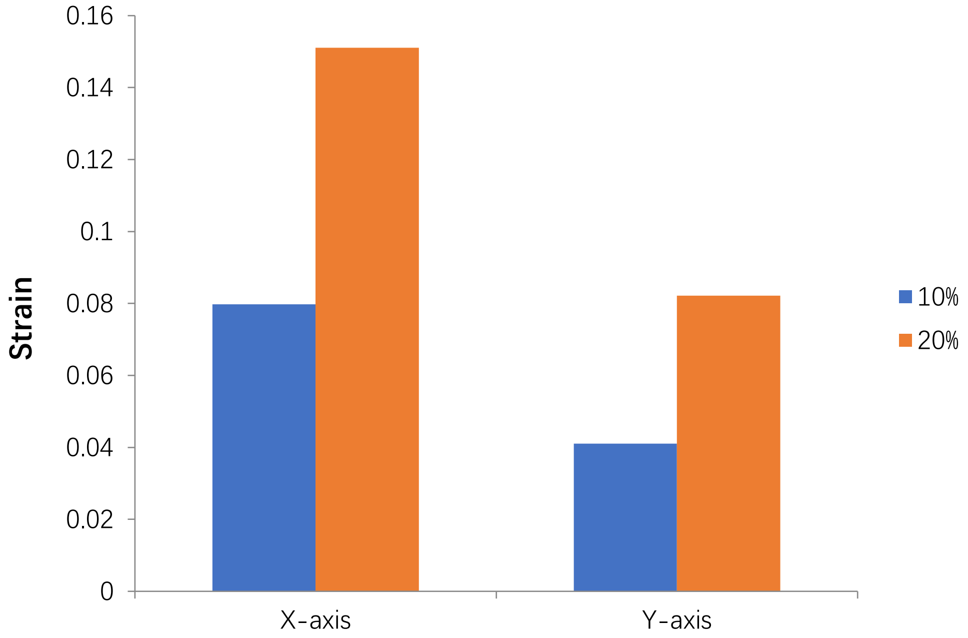

Figure 5.22 X-axis and y-axis simulation strain of cells in the middle centre of agarose.

In investigating the y-axis strain after relaxation, an interesting phenomenon was revealed. Cells at the bottom region of the construct exhibit higher y-axis strain compared with cells at the top region (Figure 5.23). This is possibly caused by the confining effect of coverslip as a fluid-impenetrable plane. (Thorpe et al 2013). Since cells at the top and bottom share similar x-axis strain while differing in y-strains it may be postulated that the nucleus receives different and directional mechanical perturbation, specifically expansion orthogonal to the loading axis. This could result in distinct patterns of chromatin deformation. Accordingly the cell and nucleus are deformed to a different degree with uniform compression to the construct. By understanding the strain distribution through this agarose construct it is possible to set pre-designed and specific loading parameters to achieve regionally varying cell and nucleus deformation to guide mechanical regulation in bioreactors which promotes tissue engineering technology (Stoppel et al 2016).

We attempted to establish a solid micro-scale model with agarose-cell-nucleus structure (shown in Figure 5.24 (A)) and used CPS4R as element type to mesh (Figure 5.24 (B). With similar multi-scale calculation and predictions, we simulated the 20% LIF mES nuclei x-axis and y-axis strain as indicated in figure 5.24(C). The predication outputs are similar to experimental results, but the assumptions inherent in this model are challenging. It is widely accepted that the nucleus is not a component in isolation within the cell, but mechanically continuous with the cytoskeletal systems, which in turn are linked to the plasma membrane (Kirby & Lammerding 2016). Novel approaches to model interaction between the cell and nucleus is required such as those reported recently which could improve micro-scale modelling of cell and nucleus in future work (Barreto et al 2013).

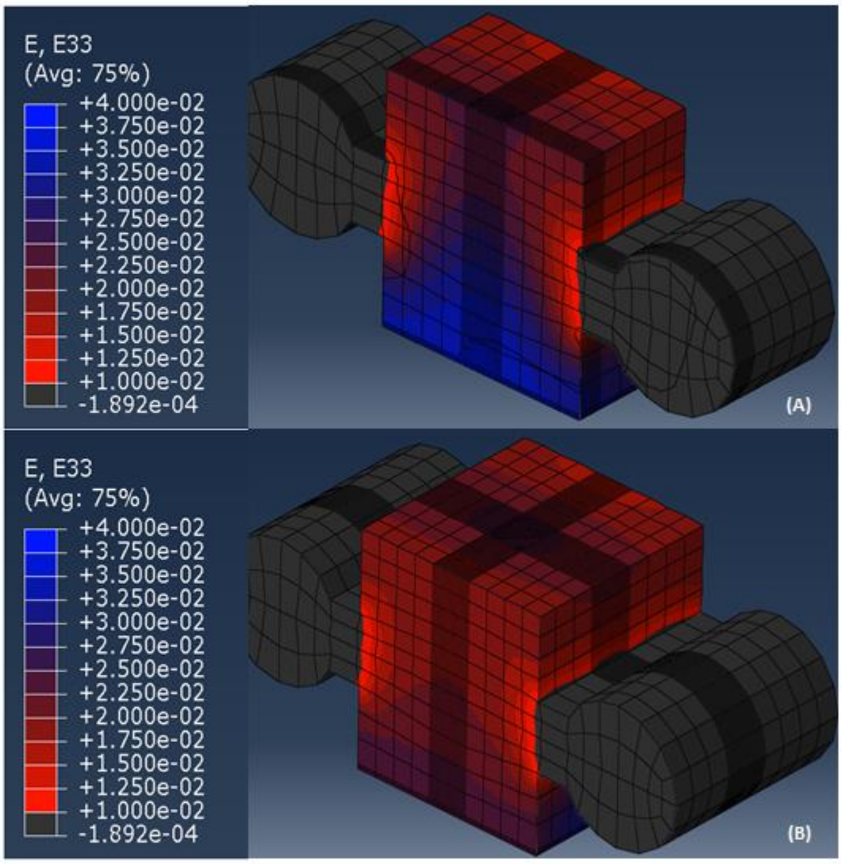

Figure 5.23 Blue-Red recording of y-axis strain at the middle surface (A) and side surface (B) after relaxation step

Although multi-scale modelling simulation proved valuable for predicting cell deformation in cell-seeded agarose compression in specific location simulation, the limitations of this multi-scale modelling simulation should be considered. The first limitation involves the use of the commercial software Abaqus. Although Abaqus offered a biphasic model simulation which was accepted as a tool to describe solid structure deformation in a liquid environment, the model type is not ideal. The biphasic model simulation in Abaqus describes the deformation of two fixed phases with stable characteristics. However, during the compression process, cells may metabolise the medium and/or interact with the medium via transfer across the cell membrane, leading to potential alteration in the characteristics of the fluid. For simulation of long-term cell-seeded scaffold compression in bioreactors, this effect on the biphasic environment may become more pronounced, and this might impact on the accuracy of the deformation in the modelling compared to actual experimentation . A further limitation is due to the homogeneous distribution of pores in the agarose modelling design. The actual sizes of pores in agarose varies widely and the pore distribution is random and disorganised. This may affect the spatial distribution of agarose deformation between simulation and observation. Accordingly the complex heterogeneity of both agarose pore distribution and cells in the real construct may lead to significant spatial variation in agarose of cell deformation that is not predicted by the model in its current form. In consideration of the limitations of the model described above, improvement to the modelling should be considered in future work. Besides, a better understanding of the scaffold material and its heterogeneity is necessary for more accurate modelling.

In summary, we established a multi-scale model to simulate our cell-seeded agarose compression studies. This model simulates the agarose compression process with details that could not be obtained experimentally and may allow predictions of spatial variations in cell and nucleus deformation to guide mechanical regulation in bioreactors which promotes tissue engineering.

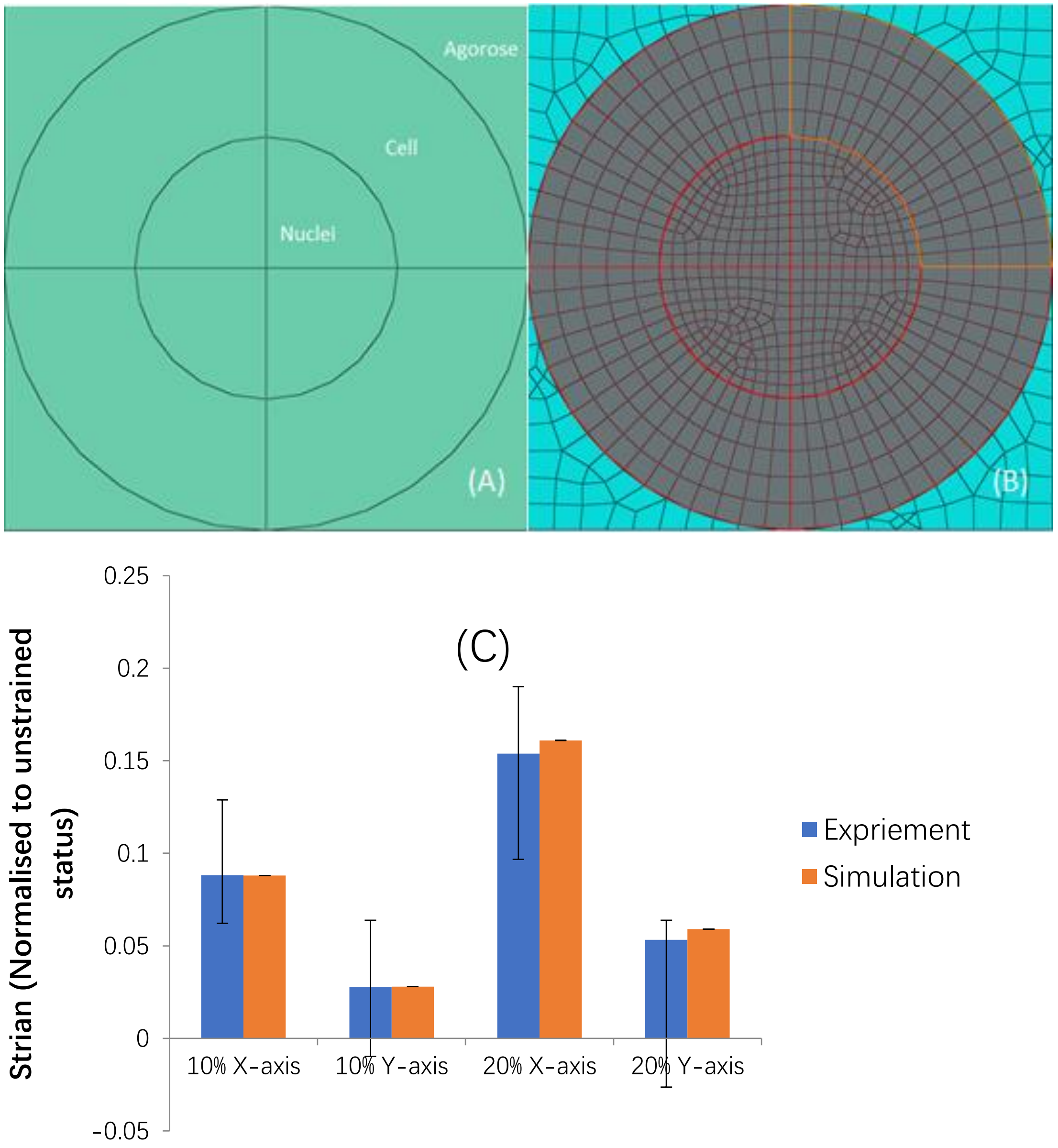

Figure 5.24 Description of micro-scale model of agarose-cell-nuclei. (A) Sketch of 2D model (B) Mesh of model (C) X-axis and y-axis simulation result of nuclei at 10% and 20% compression with real experiment of LIF cell compression. The result is analysed with median and quartile method of LIF cell (n=41).

Chapter 6 Final Discussion

6.1 Introduction

Pluripotency is a key feature of embryonic stem cells and significant research effort has investigated the mechanism of pluripotency maintenance, pluripotent gene marker expression, differentiation and reprogramming. These studies reveal the presence of a gene regulatory network with impacts pluripotency maintenance and lineage specific cell fate and differentiation. By contrast stem cell mechanobiology has received significantly less attention, with relatively few studies attempting to discover the role of the mechanical phenotype of the stem cells and the influence of mechanical perturbation in regulating functions. Many studies have described the existence of mechanotransduction pathways in cells, including stem cells, but the principle focus has been events at the cell membrane. It is well established that external mechanical perturbation starting at cell membrane may be propagated through mechanically contiguous components in the cytoplasm, such as the cytoskeleton to reach the nucleus.

Key components in the mechanotransduction include the mechanical sensing proteins on cell membrane, the cytoskeleton, LINC complex and lamins which are investigated to understand their mechanical functions and regulatory impact. The direct nucleus response to mechanical signals from the external environment is critical to understanding in cell mechanobiology as the nucleus will be a key component in mediation cellular response, either through a direct mechanical effect and/or as the site of altered transcription linked to nuclear translocation of transcription factors. In studying the nuclear mechanical response to mechanical perturbation, chromatin modification may be a key focus as this links nuclear components that affect morphology and mechanical properties with potential gene expression and epigenetic modification. To better understand epigenetic modification and other reorganization of nuclear structures in response to mechanical perturbation, the mechanical properties of nucleus need to be understood.

The aim of the research in this thesis is to investigate the cellular and nuclear mechanical characteristics of mouse embryonic stem cells in different phenotypic conditions involving distinct pluripotency states and early differentiation. A small number of previous studies have been reported in the literature that aim to determine similar characteristics, typically involving deformation induced by atomic force microscopy (AFM) and micropipette aspiration. These approaches tend to induce local mechanical perturbation at discrete sites at the cell membrane which is transferred to the nucleus via coupling components, such as the cytoskeleton and LINC complex. The current work involved a different approach whereby whole cell deformation is induced in a manner potentially more relevant to the natural 3D environment. The cell-seeded agarose compression approach used in this project is well characterized for a variety of cell types and offered mouse embryonic stem cell a 3D environment to better mimic the natural state of embryonic stem cells within embryo with the application of a simple mechanical compression via the agarose. Moreover, the 3D environment avoids the pre-stress of cytoskeleton which is a common feature for cells attached to a 2D surface in monolayer. Another highlight in this project was the discovery of the potential for rotation of the nucleus during cell-seeded agarose compression. This process allows for reorientation and re-organisation of the nucleus within the cell, without the requirement of major distortional events. Rotation and distortion may induce distinct alterations in chromatin organisaton and/or chromosome territory repositioning, with associated impact on genome function and gene expression.

In summary the key outcomes of this study are as follow:

A. Multiple phenotypes of mouse embryonic stem cells (mES cells) were obtained by modifying components of the cell culture medium. These included cells in various pluripotency states and the initial differentiated state.

B. The cell-seeded agarose compression system used in previous work in the group was adapted for mouse embryonic stem cell compression studies with an optimized protocol for nucleus staining. Cellular and nucleus deformation was achieved under compressive strain.

C. Nuclear rotation was observed in cell-seeded agarose compression studies.

D. The pluripotency and differentiation phenotypes were confirmed with molecular biology and correlated with mechanobiology analysis. Representative gene expression profiles and mechanical characteristics were characterised.

E. A multi-scale Abaqus model was develop to simulate cell-seeded agarose compression. When optimized by comparison with the experimental results, the model could describe finite element deformation in multiple locations in the constructs which overcame the limitation in experimental design.

F. The multi scale model was used to estimate the mechanical properties of cell and applied in predicting the experiments result via simulation.

A schematic diagram (Figure 6.1) briefly introduces the work contained in this thesis:

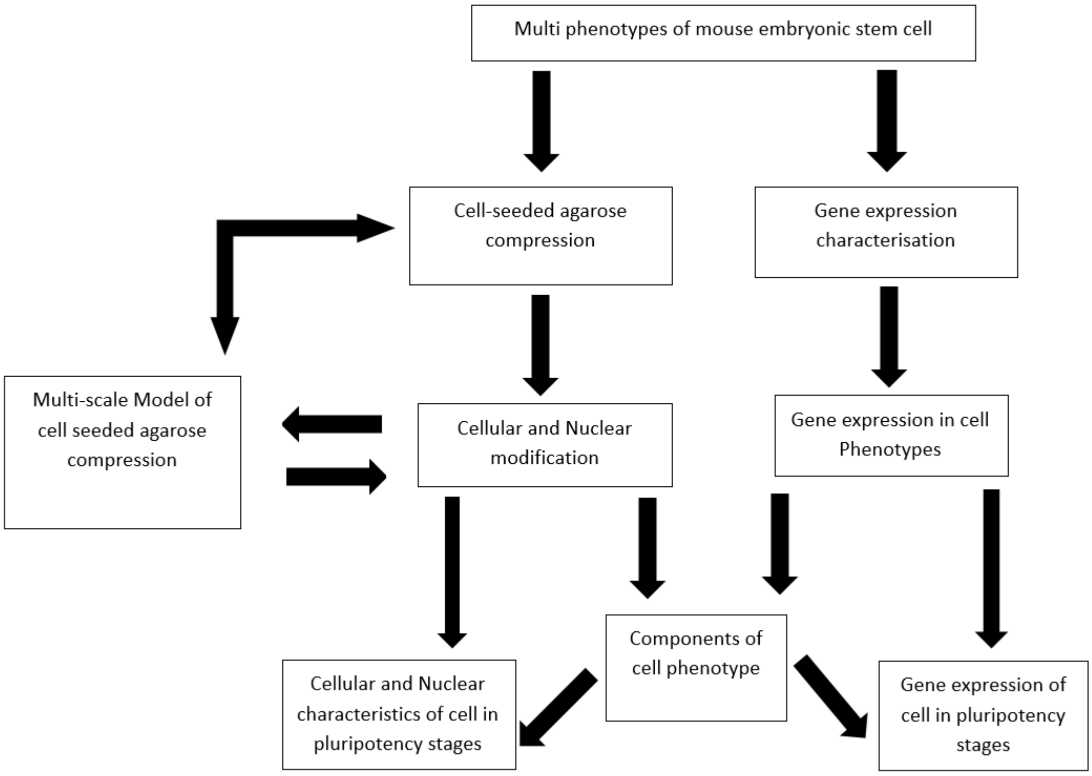

Figure 6.1 Schematic diagram that shows the work process in this thesis.

6.2 The connection between mechanical characteristics modification and gene expression modification during pluripotency state transmits

It is well accepted that mouse embryonic stem cell have two different pluripotent states, defined as naïve and primed states, and these are characterized by differing expression levels of pluripotency genes such as Oct-4 and Nanog. In this thesis, we used the 2i medium to culture mouse embryonic stem cells with overall higher pluripotency levels, consistent with the naïve-like state, when compared to the more common mouse embryonic stem cell culture conditions with serum and LIF. In our initial experiment design, we defined 2i mES cells as possessing the naïve state cell phenotype and the LIF mES cells as primed-like state cells. However, further analysis suggested that the LIF mES cell group contained sub-populations with distinct characteristics, presumably representing both the naïve-like and primed-like states. Chalut's group reported that some embryonic stem cells possessed auxetic nuclei and these cells were considered to be in transition from the naïve to the primed pluripotency states (Pagliarra et al., 2014). The data presented in this thesis is consistent with this view, with the putative primed mES cell sub-population having a greater x-axis dimension than naïve sub-population in LIF mES cell group. Further we report a sub-population of cells that exhibited a reduction in both x and y nucleus dimensions on the application of compression in agarose, consistent with auxeticity. Chalut’s group suggested that chromatin decondensation occurred when the cell exits the naïve-like state, providing a greater possibility for gene expression modification as pluripotency levels decayed (Chalut, 2015). Again the findings in this work are in agreement, notably the appearance of cells in the LIF/- P2 condition with negative y-axis strain during compression.

In this thesis, we found major alterations in nuclear morphology and mechanical phenotype in the different pluripotency states and the nuclear size and stiffness modification was complex. In this thesis, we considered that the LIF mES cell group contains both naïve-like and primed-like state cells. During differentiation following LIF withdrawal a shift in the proportions of cells in the naïve-like, primed-like and differentiating states is proposed. At LIF/- P1 the molecular and mechanical phenotypic characteristics of the mES cell population is consistent with a mixture of primed-like state cell and differentiating state cell. Analysis of nuclear x-axis dimension combining the data in chapter 3 and 4 demonstrated that the 2i mES cell population was predominantly naïve state cells with small nuclear size compared with primed-like state cells present as a sub-population in LIF mES cell system. Notably the population characteristics of the 2i/- mES cells, following LIF and inhibitor withdrawal was similar to the LIF mES cell state, suggesting induction of transition from the naïve-like to the primed-like state. When LIF was withdrawn from the LIF mES cell culture, a multistage transition is proposed, depending on the initial phenotype the heterogeneous population. The primed-like state sub-population transition directly to the differentiated state while the naïve-like state sub-population transitions first to the primed-like state prior to differentiation. Figure 4.8 indicated that the bimodal distribution of nuclear x-axis dimension in the LIF mES cells was progressively lost following LIF withdrawal with a single population evident at LIF/- P2. Notably, during LIF withdrawal the sub-population with the smallest nuclei is lost progressively during culture consistent with transition from the naïve-like to the primed-like state. Furthermore, there is evidence of a shift in the median x-axis dimension of the single population at LIF/- P2 compared to the primed-like state cell sub-population in LIF mES cells prior to LIF withdrawal suggesting that mouse embryonic stem nucleus might shrink during cell differentiation. Chalut reported that chromatin condensation was observed during differentiation (Chalut 2014) and this might explain the reduction in nuclear size when the cell exits the primed state and differentiates. In conclusion, the nucleus size might experience a series of modifications as shown in Figure 6.2.

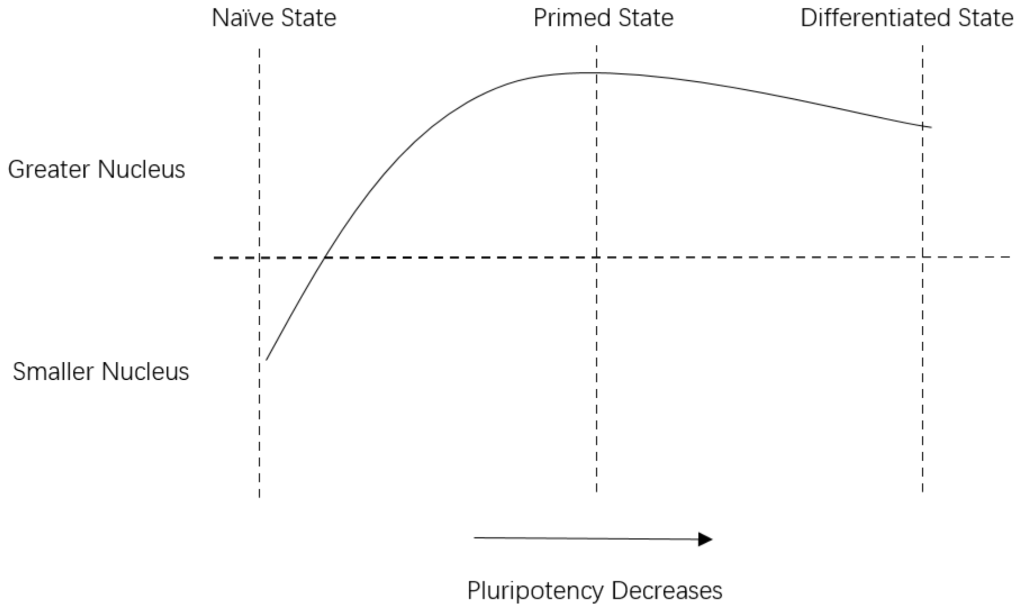

Figure 6.2 Curve describing nucleus size modification during transition from the pluripotent state toward differentiation.

As the pluripotency levels of mouse embryonic stem cells decreases, other factors may alter the nuclear stiffness beside chromatin structure modification. Figure 6.3 describes the nuclear stiffness changes when cell transited from naïve state to differentiated state. Primed state cells have softer nuclei than naïve state cell potentially due to chromatin decondensation which also leads to more active gene expression and less resistance to mechanical stimulation. Each of these factors may make the cell more conducive to the triggering of further differentiation in response to external stimuli. According to figure 6.2, as differentiation proceeds the nuclei shrink when the cell exits the primed state due to chromatin condensation, and this might cause the stiffer nucleus observed in the differentiating cell state cell, manifested in the current study as greater resistance to deformation. Furthermore, the additional effects of alterations in lamin expression and organisation in the differentiating state cells may additionally stiffen the nucleus, as described perviously (Swift et al., 2013). Additionally, the LIF-removal approach to triggering differentiation does not favour a specific lineage and the differentiating cell population may contain sub-populations differentiating toward a variety of differentiated cell lineages. Since stiffness among differentiated cells differs greatly and correlates with resultant tissue stiffness it is likely that the differentiating cell population will be heterogeneous, including some cells with nuclei softer than in primed state. This heterogeneity was evident in the LIF/- P1 and LIF/- P2 cells, for example in Figure 4.15 and 16.

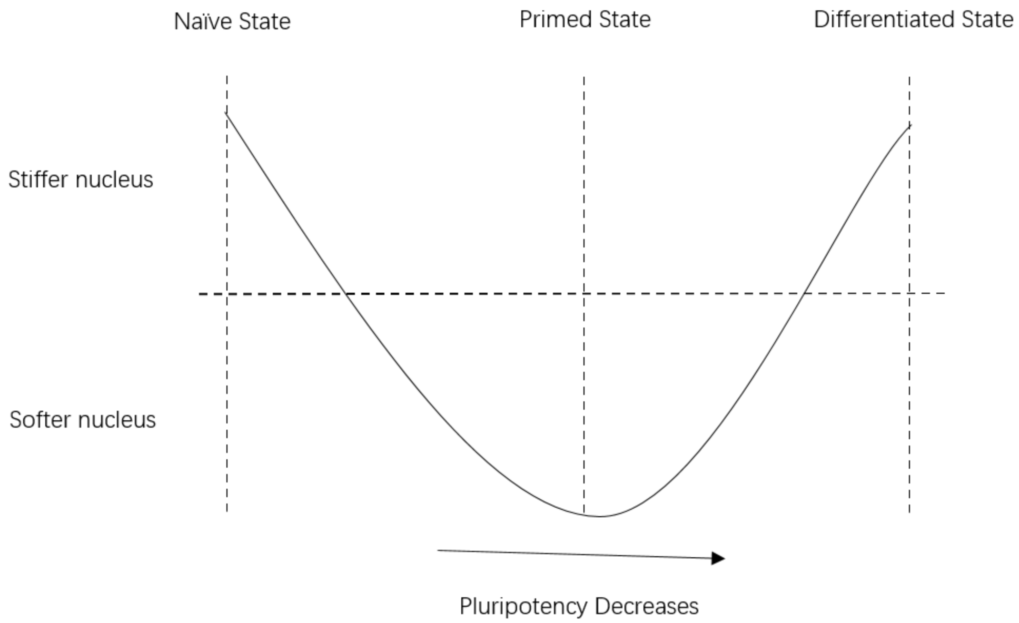

Figure 6.3 Curve describing nucleus stiffness modification during transition from the pluripotent state toward differentiation

In this thesis studies have suggested that nuclear mechanical properties and modification of the pluripotency state results from alterations in the nucleoplasm including chromatin condensation and decondensation. Accordingly these mechanical and nuclear organizational phenotypic markers may be used to determine pluripotency levels in mouse embryonic stem cell in additional to the traditional molecular biology characterization of pluripotency gene expression. Moreover, the findings suggest a role of chromatin/chormosome territory positioning in regulating the nucleus resistance to mechanical perturbation and gene expression levels. This might be key to understand the mechanisms that regulate the balance of the naïve, primed and differentiating states in cells derived from one cell colony or one embryo.

6.3 Evaluation of the multi-scale model with previous studies

Chapter 5 describes the establishment of an Abaqus muliti-scale model and its application, including calculating cellular mechanical parameters and predicting compression loading result. The multi-scale model provided two major contributions to the whole study in this thesis. The first is that the model provides accurate characterization of the agarose deformation, which helps better analysis of the confocal microscope images obtained in the experimental studies. The gross compressive strain of agarose compression was set as 0%, 10% 20% in the experimental protocol. However, the compressive strain settings were programmed to control the operation of mechanical rig and its loading platens rather than to achieve equivalent actual agarose strain in microscopy imaging area. The macro-scale model simulated that the actual agarose x-axis strain next to the coverslip ranged from 8% to 11% depending on the position immediately following the application of 10% gross x-axis strain which attained levels of 9.5% to 10.3% after relaxation period. The range of agarose strains predicted from the model simulation provides additional details and improvements in analyzing cellular and nuclear alterations in response to compressive strain. The other contribution of multi-scale model was to simulate cellular response to compression in areas which cannot be observed experimentally. For example, the model suggested the x-axis strain in the centre of the agarose construct is less than the bottom of agarose construct (See Chapter 5). This may lead to a distribution in cellular strains in different locations, resulting in different nuclear modification and gene expression regulation.

Besides its specific contribution in the thesis work, the multi-scale model is also important in the application of the outcome of this thesis for broader use. While many researchers have proposed the development of cell-seeded scaffold systems specifically designed to control differentiation via mechanical perturbation, progress has been limited. Currently the focus remains on the material synthesis and surface decoration of cell-seeded scaffold (Gutiérrez-Hernándeza et al., 2017 Griera et al., 2017), in which cells are applied as passive tool to test the biotoxicity and biocompatibility. In research of stem cell seeded scaffold systems for potential controllable differentiation, the stiffness of material may be a key parameter in influencing cell differentiation without further external mechanical perturbation. (Reboredo et al., 2016, Lin et al., 2016). Moreover research investigating external mechanical mechanical stimulation of gene expression, such as involving bioreactor design, lacks predictive analysis of the mechanical response to loading at the cellular and nuclear levels. In addition the material selection is limited (Cochis et al., 2017). This thesis emphasizes the mutually dependent effects of scaffold stiffness, nuclear resistance to mechanical perturbation, nuclear mechanical properties and regulation of gene expression. Accordingly future tissue engineering studies may adopt a multi-parameter approach to the design systems for controllable stem cell differentiation to achieve greater impact.

Figure 6.4 outlines the potential benefits of building multi-parameter approaches to achieve controllable stem cell differentiation in cell-seeded scaffold. Stem cell could be modified (i.e. cell culture modification, gene knockdown) to induce specified gene expression profiles and mechanical properties. The critical involvement of the nucleus in determining both the mechanical properties of the cell and its gene expression profile is clear. For example, the nucleoplasm stiffness in stem cells may be in a range that is not comparable to other cell types, leading to different response to mechanical perturbation. With proper model simulation, the loading process (or shear stress) could be predicted and monitored in the scaffold with an understanding of regionally-defined variations within the 3D structure. The advantage of a multi-field design is to amplify the specific mechanical perturbation to triggering epigenetic modifications which may ultimately modulate stem cell differentiation in a controllable manner.

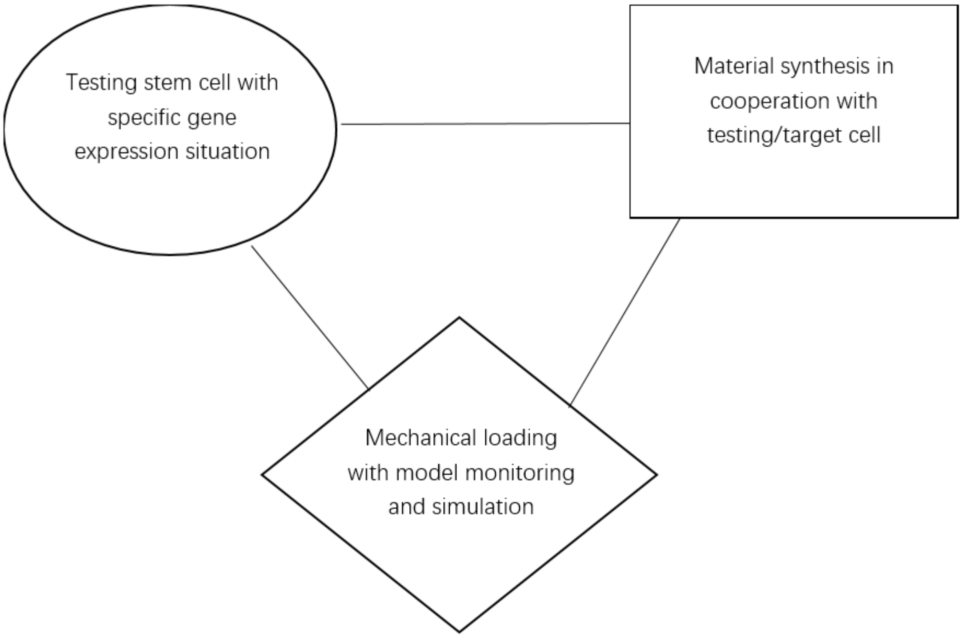

Figure 6.4 Multi-parameter approach to the design for controllable stem cell differentiation in cell-seeded scaffold systems.

6.4 Future work

In current study, the connection between the nuclear mechanical characteristics and gene expression profiles was reveal in different pluripotency and differentiating phenotypes of mouse embryonic stem cell. A balance between the primed and naïve cell states was observed in the LIF mES cells. However the relative proportions of two cell types was not determined and the mechanisms controlling maintenance of phenotype or transition from naïve to primed and differentiating states remains unclear.

In this thesis, compression loading applied to cells and nuclear strains were recorded and linked to chromatin modification. It remains to be elucidated whether chromatin modification involving condensation and decondensation events and induced by chemical or mechanical stimuli directly impacts gene expression. Chromatin condensation in embryonic stem cell is believed to be involved in the maintenance of pluripotency. Accordingly defined mechanical loading that acts to induce chromatin condensation may help maintain pluripotency in LIF mES cell. Further studies should focus on this hypothesis to determine whether the maintenance of pluripotent states and/or differentiation can be induced via mechanical perturbation alone, without alterations in the biochemical stimuli linked to different medium formulations. It is commonly accepted that transition from primed state to naïve state is only achieved through cellular reprogramming and it is tempting to speculate whether mechanical perturbation with associated chromatin modification in primed cells can trigger epigenetic modification to raise pluripotency expression to naïve state levels.

The macro-scale model of agarose was completed and tested. However, the micro-scale model required further development since it could not accurately predict alterations in the cell and nuclear morphology determined in the experimental studies. The main reason likely relates to the relatively crude assumptions of interaction of extracellular matrix (ECM) with the cell and the internal heterogeneity of mechanical properties within the cell involving the cytoplasm, cytoskeleton and nucleus. Previous studies have reported models that better incorporate the complete actin system in the cell. Moreover, the cytoplasm exhibits non-linear properties. Accordingly the micro-scale modelling of the cell-agarose construct should be developed further, notably to improve simulation of effects at the cell-nucleus level. To achieve this it is important to determine the transfer of external mechanical perturbation through the cytoplasm to the nucleus. In addition further work aimed at modelling the interactions between the nucleus, LINC complex and cytoskeleton may predict the balance between nuclear rotation and nuclear deformation within individual cells on the basis of their starting morphological features and orientations.

References

Abad, M., L. Mosteiro, C. Pantoja, M. Canamero, T. Rayon, I. Ors, O. Grana, D. Megias, O. Dominguez, D. Martinez, M. Manzanares, S. Ortega and M. Serrano (2013). "Reprogramming in vivo produces teratomas and iPS cells with totipotency features." Nature 502(7471): 340-345.

Akhremitchev, B. B. and G. C. Walker (1999). "Finite sample thickness effects on elasticity determination using atomic force microscopy." Langmuir 15(17): 5630-5634.

Al-Assaf, S., G. O. Phillips and P. A. Williams (2006). "Controlling the molecular structure of food hydrocolloids." Food Hydrocolloids 20(2-3): 369-377.

Allfrey, V. G., R. Faulkner and A. E. Mirsky (1964). "Acetylation and Methylation of Histones and Their Possible Role in the Regulation of Rna Synthesis." Proc Natl Acad Sci U S A 51: 786-794.

Barreto, S., C. H. Clausen, C. M. Perrault, D. A. Fletcher and D. Lacroix (2013). "A multi-structural single cell model of force-induced interactions of cytoskeletal components." Biomaterials 34(26): 6119-6126.

Ben-Shushan, E., J. R. Thompson, L. J. Gudas and Y. Bergman (1998). "Rex-1, a gene encoding a transcription factor expressed in the early embryo, is regulated via Oct-3/4 and Oct-6 binding to an octamer site and a novel protein, Rox-1, binding to an adjacent site." Mol Cell Biol 18(4): 1866-1878.

Betschinger, J., J. Nichols, S. Dietmann, P. D. Corrin, P. J. Paddison and A. Smith (2013). "Exit from pluripotency is gated by intracellular redistribution of the bHLH transcription factor Tfe3." Cell 153(2): 335-347.

Boiani, M., S. Eckardt, H. R. Scholer and K. J. McLaughlin (2002). "Oct4 distribution and level in mouse clones: consequences for pluripotency." Genes Dev 16(10): 1209-1219.

Boroviak T., R. Loos, P. Bertone, A. Smith and J. Nichols (2014). “The ability of inner-cell-mass cells to self-renew as embryonic stem cells is acquired following epiblast specification” Nature Cell Biology 16, 513–525.

Boroviak T., R. Loos, P.X Lombard, J. Okahara, R. Behr, E. Sasaki, J. Nichols, A. Smith and P.Bertone (2015). “Lineage-specific profiling delineates the emergence and progression of naive pluripotency in mammalian embryogenesis.” Dev Cell, 35:366-382

Brons, I. G., L. E. Smithers, M. W. Trotter, P. Rugg-Gunn, B. Sun, S. M. Chuva de Sousa Lopes, S. K. Howlett, A. Clarkson, L. Ahrlund-Richter, R. A. Pedersen and L. Vallier (2007). "Derivation of pluripotent epiblast stem cells from mammalian embryos." Nature 448(7150): 191-195.

Buckley, C. T., S. D. Thorpe, F. J. O'Brien, A. J. Robinson and D. J. Kelly (2009). "The effect of concentration, thermal history and cell seeding density on the initial mechanical properties of agarose hydrogels." J Mech Behav Biomed Mater 2(5): 512-521.

Buehr, M., S. Meek, K. Blair, J. Yang, J. Ure, J. Silva, R. McLay, J. Hall, Q. L. Ying and A. Smith (2008). "Capture of authentic embryonic stem cells from rat blastocysts." Cell 135(7): 1287-1298.

Burke, B. and C. L. Stewart (2013). "The nuclear lamins: flexibility in function." Nat Rev Mol Cell Biol 14(1): 13-24.

Calo, E. and J. Wysocka (2013). "Modification of enhancer chromatin: what, how, and why?" Mol Cell 49(5): 825-837.

Chachisvilis, M., Y. L. Zhang and J. A. Frangos (2006). "G protein-coupled receptors sense fluid shear stress in endothelial cells." Proc Natl Acad Sci U S A 103(42): 15463-15468.

Chambers, I., D. Colby, M. Robertson, J. Nichols, S. Lee, S. Tweedie and A. Smith (2003). "Functional expression cloning of Nanog, a pluripotency sustaining factor in embryonic stem cells." Cell 113(5): 643-655.

Chen, Y., L. Shi, L. Zhang, R. Li, J. Liang, W. Yu, L. Sun, X. Yang, Y. Wang, Y. Zhang and Y. Shang (2008). "The molecular mechanism governing the oncogenic potential of SOX2 in breast cancer." J Biol Chem 283(26): 17969-17978.

Cheresh, D. A., S. A. Berliner, V. Vicente and Z. M. Ruggeri (1989). "Recognition of distinct adhesive sites on fibrinogen by related integrins on platelets and endothelial cells." Cell 58(5): 945-953.

Choi, H. W., J. Y. Joo, Y. J. Hong, J. S. Kim, H. Song, J. W. Lee, G. Wu, H. R. Scholer and J. T. Do (2016). "Distinct Enhancer Activity of Oct4 in Naive and Primed Mouse Pluripotency." Stem Cell Reports 7(5): 911-926.

Chowdhury, F., S. Na, D. Li, Y. C. Poh, T. S. Tanaka, F. Wang and N. Wang (2010). "Material properties of the cell dictate stress-induced spreading and differentiation in embryonic stem cells." Nat Mater 9(1): 82-88.

Chalut, K.J., (2015) "Nuclear mechanics and shape in embryonic stem cells exiting pluripotency." Eur Biophys J S220-S22

Christophersen, N. S. and K. Helin (2010). "Epigenetic control of embryonic stem cell fate." J Exp Med 207(11): 2287-2295.

Cochis, A., S. Grad, M. J. Stoddart, S. Fare, L. Altomare, B. Azzimonti, M. Alini and L. Rimondini (2017). "Bioreactor mechanically guided 3D mesenchymal stem cell chondrogenesis using a biocompatible novel thermo-reversible methylcellulose-based hydrogel." Sci Rep 7: 45018.

Cockburn, K., and J. Rossant. (2010) “Making the blastocyst: lessons from the mouse.” J Clin Invest Apr 1; 120(4): 995–1003.

Constantinescu D., H. L. Gray, P. J. Sammak, G. P. Schatten and A. B. Csoka (2006). "Lamin A/C Expression Is a Marker of Mouse and Human Embryonic Stem Cell Differentiation." Stem cell 24(1): 177–185

Cooper G.M. and R.E. Hausman (2000). “The Cell” Boston University.

Crisp, M., Q. Liu, K. Roux, J. B. Rattner, C. Shanahan, B. Burke, P. D. Stahl and D. Hodzic (2006). "Coupling of the nucleus and cytoplasm: role of the LINC complex." J Cell Biol 172(1): 41-53.

Deboer, R. and W. Ehlers (1986). "On the Problem of Fluid-Filled and Gas-Filled Elastoplastic Solids." International Journal of Solids and Structures 22(11): 1231-1242.

Ding, X., R. Xu, J. Yu, T. Xu, Y. Zhuang and M. Han (2007). "SUN1 is required for telomere attachment to nuclear envelope and gametogenesis in mice." Dev Cell 12(6): 863-872.

Ehlers, W. (1997). "Theoretical and numerical modelling of granular liquid-saturated elasto-plastic porous media." Zeitschrift Fur Angewandte Mathematik Und Mechanik 77: S401-S404.

Ehlers, W. and B. Markert (2000). "On the viscoelastic behaviour of fluid-saturated porous materials." Granular Matter 2(3): 153-161.

Ehlers, W. and B. Markert (2001). "A linear viscoelastic biphasic model for soft tissues based on the theory of porous media." Journal of Biomechanical Engineering-Transactions of the Asme 123(5): 418-424.

Ehlers, W. and W. Volk (1997). "On shear band localization phenomena of liquid-saturated granular elastoplastic porous solid materials accounting for fluid viscosity and micropolar solid rotations." Mechanics of Cohesive-Frictional Materials 2(4): 301-320.

Ehlers, W. and W. Volk (1998). "On theoretical and numerical methods in the Theory of Porous Media based on polar and non-polar elasto-plastic solid materials." International Journal of Solids and Structures 35(34-35): 4597-4617.

Eijkelkamp, N., K. Quick and J. N. Wood (2013). "Transient receptor potential channels and mechanosensation." Annu Rev Neurosci 36: 519-546.

ESHRE Task Force on Ethics and Law (2001). "The moral status of the pre-implantation embryo". Human Reproduction 16(5): 1046-1048

Evans, M. J. and M. H. Kaufman (1981). "Establishment in culture of pluripotential cells from mouse embryos." Nature 292(5819): 154-156.

Feldherr, C. M. and D. Akin (1990). "The permeability of the nuclear envelope in dividing and nondividing cell cultures." J Cell Biol 111(1): 1-8.

Friedl, P. and S. Alexander (2011). "Cancer invasion and the microenvironment: plasticity and reciprocity." Cell 147(5): 992-1009.

Geiger, B., J. P. Spatz and A. D. Bershadsky (2009). "Environmental sensing through focal adhesions." Nat Rev Mol Cell Biol 10(1): 21-33.

Georgatos, S. D. and G. Blobel (1987). "Two distinct attachment sites for vimentin along the plasma membrane and the nuclear envelope in avian erythrocytes: a basis for a vectorial assembly of intermediate filaments." J Cell Biol 105(1): 105-115.

Gilbert S.F. (2009). “Ecological Development Biology” Wiley Online Library.

Gomez de Leon, C. T., R. D. Diaz Martin, G. Mendoza Hernandez, S. Gonzalez Pozos, J. R. Ambrosio and R. Mondragon Flores (2014). "Proteomic characterization of the subpellicular cytoskeleton of Toxoplasma gondii tachyzoites." J Proteomics 111: 86-99.

Green, A. E., P. M. Naghdi and J. A. Trapp (1970). "Thermodynamics of a Continuum with Internal Constraints." International Journal of Engineering Science 8(11): 891-&.

Grier, W. K., E. M. Iyoha and B. A. Harley (2017). "The influence of pore size and stiffness on tenocyte bioactivity and transcriptomic stability in collagen-

GAG scaffolds." J Mech Behav Biomed Mater 65: 295-305.

Gu, W. Y., W. M. Lai and V. C. Mow (1997). "A triphasic analysis of negative osmotic flows through charged hydrated soft tissues." Journal of Biomechanics 30(1): 71-78.

Gu, W. Y., H. Yao, C. Y. Huang and H. S. Cheung (2003). "New insight into deformation-dependent hydraulic permeability of gels and cartilage, and dynamic behavior of agarose gels in confined compression." Journal of Biomechanics 36(4): 593-598.

Guilak, F. and V. C. Mow (2000). "The mechanical environment of the chondrocyte: a biphasic finite element model of cell-matrix interactions in articular cartilage." J Biomech 33(12): 1663-1673.

Guilak, F., J. R. Tedrow and R. Burgkart (2000). "Viscoelastic properties of the cell nucleus." Biochem Biophys Res Commun 269(3): 781-786.

Gulrez S.K.H., S. Al-Assaf, G.O. Philips (2011) " Chapter 5: Hydrogels: methods of preparation, characterisation and applications." From "Progress in Molecular and Environmental Bioengineering - From Analysis and Modeling to Technology Applications" Published by InTech

Guo, G., J. Yang, J. Nichols, J. S. Hall, I. Eyres, W. Mansfield and A. Smith (2009). "Klf4 reverts developmentally programmed restriction of ground state pluripotency." Development 136(7): 1063-1069.

Hackett, J. A. and M. A. Surani (2014). "Regulatory principles of pluripotency: from the ground state up." Cell Stem Cell 15(4): 416-430.

Hatami-Marbini, H. and E. Etebu (2013). "Hydration dependent biomechanical properties of the corneal stroma." Exp Eye Res 116: 47-54.

Hayes, W. C. and A. J. Bodine (1978). "Flow-Independent Viscoelastic Properties of Articular-Cartilage Matrix." Journal of Biomechanics 11(8-9): 407-419.

Hayes, W. C. and A. J. Bodine (1978). "Flow-Independent Viscoelastic Properties of Articular-Cartilage Matrix." Journal of Biomechanics 11(8-9): 407-419.

Heo, S. J., T. P. Driscoll, S. D. Thorpe, N. L. Nerurkar, B. M. Baker, M. T. Yang, C. S. Chen, D. A. Lee and R. L. Mauck (2016). "Differentiation alters stem cell nuclear architecture, mechanics, and mechano-sensitivity." Elife 5.

Huang, C. Y. C., K. L. Hagar, L. E. Frost, Y. B. Sun and H. S. Cheung (2004). "Effects of cyclic compressive loading on chondrogenesis of rabbit bone-marrow derived mesenchymal stem cells." Stem Cells 22(3): 313-323.

Huang, C. Y. C., K. L. Hagar, L. E. Frost, Y. B. Sun and H. S. Cheung (2004). "Effects of cyclic compressive loading on chondrogenesis of rabbit bone-

marrow derived mesenchymal stem cells." Stem Cells 22(3): 313-323.

Huangfu, D., R. Maehr, W. Guo, A. Eijkelenboom, M. Snitow, A. E. Chen and D. A. Melton (2008). "Induction of pluripotent stem cells by defined factors is greatly improved by small-molecule compounds." Nat Biotechnol 26(7): 795-797.

Irianto, J., J. Swift, R. P. Martins, G. D. McPhail, M. M. Knight, D. E. Discher and D. A. Lee (2013). "Osmotic Challenge Drives Rapid and Reversible Chromatin Condensation in Chondrocytes." Biophysical Journal 104(4): 759-769.

Irianto, J., Y. Xia, C. R. Pfeifer, R. A. Greenberg and D. E. Discher (2017). "As a Nucleus Enters a Small Pore, Chromatin Stretches and Maintains Integrity, Even with DNA Breaks." Biophys J 112(3): 446-449.

Irianto, J., Y. T. Xia, C. R. Pfeifer, R. A. Greenberg and D. E. Discher (2017). "As a Nucleus Enters a Small Pore, Chromatin Stretches and Maintains Integrity, Even with DNA Breaks." Biophysical Journal 112(3): 446-449.

Kabla A.J., K. Chalut (2014). "Auxetic nuclei in embryonic stem cells." Biophysical Journal 112(3): 446-449. Medecine sciences: M/S 30(12): 1061-1063

Kanatsu-Shinohara, M., K. Inoue, J. Lee, M. Yoshimoto, N. Ogonuki, H. Miki,

S. Baba, T. Kato, Y. Kazuki, S. Toyokuni, M. Toyoshima, O. Niwa, M. Oshimura, T. Heike, T. Nakahata, F. Ishino, A. Ogura and T. Shinohara (2004). "Generation of pluripotent stem cells from neonatal mouse testis." Cell 119(7): 1001-1012.

Keller G., M. Kennedy, T. Papayannopoulou, M. V. Wiles (1993)."Hematopoietic commitment during embryonic stem cell differentiation in culture." Mol. Cell. Biol. January 13(1) 473-486.

Kim, D., C. H. Kim, J. I. Moon, Y. G. Chung, M. Y. Chang, B. S. Han, S. Ko, E. Yang, K. Y. Cha, R. Lanza and K. S. Kim (2009). "Generation of human induced pluripotent stem cells by direct delivery of reprogramming proteins." Cell Stem Cell 4(6): 472-476.

Kim Y., A. A. Sharov, K. McDole, M. Cheng, H. Hao, C. Fan, N. Gaiano, M.S.H. Ko and Y. Zheng (2011). "Mouse B-Type Lamins Are Required for Proper Organogenesis But Not by Embryonic Stem Cells." Science 334(6063): 1706-1710

Kirby, T. J. and J. Lammerding (2016). "Cell mechanotransduction: Stretch to express ." Nat Mater 15(12): 1227-1229.

Knochel, S., K. Dillinger, M. Koster and W. Knochel (2001). "Structure and expression of Xenopus tropicalis BMP-2 and BMP-4 genes." Mech Dev 109(1): 79-82.

Krause, M., J. Te Riet and K. Wolf (2013). "Probing the compressibility of tumor cell nuclei by combined atomic force-confocal microscopy." Phys Biol 10(6): 065002.

Lammerding, J., L. G. Fong, J. Y. Ji, K. Reue, C. L. Stewart, S. G. Young and R. T. Lee (2006). "Lamins A and C but not lamin B1 regulate nuclear mechanics." J Biol Chem 281(35): 25768-25780.

Lansman, J. B., T. J. Hallam and T. J. Rink (1987). "Single stretch-activated ion channels in vascular endothelial cells as mechanotransducers?" Nature 325(6107): 811-813.

Lee, D. A., S. P. Frean, P. Lees and D. L. Bader (1998). "Dynamic mechanical compression influences nitric oxide production by articular chondrocytes seeded in agarose." Biochem Biophys Res Commun 251(2): 580-585.

Lee, D. A., M. M. Knight, J. F. Bolton, B. D. Idowu, M. V. Kayser and D. L. Bader (2000). "Chondrocyte deformation within compressed agarose constructs at the cellular and sub-cellular levels." J Biomech 33(1): 81-95.

Lee, Y. W., C. B. Klein, B. Kargacin, K. Salnikow, J. Kitahara, K. Dowjat, A. Zhitkovich, N. T. Christie and M. Costa (1995). "Carcinogenic nickel silences gene expression by chromatin condensation and DNA methylation: a new model for epigenetic carcinogens." Mol Cell Biol 15(5): 2547-2557.

Leeb, M., R. Walker, B. Mansfield, J. Nichols, A. Smith and A. Wutz (2012). "Germline potential of parthenogenetic haploid mouse embryonic stem cells." Development 139(18): 3301-3305.

Leitch H.G., McEwen K.R., Turp A, Encheva V, Carroll T, Grabole N, Mansfield W, Nashun B, Knezovich J.G., Smith A et al. (2013) “Naive pluripotency is associated with global DNA hypomethylation.” Nat Struct Mol Biol 20:311-316.

Lieberman-Aiden, E., N. L. van Berkum, L. Williams, M. Imakaev, T. Ragoczy, A. Telling, I. Amit, B. R. Lajoie, P. J. Sabo, M. O. Dorschner, R. Sandstrom, B. Bernstein, M. A. Bender, M. Groudine, A. Gnirke, J. Stamatoyannopoulos, L. A. Mirny, E. S. Lander and J. Dekker (2009). "Comprehensive mapping of long-range interactions reveals folding principles of the human genome." Science 326(5950): 289-293.

Lim, Y. C., M. T. Cooling and D. S. Long (2015). "Computational models of the primary cilium and endothelial mechanotransmission." Biomech Model Mechanobiol 14(3): 665-678.

Lin, Y. L., C. P. Chen, C. M. Lo and H. S. Wang (2016). "Stiffness-controlled three-dimensional collagen scaffolds for differentiation of human Wharton's jelly mesenchymal stem cells into cardiac progenitor cells." J Biomed Mater Res A 104(9): 2234-2242.

Liu, J., T. Rolef Ben-Shahar, D. Riemer, M. Treinin, P. Spann, K. Weber, A. Fire and Y. Gruenbaum (2000). "Essential roles for Caenorhabditis elegans lamin gene in nuclear organization, cell cycle progression, and spatial organization of nuclear pore complexes." Mol Biol Cell 11(11): 3937-3947.

Loh, Y. H., Q. Wu, J. L. Chew, V. B. Vega, W. Zhang, X. Chen, G. Bourque, J. George, B. Leong, J. Liu, K. Y. Wong, K. W. Sung, C. W. Lee, X. D. Zhao, K. P. Chiu, L. Lipovich, V. A. Kuznetsov, P. Robson, L. W. Stanton, C. L. Wei, Y. Ruan, B. Lim and H. H. Ng (2006). "The Oct4 and Nanog transcription network regulates pluripotency in mouse embryonic stem cells." Nat Genet 38(4): 431-440.

Lombardi, M. L., D. E. Jaalouk, C. M. Shanahan, B. Burke, K. J. Roux and J. Lammerding (2011). "The interaction between nesprins and sun proteins at the nuclear envelope is critical for force transmission between the nucleus and cytoskeleton." J Biol Chem 286(30): 26743-26753.

Mak, A. F., W. M. Lai and V. C. Mow (1987). "Biphasic Indentation of Articular-Cartilage .1. Theoretical-Analysis." Journal of Biomechanics 20(7): 703-714.

Martin, G. R. (1981). "Isolation of a pluripotent cell line from early mouse embryos cultured in medium conditioned by teratocarcinoma stem cells." Proc Natl Acad Sci U S A 78(12): 7634-7638.

Mauck, R. L., B. A. Byers, X. Yuan and R. S. Tuan (2007). "Regulation of cartilaginous ECM gene transcription by chondrocytes and MSCs in 3D culture in response to dynamic loading." Biomech Model Mechanobiol 6(1-2): 113-125.

Mauck, R. L., X. Yuan and R. S. Tuan (2006). "Chondrogenic differentiation and functional maturation of bovine mesenchymal stem cells in long-term agarose culture." Osteoarthritis and Cartilage 14(2): 179-189.

Mercey, E., P. Obeid, D. Glaise, M. L. Calvo-Munoz, C. Guguen-Guillouzo and B. Fouque (2010). "The application of 3D micropatterning of agarose substrate for cell culture and in situ comet assays." Biomaterials 31(12): 3156-3165.

Michalczyk, K. and M. Ziman (2005). "Nestin structure and predicted function in cellular cytoskeletal organisation." Histol Histopathol 20(2): 665-671.

Mitchell M. (1998). " An introduction to genetic algorithms." MIT Press

Moeendarbary, E., L. Valon, M. Fritzsche, A. R. Harris, D. A. Moulding, A. J. Thrasher, E. Stride, L. Mahadevan and G. T. Charras (2013). "The cytoplasm of living cells behaves as a poroelastic material." Nat Mater 12(3): 253-261.

Mow, V. C., S. C. Kuei, W. M. Lai and C. G. Armstrong (1980). "Biphasic creep and stress relaxation of articular cartilage in compression? Theory and experiments." J Biomech Eng 102(1): 73-84.

Nichols, J., and A. Smith (2009). “Naive and Primed Pluripotent States” Cell Stem Cell Volume 4, Issue 6, 5, Pages 487-492

Nichols, J., B. Zevnik, K. Anastassiadis, H. Niwa, D. Klewe-Nebenius, I. Chambers, H. Scholer and A. Smith (1998). "Formation of pluripotent stem cells in the mammalian embryo depends on the POU transcription factor Oct4." Cell 95(3): 379-391.

Normand, V., D. L. Lootens, E. Amici, K. P. Plucknett and P. Aymard (2000). "New insight into agarose gel mechanical properties." Biomacromolecules 1(4): 730-738.

Orr, A. W., B. P. Helmke, B. R. Blackman and M. A. Schwartz (2006). "Mechanisms of mechanotransduction." Dev Cell 10(1): 11-20.

Pagliara, S., K. Franze, C. R. McClain, G. W. Wylde, C. L. Fisher, R. J. Franklin, A. J. Kabla, U. F. Keyser and K. J. Chalut (2014). "Auxetic nuclei in embryonic stem cells exiting pluripotency." Nat Mater 13(6): 638-644.

Phillips, R. J. (2000). "A hydrodynamic model for hindered diffusion of proteins and micelles in hydrogels." Biophysical Journal 79(6): 3350-3353.

Prevost, J. H. (1982). "Non-Linear Transient Phenomena in Saturated

Porous-Media." Computer Methods in Applied Mechanics and Engineering 30(1): 3-18.

Puckelwartz, M. J., E. Kessler, Y. Zhang, D. Hodzic, K. N. Randles, G. Morris, J. U. Earley, M. Hadhazy, J. M. Holaska, S. K. Mewborn, P. Pytel and E. M. McNally (2009). "Disruption of nesprin-1 produces an Emery Dreifuss muscular dystrophy-like phenotype in mice." Hum Mol Genet 18(4): 607-620.

Rahman E., B. Bordignon, R. Culerrier, F. Peiretti, S. Spicuglia, M. Djabali, J. F. Landrier and M. Fontes (2017). "Ascorbic acid drives the differentiation of mesoderm-derived embryonic stem cells. Involvement of p38 MAPK/CREB and SVCT2 transporter." Molecular Nutrition & Food Research.

Reboredo, J. W., T. Weigel, A. Steinert, L. Rackwitz, M. Rudert and H. Walles (2016). "Investigation of Migration and Differentiation of Human Mesenchymal Stem Cells on Five-Layered Collagenous Electrospun Scaffold Mimicking Native Cartilage Structure." Adv Healthc Mater 5(17): 2191-2198.

Reik W., Dean W., Walter J (2001) “Epigenetic reprogramming in mammalian development.” Science 293:1089-1093

Richards, E. J. and S. C. Elgin (2002). "Epigenetic codes for heterochromatin formation and silencing: rounding up the usual suspects." Cell 108(4): 489-500.

Rohlmann, A., T. Zander, H. Schmidt, H. J. Wilke and G. Bergmann (2006). "Analysis of the influence of disc degeneration on the mechanical behaviour of a lumbar motion segment using the finite element method." Journal of Biomechanics 39(13): 2484-2490.

Russell, A. J. and L. Silpa (2016). "Chemical-Induced Naive Pluripotency." Cell Chem Biol 23(5): 532-534.

Sanz-Moreno, V., G. Gadea, J. Ahn, H. Paterson, P. Marra, S. Pinner, E. Sahai and C. J. Marshall (2008). "Rac activation and inactivation control plasticity of tumor cell movement." Cell 135(3): 510-523.

Scholer, H. R., G. R. Dressler, R. Balling, H. Rohdewohld and P. Gruss (1990). "Oct-4: a germline-specific transcription factor mapping to the mouse t-complex." EMBO J 9(7): 2185-2195.

Schonfeld, G., S. W. Weidman, J. L. Witztum and R. M. Bowen (1976). "Alterations in Levels and Interrelations of Plasma Apolipoproteins Induced by Diet." Metabolism-Clinical and Experimental 25(3): 261-275.

Shi, W., H. Wang, G. Pan, Y. Geng, Y. Guo and D. Pei (2006). "Regulation of the pluripotency marker Rex-1 by Nanog and Sox2." J Biol Chem 281(33): 23319-23325.

Shi, Y., J. T. Do, C. Desponts, H. S. Hahm, H. R. Scholer and S. Ding (2008). "A combined chemical and genetic approach for the generation of induced pluripotent stem cells." Cell Stem Cell 2(6): 525-528.

Shimozaki, K., K. Nakashima, H. Niwa and T. Taga (2003). "Involvement of Oct3/4 in the enhancement of neuronal differentiation of ES cells in neurogenesis-inducing cultures." Development 130(11): 2505-2512.

Smith Z.D., Chan M.M., Mikkelsen T.S., Gu H., Gnirke A., Regev A., Meissner A (2012) “A unique regulatory phase of DNA methylation in the early mammalian embryo. “Nature 484:339-344.

Solovei, I., A. S. Wang, K. Thanisch, C. S. Schmidt, S. Krebs, M. Zwerger, T. V. Cohen, D. Devys, R. Foisner, L. Peichl, H. Herrmann, H. Blum, D. Engelkamp, C. L. Stewart, H. Leonhardt and B. Joffe (2013). "LBR and lamin A/C sequentially tether peripheral heterochromatin and inversely regulate differentiation." Cell 152(3): 584-598.

Sosa, B. A., A. Rothballer, U. Kutay and T. U. Schwartz (2012). "LINC complexes form by binding of three KASH peptides to domain interfaces of trimeric SUN proteins." Cell 149(5): 1035-1047.

Spilker, R. L., J. K. Suh and V. C. Mow (1992). "A Finite-Element Analysis of the Indentation Stress-Relaxation Response of Linear Biphasic Articular-Cartilage." Journal of Biomechanical Engineering-Transactions of the Asme 114(2): 191-201.

Sridharan, R., J. Tchieu, M. J. Mason, R. Yachechko, E. Kuoy, S. Horvath, Q. Zhou and K. Plath (2009). "Role of the murine reprogramming factors in the induction of pluripotency." Cell 136(2): 364-377.

Stejskal, S., L. Tesarova and I. Koutna (2014). "Mysterious role of H3K56ac in embryonic stem cells." Folia Biol (Praha) 60 Suppl 1: 71-75.

Stephens A.D., E. J. Banigan, S.A. Adam, R.D. Goldman, and J. F. Marko (2016). "Chromatin and lamin A determine two different mechanical response regimes of the cell nucleus." Mol. Biol. Cell

Stewart-Hutchinson, P. J., C. M. Hale, D. Wirtz and D. Hodzic (2008). "Structural requirements for the assembly of LINC complexes and their function in cellular mechanical stiffness." Exp Cell Res 314(8): 1892-1905.

Stoppel, W. L., D. L. Kaplan and L. D. Black, 3rd (2016). "Electrical and mechanical stimulation of cardiac cells and tissue constructs." Adv Drug Deliv Rev 96: 135-155.

Stow, D. A. V. and A. J. Bowen (1980). "Physical Model for the Transport and Sorting of Fine-Grained Sediment by Turbidity Currents." Sedimentology 27(1): 31-46.

Stuurman, N., S. Heins and U. Aebi (1998). "Nuclear lamins: their structure, assembly, and interactions." J Struct Biol 122(1-2): 42-66.

Swift, J., I. L. Ivanovska, A. Buxboim, T. Harada, P. C. Dingal, J. Pinter, J. D. Pajerowski, K. R. Spinler, J. W. Shin, M. Tewari, F. Rehfeldt, D. W. Speicher and D. E. Discher (2013). "Nuclear lamin-A scales with tissue stiffness and enhances matrix-directed differentiation." Science 341(6149): 1240104.

Takahashi, K., K. Tanabe, M. Ohnuki, M. Narita, T. Ichisaka, K. Tomoda and S. Yamanaka (2007). "Induction of pluripotent stem cells from adult human fibroblasts by defined factors." Cell 131(5): 861-872.

Tesar, P. J., J. G. Chenoweth, F. A. Brook, T. J. Davies, E. P. Evans, D. L. Mack, R. L. Gardner and R. D. McKay (2007). "New cell lines from mouse epiblast share defining features with human embryonic stem cells." Nature 448(7150): 196-199.

Thorpe, S. D., C. T. Buckley, T. Vinardell, F. J. O'Brien, V. A. Campbell and D. J. Kelly (2008). "Dynamic compression can inhibit chondrogenesis of mesenchymal stem cells." Biochemical and Biophysical Research Communications 377(2): 458-462.

Thorpe, S. D., C. T. Buckley, T. Vinardell, F. J. O'Brien, V. A. Campbell and D. J. Kelly (2010). "The Response of Bone Marrow-Derived Mesenchymal Stem Cells to Dynamic Compression Following TGF-beta 3 Induced Chondrogenic Differentiation." Annals of Biomedical Engineering 38(9): 2896-2909.

Thorpe, S. D. and M. Charpentier (2017). "Highlight on the dynamic organization of the nucleus." Nucleus 8(1): 2-10.

Thorpe, S. D., T. Nagel, S. F. Carroll and D. J. Kelly (2013). "Modulating gradients in regulatory signals within mesenchymal stem cell seeded hydrogels: a novel strategy to engineer zonal articular cartilage." PLoS One 8(4): e60764.

Tong, Z., E. M. Balzer, M. R. Dallas, W. C. Hung, K. J. Stebe and K. Konstantopoulos (2012). "Chemotaxis of cell populations through confined spaces at single-cell resolution." PLoS One 7(1): e29211.

Uzer, G., C. T. Rubin and J. Rubin (2016). "Cell Mechanosensitivity is Enabled by the LINC Nuclear Complex." Curr Mol Biol Rep 2(1): 36-47.

Valhmu, W. B., E. J. Stazzone, N. M. Bachrach, F. Saed-Nejad, S. G. Fischer, V. C. Mow and A. Ratcliffe (1998). "Load-controlled compression of articular cartilage induces a transient stimulation of aggrecan gene expression." Archives of Biochemistry and Biophysics 353(1): 29-36.

Wagner, M., M. P. Schlusener, T. A. Ternes and J. Oehlmann (2013). "Identification of Putative Steroid Receptor Antagonists in Bottled Water: Combining Bioassays and High-Resolution Mass Spectrometry." Plos One 8(8).

Wang, J., S. Rao, J. Chu, X. Shen, D. N. Levasseur, T. W. Theunissen and S. H.

Orkin (2006). "A protein interaction network for pluripotency of embryonic stem cells." Nature 444(7117): 364-368.

Wang, N. (2014). "Stem cell mechanics: auxetic nuclei." Nat Mater 13(6): 540-542.

Wang, N., J. D. Tytell and D. E. Ingber (2009). "Mechanotransduction at a distance: mechanically coupling the extracellular matrix with the nucleus." Nat Rev Mol Cell Biol 10(1): 75-82.

Weinberger L., M. Ayyash, N. Novershtern and J.H. Hanna (2016). "Dynamic stem cell states: naive to primed pluripotency in rodents and humans." Nature Reviews Molecular Cell Biology 17: 155–169

Wei, F., H. Yang, L. Liu and G. Li (2017). "A novel approach for extracting viscoelastic parameters of living cells through combination of inverse finite element simulation and Atomic Force Microscopy." Comput Methods Biomech Biomed Engin 20(4): 373-384.

Wolf, K., M. Te Lindert, M. Krause, S. Alexander, J. Te Riet, A. L. Willis, R. M. Hoffman, C. G. Figdor, S. J. Weiss and P. Friedl (2013). "Physical limits of cell migration: control by ECM space and nuclear deformation and tuning by proteolysis and traction force." J Cell Biol 201(7): 1069-1084.

Worman, H. J. and G. G. Gundersen (2006). "Here come the SUNs: a nucleocytoskeletal missing link." Trends Cell Biol 16(2): 67-69.

Ying, Q.L., Wray. J, Nichols. J, Batlle-Morera. L, Doble .B.,Woodgett J, Cohen P, Smith, A (2008). “The ground state of embryonic stem cell self-renewal. “ Nature 453:519-523.

Zhang, X., K. Lei, X. Yuan, X. Wu, Y. Zhuang, T. Xu, R. Xu and M. Han (2009). "SUN1/2 and Syne/Nesprin-1/2 complexes connect centrosome to the nucleus during neurogenesis and neuronal migration in mice." Neuron 64(2): 173-187.